A mobile, scanning eye-safe lidar for the study of atmospheric aerosol particles and transport processes in the lower troposphere

Dissertation zur Erlangung des Doktorgrades

der Naturwissenschaften (Dr. rer. nat.)

Fakultät Naturwissenschaften

Universität Hohenheim

Institut für Physik und Meteorologie

Vorgelegt von
Sandip Pal

aus Cooch Behar, Indien

2009

This thesis was accepted as a doctoral dissertation in fulfillment of the requirements for the degree "Doktor der Naturwissenschaften" by the Faculty of Natural Sciences at the University of Hohenheim, Stuttgart, Germany on 4 December 2008.

Date of oral examination: 23 January 2009

Examination committee:

Supervisor and reviewer:	Prof. Dr. V. Wulfmeyer Institute for Physics and Meteorology, University of Hohenheim
Co-reviewer:	Prof. Dr. Th. Foken Institute for Micrometeorology, University of Bayreuth
Additional examiner:	Prof. Dr. K. Jetter Institute for Applied Mathematics and Statistics, University of Hohenheim
Dean:	Prof. Dr. H. Breer Faculty of Natural Sciences, University of Hohenheim

Abstract

A high-power eye-safe scanning aerosol lidar system in the ultraviolet wavelength region is introduced for the study of the optical properties of aerosol particles and transport processes in the atmosphere, especially in the atmospheric boundary layer (ABL). This system operates with an average power of 9 W in combination with a 40-cm scanner with a speed of up to $10° s^{-1}$. A modified version of the lidar inversion algorithm is developed for the retrieval of optical properties of aerosols from scanning lidar measurements. The lidar data can be analyzed with previously unachieved temporal and spatial resolution of 0.03 s and 3 m, respectively.

New methods are developed for both scanning and non-scanning lidar systems to study the evolution and structure of the convective boundary layer (CBL). Three advanced techniques namely: logarithm gradient method, inflection point method, and the Haar wavelet transform method are demonstrated for determining the instantaneous CBL height from the high-resolution lidar measurements. The Haar wavelet-based approach is found to be a robust technique for the automated detection of the ABL height. Vertical lidar measurements over an urban valley-like location provided the ABL top to be within 0.7–2.3 km above ground level (AGL). The mean entrainment zone thickness for the quasi-steady CBL is of about 75 m. The aerosol load showed high variability both for a quasi-stationary well-mixed CBL and a CBL during its rapid growth in the morning. The fast Fourier transform based spectral analysis of the instantaneous CBL height time series has yielded a spectral exponent value of 1.502 ± 0.08314, confirming non-stationary behavior of CBL in the morning.

Higher-order moments are calculated with respect to fluctuations of the particle backscatter coefficients for well-mixed CBL conditions under which hygroscopic growth of the aerosol particles can be neglected. The variance spectra show an $f^{-5/3}$ roll-off (inertial subrange) inside the quasi-steady CBL. It is demonstrated that the major part of the inertial subrange is detected and that the integral scale (60-70 s) is significantly larger than the temporal resolution of the lidar system. Consequently, the major part of turbulent fluctuations is resolved. Vertical distribution of the variance, skewness, and kurtosis have reflected the turbulence features with an accuracy that is mainly limited by sampling errors due to turbulence statistics. Negative values of skewness are found inside the CBL while positive values are found in the entrainment zone near the top of the CBL for the quasi-stationary regime. But for the case of a rapidly growing CBL, skewness profile has shown a high variability even inside the CBL, most probably due to the presence of a rapid growth rate of 4-5 m/minute, non-stationarity, and strong residual layer above the CBL.

The optical properties of aerosol particles emitted from a faint source (a livestock farm, located in flat terrain) are determined by means of spatially and temporally high-resolved scanning lidar measurements in combination with a high-resolved atmosphere-microphysics-chemistry model and in-situ aerosol measurements at ground. Both model and lidar results have yielded the particle backscatter coefficient of the aerosol plume to be of about 30 % higher than that of the background aerosol load near the facility. Results show a high spatial and temporal variability of the plume. The lifting height of the plume is found to be of about 20 m AGL near the source and of about 115 m AGL over long distances up to 3 km due to transport in downwind. The aerosol plume has caused an increase of the aerosol number density downwind of up to 5 % in the lowermost 50 m of the ABL.

Combined high-resolution measurements of aerosol optical properties and temperature field over a complex mountainous region with the rotational Raman lidar revealed undulating aerosol-rich layers in the preconvective environment and a gradual warming trend of the lower troposphere as the nearby storm system evolved. Simultaneous measurements of particle backscatter and extinction coefficients, and respective lidar ratios confirm the presence of different particle types in different altitudes. Lidar ratios inside the CBL are found to vary around 35 sr. High-resolution scanning and vertical measurements has shown the CBL height to vary between 0.8 and 1.2 km over the mountain peak. Measurements of aerosol distributions and collocated Doppler lidar derived wind field confirm mountain induced flow modifications.

RHI scan measurements of aerosol optical properties and temperatures showed some more features that were consistent with ascending air motion due to overflow over the ridge. The aerosol layers showed the terrain following flow features. The particle backscatter coefficient is found to be slightly increased within a potential temperature tongue. Small-scale wave structures are determined from the wavelet spectra of the time series of the lidar signal intensity at cirrus layer. Lidar ratio values between the altitudes of cirrus cloud base (5.2 km) and top (8 km) show high vertical variability with a minimum and maximum values of 3 sr and 25 sr, respectively.

Zusammenfassung

Zur Untersuchung optischer Eigenschaften von Aerosolpartikeln und Transportprozessen in der Atmosphäre, speziell in der atmosphärischen Grenzschicht (atmospheric boundary layer, ABL), wird ein augensicheres Hochleistungs-Scanning-Lidarsystem im ultravioletten Wellenlängenbereich vorgestellt. Das System arbeitet mit einer durchschittlichen Leistung von 9 W in Kombination mit einem 40 cm Scanner mit einer Geschwindigkeit bis zu $10° s^{-1}$. Eine modifizierte Version des Lidar-Inversionsalgorithmus zur Rekonstruktion der optischen Eigenschaften von Aerosolpartikeln aus den Scanning-Lidar-Messungen wird entwickelt. Die Lidar-Daten können mit einer bisher nicht erreichten zeitlichen und räumlichen Auflösung von 0,03 s bzw. 3 m analysiert werden.

Zur Untersuchung von Entwicklung und Struktur der konvektiven Grenzschicht (convective boundary layer, CBL) werden neue Verfahren, sowohl für scannende als auch für nicht-scannende Lidar-Systeme, entwickelt. Zur Bestimmung der Höhe der instantanen CBL aus den hochaufgelösten Lidar-Messungen werden drei fortschrittliche Techniken, und zwar: die Methode des logarithmischen Gradienten, die Inflection-Point-Methode und die Wavelet-Transformation nach Haar, angewendet. Die auf Wavelets basierende Methode nach Haar zeigte bemerkenswert gute Resultate. Vertikale Lidar-Messungen über einem städtischen talähnlichen Messplatz ergaben eine Obergrenze der ABL zwischen 0,7 km und 2,3 km über Grund. Die abgeschätzte mittlere Dicke der Entrainmentzone für die quasistabile CBL war etwa 75 m. Die Aerosolpartikelbeladung zeigte eine hohe Variabilität sowohl für eine quasistationäre gut durchmischte CBL wie auch für eine CBL während des schnellen morgendlichen Anwachsens der Schicht. Die auf einer Fast-Fourier-Transformation basierende spektrale Analyse der Höhe der instantanen CBL ergab einen spektralen Exponentenwert von 1,502±0,0314, was das nicht-stationäre Verhalten der CBL am Morgen bestätigt.

Für gut durchmischte CBL-Bedingungen unter denen hygroskopisches Wachstum der Aerosolpartikel vernachlässigt werden kann, Momente höherer Ordnung unter Berücksichtigung von Fluktuationen des Partikelrückstreukoeffizienten berechnet. Die Varianz-Spektren zeigen ein von $f^{-5/3}$ Roll-Off (Inertialbereich) im Innern der quasistabilen CBL. Es wird gezeigt, dass der Großteil des Inertialbereichs nachgewiesen wird und dass die integrale Skala (60 s –70 s) signifikant größer ist als die zeitliche Auflösung des Lidar-Systems. Folglich wird der Großteil der turbulenten Fluktuationen aufgelöst. Die vertikale Verteilung von Varianz, Schiefe und Wölbung spiegelt die Turbulenzeigenschaften mit einer Genauigkeit wider, die hauptsächlich durch Fehler aufgrund der Turbulenzstatistik bestimmt wird. Negative Werte der Schiefe finden sich im Innern der CBL, während positive Werte in der Entrainmentzone nahe der Obergrenze der CBL im quasistationären Bereich beobachtet werden. Im Fall einer schnell anwachsenden CBL zeigte das Schiefe-Profil jedoch selbst im Innern der CBL eine hohe Variabilität, höchstwahrscheinlich aufgrund einer hohen Anwachsrate von 4 m –5 m / Minute, der Nicht-Stationarität und einer starken Restschicht oberhalb der CBL.

Die optischen Eigenschaften der Aerosolpartikel einer schwachen Quelle (ein Bauernhof mit Viehhaltung in ebenem Gelände) werden mittels Messungen mit räumlich und zeitlich hoch aufgelösten Scanning-Lidar-Messungen, in Kombination mit einem hochauflösenden Atmosphären-Mikrophysik-Chemie-Modell und in situ Aerosolpartikel-Messungen am Boden bestimmt. Sowohl die Modell- als auch die Lidar-Ergebnisse ergaben, dass der Partikelrückstreukoeffizient der Abluftfahne etwa 30 % höher ist als der Partikelrückstreukoeffizient der Hintergrund-Aerosolpartikelbeladung nahe der Anlage. Die Ergebnisse zeigen eine große räumliche und zeitliche Variabilität in der Aerosolpartikel-Abluftfahne. Die Anhebung der Aerosolpartikel-Abluftfahne ergibt sich zu etwa 20 m über Grund in Quellennähe und zu etwa 115 m über weite Entferungen bis zu 3 km aufgrund des Transports in Windrichtung. Die Aerosolpartikel-Abluftfahne bewirkte ein Anwachsen der Aerosolpartikel-Anzahldichte in Windrichtung von bis zu 5 % in den untersten 50 m der ABL.

Kombinierte hochauflösende Messungen von Aerosolpartikel-Eigenschaften und Temperaturfeldern mit dem Rotations-Raman-Lidar über einem komplexen bergigen Gebiet machten einerseits wellenförmig verlaufende aerosolpartikelreiche Schichten in der präkonvektiven Umgebung, sowie einen graduellen Erwärmungstrend der unteren Troposphäre, während sich das nahegelegene Sturmsystem entwickelte, deutlich. Simultane Messungen von Partikelrückstreu- und Extinktionskoeffizienten und entsprechenden Lidar-Verhältnissen bestätigen die Anwesenheit verschiedener Arten von Aerosolpartikeln in verschiedenen Höhen. Die Lidar-Verhältnisse im Innern der CBL variieren um einen Wert von 35 sr. Mit hochaufgelösten Scanning- und Vertikalmessungen ergab sich eine CBL-Höhe zwischen 0,8 km und 1,2 km über der Bergspitze. Messungen des Aerosolpartikel-Verteilung und aus Doppler-Lidar ermittelte Windfelder bestätigen durch die Berge induzierte Flussmodifikationen.

RHI-Scan Messungen von Temperatur und optischen Eigenschaften der Aerosolpartikel zeigten einige weitere Merkmale, die mit der Bewegung der Luft über den Bergrücken hinweg konsistent sind. Die Aerosolpartikel-Schichten zeigten Flussmerkmale, die dem Gelände folgen. Der Partikelrückstreukoeffizient zeigte sich innerhalb eines ‘tounges’ der potentiellen Temperatur leicht erhöht. Kleinskalige Wellenstrukturen werden aus den Wavelet-Spektren der Zeitreihen der Rückstreuintensität an Cirrusschichten bestimmt. Werte der Lidarverhältnisse zwischen Cirruswolkenuntergrenze (5,2 km) und Obergrenze (8 km) zeigen hohe vertikale Variabilität mit einem Minimalwert von 3 sr und einem Maximalwert von 25 sr.

CONTENTS

Acronyms

ABL	Atmospheric Boundary Layer
ADC	Analog-to-Digital Converter
AGL	Above Ground Level
ASL	Above Sea Level
APD	Avalanche Photodiode
BD	Beam Dump
BE	Beam Expander
BS	Beam Splitter
BSM	Beam Steering Mirror
BSU	Beam Steering Unit
BW-PLUS	Baden-Württemberg Program Lebensgrundlage Umwelt and ihre Sicherung
CAPE	Convective Available Potential Energy
CBL	Convective Boundary Layer
COPS	Convective and Orographically-induced Precipitation Study
COSI-TRACKS	Convective Storms Virtual Institute, with contribution to TRACKS, Transport and Chemical Conversion in Convective Systems
CIN	Convective Inhibition
DAC	Data Acquisition Code
DFA	Detrended Fluctuation Analysis
DIAL	DIfferential Absorption Lidar
DWD	Deutscher WetterDienst
EZ	Entrainment Zone
EZT	Entrainment Zone Thickness
FFT	Fast Fourier Transform
FWHM	Full Width at Half Maximum
HWT	Haar Wavelet Transform
IF	Interference Filter
IHOP	International H2O Project
ILRC	International Laser Radar Conference
IMK	Institut für Meteorologie und Klimaforschung
IOP	Intensive Observation Period
IPCC	Intergovernmental Panel for Climate Change
IP	Inflection Point
IR	Infrared
K-H	Kelvin-Helmohltz
L	Lenses
LES	Large-Eddy Simulation
LGM	Logarithm Gradient Method
LIDAR	Light Detection And Ranging
LM	Laser Mirror
LOS	Line Of Sight
NBL	Nocturnal Boundary Layer
PD	Photo-Diode
PMT	Photomultiplier Tube
PPI	Plan Position Indicator
PRINCE	PRediction, Identification and trackiNg of Convective cElls
RH	Relative humidity
RHI	Range-Height Indicator
RL	Residual Layer
RRL	Rotational Raman Lidar
RS	RadioSonde
RTI	Range-Time Indicator
UHOH	University of HOhenHeim
UV	UltraViolet
WT	Wavelet Transform

Acknowledgement

With great pleasure, I express my deep sense of gratitude and heartfelt thanks to my supervisor Prof. Dr. Volker Wulfmeyer, Director, Institute of Physics and Meteorology, University of Hohenheim, for giving me the opportunity to conduct the research that was the basis for this dissertation. I am grateful for his untiring efforts, valuable guidance, keen interest and encouragement throughout the course of this work.

I take this opportunity to thank my co-advisor Dr. Andreas Behrendt, Head of the lidar group, Institute of Physics and Meteorology, University of Hohenheim, for enormous help that he had extended from time to time during the period of the work. His scientific vision and enormous encouragement at each step provided me a terrific help to finish this work.

I thank Alvaro Valdebenito, Max Planck Institute of Meteorology, Hamburg, Germany and Dr. Gerhard Lammel, Max Planck Institute of Meteorology; Hamburg, Germany who contributed the LES results and helped to fulfill all the goals of the collaborative project, an important part of this dissertation.

A special thanks belongs to Marcus Radlach, a member of our lidar group, for his friendly support during the various stages of lidar development and experiments. It was a nice experience to work with him.

I acknowledge with thanks the supports from Dr. Andrea Riede and Max Schiller of our lidar group during the COPS field campaign in 2007.

I am grateful to Dr. Christoph Senff, NOAA, USA for providing several IDL tools and fruitful discussion during data analysis.

My thanks are also due to Mr. Heinz Bauer and Mr. Olaf Tapfer for their help during development of data analysis and data acquisition tools.

Thanks to Prof. Roland Wurster and Ms. Küffer for their hard work on the analysis of mass spectra of particle samples collected during PLUS1 campaign. Moreover, Prof. Wurster was kind to proof read my thesis.

Many colleagues at our institute helped me in one way or another including Gerd Wagner, Matthias Grzeschik, Thomas Schwitala, Florian Zus, and Dr. H. -S. Bauer.

I appreciate the help from our colleagues Andreas Wieser and Pieter Groenemeijer at Karlsruhe Institute of Technology, Germany, for proving me the Doppler lidar data and satellite images.

I thank all of my family members and especially my father whose patience and support have been the most important factors in the completion of my goals. I also thank my elder brother Joy and my sister-in-law Jaya for their encouragement. My three sisters were always beside me. I simply cannot express in words their love and support for me. Biggest thanks belong to my girlfriend Parama for her loving support.

I thank my friends for their encouragement and moral support during my stay in Stuttgart. Especially Amar, Amrit, Arun, Sayak, and Rima made my stay in Stuttgart most exciting.

Last but not the least, I thank all my teachers who taught me during my school, college and universities. I received tremendous encouragement from them even during my stay in Germany.

This work is a part of a collaborative project (Baden-Württemberg Program Lebensgrundlage Umwelt und ihre Sicherung) between University of Hohenheim, Stuttgart, Germany and Max Planck Institute for Meteorology, Hamburg, Germany, funded by the Ministry of Environment and Transport of the State of Baden-Württemberg, Germany. The Nd:YAG laser was kindly provided by the Institute for Tropospheric Research (IfT). I thank GKSS Research Center, Germany for donating the mobile platform. I highly acknowledge the support from Jack Fox and his team at National Center for Atmospheric Research (NCAR), Boulder, USA for fabricating and delivering the scanner of the system. I also appreciate the useful information that Jack provided while giving a brief demonstration of the scanner in Hohenheim during his visit in 2005. Many people at our university workshop contributed mechanical works for the modification of the mobile platform.

To my mom

Chapter 1
Introduction and motivation

1.1 Atmospheric aerosol

Aerosols belong to the great group of general disperse systems dealing with very fine particulate collectives in solid, liquid, and gaseous medium. Aerosols are a minor component of the atmosphere, a trace constituent, but their role is amplified by their ubiquity and their interaction with the atmospheric radiation. Typical sizes of aerosol vary from 10^{-4} μm to tens of micrometers. They can be found in concentrations ranging from about 10^{7} to 10^{-6} cm^{-3}, depending upon their size, origin, and location. The study of the atmospheric aerosols is important for a variety of reasons, three of which are: (i) Aerosols influence the climate directly and indirectly by altering the radiative energy transfer through their optical properties (Patadia et al., 2008). Among all other forcing mechanisms, uncertainties in the radiative forcing of earth's radiative budget due to aerosols are maximum (IPCC, 2001), (ii) By serving as cloud condensation nuclei, they influence cloud-microphysical processes and therefore the development of clouds and precipitation which are important for weather and climate prediction and earth's hydrological cycle, and (iii) Aerosols influence air quality (see, Aneja et al., 2008 and references therein), environmental pollution and often cause severe health-hazardous problems in human and any other animals.

Technological advancement, industrial expansion, population growth, urbanization, and man's constant striving for a higher living standard have been responsible for the fast growing of the anthropogenic aerosol concentration (Charlson et al., 1992; IPCC, 2001, 2007). Much interest in atmospheric aerosols has been stimulated by the observed impact of anthropogenic emissions (IPCC, 2007).

Very recently, the fourth assessment report of the Intergovernmental Panel on Climate Change (Forster et al., 2007) has been published. Climate change is acknowledged as the ultimate political challenge worldwide due to the release of IPCC working group report in 2007. According to this report, large uncertainties in the assessment of climate forcing arise from an incomplete understanding of dust processes including production, transport, and removal. Uncertainties include "*both an uncertainty range (value uncertainty) and a level of scientific understanding (structural uncertainty)*". This incomplete knowledge sets an important limit to accurate modeling and forecasting (Ghan and Schwartz, 2007, Gobbi et al., 2000). For instance, due to high temporal and spatial variability of

aerosols, their characterization into climate models is highly uncertain. Therefore, there is an immense importance to emphasize at least on the second one "structural uncertainty" through performing field campaigns for process studies.

Optical properties of aerosol particles are dependent on the distribution of atmospheric temperature (therefore on stability), and the humidity, while the dynamical structures of aerosols are mainly governed by wind direction and speed, and underlying orography. In this regard, the vertical distribution of aerosol optical properties such as particle backscatter coefficient, particle extinction coefficient, and corresponding extinction-to-backscatter ratio in two-three dimensions is considered as one of the relevant and important parameters needed to investigate atmospheric aerosol processes. The quantification of optical properties is necessary for modeling the impact of aerosols on climate.

Aerosols distributed from lower to upper tropospheric region are termed as tropospheric aerosol. The tropospheric aerosol most probably fills 80 % of the whole atmospheric content. Consequently, it consists of the particles having penetrated the active cloud filters (Gong et al., 2007), stirred up in the convective system (Khain et al., 2005) or mixed downward from the stratosphere (Menzies and Tratt, 1995). It is considered as a typically aged aerosol, with some added products released from clouds.

The temporal and spatial variability of the tropospheric aerosols are much higher than any other constituent because of the great diversity and wide distribution of the sources and short residence time of the aerosol particles. Tropospheric aerosols are generally concentrated in the lower-most atmospheric layer, which is called the atmospheric boundary layer (ABL). Investigation of aerosol distribution and aerosol transport processes in the ABL in urban regions are of particular interest due to large pollution events for various anthropogenic activities taking place in these regions. However, our ability to assess these possible impacts is constrained by our limited knowledge of the physical and chemical properties of aerosols of both anthropogenic and natural origin. The spatial and temporal variation of aerosols is important for determining air quality over a given area. Therefore, the physical and chemical properties of aerosols, size distribution, single scattering albedo and their effects on climate change in accordance with the measurement techniques of various parameters related to aerosols are some of the important issues in the present-day aerosol studies.

There are two major aspects of aerosol science. One is related to the long-term measurements of physicochemical properties of aerosols and their distribution in a diverse area or over any particular region and the second one is related to the investigation of the aerosol particles, their properties, and their relationship to the diverse atmospheric processes. First one has an unique benefit so that these can help to develop an aerosol climatology while the second one yields an advantage to advance our knowledge about the aerosol processes taking place in the atmosphere by performing case studies with the measurements obtained during field campaigns (process study). The aerosol process study should always be performed in such a direction that both qualititative and quantitative results are obtained. These results can then help to characterize and classify the processes involved in diverse

meteorological situations. For instance, investigations of optical properties of aerosols, different aerosol layers (e.g., residual layer) during different ABL regimes and aerosol transport processes in different orographical locations (e.g., over valley, flat terrain, complex topography), physical characterization of harmful anthropogenic aerosols leading to environmental pollution, are some of the important areas.

Among various anthropogenic aerosols, hardly studied aerosol particulates are that originated from livestock buildings. There is an increasing awareness of the impact that the livestock facilities have on the environment, especially in countries or regions (e.g., Germany, The Netherlands) with dense animal populations (e.g., Mackiewicz, 1998; Jongbloed and Lenis, 1998; Denby et al., 2008). Emission of varieties of particulates and gases from livestock facilities has been found to be a major source for degrading air and water quality in the vicinity of the livestock buildings. To date little is known about the physical/optical properties of these anthropogenic aerosols from such facilities. Close to such sources, aerosol properties are undergoing rapid changes that affect their properties far away from the source (Lammel et al., 2005).

Some research efforts have been made in the last two decades about the adverse effects of the livestock farming contributing serious environmental pollution (see, among others, Lange et al., 1999; Jongbloed and Lenis, 1998). These emissions are also a major threat to the health of the inhabitants, surrounding the region and to the farmers working inside the facilities (see Praml, 1990; Heederik et al., 1991; Ryalander et al., 1986; Mackiewicz, 1998; and references therein for a brief review of health effects of various dusts emitted from farms). Farm animals and their manure contributes largely to the emission of methane, nitrous oxide, carbon dioxide, ammonia, various sulfates, several inorganic ions etc. (see, Dong et al., 2007; Lammel et al., 2004, 2005; among others for different sources of aerosol types and their constituents in and around livestock facilities).

All these studies have various limitations which are: (a) they can not adequately provide spatial and temporal distributions of the aerosol plume to an extended region, (b) they can not resolve the transport processes in variable environmental conditions, (c) wind-driven dynamics is not fully clear since plumes are measured at certain points, (d) emissions from the farms are not necessarily continuous and point measurements techniques can give erroneous results in those cases when the emission rates are varying, and (e) point sampling arrays may fail to detect the fraction of emitted dust since the dynamic behavior of these aerosol plumes may vary within a fraction of a second.

Therefore, the important questions concerning the detailed transport and vertical extent of these plumes, which are closely related to the respiratory hazards of the inhabitants in the surrounding and to the environmental pollution are still unsolved. Furthermore, Fraigneau et al. (1996) suggested that the prediction of mean concentration might lead to erroneous results if the effect of turbulence is neglected.

A measurement technique should be used which can provide a 3-dimensional distribution of the aerosol optical properties. Such measurements are also important for detailing the relationship/dependencies of aerosol optical properties with/on the prevailing meteorological

parameters/conditions. Furthermore, the measured aerosol optical properties should be compared with the model results in order to obtain a consistent picture of the distribution of the aerosol physical properties.

In addition to the investigation of physical properties of aerosols, another important part in aerosol science is to investigate aerosol transport processes taking place inside the ABL, which is closely related to their physical properties. Investigations of both mean and instantaneous structure of the aerosol processes over an ideal and nearly homogeneous terrain have been extensively studied so far. But, the studies concerning convectively driven atmospheric boundary layer (CBL) structure over mountainous regions have received relatively little attention. In contrast to the aerosol dynamics over flat and horizontally homogeneous terrain, aerosol processes over low-mountain regions are complex due to the effects of orography-induced gravity waves and fully inhomogeneous flow modification due to the presence of valleys in the surroundings. Furthermore, investigation of the aerosol optical properties prior to the development of convective systems over low mountain regions brings additional challenges to the experimentalist but at the same time yields an opportunity to explore at least the physical processes involved in the pre-convective situations over such regions (Rotach and Zardi, 2007). To date, a few research efforts have been initiated in this direction.

1.2 Atmospheric boundary layer

According to the definition of Stull (1988), the ABL is identified as the part of the atmosphere, *"that is directly influenced by the presence of the earth's surface, and responds to surface forcing with a time scale of about an hour or less"*. The temporal and spatial variability of the depth of the ABL, ranging from a few hundred meters to a few km, generally depends upon the nature of the surface (land or ocean) and the prevailing meteorological conditions.

The main contributing factors for the high variability of the ABL over the land surface are radiative heating, orography, and inhomogeneous land use. Over the ocean, which is less dynamic in space and time, the major factors are the advection of air masses and sea surface temperature. Four different sub layers classify the ABL regime which are the mixed layer (ML), the entrainment zone (EZ), the stable boundary layer (SBL), and the residual layer (RL). The classification is available in more detailed in Stull (1988).

Figure 1.1 illustrates an idealized diurnal variation of the structure of the lower atmosphere together with different layers. Solar heating of the Earth's surface drives a convective mixed layer that grows to a maximum height varying from several hundred meters to 3 km or more. The EZ at the top of the mixed layer is an elevated layer characterized by a stable temperature lapse rate that controls the entrainment of air from the free atmosphere.

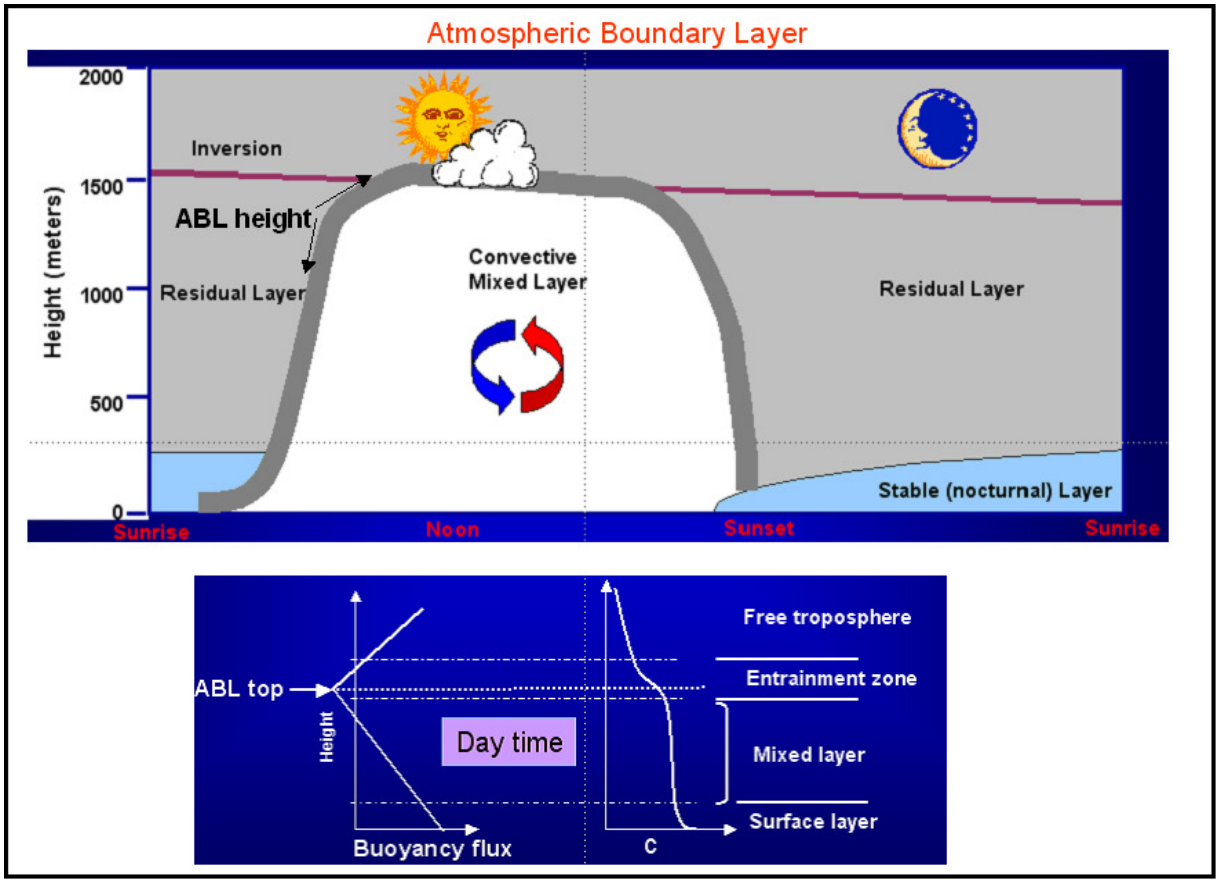

Figure 1.1: Schematic of a classical ABL (adapted from Stull, 1988) evolution (upper panel) and vertical distributions of buoyancy flux (lower left) and the pollutant concentration, C (lower right) during daytime, depicting the various layers of the lower troposphere. Upper panel shows three distinct parts: a very turbulent CBL, a less turbulent residual layer, and a stable boundary layer.

Monitoring of the ABL is an urgent issue in atmospheric science. This layer is characterized by largest variability contrary to any other part of the Earth's atmosphere, while the majority of the sources and sinks are located in the ABL.

The temporal and spatial variability of the ABL depth generally depends on surface forcing, entrainment, and lifting or subsidence. The surface forcing mainly includes frictional drag, evaporation and transpiration, heat transfer, and terrain-induced flow modification. An accurate and precise study of ABL processes is of importance either in the case of parameterization in a general circulation model (Ghan and Schwartz, 2007) or in the case of relatively small-scale feature detection by large-eddy simulation (LES) method (Mayor, 2001; Mayor et al., 2003).

Another interesting aspect of the ABL research is the investigation of stable nocturnal boundary layer (NBL), also called SBL. The SBL develops during nighttime; sometimes a nocturnal jet determines aerosol mixing and transport processes (see, Banta et al., 2003; Newsom and Banta, 2003; among others). A stable layer at the top of the mixing layer acts as a lid to the rising thermals, thus restraining the domain of the turbulence. It is called EZ because entrainment into the ML occurs here. Elevated stable layers play an important role in local circulations, vertical transport, and mixing. The

dynamics and evolution of elevated stable layers during transition and nighttime periods are controlled primarily by moisture and stable aerosol layers within the layer as well as the wind and temperature differences across the layer.

Determination of ABL height in terrain induced urban area and in highly complex topographical regions are of uttermost importance in the atmospheric science community. These processes may include the complexities in the aerosol distribution in different regimes of CBL, interaction of residual layers with the underlying CBL, modification of the aerosol field with atmospheric humidity distribution and stability of the atmosphere, modification of the CBL by the underlying orography, and multitude of dynamical behavior associated with the wave activities and the wind field. Investigation of the ABL processes is an essential element in the improvement of present day weather forecasting model. They play an important role in air mass convection, weakly forced convection, strongly forced convection, and the modification of convergence lines.

The initiation of air mass convection in cases of weak forcing over complex terrain has been identified as a major problem of the numerical weather prediction models (Meißner et al., 2007). There is evidence that the wrong simulation of the boundary layer, entrainment zone, and residual layer including the diurnal/inter-diurnal development is crucial for the deficiencies (Weigel, 2005; Rotach et al., 2008). To develop a new ABL scheme and to evaluate the model performance, simultaneous highly range-resolved measurements of the aerosol optical properties, temperature and humidity fields, ABL height, entrainment layer structure, clouds, residual layer properties are necessary.

The ABL height is also an important parameter characterizing the potential of the boundary layer to take up emitted air pollutants. This height defines the volume for the dilution of air pollutants emitted or formed near the surface and thus the near-surface pollutant concentrations. In earlier studies, it was partly found that the correlation between air pollution and ABL height is inconsistent (Aron, 1983). Those data gave no reliable information on the daily mean ABL height and the diurnal variation of ABL height. With today's availability of remote sensing devices for monitoring the structure of the ABL and the ABL height, a reinvestigation of this correlation is meaningful.

Chapter 2
Lidar remote sensing of aerosol and atmospheric boundary layer

2.1 General perspective

Observations of aerosol dynamics and the characterization of aerosol optical properties in variable atmospheric conditions are of significant importance in many areas of atmospheric science. An important aspect lies in this regard at the measurements of two-to-three dimensional distributions of aerosol optical properties with an unprecedented accuracy both for environmental and meteorological purposes. In general, measurements obtained with active, passive, and in-situ sensors are complementary. Some advantages of remote sensing technique over conventional direct measuring techniques are: (a) the remote sensor does not need to be carried into the medium which is to be measured, (b) the measurement system does not modify the variable being measured, and (c) the atmosphere can be scanned by remote sensing means in two-three dimension, at different altitudes and remote places unlike the single point measurement capabilities of most in-situ systems. All these reasons call for the remote sensing techniques for the purpose of atmospheric aerosol studies.

Optical remote sensing has been extensively used to study the atmospheric aerosol pollutants. These techniques fall into two categories: active and passive remote sensing techniques. Remote sensors can be classified into three different types on the basis of the platform used: ground-based, air borne, and satellite borne.

In passive remote sensing techniques, the changes in properties of electromagnetic waves including energy (absorption and emission), wavelength (frequency shifts), and polarization are measured with an external source of radiation. The natural sources like sun, moon, sky or stars are used for this purpose, and the change observed in the backscattered power and spectral distributions of the corresponding source is utilized to derive information about atmospheric constituents. Vertical distribution of molecules, pressure and temperature can also be inferred through the use of inversion algorithms. But these systems cannot provide high range resolved information of the measured parameter of interest with high accuracy.

In active remote sensing techniques, sources like lasers or artificial lamps, in the ultraviolet (UV), visible and infrared (IR) portion of the spectrum are used in a similar way as in a radar (RAdio

Detection And Ranging) system. The change observed in the backscattered power and spectral distribution of the sources after the propagation through the atmosphere is utilized to derive the information of the atmospheric variables.

2.2 Lidar applications and requirements

2.2.1 Contributions to atmospheric boundary layer studies

Lidar, an acronym for LIght Detection And Ranging is an active remote sensing instrument that transmits electromagnetic radiation and measures radiation after being backscattered by particles and molecules of the atmosphere. The time delay between the emitted pulse and the time of observation is related to the distance at which the scattering has occurred via the velocity of light (Collis, 1966). Lidar uses radiation in the ultraviolet, visible or infrared wavelength region of the electromagnetic spectrum (i.e., 1000 times shorter than that is used in used in radar systems). Consequently, the lidar signal is sensitive to molecules and aerosol particles of the atmosphere. High repetition rate of the laser transmitter and short pulses with high pulse energy permits measurement with high temporal and spatial resolution, respectively. Because the laser pulse is short and the diameter of the beam small, very small volume sections along the laser path in the atmosphere are consecutively probed. For lidar, the small divergence of the laser beam defines lidar volumes of typically only a few cubic meters at ranges of tens of km.

Unlike radars, lidars do not have the problem arising due to ground clutter. Lidar remote sensing technique allows continuous monitoring of the profiles of atmospheric variables with very high temporal and spatial resolution. Lidar signals can readily be interpreted. Different scattering mechanisms permit different kinds of measurements. Detailed descriptions of the principles and applications of different lidar techniques are available in Kovalev and Eichinger (2002) and in Weitkamp (2005).

Lidar systems do not have the potential to make direct measurements of cloud-microphysics. They cannot make measurement in the presence of optically thick clouds. A precise alignment must be maintained all the time during measurements.

An elastic-backscatter lidar signal results mainly due to the Rayleigh scattering and Mie scattering processes. This feature makes lidar remote sensing systems also attractive for studying the ABL, where high-resolution sounding is necessary to capture the variability of the parameters of interest. The ABL dynamical processes that can be studied by lidar include the instantaneous depth of the ABL and its evolution in time, the entrainment zone, and varieties of convective activity patterns with associated dynamics.

The ABL height is determined by characteristic features in profiles of atmospheric variables. Different methodologies are used for the determination of the instantaneous ABL height, which are based on different properties of the turbulent well-mixed boundary layer. The most conventional

method uses in-situ soundings by radiosonde, which gives profiles of wind, temperature, relative humidity (RH), and pressure. The radiosonde profile yields a "snapshot"–view of the atmosphere. This technique has the limitations arising due to poor sampling (Weckwerth et al., 1996). Tethered balloons and aircraft observed profiles are also means for estimating the ABL depth. All these approaches had been found to consist of some shortcomings and measurement uncertainties (see, Seibert et al., 2000 for an intercomparison and review of these methods).

In contrast to radio soundings, active remote sensing systems are capable of providing continuous monitoring of the key-variables of the atmosphere in high spatial and temporal resolutions, leading to much better sampling statistics of the instantaneous ABL height. For this purpose, sodar (e.g., Beyrich and Gryning, 1998), radar wind profilers (e.g., Angevine et al., 1994), lidar system (e.g., Russel et al., 1974) are in use. For more than two decades, ground-based or/and airborne remote sensing techniques are being used as tools to monitor atmospheric parameters and associated dynamics. With lidar a multitude of atmospheric parameters can be observed (see Weitkamp, 2005 for a recent review) which allows investigating also cross-correlations between the lidar backscatter signal and relative humidity (Wulfmeyer and Feingold, 2000). Among all remote sensing techniques, lidar is thus the most comprehensive one because the high-resolution tempo-spatial variability of various scales involved in boundary layer processes can be investigated by this technique. Just recently, also space borne lidar provided (see, Vaughan et al., 2004 for a brief overview of CALIPSO) a global coverage for aerosol monitoring.

Several studies have been performed using lidar systems to determine the structure and variability of the ABL height and to retrieve the entrainment zone thickness (EZT); e.g., Senff et al. (1996), Kiemle et al. (1997), Davis et al. (1997), Cohn et al. (1998), Steyn et al. (1999), Dupont et al. (1999), Menut et al. (1999), Wulfmeyer (1999a, b), Cohn and Angevine (2000), Brooks et al. (2003), He et al. (2006). Furthermore, networks of aerosol lidar systems such as the European Aerosol Research Lidar Network (EARLINET, Matthias et al., 2004), the Asian Dust Network (ADNET, Murayama et al., 2001), and the Micro-Pulse Lidar Network (MPLNET, Welton et al., 2001) are performing observations for building aerosol climatology.

2.2.2 Lidar developments related to aerosol observation

In the last two decades lidar development for studying the atmospheric aerosols and clouds has made a good progress. A Small, autonomous, eye-safe micro pulse lidar (MPL) system (Spinhirne, 1993) is being used for continuous observations of the vertical distribution of cloud and aerosol layers (see also, Spinhirne et al. 1995a,b). The MPL was first developed as an aerosol research tool within the Atmospheric Radiation Measurement (ARM) program in USA (Stokes and Schwartz, 1994). But the MPL signals require sufficient correction and uncertainty analysis to derive correctly the aerosol properties or information (see, a short note by Welton and Campbell, 2002). A depolarization

backscatter lidar developed by Grund and Sandberg (1996) can yield the same parameters as previous one together with the information about water phase in clouds. This system has the limitation with respect to the calibration issue: backscatter and extinction signal cannot be separated. Bissonnette and Hutt (1990) developed a multiple scattering lidar system, which delivers detailed information on the microphysical parameters. This system is simple and affordable but the data analysis technique is challenging. Piironen and Eloranta (1994) developed the high-spectral resolution lidar technique, which delivers aerosol backscatter and extinction coefficient, simultaneously. The development of the system is challenging and needs attention for eye-safe operation.

A vibronic Raman lidar system developed by Ansmann et al. (1992) uses both elastic and inelastic signal scattered from aerosols and molecules, respectively to derive optical properties of aerosol particles. But the reduced range and poor resolution of the system are two major limitations. Furthermore, a high-power laser transmitter is needed and this system also needs attention for the non eye-safe laser beam transmission. Althausen et al. (1999) applied a 6-wavelength 11-channel lidar system to study atmospheric aerosols while Mueller et al. (1998) developed the retrieval algorithms for the estimation of aerosol optical properties at those wavelengths. But the system development is not straightforward and can hardly be applied in urbanized regions due to the transmission of non eye-safe wavelengths. This system also has limitations in daytime operation and insufficient range-resolved information.

Several research efforts have been performed in the last two decades for the development and application of scanning lidar system for atmospheric aerosol research (chapter 4 in Weitkamp, (2005) and references there in). By pointing a laser beam in various directions at various angles (scanning) with respect to the surface, a ground-based aerosol lidar system can provide a description of the three-dimensional distribution of aerosols in the atmosphere. Eloranta and Forrest (1992) applied a volume imaging lidar system to observe aerosol structures in a CBL. Nevertheless, the ocular hazard associated with this scanning lidar prevents it from being widely deployed. Soriano et al. (2001) and Kunz et al. (2002) developed a scanning backscatter lidar, which has same limitation due to eye-hazardous laser beam transmission. In contrast to these efforts, Strawbridge and Snyder (2004) aided the safe operation of scanning aerosol lidar with marine radar to detect aircraft. But this system is also not versatile due to its limitation of using the same radar in the urban regions. Low power multi-angle micro-pulse lidar systems are inexpensive tools for achieving eye-safe operation (e.g., Powell et al., 2000). But they do not provide high temporal resolution and long-range data simultaneously and are therefore not well suited for scanning measurements.

Mayor and Spuler (2004), Spuler and Mayor (2005, 2007) made extensive research efforts to develop a scanning eye-safe aerosol lidar system to study the ABL processes by interpreting relative aerosol backscatter intensity at the wavelength of 1.54 μm. The large dynamic range of their system is an attractive feature but their results have not yet been used to quantify the optical properties of atmospheric aerosols. Very recent progresses in scanning lidar techniques and their applications are

documented in revised and reviewed papers of the International laser radar conference; ILRC-2008. See, among others Behrendt et al. (2008), Wulfmeyer et al. (2008b), Brewer et al. (2008), and Siefert et al. (2008).

Therefore, large numbers of lidar systems exist but only some selected numbers of these are well suited for aerosol research – but of this group most of them are limited in operation by range, resolution, and/or eye-safety.

2.2.3 Required specifications of suitable lidar systems

Two key research issues concerning the applicability of eye-safe scanning lidar systems and the advantages of using high-resolution lidar measurements for the study of aerosols in the ABL are addressed in the following.

With scanning lidar, another dimension is added so that the sources and tracks of the aerosol particles and the aerosol plume structures can be identified. For instance, vertical scanning can yield a detailed picture of the upper hemisphere while the horizontal scanning measurements can evince the aerosol sources with high accuracy and can track dynamics of aerosol plumes. Furthermore, unlike vertically pointing lidar measurements, scanning lidar can provide aerosol optical properties down to the ground level starting from a location very close to the lidar (~ limited beyond a few hundred meters due to partial overlap factor of the system up to that distance).

Lidar signal with high value of signal-to-noise ratio (SNR) and rapid scanning capability are two of the important requirements for obtaining 2-3 dimensional aerosol dynamics inside and above the CBL. Appropriate scan strategies are also important elements to overcome the trade-off between high SNR and scan speed. The scan strategies again concern the trade-off between the spatial and temporal resolution of lidar measurements, coverage area, and scan speed. Therefore, a suitable scanning lidar system also needs an automated high-speed data acquisition facility so that above requirements can be achieved with sufficient accuracy and precision.

For scanning lidar systems, eye safety of the transmitted laser radiation is an important issue in order to prevent damages to the eyes of humans and animals. Furthermore, the wavelength of the lidar beam is another important issue. Differences between the UV and IR lidar concepts are due to the wavelength dependency of the atmospheric backscatter signals: while in the IR the molecular backscatter coefficient is mostly negligible compared to the particle backscatter signal so that particle backscatter signals are detected (almost) directly, the situation is much different in the UV where – outside of clouds – the major portion of the signal typically comes from molecular backscattering. In the UV, one needs to separate the molecular and particle backscatter signal portions. This separation allows the calibration of the system using clear air signals for the derivation of the particle backscatter coefficient. Therefore, lidar systems operating at UV wavelength offer the correct estimate of the boundary value, at least at the far end of the lidar range.

High-temporal-resolution analysis of CBL microscale structure involves the high signal-to-noise ratio and therefore high power laser transmitter. Such high-resolution lidar measurement can reveal highly resolved aerosol features (< 5 meters in some instances) present especially inside the CBL. However, the small-scale structure that can be detected is limited by the lidar pulse length. For instance a range resolution of the lidar of 1.5 m corresponds to a lidar pulse length of 10 ns. With the advancement of high-power laser technology (e.g., Schiller, 2007; Petrova, 2008;) and with the availability of the commercial high-speed data acquisition card, development of the high-resolution lidar system is feasible.

Within this dissertation, a scanning, high-resolution mobile aerosol lidar system is developed which can be widely deployed especially near urban areas/coastlines/near airports since the laser beam transmitted from this system does not create ocular hazards. The optical properties of the aerosol particles can be retrieved with the University of Hohenheim (UHOH) mobile scanning eye-safe aerosol lidar system. This system consists of unique features so that it can be used as a tool both for meteorological and environmental research purposes.

2.2.4 Combination of lidar measurements with modeling and synergy with other instruments

Although single wavelength elastic lidar measurements are necessarily limited in space and time and in their ability to differentiate among various types of aerosol particles, lidar measurements of aerosol optical properties in two-three dimensions and in time by performing process research (field studies) are beneficial to improve the understanding of aerosol processes. But, application of a single lidar alone cannot benefit the aerosol process study and the ABL dynamics. Combination of data from active, passive and in-situ sensors is the most promising way for profiling thermodynamic variables throughout the full depth of the troposphere (Westwater, 1997).

To study atmospheric processes in detail, lidar measurements should be complemented by other active and passive remote sensing measurements. For instance, synergetic remote sensing data like relative humidity, potential temperature, virtual potential temperature, gradients of these parameters, buoyancy, convective inhibition (CIN), convective available potential energy (CAPE) in clear air and around cumulus clouds can yield important additional information for studying different meteorological processes (e.g., convection initiation) in an advanced manner.

Two more important issues are the evaluation of models like LES with lidar-measured variables and lidar data assimilations into present day weather forecast models (e.g., mesoscale model). Wulfmeyer et al. (2006) and Grzeschik et al. (2008) showed the impact of the lidar data assimilation of water vapor on mesoscale model forecast.

Within this dissertation, the UHOH scanning aerosol lidar was applied for resolving the problem concerning the aerosol emission and transport processes close to the source through estimating

the optical properties of aerosol plumes and investigation of the transport processes inside the ABL. The lidar results were then compared with a high-resolving atmosphere-microphysics-chemistry model for better prediction of aerosol flow. In-situ point measurements of aerosol size distribution provide a better initialization of the LES model. Such combination of experimental and modeling approach is considered to be a novel approach to the description of plumes from different aerosol sources (e.g., livestock buildings).

2.3 Lidar system development plans and outline

Main goal of this thesis is the development and application of an eye-safe scanning lidar system for atmospheric aerosol research and thereafter the understanding of the processes inside and above the ABL, the most complex part of the lower troposphere.

A vertical-pointing elastic backscatter lidar system using an infrared wavelength was first developed which served as a test-bed for the development of a mobile, scanning eye-safe aerosol lidar system operating at 355 nm wavelength for detailed studies of the ABL dynamics and aerosol processes.

In contrast to lidar systems in the infrared (wavelength about 1500 nm; Spuler and Mayor, 2005), eye safety is technically much easier to obtain in the UV. The typical range and time resolution of the lidar system are 3 m and 0.03 s, respectively. Such scanning eye-safe aerosol lidar is a unique instrument for obtaining objective characteristics of the ABL owing to a combination of properties such as remoteness, mobility, resolution, and information content.

In early 2006, the scanning aerosol lidar system was transformed to the world's first scanning rotational Raman lidar system (Radlach et al., 2006) for the simultaneous measurements of atmospheric temperature and both the particle extinction coefficient and the particle backscatter coefficient. Development of the scanning RRL is a part of the PhD thesis of Radlach (2008c) while this dissertation emphasizes on the development of the data acquisition software and data analysis facilities for the RRL. Technical descriptions of new lidar system are available in chapter 3.

A detailed description of the analysis techniques for data obtained with the lidar operating at different wavelengths is presented in chapter 4.

Chapter 5 concerns the application of a vertically pointing lidar system developed for the characterization of ABL structures and the investigation of related statistics for the better understanding of the ABL processes. This chapter mainly focuses on the investigation of the complexities involved in both daytime CBL and nighttime boundary layer over an urban valley-like location.

Chapter 6 describes the development of a mobile, scanning eye-safe aerosol lidar system at the UV wavelength. Selected results obtained during a field campaign in northern Germany during September 2005 are presented. The main aim is to demonstrate the potential benefit of applying a

scanning aerosol lidar in the UV to investigate aerosol emissions from a livestock facility having rather low concentrations and thereafter the retrieval of the optical properties of the aerosol plume.

In Chapter 7, results from the field campaign PRINCE (PRediction, Identification and trackiNg of Convective cElls) are presented. This field campaign was the part of a project COSI-TRACKS (Convective Storms Virtual Institute, with contribution to TRACKS, Transport and Chemical Conversion in Convective Systems). Combined measurements of aerosol optical properties and atmospheric temperature distributions in pre-convective environments were the major goal of this campaign.

Selected results obtained during the international field campaign COPS (Convective and Orographically-induced Precipitation Study, Wulfmeyer et al., 2008a) are presented in chapter 8. For the first time RRL technique is applied for RHI scanning data so that aerosol optical properties in 2-3 dimensions could be estimated. The COPS field campaign took place during summer 2007 in southwestern Germany and eastern France.

Chapter 9 gives a brief summary of the work performed within this dissertation. An outlook for the future application of the lidar techniques and data analysis facilities developed is also outlined.

Chapter 3
Experimental set ups of the aerosol lidar system of University of Hohenheim

3.1 Vertically pointing elastic lidar system

The vertically pointing elastic lidar system of UHOH was operated in an intermediate configuration on the way to the development of a scanning lidar system for aerosol backscatter and temperature measurements (Behrendt et al., 2005; Pal et al., 2006; Radlach et al., 2008a).

This version of the lidar system worked in monostatic biaxial configuration with a maximum spatial and temporal resolution of 3 m and 0.033 s, respectively. The data acquisition system stores the lidar data with a frequency of 30 Hz as it is triggered by the laser pulse repetition frequency (also 30 Hz). The lidar system was equipped with a flash-lamp-pumped Nd:YAG laser emitting simultaneously the fundamental (1064 nm) and the second harmonic (532 nm) wavelengths. Pulses of ~ 10 ns duration with pulse energy of 600 mJ at both wavelengths were emitted. The schematic set up and specifications of this lidar instrument are shown in Figure 3.1 and Table 3.1, respectively.

The backscattered light was sampled with a Ritchey-Chretien-type telescope with a 40-cm-diameter primary mirror. The same telescope was used for the scanning aerosol lidar and scanning RRL described in this study while the laser wavelength differed. The backscattered light passed a lens and was then split by a dichroic beam splitter, separating the signals of the two transmitted wavelengths. The two beams were analyzed by means of two interference filters, both with 5 cm diameter and 10 nm half-width-at-half-maximum (FWHM) band-pass before reaching the detectors: a photomultiplier tube (PMT, Hamamatsu R7400-U02) for 532 nm and a silicon avalanche photodiode (Si-APD, Perkin & Elmer C3095E) for 1064 nm. Sensitive area of the APD and the PMT are 0.8 mm and 8 mm, respectively.

The data acquisition and processing unit was comprised of: a two-channel Gage CS 14100 card with 14 bit resolution analog-to-digital converter (ADC) sampling the backscattered signal with 50 MHz to provide data in 3 m vertical resolution, and a standard personal computer, where the data were processed using an automated LabView code and then stored on a hard disk. The raw and the

range-square-corrected backscatter signal and time-versus altitude image of the lidar signal for both channels were displayed in real time.

Figure 3.2 shows examples of the range-square corrected signal intensity for the 1064 and 532 nm wavelengths collected simultaneously with the UHOH lidar at UHOH weather station in the afternoon of 7 July 2005. Both images show detailed vertical structures of the CBL up to an altitude ~ 2.0 km above ground level (AGL) and a cirrus cloud layer between 6 and 7 km AGL. Zoom-in-views of the range corrected signal at the IR wavelength for region of the CBL (marked by 'A' in Figure) and of a cirrus layer (marked by 'C') are shown in Figure 3.3. This figure shows high resolved information of the aerosol field inside the CBL associated with enhanced turbulent structure. Cirrus layer is also visible with an unprecedented resolution. Such high-resolution lidar measurements can yield information about the entrainment driven small-scale features present in the CBL.

With the configuration of the UHOH lidar used here, observations could not be made from the ground to a height of about 400 m because the transmitted laser beam was not completely in the field of view of the receiver. This version of the UHOH aerosol lidar system was deployed in Stuttgart downtown during summer 2004 and the results obtained from these measurements are discussed in chapter 5.

Table 3.1: Technical parameters of the vertically pointing UHOH elastic aerosol lidar system

TRANSMITTER	
Nd:YAG laser	
Wavelengths:	1064 nm and 532 nm
Pulse energy:	600 mJ @1064nm and 600 mJ @532nm
Pulse repetition rate:	30 Hz
Pulse duration:	10 ns
TELESCOPE	
Type:	Ritchey-Chretien (Astro Optic)
Diameter of primary mirror: 40 cm	
Diameter of secondary mirror: 10 cm	
Focal ratio: f/10	
Coating: Aluminum with quartz protective coating	
DETECTORS	
Si-APD for 1064 nm and PMT for 532 nm	
ANALOG-TO-DIGITAL CONVERTER	
Compu-Scope 14100	
Analog-to-digital resolution: 14 bits	
Sampling rate: 50 Ms/s (for 2 channel)	
Sampling in range: 3 m	

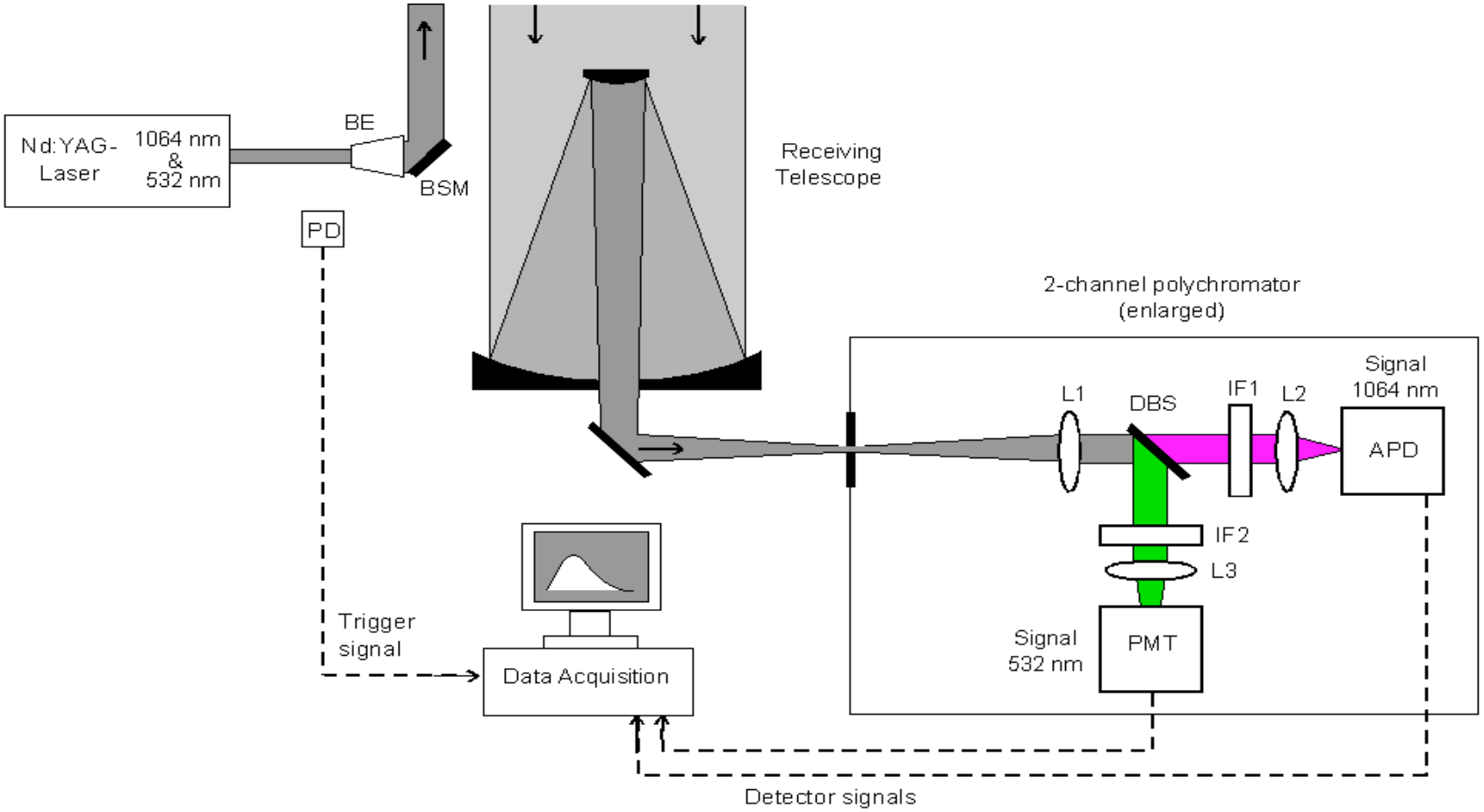

Figure 3.1: Scheme of the vertically pointing elastic backscatter lidar of UHOH. APD: Avalanche photodiode, BE: Beam expander, BSM: Beam steering mirror, DBS: Dichroic beam splitter, IF1 - IF2: Interference filter, L1-L3: Lenses, PMT: Photomultiplier tube, PD: Photodiode.

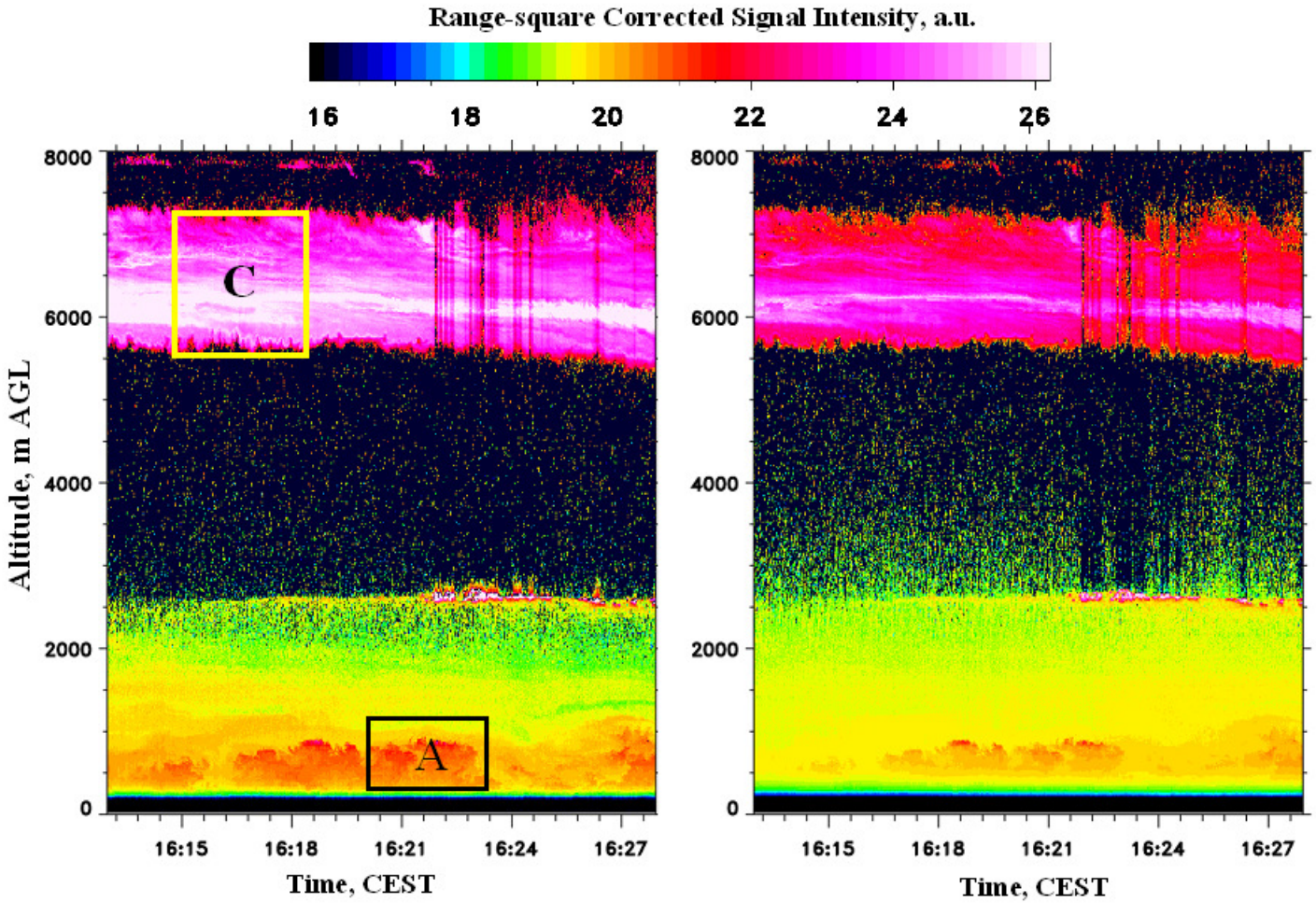

Figure 3.2: Time-versus-height cross-section of aerosol optical backscattering at 1064 nm (left) and 532 nm (right) from ground to 8.0 km AGL over a 15-minute period collected on 7 July 2005 at UHOH weather station, Stuttgart, Germany. These data show the simultaneous measurements of aerosol and cirrus cloud structures with a temporal resolution of 1 s and a vertical resolution of 3 m. Two regions labeled by 'A' and 'C' corresponding to the ABL and cirrus layer, respectively are shown in Figure 3.3.

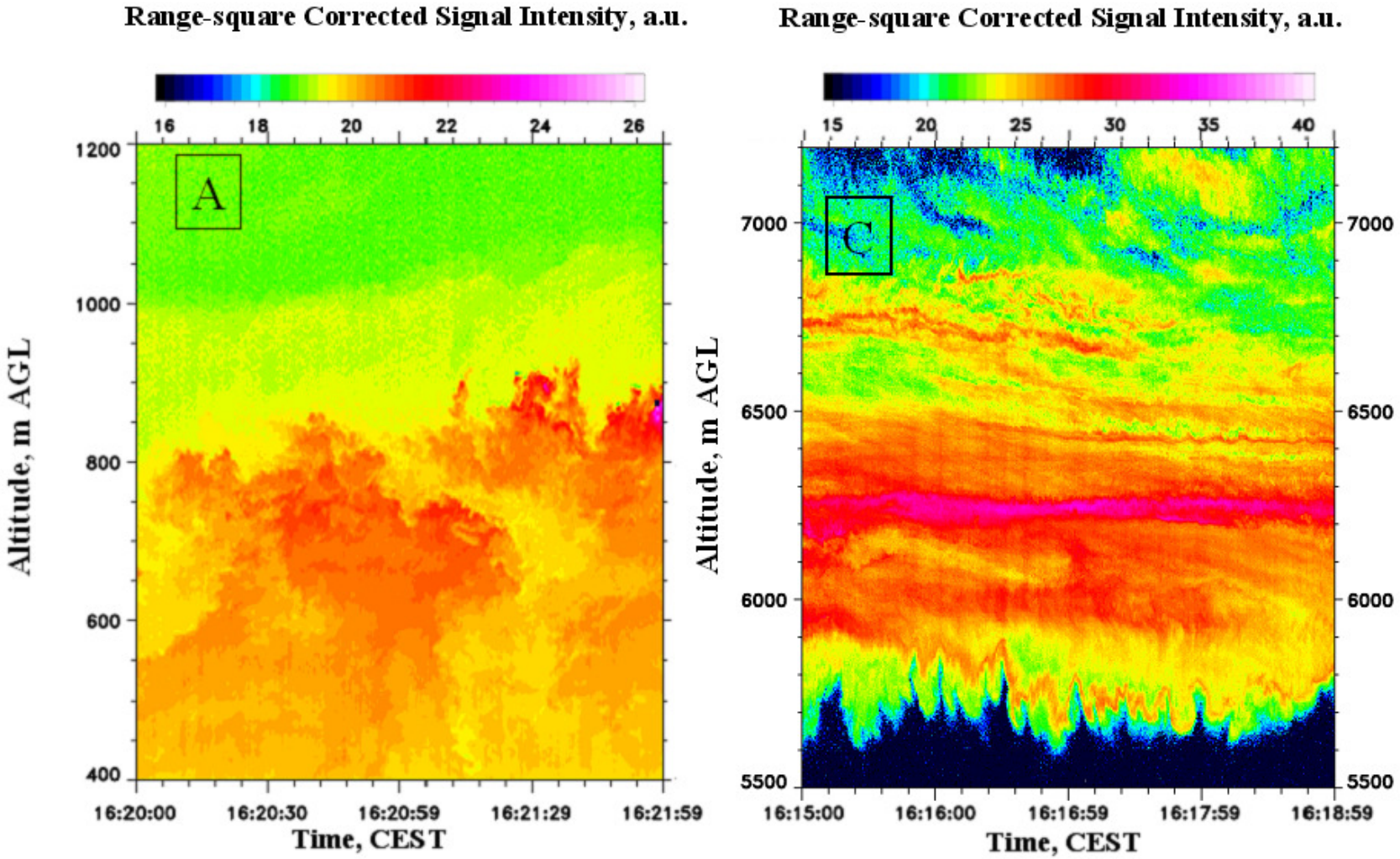

Figure 3.3: Zoom-in-views of the regions marked by 'A' and 'C' (see, Figure 3.2) illustrating enhanced turbulence in the CBL (left panel) and detailed vertical structure of the cirrus cloud layer (right panel).

3.2 Mobile, scanning eye-safe aerosol lidar system using ultraviolet wavelength

Significant modifications were made for transforming the vertically pointing UHOH aerosol lidar to a scanning system allowing: the facility of field-operation by using a compact mobile platform, the capability of transmitting eye-safe laser beam with scanning facility, and a high-speed data acquisition software for applying four different scan patterns. The fundamental components of the UHOH scanning lidar system consisting of a laser transmitter, beam steering unit, receiving optics, telescope, data acquisition system, and the mobile platform are briefly described in the following.

Transmitter

The UHOH scanning aerosol lidar system uses the frequency-tripled output of the same Nd:YAG laser used in the earlier version of the lidar system but with pulse energy of 300 mJ at a wavelength of 355 nm. In contrast to its earlier configuration, this system works in a monostatic coaxial configuration as shown in Figure 3.4. The specifications of the key components are summarized in Table 3.2. The laser radiations at 532 nm and 1064 nm are not transmitted into the atmosphere. Only radiation at 355 nm separated with a beam splitter is transmitted at a pulse repetition rate of 30 Hz after 6-times beam expansion. This is performed mainly to avoid damages to the eyes of humans and animals. Furthermore, this reduces the beam divergence and protects the output mirror coatings.

For laser radiation of 400-1400 nm, the main eye threats are connected with retina damage because the retina, lens, aqueous humor and vitreous body transmit this range of wavelengths. The situation is different for 355 nm because radiation with this wavelength is already absorbed in the outer parts of the eye. Taking the energy distribution within the beam profile into account, it is found that a beam diameter of 14 cm is sufficient for a pulse energy of 300 mJ and pulse duration of 5 ns in order to be eye safe at 355 nm as shown in Figure 3.5. Due to the divergence of the transmitted beam, this diameter is reached at distances larger than 270 m.

Receiver and beam steering unit

The laser beam is emitted coaxial to the receiving telescope (Ritchey-Chretien type telescope used in the vertically pointing lidar). A laser-bending mirror is mounted directly on the backside of the secondary mirror of the telescope, so that the outgoing laser beam is exactly centered in the middle of the telescope. The light backscattered from the atmosphere is directed via the two scanner mirrors towards the telescope.

Table 3.2: Technical parameters of the UHOH scanning aerosol lidar

TRANSMITTER	
Type:	Flash-lamp-pumped frequency tripled Nd:YAG (Spectra-Physics, GCR5-30)
Wavelength:	354.66 nm
Pulse energy:	~ 300 mJ
Repetition rate:	30 Hz
Pulse duration:	5 ns
Beam diameter:	6.5 cm (after expansion)
RECEIVER (with the same configuration as used in chapter 1)	
Telescope:	Ritchey-Chretien type
Diameter of primary mirror:	40 cm
Diameter of secondary mirror:	10 cm
Focal length ratio:	f/10
Coating: Aluminum with quartz protection layer	
INTERFERENCE FILTER	
Wavelength:	355 nm
FWHM:	8 nm
Transmission:	50 – 55 %
Diameter:	50 mm.
SCANNER	
Manufacturer:	National Center for Atmospheric Research (NCAR), Boulder, USA.
Mirror coating:	Protected silver enhanced at 355 nm
Substrate:	Zerodur
Motor type:	Servomotors (SM2340 and SM3420 from Animatics, USA)
Encoder:	Resolution with 4000 counts/revolution
Scan speed:	$10° s^{-1}$ in azimuth and elevation
Dimensions:	Octagonal, Main axes: 609.6 mm x 431.8 mm
	Thickness: 25.4 mm
DETECTOR (PMT)	
Type:	Hamamatsu R7400- U02
Diameter:	8 mm
Typical gain:	$\sim 10^5$
ANALOG-TO-DIGITAL CONVERTER	
Compu-Scope	14100
Analog-to-digital resolution: 14 bits	
Sampling rate:	50 Ms/s (for 2 channel)
Sampling resolution:	3 m

The beam steering unit is powered by two servomotors. Lidar scan speeds of up to $10° s^{-1}$ are obtainable. With the use of sliding contacts, uni-directional non-stop scanning is possible. The technical details of the scanner are also summarized in Table 3.2. The wide-band high reflectivity of the mirrors reaches more than 95 % within the wavelength range 350 - 1500 nm. A photograph of the scanner on the roof of the mobile platform during one measurement is shown in Figure 3.6. A 3-dimensional view of the scanner solid model is also shown in the figure (right panel).

The beam steering unit is connected by a serial line to the data acquisition computer and controlled with the graphical programming language LabView. After passing the telescope the light is collimated with a lens and the background is reduced with an interference filter of a FWHM of 8 nm.

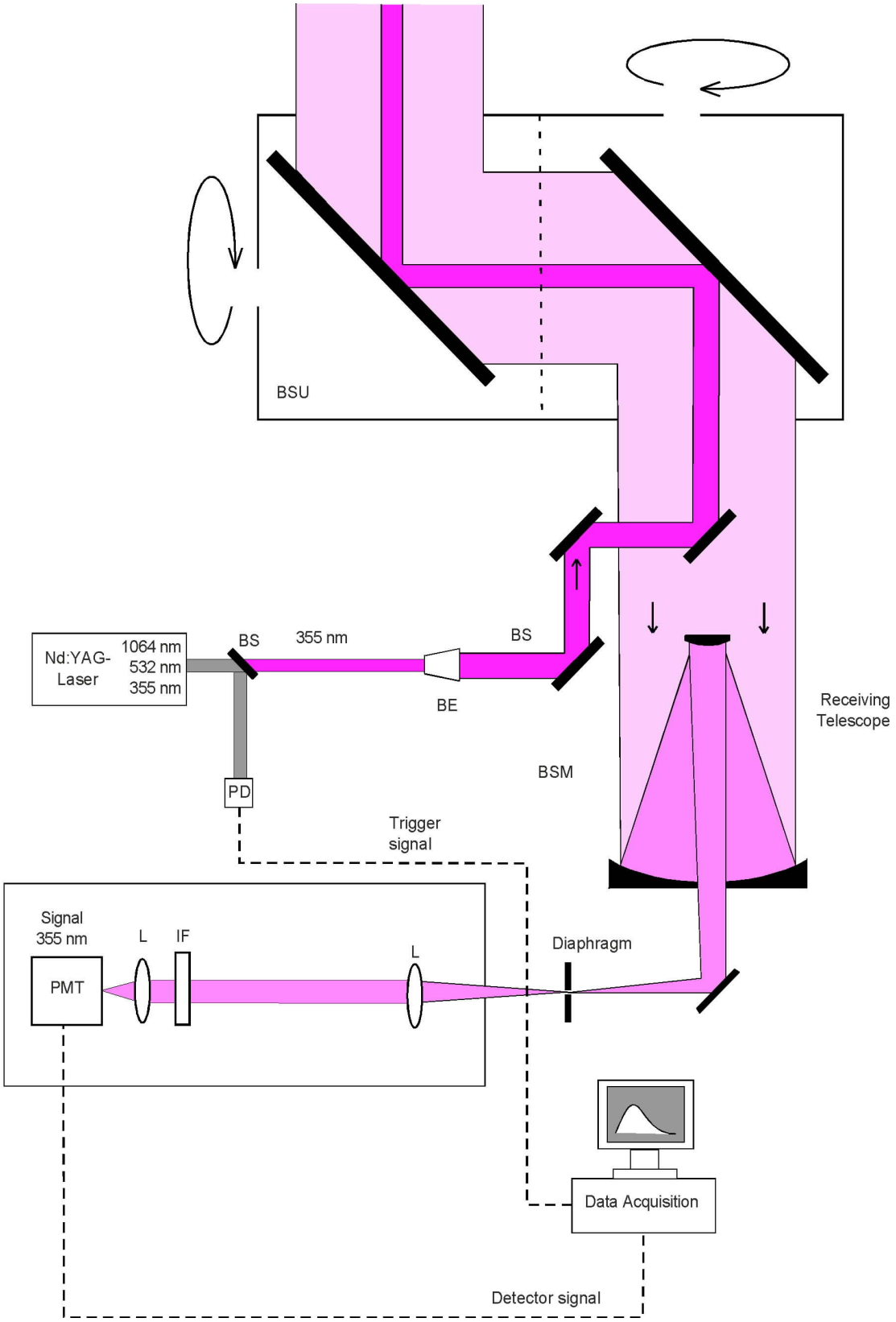

Figure 3.4: Schematic set up of the UHOH scanning aerosol lidar system. BD: beam dump, BE: beam expander, BSU: Scanner (beam steering unit), IF: interference filter, L: lenses, LM: laser mirrors, PMT: photomultiplier tube, BS: Beam Splitter, BSM: Beam Steering Mirror, PD: Photo-Diode.

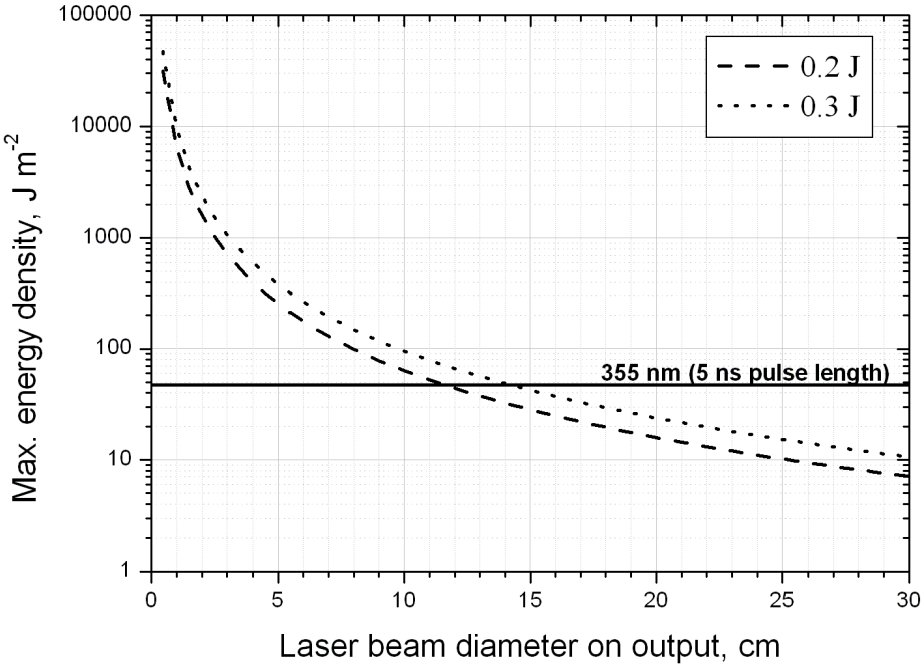

Figure 3.5: Eye safety considerations for the scanning aerosol lidar: Energy density against beam diameter, taking the maximum energy density within the inhomogeneous laser beam profile of the Nd:YAG laser into account. The dashed line shows the maximum allowed energy density of 56 J/m^2. For a diameter larger than 14 cm, the laser beam is eye safe according to DIN (Deutsche Industrie Norm) rules available at: http://www.pr-o.info/bc/uvv/93/anh2.htm

Figure 3.6: The UHOH lidar scanner during measurement in a field campaign in 2005 (left). A 3-dimensional view of the scanner solid model (right); Source: NCAR, USA.

The received signal is then focused and detected on an 8 mm R7400-U02 PMT (Hamamatsu). An inbuilt high-precision 8-stage electron multiplier is incorporated to the PMT package to produce a noise free gain of the order of 10^5. The amplified signal is then sent to the 14-bit ADC (CS14100).

Data acquisition

The same data acquisition and processing unit as used in the vertically pointing IR lidar system (section 3.1) was implemented to the scanning aerosol lidar. The complete data acquisition code (DAC) was modified to collect and analyze backscatter signal digitized through the ADC so that it permits the scanning facility. This software fully controls the scanner movement, data acquisition system, data display and storage with high speed, accuracy, and precision.

In this configuration of the UHOH scanning lidar, four different sorts of scan patterns are possible: (i) RHI (range-height indicator) scan, where the elevation angle is varied at a constant rate keeping the azimuth angle constant, (ii) PPI (plan-position indicator) scan where the azimuth angle is changed at a constant rate keeping the elevation angle fixed, (iii) RHI volume scan where a set of RHI scans is performed with equidistantly changed azimuth angle, and (iv) PPI volume scan where a set of PPI scans is performed with equidistantly changed elevation angle.

The software includes a real time pseudo-colored display of the backscattered signal, range-square corrected lidar signal in range-time indicator (RTI) panel. Features include a graphical user interface to specify time resolution, range resolution, maximum range, sampling rate, scan speed, scan type, scan sectors, and plot type, which facilitated the UHOH lidar to be useful for a multitude of measuring tasks. The scanner position is updated at a 30-Hz rate via a parallel port connection to the computer. This full software provides a flexible and high quality remote probing capability through various scanning mode for a better understanding of dynamical processes, taking place in the atmosphere. A complete description of the UHOH scanning lidar dataflow is outlined in section 4.6.

Mobile platform

The mobile laboratory is based on a truck of Mercedes-Benz (model 814) to allow field-able configuration of the UHOH scanning lidar at any accessible site. This platform for the scanning lidar is heritage of ARGOS, which was developed in GKSS Research Center, Geesthacht, Germany for mobile lidar measurements as a part of the PhD thesis of Wandinger (1994). A photograph of the mobile platform is seen in Figure 3.7. Several mechanical infrastructures were made inside the truck to accommodate optical bench, telescope mount and scanner adaptor ring.

The full mobile platform was made compact, highly stable, and sensitive to any sort of mechanical perturbation. The Nd:YAG laser, beam expander, bending mirrors, telescope and the whole detection system are mounted on a stable and stiff frame (120 x 60 mm^2, Item GmbH) with breadboard of Newport. Other exterior fittings included an adapter ring for mounting the scanner on the roof of the truck, a mobile crane that can be mounted directly on the roof.

Figure 3.7: Mobile platform including the scanner of the UHOH scanning lidar in operation during a field campaign in 2005.

The UHOH scanning aerosol lidar system developed within the part of this thesis is found to be an efficient tool for the atmospheric aerosol research. The important features include the following:

- Eye-safety (operating at 355 nm).
- Field mobility (compact mobile truck) with geographical positioning system (GPS) or server based time synchronization.
- Large dynamic range (of around 10 km) with high temporal (< 0.3 s) and spatial resolution (< 3 m).
- Retrieval of aerosol optical properties (particle backscatter and extinction coefficient at wavelength of 355 nm).
- Continuous operation (around the clock except prohibitive weather condition arising due to shower and/or during extreme humid and foggy weather situation).
- Real-time display of lidar data applying LabView tools and near real-time instantaneous backscatter plots using sophisticated tools.
- Numerous scan images through batch file and time-lapse animation of these images. These animations are of particular importance to observe the two-three dimensional flows of the atmospheric aerosols.

First field deployment of the UHOH scanning aerosol lidar system was in Autumn 2005 during a field campaign in Mettingen near Osnabruck in northern Germany and results obtained are subject of chapter 6.

3.3 Mobile, scanning rotational Raman lidar system

The existing eye-safe scanning aerosol lidar at 355 nm was extended to a scanning rotational Raman lidar system by integrating two rotational Raman channels in the receiver module. The laser transmitter, telescope, scanner, beam steering unit are used in the same configuration as in the UHOH scanning aerosol lidar. The elastically scattered signal and two signals out of the rotational Raman bands are separated with a sequential set-up of 3-channels (Behrendt and Reichardt, 2000). The signals are detected with photomultiplier tubes and digitized simultaneously in analog and photon-counting mode with a temporal and spatial (or range) resolution of 10 s and 3.75 m, respectively with a Licel transient recorder.

In contrast to most other rotational Raman lidar systems, this new lidar developed within COSI-TRACKS, uses an eye-safe laser transmitter in the near UV (wavelength of 354.7 nm). This minimized restrictions for scanning operation in the field. This wavelength yields also temperature data of better performance with latest advancements in narrow-band interference filter technology than measurements at longer wavelength do. This is due to a larger backscatter cross-section and lower daylight background in the UV. The particle backscatter coefficient and extinction coefficient can be determined independently with the elastic and rotational Raman signals (Ansmann et al., 1992; Behrendt et al., 2002).

A detailed description of the scanning RRL can be found in Radlach (2008c). As a part of this thesis, several software tools were developed which handle the complete data acquisition system together with scanner movement with numerous scan patterns, storage and display of the data. Several data analysis algorithms were developed to calculate the aerosol optical properties as well as to present them through high-quality images. A Brief description of this software is given in Appendix-A and B.

The profiles of the particle extinction and backscatter coefficients and then the lidar ratio reveal several microphysical properties of aerosol or cloud layers since the backscattering and extinction due to aerosol particles depend in different ways on the size, shape of the scattering particles.

The first field deployment of the scanning RRL was in summer 2006 during the field campaign PRINCE at the summit of Hornisgrinde mountain in northern Black Forest. Results obtained from some selected measurements of the PRINCE campaign are discussed in chapter 7. Some technical improvements of the scanning RRL system were realized a prior to an international field campaign (COPS) in 2007 (Radlach et al., 2008b). For instance, an injection-seeded flash-lamp-pumped Nd:YAG laser was implemented which emits pulses at 50 Hz with a power of 10 W at the frequency-tripled wavelength of 355 nm.

A brief summary of the three different configurations of the lidar system is shown in Table 3.3.

Table 3.3: Summary of the configuration of the lidar systems used during four different field campaigns

Lidar system	**Wavelength**	**Configuration and operation mode**	**Deliverable data product/s**		**Field campaign/s**			
			Primary	**Secondary**	**Name and location**	**Year**	**Orography**	**Major aim/s**
Elastic lidar	532 nm and 1064 nm	Vertically pointing, monostatic, biaxial, non-eye-safe, laboratory based	Relative particle back-scatter @ 1064 nm and 532 nm wavelengths	Aerosol dynamics, ABL height, EZT, higher-order-moments, statistical properties of ABL dynamics	Stuttgart measurement, Schlossplatz, near downtown Stuttgart	2004	"U-shape" valley	Observation of ABL dynamics over an urban-valley
Scanning aerosol lidar	355 nm	Scanning, monostatic, co-axial, eye-safe, mobile	Particle backscatter and extinction coefficient @ 355 nm wavelength	As above	PLUS1 campaign, Mettingen near Osnabrück, north Germany	2005	Flat terrain	Investigation of optical properties, and transport of the plume from a livestock facility
Scanning rotational Raman lidar	355 nm	As above	Temperature field, particle backscatter and extinction coefficient, and aerosol lidar ratio @ 355 nm wavelength.	As above together with stability parameters after gradient of potential temperature profiles	PRINCE, at the summit of Hornisgrinde mountain in the northern Black Forest.	2006	Complex mountaino-us region	Investigation of aerosol optical properties and temperature field in preconvective weather situation in a low-mountainous region
As above but with improved system efficiency by a factor of 10	355 nm	As above	As above	As above	COPS, same location as above	2007	As above	As above but with additional advantages of multi-instruments synergies

Chapter 4
Lidar data analysis techniques

4.1 Determination of the atmospheric boundary layer height

In the following, data analysis procedures applied for the evaluations of the lidar data obtained at IR wavelength are outlined. These include three different methods for the determination of the instantaneous ABL height from vertically pointing lidar measurements. The EZT is estimated from the time evolution of ABL height. Furthermore, three different procedures for the statistical analyses of the ABL height time series are presented. Non-stationarities embedded in the time series and then determination of multi-fractal dimension, higher-order moments estimation of the lidar backscatter signal intensity for investigating the turbulence nature of ABL are evaluated. Finally, a brief overview of the wavelet-based spectral analysis to extract several scales/frequencies present in the time series of the particle backscatter signal in the different atmospheric layers is given.

Aerosol particles, which are suspended in the ABL, produce strong signatures in backscatter lidar signals. Generally, the lidar signal intensity decreases from the top of ABL to the free troposphere if there is no cloud layer or RL. Daytime ABL yields vertical transport and strong turbulent mixing and hence different entrainment regimes. The procedures for estimating the ABL height by the logarithm gradient method (LGM), the inflection point (IP) method, and the Haar wavelet transform (HWT) method are described in the following.

ABL height is defined as the height of the inversion level separating the free troposphere (FT) from the boundary layer (Stull, 1988). The inversion layer is finite in depth, and thus covers a range of heights not a single discrete and easily confined value. According to Stull (1988), ABL depth is defined as the "*average height of the inversion base*". But the entrainment near the top of the ABL consists of complex processes and therefore, the instantaneous ABL height is often not well defined. The ABL height is differently characterized as:

- The height of the inversion base (commonly denoted as z_i), which is also the top of the well-mixed layer, and approximately equal to the level at which the buoyancy flux becomes zero in a CBL.
- The top of the inversion (top of BL as a whole), equal to the height above which the turbulence intensity becomes zero, and the upper limit of negative buoyancy flux.

- A point within the inversion layer– the location of the maximum vertical gradient is frequently used since it is relatively easy to identify by automated algorithms, the level of the minimum (max negative value) buoyancy flux might also be used – this is approximately the midpoint of the inversion layer.

The definitions of the ABL height differ not only in the precise value obtained, but more fundamentally in that they are defined by different physical quantities or processes. The different algorithms used on the lidar backscatter signals similarly result in different levels because they are defined by or they represent different physical quantities/processes. These distinctions are important when comparing results from different algorithms, and some precision should be used in the definition of exactly what feature is being identified. It is further important to note that the inversion that defines the top of the boundary layer is a thermodynamic feature. Lidar backscatter is considered to reflect the thermodynamic inversion closely because it is proportional to the aerosol concentration if the change in the particle size distribution and particle composition are neglected. The aerosol concentration is much lower in the free troposphere as compared to that in the CBL and thus has a transition that closely matches the inversion. Aerosol size, however, is a function of humidity, which often falls dramatically across the inversion layer; the lidar backscatter is thus not truly conserved and differences between the transition zone limits of lidar backscatter profile and thermodynamic inversion might exist, at least for some conditions.

The EZ at the upper boundary of the mixed layer is characterized by a capping (temperature lid) to the rising thermals. The methods to estimate EZT are discussed in section 4.2. Stull (1988) defined entrainment zone as the region where the buoyancy flux is negative or the region where more than 5 % and less than 100 % of air on a horizontal plane has free tropospheric (FT) characteristics. The ABL height (z_i) may be taken as the height at which 50 % of the air has free atmosphere characteristics or when buoyancy flux is minimum.

4.1.1 Lidar equation

Elastic backscatter lidar is an efficient technique for remote sounding of the ABL. Suspended aerosols act as tracers and allow getting a detailed characterization of the ABL structure and especially the height of the ABL. The monostatic elastic lidar signal is expressed as

$$P_\lambda(R) = P_0 \frac{ct_p}{2} K \frac{A}{R^2} O(R) \beta_\lambda(R) \exp\left(-2 \int_0^R \alpha_\lambda(R) \mathrm{d}r \right) \qquad [4.1]$$

where

R is the range

$P_\lambda(R)$ is the received signal intensity at the wavelength of λ (here, 355 nm) from range R

$P_{0,\lambda}$ is the peak power of the single laser pulse

c is the velocity of light

t_P is the laser pulse width

K is the efficiency of the detector system

A is the receiving area of the telescope

$O(R)$ is the laser-beam receiver-field-of-view overlap function

β_λ is the total backscatter coefficient due to atmospheric particles and molecules

α_λ is the total extinction coefficient due to atmospheric particles and molecules

Total backscatter coefficient can be expressed as $\beta_\lambda(R)=\beta_{\lambda,mol}(R)+\beta_{\lambda,par}(R)$ [4.2]

where $\beta_{\lambda,mol}(R)$ and $\beta_{\lambda,par}(R)$ are the molecular backscatter coefficient and particle backscatter coefficient, respectively. A similar relationship as Eqn. 4.2 can also be obtained for the total extinction coefficient

$$\alpha_\lambda(R)=\alpha_{\lambda,mol}(R)+\alpha_{\lambda,par}(R) \quad [4.3]$$

where $\alpha_{\lambda,mol}(R)$ and $\alpha_{\lambda,par}(R)$ are the molecular and particle extinction coefficient, respectively. The relationship between lidar backscatter intensity and aerosol concentration is complicated and can be tackled with the multiwavelength Raman or high-spectral resolution lidar (Wandinger et al., 1995; Mueller et al., 1998).

In the IR wavelength region, the range-square-corrected backscatter signal intensity is approximately proportional to the particle backscatter coefficient if the aerosol extinction is small. The Rayleigh scattering due to the atmospheric molecules at this wavelength is negligible. Therefore, Eqn. 4.1 can be approximated as

$$P(R)\cong\frac{C}{R^2}\beta_{par}(R) \quad [4.4]$$

where C is a constant containing the system constant, receiver area, and overlap function.

Eqn. 4.4 is not aimed at the retrieval of the absolute value of particle backscatter coefficient. But using aerosols as tracers, characterization of the ABL structures and investigation of related statistics are feasible.

4.1.2 Logarithm gradient method

The first approach adopted here for retrieving the ABL height is based on the calculation of the vertical gradient of the logarithm of the range-square-corrected lidar backscattered signal (Senff, 1996; Wulfmeyer, 1999a; Wulfmeyer and Janjic, 2005) which is expressed as

$$D(z)=\frac{\mathrm{d}\left(\mathrm{Log}\left(P(z)z^2\right)\right)}{\mathrm{d}z}\approx\frac{\mathrm{Log}\left(P(z_2)z_2^2\right)-\mathrm{Log}\left(P(z_1)z_1^2\right)}{z_2-z_1} \quad [4.5]$$

where z_2 and z_1 are two different heights ($z_2 > z_1$) from the lidar. Please note that range (R) is replaced by height (z) in the lidar equation as this technique is applied for the vertically pointing lidar measurements. The use of the derivative of the logarithm of range-squared corrected signal yields one advantage compared to the use of derivative of only range-squared corrected signal. The benefit is to have the extinction coefficient (although small) in linear form allowing maxima and minima to appear with better-expressed contrast.

The lidar signal generally shows a local discontinuity or transition zone between the mixed layer and the free troposphere, more or less well marked, depending on the turbulent activity and the aerosol distributions present. The altitude corresponding to the minimum of $D(z)$ is defined as the instantaneous ABL top. This height is denoted throughout the text and in the figures as h_{LGM} and is expressed as

$$h_{\mathrm{LGM}} \equiv \min\left(D\left(z\right)\right) \quad [4.6]$$

According to Stull (1988), the top of the ABL is the height of the most negative sensible heat flux and may be situated well in the middle of the entrainment zone. Since passive scalars are accumulated in the ABL, large gradients of aerosol concentration or water vapor density occur at the inversion capping the ABL; those gradients are also suited for defining the top of the ABL (Stull, 1988). In ideal cases, the location of this gradient coincides to the minimum in the buoyancy flux profile. A sharp potential temperature jump also determines the ABL top (Boers et al., 1984).

One should remember that the quantity $D(z)$ is sensitive to the presence of noise in the lidar signal and special care should be taken in the averaging scheme before this technique is applied.

4.1.3 Inflection point method

The retrieval of the ABL height by IP method (Menut et al., 1999) is based on the estimation of the altitude corresponding to the minimum of the second derivative of the logarithm of the range-square-corrected signal and can be expressed as

$$h_{\mathrm{IP}} \equiv \min\left[\frac{\mathrm{d}^2\left(\mathrm{Log}\left(P\,z^2\right)\right)}{\mathrm{d}\,z^2}\right] \quad [4.7]$$

This definition is slightly different from the LGM. The IP method searches for the altitude where the inflection point of $D(z)$ occurs. h_{IP} is in general less than h_{LGM} since second derivative changes sign each time the first derivative changes direction. Second derivative function exhibits various minima below and above h_{LGM}. In this regard, Sicard et al. (2006) demonstrated that the best estimator with the IP method is the minimum of the second derivative located just below h_{LGM}.

4.1.4 Haar wavelet transform method

The concept of wavelet transform (WT) was introduced in the early 1980's and then was used by many authors for atmospheric and oceanographic studies (Farge, 1992; Meyers et al., 1993; Torrence and Compo, 1998). The most simple orthogonal mother-wavelet function is the Haar wavelet (Daubechies et al., 1992). Using this as kernel, studies that successively determined the ABL height are Davis et al. (2000), Cohn and Angevine (2000), Brooks (2003), among others. The HWT-based method applied here is an application of wavelets for feature recognition. The Haar wavelet function returns large coefficient values where a profile has large backscatter gradients, so this is used with lidar profiles.
The Haar wavelet is defined as

$$H\left(\frac{z-b}{a}\right) = \begin{cases} 1 & \text{for} \quad b - a/2 \le z \le b \\ -1 & \text{for} \quad b \le z \le b + a/2 \\ 0 & \text{otherwise} \end{cases} \qquad [4.8]$$

where z is height and a and b are the dilation and translation of the function, respectively. A functional diagram of the Haar wavelet is shown in Figure 4.1.

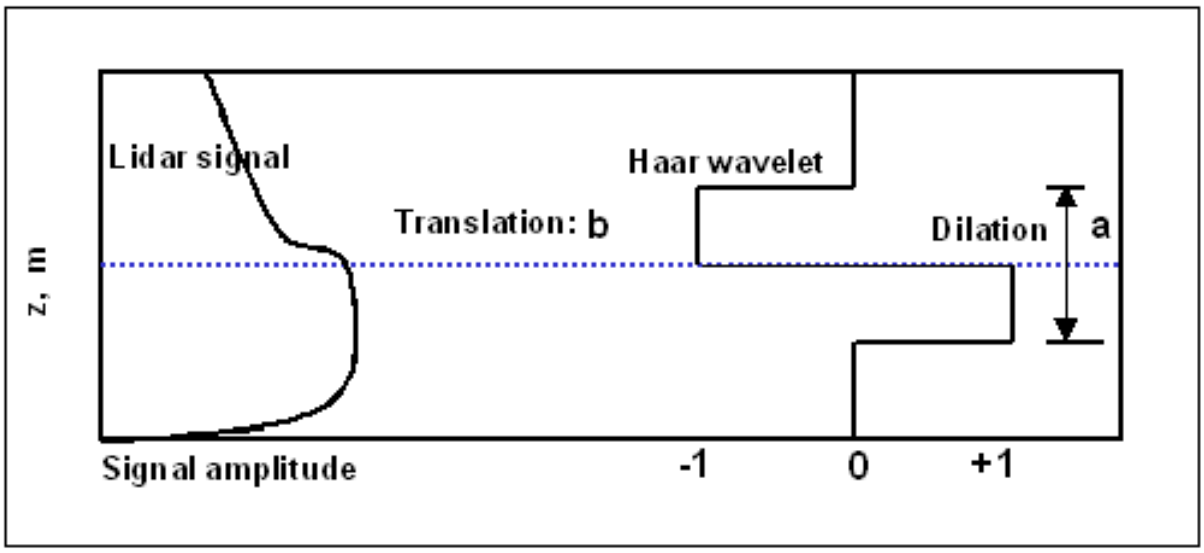

Figure 4.1: Sketch of the Haar wavelet function used in the determination of the ABL height. The blue dotted line marks the expected h_{HWT}.

For a signal *f(z)* (here range-corrected signal, $P(z)\,z^2$ and the Haar wavelet *H*, the convolution, $W_f(a,b)$ of the Haar function with the backscatter profile, is defined as the covariance transform (Gamage and Hagelberg, 1993). This function after normalized with the dilation value is expressed as

$$W_f(a,b) = \frac{1}{a}\int_{z_{min}}^{z_{max}} \left\{ P(z)\,z^2 \; H\left(\frac{z-b}{a}\right) \right\} \mathrm{d}z. \qquad [4.9]$$

Here z_{min} and z_{max} are the lower and upper altitude of the lidar profile between which the HWT is to be applied. Now, the maximum value of the covariance transform corresponds to the strong step-like decrease in backscatter at the top of the ABL. The corresponding altitude of the resulting maximum is identified as the ABL top and is expressed as

$$h_{HWT} \equiv \max\left(W_f(a,b)\right) \quad \text{for } z_{\min} < b < z_{\max} \quad . \qquad [4.10]$$

This technique works well except for complicated cases, e.g., when the boundary layer consists of the newly developing CBL and one or more RL in the lower troposphere like possibly in the morning time (see section 5.3.2.1).

4.2 Estimation of entrainment zone thickness from ABL height time series

The existence of different entrainment regimes and hysteresis effects in the daytime evolution of the EZ makes the retrieval of the EZT complicated (see, Flamant et al., 1997). An entrainment zone is basically characterized by a region near the top of the boundary layer where an enormous mixing of the free-tropospheric (FT) air (by downdraft) and the thermals (by updraft) of the CBL occurs (Stull, 1988). The top of the entrainment zone can be easily determined, but the bottom height of the same is characterized by an altitude where 5-10 % of the air that has the FT characteristics. In this study this definition is used to estimate EZT. This definition was confirmed by Deardorff et al. (1980) through his water tank experiment. This experiment yielded a comprehensive description of the normalized depth of the entrainment zone and the "overall" Richardson number, R_i^*

$$\Delta h / h_0 = f\left(R_i^*\right)$$

where

$$R_i^* = \frac{g}{\overline{\theta}} \frac{\Delta\theta\, \overline{h}}{w_*^2} \qquad [4.11]$$

and

g is the acceleration due to gravity

$\Delta\theta$ is the potential temperature jump across the entrainment zone

$\overline{\theta}$ is the mean ABL potential temperature.

w_* is the convective velocity scale defined as $w_* = \left[\frac{g}{\overline{\theta}}\left(w'\theta'\right)_s \overline{h}\right]$

The definition of Richardson number (Melfi et al., 1985) is important while discussing the EZT: Deardorff et al. (1980) suggested that the ratio of the EZT and the ABL depth is directly related to R_i*.

EZT can be determined from cumulative frequency distribution of the instantaneous ABL height measurement from lidar (e.g., Stull and Eloranta, 1984; Melfi et al., 1985). This procedure

consists of the calculation of height differences between the 5 %-10 % and 90 %-95 % values of the cumulative frequency distributions of the instantaneous ABL height evolution.

This analysis is not directly comparable with that of Melfi et al. (1985) since they considered the EZ in a spatially averaged sense whereas EZ in a time averaged sense is considered in this work. The EZT is computed from the time series from a vertically pointing ground-based lidar while their study used backscatter signal collected from aircraft. It is assumed in this case that the EZ is "*a measure of the averaged vertical size of the ABL-height fluctuations*" as defined in Boers et al. (1995). This should be mentioned here that Taylor's "frozen turbulence" hypothesis could be used to transform temporal data into the spatial domain (Taylor, 1921; Powell and Elderkin, 1974). These results are then compared with the standard deviation approach (Davis et al., 1997; Hägeli et al., 2000; Schwemmer et al., 2004).

Estimation of the EZT is important since it can describe the growth of the CBL and accompanying vertical mixing of the pollutants that largely depends on the surface forcing as well as on entrainment at the CBL top.

4.3 Statistical analyses

All geophysical datasets show non-stationary behavior both in time and space. ABL is the most variable atmospheric layer in the troposphere due to the variety of physical processes. Major challenges lie in the development and application of the best suitable statistical approach to the problem of non-stationarities in the signal.

The CBL consists of highly fluctuating and irregular structures and the CBL height necessarily carries this information by its irregularity in space and time. Therefore, the top of the CBL is an implicative of this fluctuation. Variability in the CBL top could be an indicator of multi-scaling properties. To quantify the aspects of variability and correlations at different temporal and spatial scales, one needs to apply advanced statistical approaches. To do this, different statistical techniques have been applied here: Fast Fourier transformation (FFT)-based power spectral analysis, detrended fluctuation analysis (DFA) and multifractal analysis.

Davis et al. (1994) presented a detailed discussion on the spectral properties and stationary issues for time series of geophysical datasets. The basic concept of their technique is to search for the scaling regime of those data, the energy/power spectra of which show a power law dependency. They showed that computation of the power/energy spectra could easily test the scale invariance. For a scaling process, one can always expect a power law behavior (Davis et al., 1994). Here, the aim is to illustrate the statistical behavior of the CBL height time series on the basis of multifractal framework. Using these techniques, very recently, through a series of three papers Lovejoy et al. (2008), Lilley et al. (2008) and Radkevich et al. (2008) demonstrated lidar data of atmospheric aerosols (considering passive tracers) to estimate turbulent scaling in the atmosphere.

High-resolution time series of lidar derived CBL height is considered for applying these methods. Firstly, it is tried to find a power law dependency to examine the existence of self-affined properties of the CBL height time series. Secondly, same time series is treated by the DFA. Then the effects of local trends by fitting polynomials of degree 1 or/and 2 are demonstrated. Finally, local correlations and scaling properties of the CBL height time series are studied by the multifractal approach. Similar analyses can be found in Ivanova et al. (2002) for the case of a time series of stratus cloud base height. To my best knowledge, to date such analyses have not yet been applied to a time series of CBL height obtained from a ground-based lidar system.

The main objectives in performing statistical analyses of the CBL height evolution (i.e., time series) are three-fold:

- To determine the characteristic features of the local correlations in the CBL evolution
- To investigate its multi-fractal behavior
- To classify the non-satationarities involved in the CBL

4.3.1 Spectral analysis

The FFT-based spectral analysis is performed on the instantaneous CBL height time series. First of all, removal of outliers (due to erroneous profiling) from the time series is performed since these outliers yield significant errors in the calculation (Lenschow et al., 2000). The time series is then corrected for a linear trend and then is high-pass filtered to get rid of the long-term variations in the data. This is necessary to perform a clear separation between large-scale and small-scale phenomena. The high-pass filtering process is performed by the fast Fourier transform of the time series and then multiplying the transforms with an appropriate filter function; see Senff et al. (1996) and Wulfmeyer (1999a) for outlier removal technique and high-pass filtering procedure.

The power-law dependence can be found from $S_F(f) \sim f^{-\gamma}$ where S_F is the power and f is the frequency and γ is the corresponding spectral exponent. The slope of $\ln[S_F(f)]$ versus $\ln[f]$ yields the value of γ. The value of γ determines whether the process is self-affined or not. If $1< \gamma<3$ then, the signal is a non-stationary process with stationary increments.

4.3.2 Detrended fluctuation analysis

Detrended fluctuation analysis (DFA) is a method for quantifying the correlation property of a non-stationary time series based on computation of a scaling exponent by means of a modified root mean square calculation of a random walk. The DFA method reveals the extent of long-range correlations in a time series. Briefly, the time series to be analyzed (with N samples) is first integrated. Next, the integrated time series is divided into boxes of equal length n. In each box of length n, (a polynomial of the order of 1 or 2) a least squares line is fitted representing the local trend in that box. The y coordinate

of the straight-line segments is denoted by $y_n(i)$. Next, the integrated time series, y_N(i) is detrended by subtracting the local trend, $y_n(i)$, in each box so that

$$Y(i) = y_N(i) - y_n(i) \quad [4.12]$$

For a given window of size n (in this case, the profile number), the root-mean-square fluctuation of this integrated and detrended time series is called detrended fluctuation function and is calculated as

$$F(n) = \sqrt{\left[1/N \sum_{i=1}^{N_{max}} [Y(i)]^2\right]}. \quad [4.13]$$

The above computation is repeated for different box sizes n (different scales) to provide a relationship between $F(n)$ and n. A power-law relation between $F(n)$ and the box size n indicates the presence of scaling: $F(n) \sim n^{\alpha^*}$. The parameter α^*, called the scaling exponent or correlation exponent (self-similarity parameter) represents the correlation properties of the signal: if $\alpha^* = 0.5$, there is no correlation and the signal is an uncorrelated signal (white noise- the value at one instant is independent of all previous values), if $\alpha^* < 0.5$, the signal is anti-correlated; if $\alpha^* > 0.5$, there are positive correlations in the signal. $0 < \alpha^* < 0.5$ indicates power-law anti-correlations (large values are more likely to be followed by small values and vice versa); for $\alpha^* > 1$ correlations exist but cease to be of a power-law form. As quantified by the parameter α^*, this method enables identification of the timescales over which noise dominates the time series and characterizes the temporal range of correlations in the time series. For DFA, presence of a positive alpha value defines a scaling range where a relationship $\gamma = 1+2\alpha^*$ holds (Davis et al., 1994). Later, this relationship was recognized as Heneghan and McDarby (2000) relationship.

The most important advantage of DFA over conventional methods (e.g., autocorrelation, spectral, and Hurst-analysis) is that it permits the detection of intrinsic self-similarity embedded in a seemingly non-stationary time series (Hurst et al., 1965; Pelletier, 1997). Following the work of Peng et al. (1994), several theoretical studies elucidated the power and limitations of filtering out various trends from synthetic data series (Heneghan and McDarby, 2000, Talkner and Weber, 2000, Hu et al., 2001). It is considered that the DFA is a reliable tool to accurately quantify the correlation within a signal. Additionally, the scaling and crossover features of $F(n)$ can be used to determine the order of polynomial trends present in the data.

4.3.2 Multifractal analysis

The intermittency is quantified adopting the singular measure analysis. Following Davis et al. (1994), the first step that this technique requires is to define a basic measure $\varepsilon(1;l)$ as

$$\varepsilon(1;l) = \frac{|\Delta y(1;l)|}{<\Delta y(1;l)>}, \; l = 0,1,2,.....,N-1 \quad [4.14]$$

where $\Delta y(1;l)= y(t_{i+1})-y(t_i)$ is the small scale gradient field and <> denotes an average over the N data points

$$\langle \Delta y(1;l) \rangle \frac{1}{N} \sum_{l=0}^{N-1} |\Delta y(1;l)| \quad . \tag{4.15}$$

Next, one can define a series of ever more coarse-grained and ever shorter fields ε(r; l) where $0 < l < N\text{-}r^*$ and r*=1,2,4,8…N. Thus the average measure of in the interval [l; l+r] is

$$\varepsilon(r^*,l) = \frac{1}{r^*} \sum_{r^*=l}^{l+r^*-1} \varepsilon(1;l') \quad . \tag{4.16}$$

The scaling properties of the generating function are then obtained through the equation

$$\left\langle \varepsilon(1;l)^q \right\rangle \sim \left(\frac{r^*}{N} \right)^{-K(q)}, for\ q \geq 0 \qquad . \tag{4.17}$$

Using $K(q)$ function one can define the generalized multifractal dimension

$$D_m(q) = 1 - \frac{K(q)}{q-1} \qquad . \tag{4.18}$$

Results obtained for a CBL height time series after applying these three techniques are described in section 5.3.5.

4.4 Procedure to determine higher-order moments

Statistical results concerning turbulent moment analysis of the fluctuation of particle backscatter coefficients inside the boundary layer is an area of major interest. In spite of its importance, no study exists so far that illustrates potential of this technique (higher-order moments estimation) for aerosol backscatter in the CBL.

The idea of estimating the higher-order moments of the range corrected lidar backscatter signal lies in assuming the aerosols as passive tracers of the atmospheric dynamics. In this case, this is assumed that fluctuations of the backscatter coefficient are mainly due to changes of total aerosol number density but not due to fluctuations of the microphysical properties of the aerosol particles. The latter may be due to aerosol swelling and advection of different particle types. The analysis presented below can be improved if more information concerning the vertical profile of aerosol microphysical properties becomes available, e.g., by in-situ profiling or the use of more sophisticated lidar systems.

Here, the main aim is to determine the turbulent moments of particle backscatter and its scientific interpretation if fluctuations of their microphysical properties can be neglected. One of the important factors is the change of aerosol optical properties in environments with variable RH (hygroscopic factor). But for a well-mixed CBL, one can approximate the RH to be constant in height within the CBL. Changes in the entrainment zone may be significant, however, as far as RH < 80%, also in this region aerosol swelling can be neglected (Wulfmeyer and Feingold, 2000). Under these

conditions, the fluctuation in the range-square corrected backscatter signal is approximately proportional to the fluctuations in the aerosol number density as shown in the following.

It was mentioned earlier that the range-square corrected lidar signal is directly proportional (Eqn. 4.4) to the particle backscatter coefficient, i.e., $\beta_{par}(z)$. So, the backscatter signal can be considered as a surrogate for the concentration of a passively advected tracer i.e. aerosols. According to the Mie theory (Boheren and Huffman, 1983), the particle backscatter coefficient at a certain height *z* and at time *t* can be expressed

$$\beta_{\lambda,par}(z,t) = \sum_{i=1}^{N} \int_{0}^{\infty} Q_{bsc,\pi,i,z}^{par}(r(t), m(t), \lambda)\, \pi\, r^2 n_{i,z}(r(t))\, \mathrm{d}\, r \quad . \qquad [4.19]$$

$Q_{bsc,\pi,z}^{par}(r(t), m(t), \lambda)$ stands for the backscatter efficiency at the lidar wavelength λ, *r* is the particle radius and *m* is the complex refractive index of the particle, *n(r(t))* is the number of particles with radius *r* at time *t.* The index *i* in Eqn. 4.19 describes various particle types.

If one neglects the variation of the aerosol size with the relative humidity and assumes similar types of aerosol particles in the study region, then the fluctuation of $\beta_{\lambda,par}(z,t)$ can be expressed as

$$\beta_{par}(z,t) \approx \int_{0}^{R} \overline{Q_z}(r(t), m(t), \lambda)\, \bar{n}_z(r(t))\, r^2\, \mathrm{d}\, r \qquad [4.20]$$

$$\beta_{par}(z,t) \approx N_0(t) \int_{0}^{R} \overline{Q_z}(r(t), m(t), \lambda) \frac{\overline{n(r(t))}}{N_0(t)} r^2 \mathrm{d}\, r \quad . \qquad [4.21]$$

Generally, the aerosol number density can be expressed by a log-normal distribution

$$\mathrm{d}n_{i,z}(r(t)) = \sum_i \frac{N_{i,z}(t)}{\sqrt{2\pi} \cdot \log \sigma_{i,z}(t)} \exp\left(-\frac{1}{2} \left(\frac{\log\left(\frac{r(t)}{\mu_{i,z}(t)} \right)^2 r_{i,z}(t)}{(\log \sigma_{i,z}(t))^2} \right)^2 \right) \mathrm{d} \log r(t) \qquad [4.22]$$

where μ_i, and σ_i are the mean geometrical radius, and the standard deviation in each case, respectively.

If we can express the backscatter profile by a single type of aerosol particle,

$$\mathrm{d}n_z(r(t)) = \frac{N_{0,z}(t)}{\sqrt{2\pi} \cdot \log \sigma_{i,z}(t)} \exp\left(-\frac{1}{2} \left(\frac{\log\left(\frac{r(t)}{\mu_z(t)} \right)^2 r_{i,z}(t)}{(\log \sigma_z(t))^2} \right)^2 \right) \mathrm{d}\, r(t) \,. \qquad [4.23]$$

Now, we introduce the assumption that the fluctuations of the aerosol microphysical properties are significantly smaller than the fluctuations of the total number density in the observed volume of the lidar. In this case,

$$\beta_{par}(z,t) \approx N_{0,z}(t) \int_0^R \overline{Q_z}(r,m,\lambda) \frac{\overline{n_z(r)}}{N_0} r^2 \mathrm{d}r \approx N_{0,z}(t)\, C(z) \qquad [4.24]$$

which leaves a time independent function C(z) under the integral. This constant is characteristic for a particular type of aerosol particles. The temporal fluctuations can be written as

$$\Delta\beta_{par}(z,t) \approx \Delta N_z(t)\, C(z)\,. \qquad [4.25]$$

Consequently, for each height

$$\beta'_{par}(t) \approx N'(t) \qquad [4.26]$$

and

$$\frac{\beta'_{par}(t)}{\beta_{par}(t)} \approx \frac{N'(t)}{N(t)} \qquad [4.27]$$

which states that the fluctuation of the particle backscatter coefficient is directly proportional to the aerosol number density fluctuation in the atmosphere if the assumptions are valid. Furthermore, the relative fluctuation of the backscatter coefficient becomes equal to the relative fluctuation of the aerosol number density.

Profiles of higher-order moments of fluctuations of the lidar retrieved aerosol backscatter intensity i.e., variance (V), skewness (S_k), and kurtosis (K) are derived here following the methods, introduced in Lenschow et al. (2000) and applied in Wulfmeyer and Janjić (2005). Previous studies in turbulence analysis inspired to use high-resolution dataset for a better understanding of turbulent characteristics of the CBL by examining the ranges and scales of variability involved. Spectral analysis is performed in the same fashion as mentioned in the section 4.3.1 but for the measured relative particle backscatter coefficient at each altitude levels. During the error analysis, the system noise errors and the sampling errors were taken into consideration. The techniques for the determination of these noise terms were extensively discussed in Senff et al. (1994) and Wulfmeyer (1999a).

4.5 Wavelet-based spectral analysis

Studies of the oscillatory phenomena have traditionally been based on the FFT-based analysis (Cooley and Tukey, 1965). In the recent years, it was found that many of the processes in the ABL are non-Gaussian and non-stationary and have essential asymmetry in their probability distribution. FFT-based analysis alone cannot provide a comprehensive description of the properties of these processes because it yields a mapping of a process that is localized in frequency but global in time. This calls for the application of wavelet-based spectral analysis technique since this procedure in contrast to the FFT allows one to localize irregularities both in time and scale (frequency) domains and then to resolve

isolated features in a time series. By decomposing a time series into time, frequency, space, one is able to determine both the dominant modes of variability and how those modes vary in time. It provides a time-frequency representation since wavelet transform is capable of providing the time frequency information simultaneously, hence giving the time frequency representation of the signal.

FFT-based spectral analysis can estimate the frequency and power of the spectra in the time series but wavelet-based technique has added advantage that the time is known. Furthermore, FFT analysis is better choice for the identification of the larger-scale peaks due to convective activity or other wave-like motions. However, they fail to show smaller-scale peaks due to local small-scale turbulence or weak turbulence unless small time series is chosen so that the local phenomenon takes up a reasonable fraction of the time series. With the aid of wavelet technique multi-scale (large scale as well as small-scale localized processes) analysis from time series is possible and therefore applied here. A comparison of Fourier spectra and wavelet spectra can be found in Hudgins et al. (1993) while a theoretical discussion is given in Perrier et al. (1995).

Only in the last two decades, the application of wavelet technique to the atmospheric processes has gained immense acceptance both in short time series cases (Turner and Leclerc, 1994; Frey et al., 2000; Terradellas et al., 2005; Salmond, 2005) and in long time series cases (Torrence and Compo, 1998; Pal, 2004; Devara and Pal, 2004).

The steps involved in using wavelet analysis are described in Torrence and Compo (1998). A brief outline is presented in the Appendix-D. The analyzing mother wave function adopted for the continuous WT analysis in this work is Morlet since Morlet provides a better localization in the observed frequency (Torrence and Compo, 1998). Results obtained from wavelet spectral analysis are represented through scalograms (time/period) of the wavelet coefficient.

A flow chart is shown in Figure 4.2 summarizing the data analysis schemes applied as a part of post-processing of the data collected with the vertically pointing UHOH lidar system.

4.6 Scanning aerosol lidar data flow

Scanning lidar data flow consists of retrieval of the optical properties of atmospheric aerosols from the lidar range resolved signal intensity (raw data) and display of the particle backscatter field in 2-3 dimensions applying advanced graphics. Within the part of this thesis, complete data acquisition program and numerous dedicated programs for the post processing the lidar data were developed for analyzing the UHOH scanning aerosol lidar data.

A sophisticated and developed data acquisition code is of uttermost importance for immediate interpretation of the collected lidar data. Figure 4.3 shows the schematic representation of the lidar data flow, which explains how the lidar signal intensity, backscattered from atmospheric particles, clouds and molecules are represented through the images of the optical properties of the atmospheric aerosols,

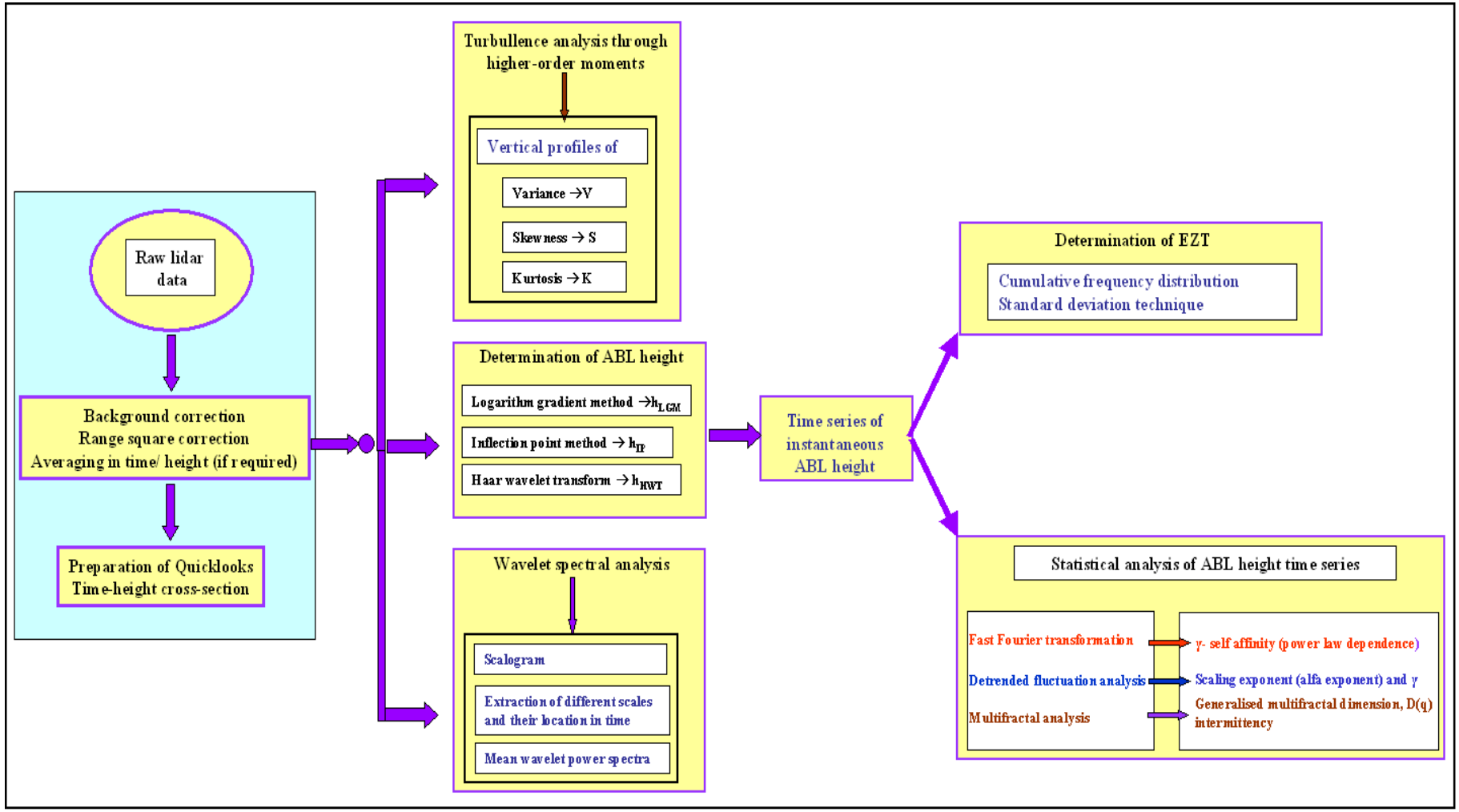

Figure 4.2: Flow chart showing the lidar data analysis methodologies including estimation of instantaneous ABL height, entrainment zone thickness and related statistical analysis for characterization of ABL dynamics. For details, see text.

and cloud particles. Each block is discussed briefly in the following to give an overview of the data recording, post-processing, and display techniques.

An important aspect of lidar application lies in the accurate recording and processing of the lidar return signals to take an advantage of the sophisticated lidar techniques and thereof the potential wealth of information about the atmosphere. The UHOH scanning lidar signal comprises the elastically backscattered signals from the atmospheric aerosols and molecules and cloud particles. Elastic scattering refers to the scattering process where the wavelength of the incident radiation remains unchanged. Molecular scattering or Rayleigh scattering intensity which is proportional to the λ^{-4} (λ, the wavelength of incident radiation) is sufficiently large at the UV wavelength region compared to the IR wavelength region. Normally nitrogen and oxygen contribute a major portion (of around 98 %) of the atmospheric molecules. On the other hand, the elastic scattering from particles with sizes comparable to the wavelength of the incident radiation or larger is called Mie scattering. This is worthwhile to mention that the Mie theory is valid for radiation of arbitrary wavelength by a sphere of arbitrary radius and complex refractive index.

The complete flow of the UHOH scanning aerosol lidar data consists of three major parts: real time data acquisition, post processing of the lidar data through lidar inversion technique for determining the aerosol optical properties and lidar data display techniques.

4.6.1 Data acquisition in real time

The main aim lies here to represent a complete view of the dataflow during data acquisition. Signal received by the detector is converted to binary bits with the Gage CS14100 card, which serves as ADC. Data flow during the acquisition in principle comprises of two inter-related blocks as shown in the flowchart. The DAC developed as a part of this thesis consists of a useful graphical user interface facility providing the user the following advantages:

- Choice of the scanning sector, scan type, scan step resolution or scan speed, number of scan steps or scan numbers, time resolution, range resolution, and option for time-synchronized scan either by selectable switches/fields or by some numbers.
- User can put the above values through a batch file and run the lidar system continuously unless it is intended to be stopped.
- Continuous display of several important update information, e.g., GPS time, number of dataset and scan completed, azimuth and elevation angle the lidar beam is pointing at, instantaneous time of each profile, indication of the backward movement of the scanner when lidar is not acquiring data.
- Time-synchronized scan with combinations of different scan patterns.

The complete DAC initializes the data acquisition card and the scanner motors simultaneously. Initialization of the CS14100 consists of the choice of the number of samples (4096 bins) to be stored,

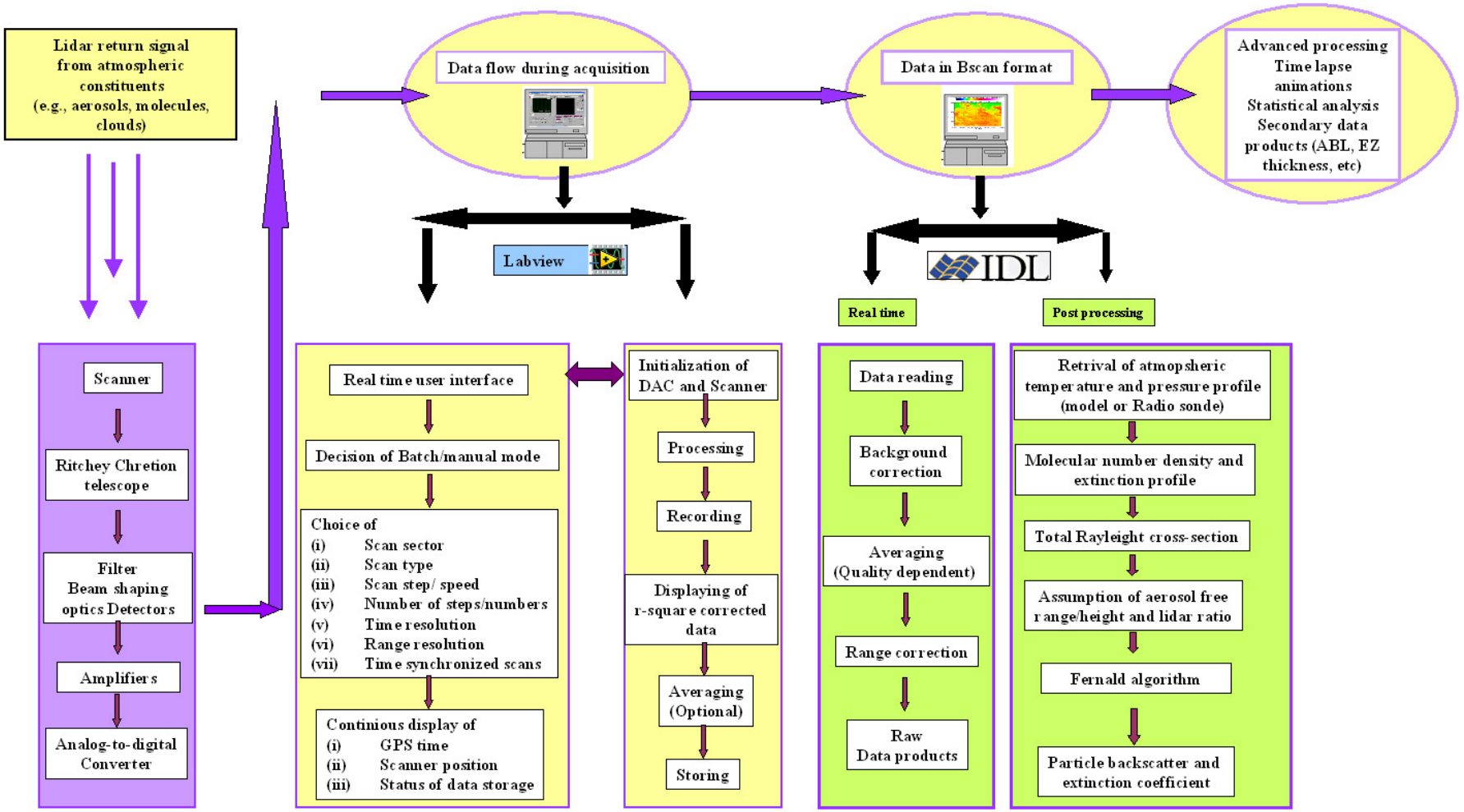

Figure 4.3: Flowchart showing the summary of the major steps involved in the data acquisition, storage, post processing and presentation of the UHOH scanning aerosol lidar data. For details, see text.

sampling rate (usually 50 MHz, but 100 MHz also possible), selection of input mode, trigger mode and configuration, capture mode, and selection of the impedance (50 Ω or 1 MΩ).

All these parameters are of particular importance for the initialization of the CS14100 card and properties of the stored lidar data (binaries). For instance, choice of 50 MHz sampling rate ensures the lidar data range resolution of 3 m, 4096 number of bins configures such high-resolved data up to a range of around 12 km. Configuration of the data acquisition card is detailed in the Appendix-B.

Initialization of the scanner motors consists of providing two particular values of revolution in degrees (both azimuth and elevation) of the motors so that the encoders provide a measure of the revolution of the laser beam emitting the center of the scanner mirror with respect to the initialized value of zero angles. The DAC yields an advantage to check the alignment of the lidar system for obtaining full overlap at sufficient lower range/height. This needs sufficient experience of the experimentalist. During this time, data storage is not active but the user has the possibility to start data storing at any time by switching on a binary switch after aligning the lidar system.

The display window on the DAC includes the raw lidar profile (instantly obtained), range-square corrected profile, and time versus range/height false color plot of the background corrected and range-square corrected signal intensity in arbitrary unit (a.u.) through a predefined pseudo-color scale. Once a lidar profile is corrected for range-square dependencies, this gives the experimentalist an opportunity to obtain a result proportional to the backscatter coefficient of the targets. Particularly, the range-height image of the lidar signal intensity yields the user an opportunity for interpreting the collected data in real time and for obtaining qualitative information about the temporal variation of the structure of the troposphere, especially the ABL.

The real-time display of the range-square corrected profile yields the facility to achieve proper alignment of the transmitter and receiver optical systems and to obtain full overlap at the closest height/range possible. This is performed at the beginning of the lidar measurements through examining the vertical behavior of the lidar signal as the alignments of the necessary optics are changed. During this check, the largest profile (maximum in amplitude after the full-overlap region) corresponds to the optimal alignment of the system. Typical behavior of the lidar signal is checked in all direction of interest and optimized alignment is then obtained. Apart from the single shot acquisition at 30 Hz, the DAC facilitates the user to average the data both in time and/or in range to decrease the amount of stored data whenever necessary.

The DAC developed for the UHOH scanning lidar is found to consist of the facility of obtaining continuous time-synchronized scanning measurements. The scan speed is widely variable ranging from $10° s^{-1}$ for motion of the azimuth and elevation angle, so that a full 360°-turn (180°-turn in elevation) needs 36 s (18 s), down to less than $0.1° s^{-1}$. The angle resolution that the decoder can provide is of about 0.003°. During the tracing back motion of the scanner, the lidar does not acquire data. This facilitates to keep a time-synchronized data acquisition in the following scans. This is performed to achieve uni-directional scans separated by a constant time interval among them. This strategy yields the

user an advantage to assess the atmospheric flow features. Sun safety of the PMT is taken care while providing the input of the azimuth and elevation angles for particular scan measurements after reading a sun chart, available from Landeshauptstadt Stuttgart, Amt für Umweltschutz, Abt. Stadtklimatologie (http://cgi.stadtklima-stuttgart.de/mirror/sonnefre.exe).

The DAC controls the storage of the raw lidar signal intensity as a function of height/range through a special binary format, called Bscan format. This format yields the user several advantages after providing shot-to-shot variation of GPS time, azimuth and elevation angles of the lidar signals, altitude. Additionally, this format takes care of some important information for the lidar operations, e.g., number of lidar profiles averaged, length of the data, wavelength, and location of lidar site including co-ordinates. These headers are repeated for each lidar profile and written to the Bscan file, specified by the user. A detailed description of the Bscan header information can be found under the Appendix- A.

4.6.2 Post processing of the scanning lidar data

The elastic-backscatter signal at 355 nm allows for calculating the particle backscatter coefficient through analytical inversion of the lidar equation (Klett, 1981; Sasano et al., 1985; Fernald, 1984). The molecular backscatter and extinction profiles are determined along the line of sight (LOS) of the lidar signal using pressure and temperature values measured at ground in combination with the hydrostatic equation and information about atmospheric stability, respectively.

Calibration of the lidar can be accomplished using clear-air signals in the far range for each profile. As multiple scattering effects can usually be neglected, accurate fields of the backscatter coefficient can be derived even though some uncertainties arise from the prescribed lidar ratio profile (Kovalev, 1995).

The steps for the determination of the particle backscatter coefficient are the following: (a) background level subtraction, (b) cancellation of erroneous profiles, arising from undesired hard targets like trees or buildings, or saturation in the detector hence in ADC, (c) averaging in time and in range with discrete boxcar window e.g., 20 profiles (e.g., time resolution of 0.66 s, for 1° s^{-1} scan speed and 0.66° which gives out 12 m spatial resolution in 1 km range and 36 m at 3 km) and in range e.g., 10 bins yielding 30 m, and (d) application of the inversion technique, to calculate particle backscatter coefficient (Fernald, 1984). This step inherently uses few assumptions and calculations: (i) a constant value for extinction-to-backscattering ratio for aerosols (so called lidar ratio), (ii) reference range for calibrating lidar signal, (iii) assumption of particle backscatter coefficient value at calibration range, and (iv) Rayleigh scattering cross-section following the formulation introduced in Bucholtz et al. (1995) from known atmospheric temperature and pressure profile from collocated radio sounding on the experimental days, or using surface temperature and pressure information.

4.6.2.1 Lidar inversion technique

The monostatic lidar equation (Eqn. 4.1) can be analytically solved following the method described in Fernald (1984). Since $P_{0,\lambda}(R)$, c, t_p, K are system dependent constant, Eqn. 4.1 can be expressed as

$$P_\lambda(R) = \mathrm{C}\, R^{-2}\, O(R)\left(\beta_{\lambda,mol}(R) + \beta_{\lambda,par}(R)\right) \exp\left(-2\int_0^R \left(\alpha_{\lambda,mol}(R) + \alpha_{\lambda,par}(R)\right)\right) \quad [4.28]$$

Since the lidar equation involves two different unknown variables (particle backscatter and extinction coefficient), therefore it is necessary to assume a constant ratio of the particle extinction to the backscatter coefficients to solve the lidar equation after the application of inversion technique proposed in Fernald (1984). This ratio is termed as aerosol lidar ratio and can be represented as

$$S_{\lambda,par}(R) = \left(\frac{\alpha_{\lambda,par}(R)}{\beta_{\lambda,par}(R)}\right) \quad [4.29]$$

On the contrary, ratio of the extinction to the backscatter coefficients for the molecular scatters is constant in all heights

$$S_{\lambda,mol}(R) = \left(\frac{\alpha_{\lambda,mol}(R)}{\beta_{\lambda,mol}(R)}\right) = \frac{8\pi}{3}\ \text{sr.} \quad [4.30]$$

Combining Eqn. 4.28 to 4.30, $\beta_{\lambda,par}(R)$ can be expressed as

$$\beta_{\lambda,par}(R) = \frac{P_\lambda(R)\,R^2 \exp\left[-2\int_0^R \left(S_{\lambda,par} - S_{\lambda,mol}\right)\beta_{\lambda,mol}(R')dR'\right]}{\mathrm{C} - 2S_{\lambda,par}\int_0^R P_\lambda(R)\,R^2 \exp\left[-2\int_0^{R'} \left(S_{\lambda,par} - S_{\lambda,mol}\right)\beta_{\lambda,mol}(R'')dR'\right]dR} - \beta_{\lambda,mol}(R) \quad [4.31]$$

Now, the unknown system constant C can be obtained after calibrating the lidar signal at a calibration range R_c with an assumed value of the ratio of particle backscatter to Rayleigh extinction coefficient. For simplicity, here onwards $P_\lambda(R)\,R^2$ is expressed as *X(R)*.

The most critical input parameter here is the lidar ratio $S_{\lambda,par}(R)$. This quantity depends on the microphysical, chemical, and morphological properties of the aerosol particles. For a single wavelength elastic lidar system, a constant lidar ratio value in all height is considered instead of height dependent profile of lidar ratio value. So, $S_{\lambda,par}(R)$ can be kept outside the integral in Eqn. 4.31. Due to the absence of additional information, the aerosol lidar ratio is an input for the UHOH lidar data analysis and a constant height-independent value is assumed (Pappalardo et al., 2005).

Furthermore, on using the *a priori* information of the $\beta_{\lambda,par}(R)$ at the calibration range R_c, Eqn. 4.31 can be expressed as

$$\beta_{\lambda,par}(R)+\beta_{\lambda,mol}(R)= \frac{X(R)\exp\left[-2\left(S_{\lambda,par}-S_{\lambda,mol}\right)\int_{R_c}^{R}\beta_{\lambda,mol}(R')dR'\right]}{\frac{X(R_c)}{\beta_{\lambda,par}(R_c)+\beta_{\lambda,mol}(R_c)}-2S_{\lambda,par}\int_{Rc}^{R}X(R')\exp\left[-2\left(S_{\lambda,par}-S_{\lambda,mol}\right)\int_{R_c}^{R'}\beta_{\lambda,mol}(R'')dR''\right]dR'} \quad [4.32]$$

On the other hand, the total Rayleigh-scattering cross section per molecule, σ(λ), is expressed as

$$\sigma(\lambda)=\frac{24\pi^3\left(n_s^2-1\right)^2}{\lambda^4 N_s^2\left(n_s^2+2\right)^2}\left(\frac{6+3\rho_n}{6-7\rho_n}\right) \quad [4.33]$$

where λ is the wavelength (in centimeters), n_s is the refractive index for standard air at λ, N_s is the molecular number density (2.54743 x 10^{19} cm^{-3}) for standard air and ρ_n is the depolarization factor- a term that accounts for the anisotropy of the air molecule and depends on the wavelength (Bucholtz, 1995).

Ideal gas law allows calculating the molecular number density profile either using a known ground pressure and temperature or using the radiosonde retrieved pressure and temperature profiles if available.

$$\beta_{\lambda,mol}(R)=N(R)\sigma(\lambda) \quad [4.34]$$

Molecular number density is calculated as

$$N(R)=\frac{P(R)}{kT(R)} \quad [4.35]$$

where k is the Boltzmann constant (1.380658 x 10^{-23} J K^{-1}) and T(z) and P(z) can be calculated as

$$T(z)=T_0+\frac{dT}{dz}z \quad [4.36]$$

$$P(z)=P_0 e^{\frac{-gz}{R_L T}} \quad [4.37],$$

respectively where T_0 and P_0 are standard sea level temperature (288.15 K) and pressure (1013 mb), respectively, and R_L is the universal gas constant for dry air (287.05 J kg^{-1} K^{-1}). T (z) and P (z) can also be obtained with the radiosonde profile. Further calculation for Rayleigh volume scattering coefficient is performed following Bucholtz (1995) where variation of the depolarization factor with wavelength is taken care.

The Eqn. 4.32 leads to a simple numerical integration scheme and the inversion can be accomplished analytically. A suitable calibration range is determined for each individual case by the analysis of the lidar backscattering signals. The inversion technique is numerically stable, if it is accomplished in backward direction. Furthermore, backward formulation rapidly vanishes the dependencies on the far range initial guess of particle backscatter coefficient. Therefore, the inversion procedure applied in this study is performed from the far field calibration (Fernald, 1984) height after confirming a low aerosol loading.

Furthermore, another key disadvantage of this technique arises due to the use of a height independent profile of lidar ratio. In reality, lidar ratio can strongly vary with height especially when marine, anthropogenic, and/or desert aerosol, different aerosol layers are present in layers above each other (Ansmann et al., 2001, 2002). Even in the well-mixed layer, the lidar ratio is not constant with height because RH varies with height.

Numerous studies have already been performed for finding the advantages and limitations of the inversion technique (see, Bissonnette, 1986; Kunz, 1996 ;). The key limitation arises due to the fact that both particle backscatter coefficient and particle extinction coefficient is determined from one measured quantity, the elastic lidar signal.

4.6.2.2 Determination of optical properties from scanning lidar data

If one assumes that inversion algorithm is valid in the situation that the backward integration scheme starts at a calibration range in the aerosol-free troposphere then inversion technique can easily be applied to the lidar data obtained from vertical measurement (elevation angle of 90°). But this methodology is not straightforward for the lidar data obtained from RHI scanning measurement due to the trade-off between the low signal-to-noise ratio of the lidar signal and the calibration range (to be estimated) for the inversion at the very low elevation LOS. Due to the changes in elevation angle of the LOS during RHI scanning measurement the reference range comes down from the assumed level of free troposphere to the region of ABL (while decreasing elevations of LOS from 90°). Schematic representation of this fact is shown is Figure 4.4.

In the figure the lidar system is located at point O (origin). One can assume the figure to be a mimic of a hemispherical scan covering elevation angle from 0° to 180°. Fernald's inversion can easily be applied to the LOS at an elevation angle of 90° since this corresponds to the vertical lidar measurement. Here the calibration range can easily be fixed and in Figure 4.4 calibration range is at a height/range of 4.5 km assuming that the aerosol load is vary small above the height 3.0 km. Quality of the lidar signal at this range is high enough to be analyzed with respect to signal-to-noise ratio. One can also apply the same technique to obtain the $\beta_{\lambda,par}(R)$ profile for the LOS at an elevation of 80°. Aerosol-free region is present from a height of 3.0 km, and then a critical LOS reaches at a certain elevation angle where the inversion technique cannot be applied directly due to the presence of high

aerosol content in the ABL. One can assume that such a situation arises in the figure for the LOS1 (red colored) at an elevation of 40°. In such a critical case the calibration value for lidar signal on LOS2 (black colored in Figure) at R_{C2} is obtained from the $\beta_{\lambda,par}(R)$ value at the corresponding height (not range) of previous LOS1 value; here R'_{C1}. Similarly the calibration value at R_{C3} is assumed to be similar as R'_{C2} and so on.

Very similar approach was applied in Sasano (1996) where he assumed that the aerosol was distributed almost homogenously along the horizontal direction (layered structure, see section 5 in Sasano, 1996). But the approach followed here is much advanced in the regard that high-resolution RHI scanning measurement takes the advantage to assume a closest value of $\beta_{\lambda,par}(R)$ at the calibration range from the previous LOS where the inversion technique was valid on the basis of the calibration at a height with low aerosol loading. So the method applied here can easily get rid of the assumption of layered structure and can be applied in any critical situation provided the RHI scan includes at least one LOS where inversion technique is strictly applicable and the RHI scan provides high-resolution data both in range and in time. This technique provides an advantage of relative calibration for each LOS of each RHI scan measurement. A detailed sensitivity analysis is performed for the inversion method and described in Appendix- C.

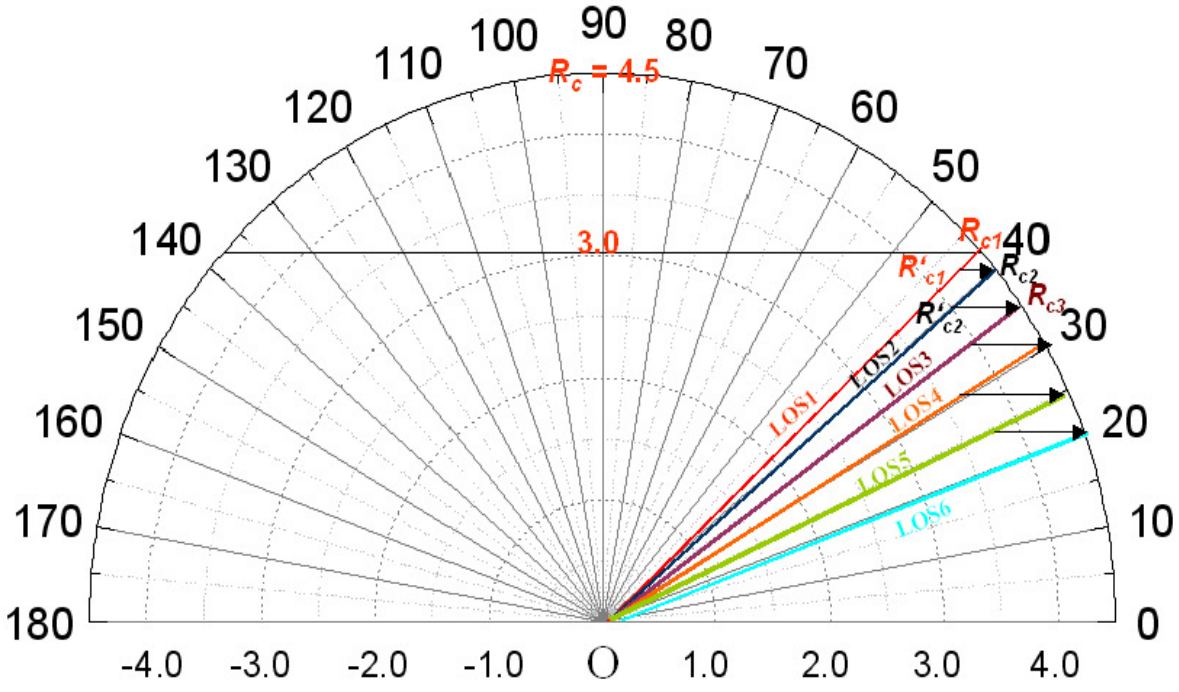

Figure 4.4: Sketch of the data analysis scheme applied to obtain particle backscatter coefficient field from RHI scan measurement (see, section 6.4.2 for further details).

4.6.3 Lidar data display

Representation via mapping of the lidar data product is a key issue for the end users concerning the usefulness of the lidar remote sensing technique for atmospheric science studies. This includes the preparations of the plot of the PPI or RHI scanning view or time-height cross-sections of the particle backscatter coefficient field through a range-range or range-height panel with averaging (moving window smoothing) or without any sort of additional averaging. Several automated mapping tools were developed to create the plot of instantaneous profile of particle backscatter coefficient. Furthermore, time-lapse animations of the consecutive vertical or horizontal scans provide a view of the evolution of the CBL so that the transport of the atmospheric aerosols inside and above the CBL can be visualized.

The vertical profile (horizontal axis is value of $\beta_{\lambda,par}(R)$ and vertical axis is height) represents the instantaneous vertical structure of the aerosol distribution. Similar profiles can also be created for the PPI and RHI scans. Here the vertical axis represents the range from the lidar system instead of height. This plot contains the information of the instantaneous azimuth and elevation angle of the lidar beam.

The time-height cross-section of the $\beta_{\lambda,par}(R)$ field is obtained through compiling a series of consecutive vertical profiles where the horizontal axis is the time of sequential profiles and vertical axis is the height in m, AGL and each pixel intensity in pseudo-color represents the value of the parameter of interest (e.g., $\beta_{\lambda,par}(R)$) at a particular time and height. If scanning data are plotted in this frame, this is called range-time indicator (RTI) and height is replaced by range from lidar. These plots help the user to investigate and understand the evolution of aerosol structures of various scales. An RHI scan or vertical scan image at a particular azimuth direction is produced after the combination of incrementally increased or decreased multiple LOS backscatter coefficient value where the horizontal axis in the image is range from lidar and the vertical axis is height above the ground level. Additionally, the image provides the user the information including direction of scan, time required to complete the scan and scan speed to enrich the direct interpretation of the results.

If produced in various azimuth angles, RHI scan images enable the user to achieve important multi-dimensional views of the atmosphere. PPI scan image is produced in the same fashion with the exception that elevation angle is constant here for a particular scan and variable azimuth angles provide the information of the aerosol features at different ranges/distances. Lidar derived $\beta_{\lambda,par}(R)$ profiles at multiple LOS as a function of azimuth is combined in PPI image. This image yields the two-dimensional view of the aerosol structures present in the atmosphere. Horizontal view (plane at the lidar height) of the aerosol flow can be achieved if PPI scan is performed at an elevation angle of zero degree. Again, the sequential PPI scans at different elevation angles yield a view of the aerosol dynamics in the ABL. Altogether, these displays provide the possibility to obtain highly vertically and spatially resolved information on aerosol particles with the added advantage of high temporal

resolution. They help to interpret the temporal variability of optical properties of aerosols within a widely inhomogeneous atmosphere.

An example of the application of inversion technique is briefly presented here to illustrate the capability of the technique to retrieve the particle backscatter coefficient field from an RHI scanning measurements. Figure 4.5 shows example of an RHI scan image of $\beta_{\lambda,par}(R)$ in m^{-1} sr^{-1} obtained on 17 March during lidar measurements at UHOH campus. The scan speed was 1.0 °/s and the RHI sector were within the elevation angles from 67.5° to 112.5°. The approach followed here depends upon the assumption of $\beta_{\lambda,par}(Rc)=0$. *R*c is reference level and selected by interpreting the lidar raw signal. For the data shown

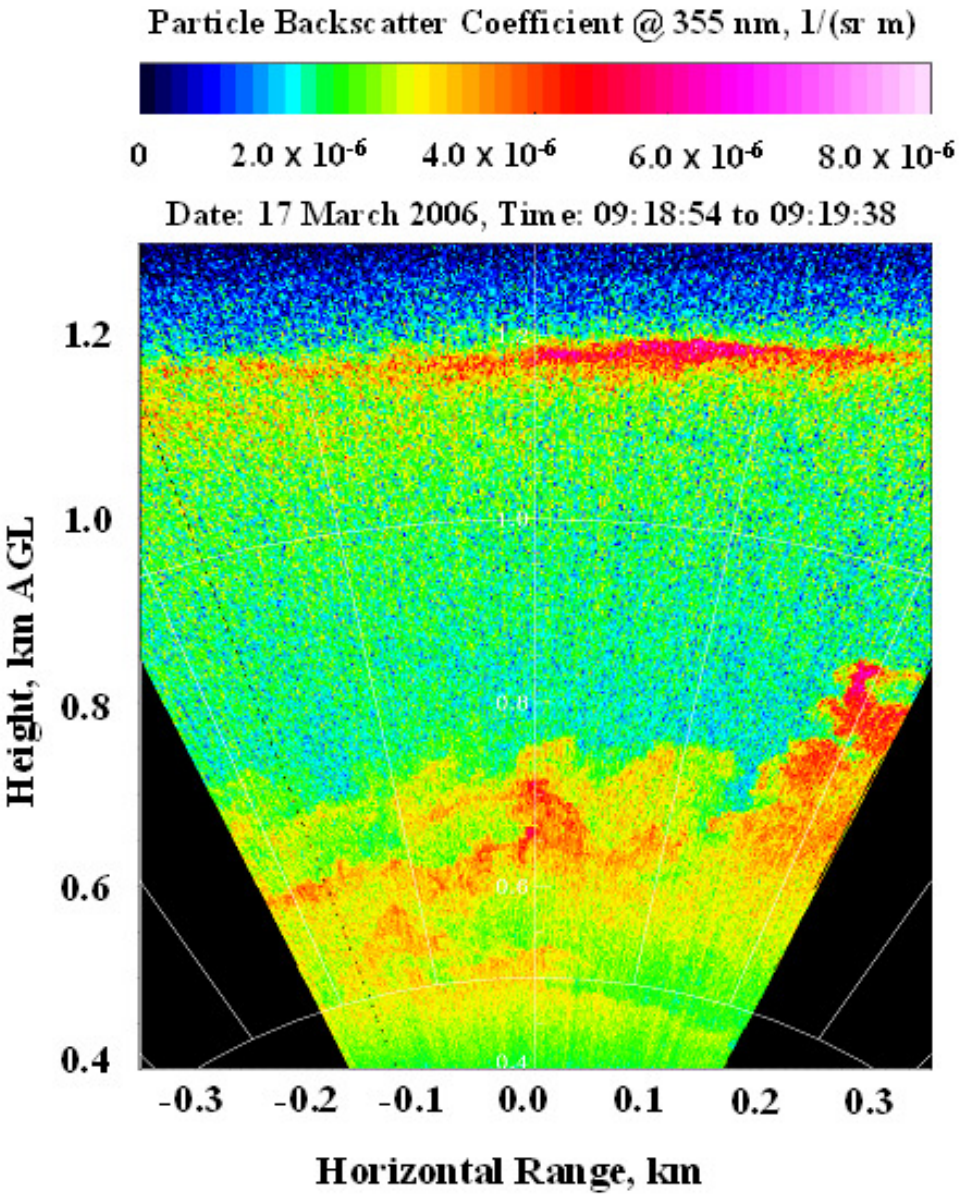

Figure 4.5: Particle backscatter coefficient of a 45-s RHI sector scan from elevation 67.5° to 112.5°, with a temporal and range resolution of 0.1 s and 3 m, respectively at 355 nm, collected on 17 March 2006, around 0919 UTC near UHOH main building. The angular resolution is 0.1°. A residual layer is present at a height of 1.2 km AGL.

here, it is 3.0 km. To reduce the effects of statistical noise during the calculation, an interval range $R_c \pm 60$ m instead of a single range bin of the free troposphere with less aerosol load is considered here. This value is used in the inversion method. Aerosol structures between 0.7 and 2 km are seen in particle backscatter coefficient field. This figure illustrates the extremely high range and temporal resolution of the particle backscatter measurements. The entrainment at the top of the CBL can be observed in detail.

4.7 Combined measurements of particle backscatter and extinction coefficient, and lidar ratio with scanning rotational Raman lidar

As described in the previous section, the classical inversion method (Fernald, 1984) requires the boundary condition of an aerosol-free layer and aerosol backscattering to extinction ratio at the calibration altitude/range. As the UHOH scanning RRL uses of the two RRL channels, this yields some advantages for retrieving the aerosol optical properties: (a) this technique is independent of the assumption of a profile of the lidar ratio (b) this technique is independent of the assumption of particle backscatter coefficient in an initialization range. The principal components of the scanning RRL received backscatter signal are Raman backscattered radiation from the molecules of nitrogen and oxygen and the elastically backscattered radiation from both air molecules and atmospheric aerosols.

The methodology and the theoretical background for the retrieval of particle backscatter and extinction coefficients are described here.

The lidar equations for the elastic and inelastic (Raman scattering) backscatter signals are

$$P_{\lambda 0}(R) = K_{\lambda 0}\frac{O(R)}{R^2}\left[\beta_{\lambda 0}^{par}(R)+\beta_{\lambda 0}^{mol}(R)\right]\times\exp\left\{-2\int_0^R\left[\alpha_{\lambda 0}^{par}(R')+\alpha_{\lambda 0}^{mol}(R')\right]dR'\right\} \quad [4.38]$$

and

$$P_{\lambda_R}(R) = K_{\lambda_0}\frac{O(R)}{R^2}N_R(R)\frac{d\sigma_{\lambda_R}(\pi)}{d\Omega}\exp\left\{-\int_0^R\left[\alpha_{\lambda_0}^{mol}(R')+\alpha_{\lambda_0}^{par}(R')+\alpha_{\lambda_R}^{mol}(R')+\alpha_{\lambda_R}^{par}(R')\right]dR'\right\} \quad [4.39],$$

respectively. $P_{\lambda 0}(R)$ and $P_{\lambda R}(R)$ are the backscattered signals from range R at the laser wavelength λ_0 and the Raman wavelength λ_R, respectively. $O(R)$ is the overlap between the laser beam and the receiver field-of-view; the value of this function is 1 for height/range above/beyond, which the laser beam overlaps completely with the field of view of the receiver. $K_{\lambda 0}$ and $K_{\lambda R}$ are the system constants. $N_R(R)$ is the molecule number density of the Raman-active gas and $\frac{d\sigma_{\lambda_R}(\pi)}{d\Omega}$ is the range-independent differential Raman cross section for the backward direction. $\beta_{\lambda 0}^{par}(R)$ and $\beta_{\lambda 0}^{mol}(R)$ are the elastic backscatter coefficients for particle and Rayleigh scattering, respectively. $\alpha_{\lambda}^{par}(R)$ and

$\alpha_{\lambda}^{mol}(R)$ describe the extinction of light of wavelength λ by atmospheric aerosol particles and gas molecules, respectively. Configuration of the RRL system allows similar values of the system constant and the overlap function for both wavelengths can be assumed to be same. Second one can be considered as a working assumption.

Rearrangement of the Eqn. 4.38 and 4.39 yields

$$\begin{aligned}
&\beta_{\lambda_0}^{par}(R)+\beta_{\lambda_0}^{mol}(R) \\
&=\left[\beta_{\lambda_0}^{par}(R_0)+\beta_{\lambda_0}^{mol}(R_0)\right] \\
&\times\frac{P_{\lambda_{\mathrm{Re}\,f}}(R_0)\,P_{\lambda_0}(R)\,N_{\mathrm{Re}\,f}(R)}{P_{\lambda_0}(R_0)\,P_{\lambda_{\mathrm{Re}\,f}}(R)\,N_{\mathrm{Re}\,f}(R_0)} \\
&\times\frac{\exp\left\{-\int_{R_0}^{R}\left[\alpha_{\lambda_{\mathrm{Re}\,f}}^{par}(R')+\alpha_{\lambda_{\mathrm{Re}\,f}}^{mol}(R')\right]dR'\right\}}{\exp\left\{-\int_{R_0}^{R}\left[\alpha_{\lambda_0}^{par}(R')+\alpha_{\lambda_0}^{mol}(R')\right]dR'\right\}}
\end{aligned} \quad . \qquad [4.40]$$

Use of the two rotational Raman lidar channels in this system gives a unique advantage to obtain a molecular reference signal (temperature independent, from temperature dependent RR signals). To minimize the temperature dependencies, a weighted sum of two RR signals (following Behrendt et al., 2002) is used

$$P_{\lambda_{\mathrm{Re}\,f}}(R)=P_{RR1}(R)+K_c * P_{RR2}(R) \qquad [4.41]$$

where $\lambda_{\mathrm{Re}\,f}$ is the molecular reference signal. This is clear from the above equation that the determination of the particle backscatter coefficient is primarily dependent on both the information of the elastic and Raman channel signals. $\beta_{\lambda 0}^{par}(R)$ is derived from the ratio $\frac{P_{\lambda_{\mathrm{Re}\,f}}(R_0)\,P_{\lambda_0}(R)}{P_{\lambda_0}(R_0)\,P_{\lambda_{\mathrm{Re}\,f}}(R)}$.

Retrieval of $\beta_{\lambda 0}^{aer}(R)$ then essentially depends upon the following choices and calculations:

(a) the reference height (R_0) is chosen such a way that $\beta_{\lambda_0}^{mol}(R_0) \rangle\rangle \beta_{\lambda_0}^{par}(R_0)$ and therefore one can approximate $\beta_{\lambda_0}^{par}(R_0)+\beta_{\lambda_0}^{mol}(R_0)\approx\beta_{\lambda_0}^{mol}(R_0)$. [4.42]

(b) The air density, molecular backscatter and atmospheric extinction profiles can be determined along the LOS of the lidar using pressure and temperature values measured at ground in combination with the hydrostatic equation and information about atmospheric stability, respectively. Collocated radiosonde profiles (whenever available) obviously give a better representation of the height/range dependencies of pressure and temperature.

Using above assumptions and calculations (Ansmann et al., 1992), Eqn. 4.40 can be simplified to

$$\beta_{\lambda_0}^{par}(R) = \left[\beta_{\lambda_0}^{mol}(R_0)\right] \times \frac{P_{\lambda_{\mathrm{Re}\,f}}(R_0)\, P_{\lambda_0}(R)\, N_{\mathrm{Re}\,f}(R)}{P_{\lambda_0}(R_0)\, P_{\lambda_{\mathrm{Re}\,f}}(R)\, N_{\mathrm{Re}\,f}(R_0)} - \beta_{\lambda_0}^{mol}(R) \qquad [4.43]$$

Now, the particle extinction coefficient can be calculated as

$$\alpha_{\lambda_0}^{par}(R) = \frac{d/dR\left\{\ln\left[N_{\mathrm{Re}\,f}(R)/P_{\lambda_{\mathrm{Re}\,f}}(R)\,R^2\right]\right\} - \alpha_{\lambda_0}^{mol}(R) - \alpha_{\lambda_{\mathrm{Re}\,f}}^{mol}(R)}{1+\left(\frac{\lambda_0}{\lambda_{\mathrm{Re}\,f}}\right)^k} \qquad [4.44]$$

where $N_{\mathrm{Re}\,f}(R)$ is the molecular number density of the reference gas. λ^{-k} denotes the wavelength dependence of the particle scattering. Configuration of the UHOH RRL system (Radlach et al., 2008a, b) allows here to assume $\lambda_0 = \lambda_{Ref}$ due to the very small difference between these two wavelengths. Height dependent lidar ratio profile $S_{\lambda_0}^{par}(R)$ can be obtained then from the ratio of the particle extinction and the backscatter coefficient at wavelength λ_0

$$S_{\lambda_0}^{par}(R) = \alpha_{\lambda_0}^{par}(R) \Big/ \beta_{\lambda_0}^{par}(R) \qquad [4.45]$$

The lidar ratio, which depends on size, shape and spatial orientation of the scattering particles, contains information about microphysical properties of the cloud, the basic quantities in the description of radiative properties.

The application of the RRL technique for the determination of aerosol optical properties described here to derive the profile of reference signal through Eqn. 4.43 is not straightforward for the RHI scanning measurements. For such cases, the constant value K_c (in Eqn. 4.41) is computed for the LOS at 90° elevation angle (corresponding to the vertical measurement) for each RHI scan and then same K_c value is used for the other LOS at other elevation angles of that scan. The only requirement for this modified approach is that the RHI scan measurement should contain at least a profile at an elevation angle of 90° so that the reference signal can be computed.

Through this novel approach one can get rid of the uncertainties involved in the inversion method to retrieve the aerosol optical properties. Additionally, the UHOH scanning RRL is found to be an excellent candidate for the exploration of ABL aerosol lidar ratio and temperature field. The approach to derive a lidar reference signal by use of pure rotational Raman backscattering signals is applied for the first time to the scanning data to obtain a 2-dimensional field of aerosol optical/physical properties in addition to the well-known time-height cross-section of the same. Both daytime and night time measurement examples with sufficient high temporal and spatial resolution after the RRL technique is rare in the literature.

Figure 4.6 shows an example of the results obtained after applying the rotational Raman lidar technique. Figure shows time-versus-altitude image of particle backscatter coefficient field obtained in the early morning of 8 June 2007 between 0430 and 0540 UTC during one of the IOP days of COPS field campaign. Altitude is in m AGL. This Figure depicts the high tempo-spatial sounding capability of the UHOH RRL system.

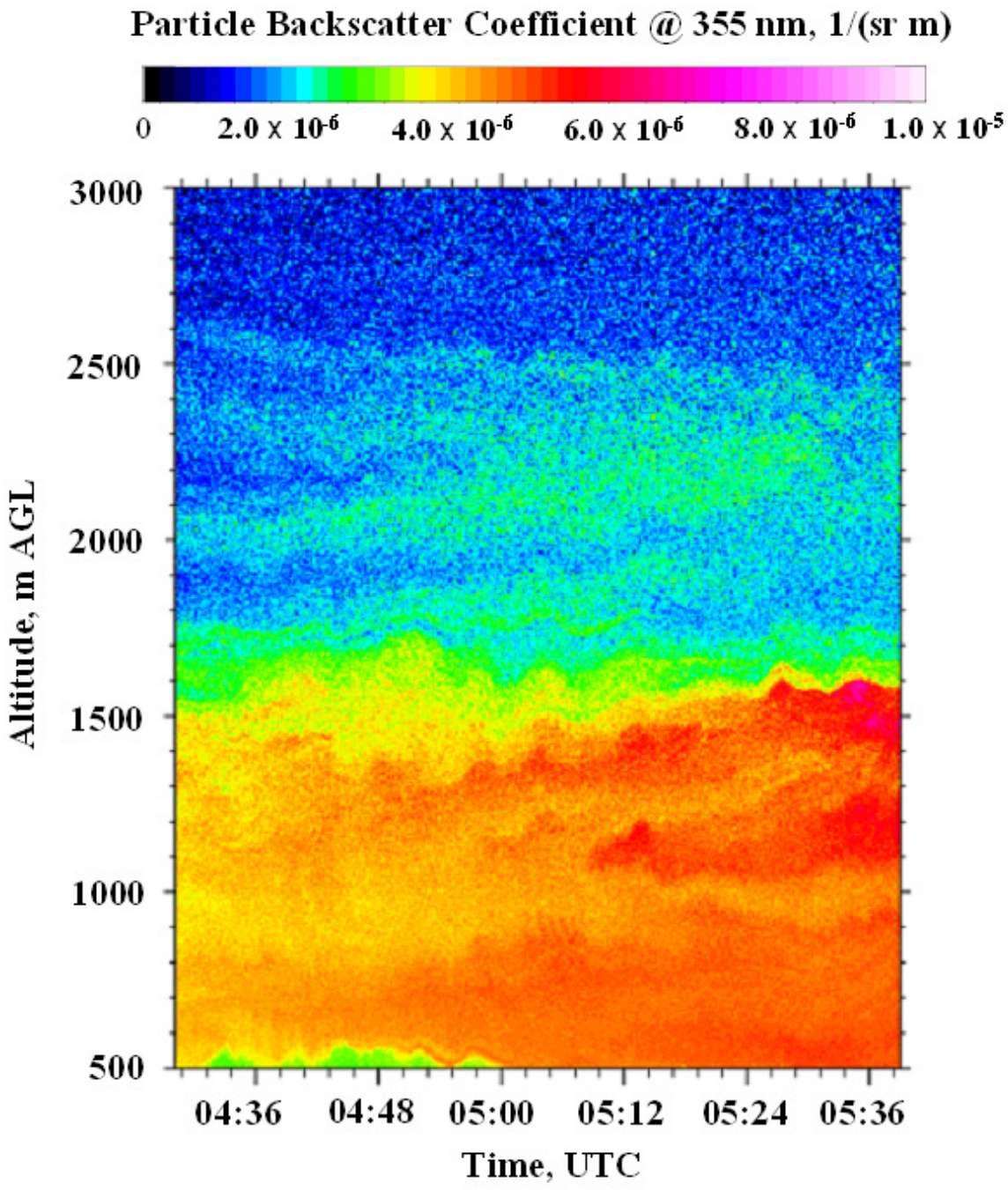

Figure 4.6: Time-height cross-section of particle backscatter coefficient yielding the wave-like features in the ABL in the early morning of 8 June 2007.

Time resolution and range resolution in the plot are 13 s (after averaging 650 consecutive shots) and 3.75 m, respectively. These are also the resolution of the stored data. No further averaging is performed. The UHOH RRL retrieved $\beta_{\lambda,par}(R)$ field presents a vivid description of boundary-layer dynamics that can, under suitable circumstances, provide insight into the mechanisms responsible for the wave generation and subsequent wave behavior. The wave-like features in the $\beta_{\lambda,par}(R)$ field may be due to the gravity waves induced by the local topography of the mountainous regions. Detection of such oscillatory motions in the NBL is only possible as long as the integration time is smaller than the period of oscillation. Wind speed was of around 7 m s^{-1} and was blowing from northeast of the lidar site.

Chapter 5
Investigation of an urban-atmospheric boundary layer with a vertically pointing elastic lidar using an IR wavelength

5.1 Introduction

The vertically pointing UHOH elastic aerosol lidar system (described in section 3.1) was deployed in downtown Stuttgart to acquire data during the "Physics Festival" in 2004 (four days from 23 to 26 June). This was a unique opportunity to study the boundary layer dynamics of an urban valley with an ultra-high-resolution aerosol lidar system. The high spatial and temporal resolution in UHOH lidar data helped to capture small-scale features in the CBL. The primary objective for using the UHOH lidar was to obtain a close picture of the depth and variability of the CBL, particularly considering the complexities involved due to the effects of the topography of that region: a roughly "u-shaped" valley surrounded by ridges of about 150 m height at several sides. This sort of orography often contributes to the complex pattern of the dispersion of pollutants emitted in the region (e.g., Chazette et al., 2005; Plamen et al., 2002). An experiment to explore the ABL in this area has not been made before.

In principle, lidar determination of the ABL height uses either of the following two methods: variance based analysis through observation of mixing processes in ABL, and gradient method based on vertical distribution of the passive tracers resulting from mixing processes. The first one concerns the determination of the mean ABL height while the second one determines the instantaneous depth of the ABL. The three different methods (logarithm gradient method, inflection point method, and the Haar wavelet transform scheme) fall in the second category. Previous lidar studies for the purpose of ABL height estimation used one or two of the three different existing techniques.

In case of the LGM, several minima exist in the profiles of gradient of the range-square corrected lidar signal complicating selection of the appropriate peak corresponding to h_{LGM}. Flamant et al. (1997) used a criterion of selecting a relevant minimum in the aerosol backscatter gradient, which was found to be more or less case sensitive. Wulfmeyer and Janjić (2005) determined the ABL height with the LGM from 1-min-averaged lidar data. They again used a 2-h running mean of the ABL height to avoid the large fluctuations in the ABL height derived with the measurements of 1-min temporal

resolution. The choice of the relevant minimum is defined differently in different publications, and is somewhat arbitrary. The HWT-based approach can be used for automated recognition of CBL top from the data with short integration times examining small CBL features. The scale, represented by the wavelet dilation, can also be used for quality control, that is, to test the reliability of the algorithm result. These two features of the HWT-based technique make the analyses very attractive (Cohn and Angevine, 2000).

To my best knowledge, no study exists so far that uses high-resolution lidar data and compares the results on ABL height obtained by the three methods mentioned. An important aspect concerns the determination of the instantaneous CBL height and the EZT by available techniques eventually deciding on the appropriate tools for the routine measurements of these quantities. As smaller scale processes often become important in the entrainment zone, high tempo-spatially resolved information of the tracers in this region would be required. Instantaneous CBL height can significantly change within very short time interval especially when convective activity is a dominant feature. Therefore, a combination of some advanced statistical approaches was applied for the exploration of the non-stationarities in the CBL height time series. Results from this new approach may serve as an indication on the variability of the CBL height.

This work is mainly focused at a study of the CBL with the UHOH lidar measurements obtained at IR wavelength. Investigation of the growth rate of the CBL top from lidar measurements is also addressed. Additionally, the CBL height in the presence of a residual layer of the previous day is considered. The interaction between these two layers is studied as to reveal the description of penetrative convection processes at the CBL top. Though Angevine et al. (1998) made similar observations with wind profiler they could not deduct any conclusion most probably due to insufficient temporal (of about 30 s) and spatial (60 m) resolution.

Turbulence in the CBL carries special signatures, which are of high importance for both atmospheric modeling and dispersion studies. Following Lenschow et al. (2000), and Wulfmeyer (1999a, b), higher order moments (i.e., variance, skewness, and kurtosis) of the range-corrected lidar backscatter signal were investigated. This highlights that aerosol lidar data can yield potential benefit to estimate turbulence features in the CBL (quantitatively). It is expected that the investigation of turbulent moment analysis in the CBL bring a new concept on the application of aerosol lidar as a reliable tool to advance boundary layer research. This type of analyses for water vapor and vertical velocity fields were performed by several authors (see, among others, Couvreux et al., 2005; Wulfmeyer and Janic, 2005; Godowitch, 1986). Additionally, the CBL height time series were subjected to spectral analysis.

Following are the key research issues discussed in this chapter:

- Demonstration of the three techniques for the estimation of the instantaneous CBL heights and subsequent determination of EZT from high-resolution lidar sounding.
- Statistical analyses of the CBL height time series to explore non-stationarities involved in a rapidly growing CBL regime.

- Higher-order moments are calculated from an aerosol lidar data. What are the advantages of this technique? Can an aerosol lidar characterize the turbulence profiles in the CBL?
- What are the major differences between the CBL regime in a quasi-steady state and in a phase of rapid growth? Do the profiles of higher-order moments help to yield more insights into their characteristic features?
- How complicated is the interaction between the growing CBL and the RL in the morning over an urban area located in a valley?
- What are the qualitative and quantitative aspects of the gravity waves and K-H filament structure that can be assessed with backscatter lidar measurements? How efficient is a wavelet-based spectral analysis technique to resolve the multi-scale features present during wave activities in the residual layer?

5.2 The experimental site

The UHOH lidar system was deployed during the measurement period near the downtown Stuttgart (48°46′43.5″ N, 9°10′48.9″ E, elevation approximately 240 m ASL) in southwestern Germany. The experimental site is located in a valley with complex topography (Figure 5.1) and is characterized by a large population density, high density of buildings, diverse anthropogenic activities, non-uniform land use, and enhanced industrial activities. The urban aspect of the city originates from the fact that it is a major transportation cross point, including a large river port, an international airport, and a considerable industrial center. The variation of the elevation in this city with the deepest point by the Neckar river (of about 200 m ASL and the highest point in Stuttgart Vaihingen (of about 550 m ASL) influences the meteorological conditions.

Stuttgart's climate is characterized by warm summers and mild winters. During the measurement period the sky was mostly cloud-free. As to weather conditions, absolute maximum temperature of 25.5 °C, absolute minimum of 9.5 °C, maximum RH of 78.4 % and minimum of 16.2 %, only fair weather cumuli, some Cirrus clouds and no precipitation were observed. The mean wind speed at 10 m height was 3-4 m s^{-1}. This meteorological dataset was collected by the weather station in Stuttgart city (Amt für Umweltschutz der Stadt Stuttgart, Schwabenzentrum-Stadtmitte, at 48°46′20″ N, 9°10′46″ E, 275 m ASL) about 500 m distant to the measurement site. The surface temperature on 26 June 2004 reached its maximum value of 25.5 °C at 1630 CEST (central European summer time). Horizontal wind obtained at 10 m height was mild (1-1.5 m s^{-1}). The RH at ground showed a classical diurnal cycle with a maximum RH of 80 % at about 0600 CEST and minimum RH of 30 % at 1700 CEST on 26 June 2004 which was one of the important measurement days when the UHOH lidar continuously monitored the CBL for more than eight hours.

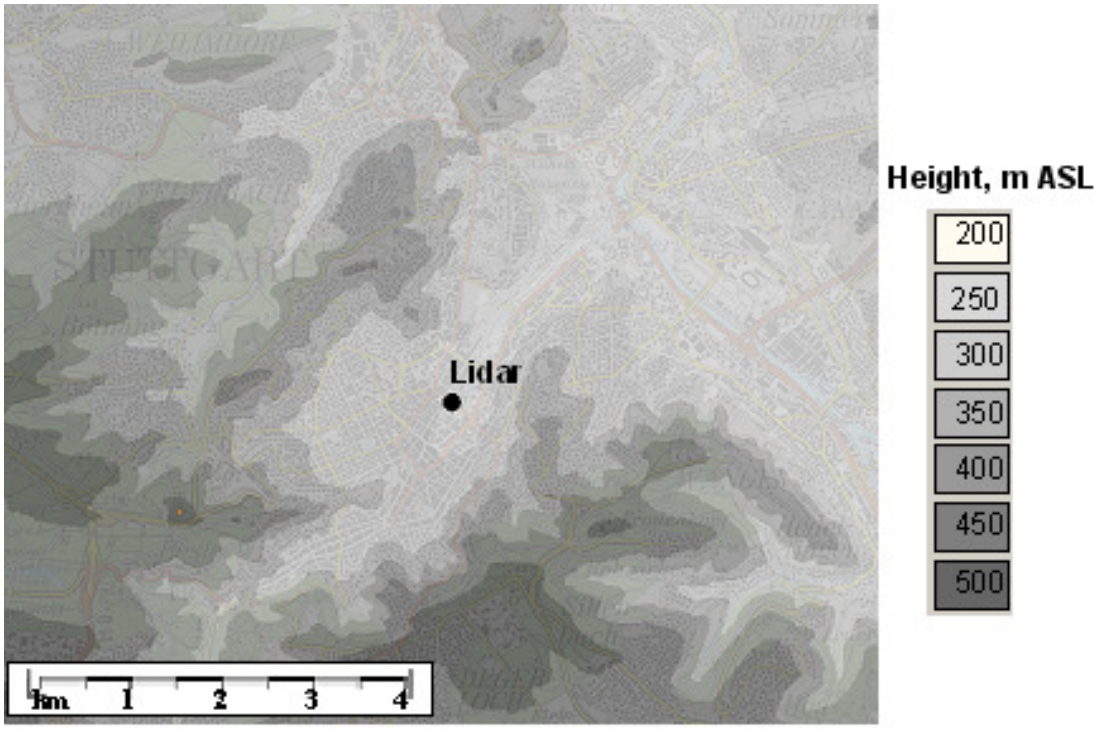

Figure 5.1: Topographic map showing the elevation variation (m, ASL) of Stuttgart city region with the lidar site marked by a circle.

5.3 Results and Discussion

Vertically pointing aerosol backscatter lidar provides two-dimensional observations of the lower troposphere. During measurements in Stuttgart downtown, UHOH lidar system in general collected data up to 12 km. The present study mainly deals with the data obtained in the ABL. Figure 5.2 depicts time-height cross-section for eight hours observations of the background-subtracted and range-square-corrected signal in the 1064-nm channel collected from 0955 to 1800 CEST on 26 June 2004. Temporal and spatial resolutions are 0.03 s and 3 m, respectively. Two white bands on the image (around 1150 CEST and 1300 CEST) are the time when no data were available.

Sources of the background signal in the lidar data are: scattered sunlight during daytime observation, and moon, stars, as well as artificial light during nighttime measurements. Further processing of the lidar signal is always performed after removing this background signal. Lidar signals collected beyond the heights where intensities become nearly constant (typically at around 11 km AGL, if no high altitude cirrus clouds are present) are considered to be the background signal level. In good approximation, the arbitrary intensity values of the pseudo-color scale are proportional to the relative particle backscatter coefficient (Eqn. 4.4).

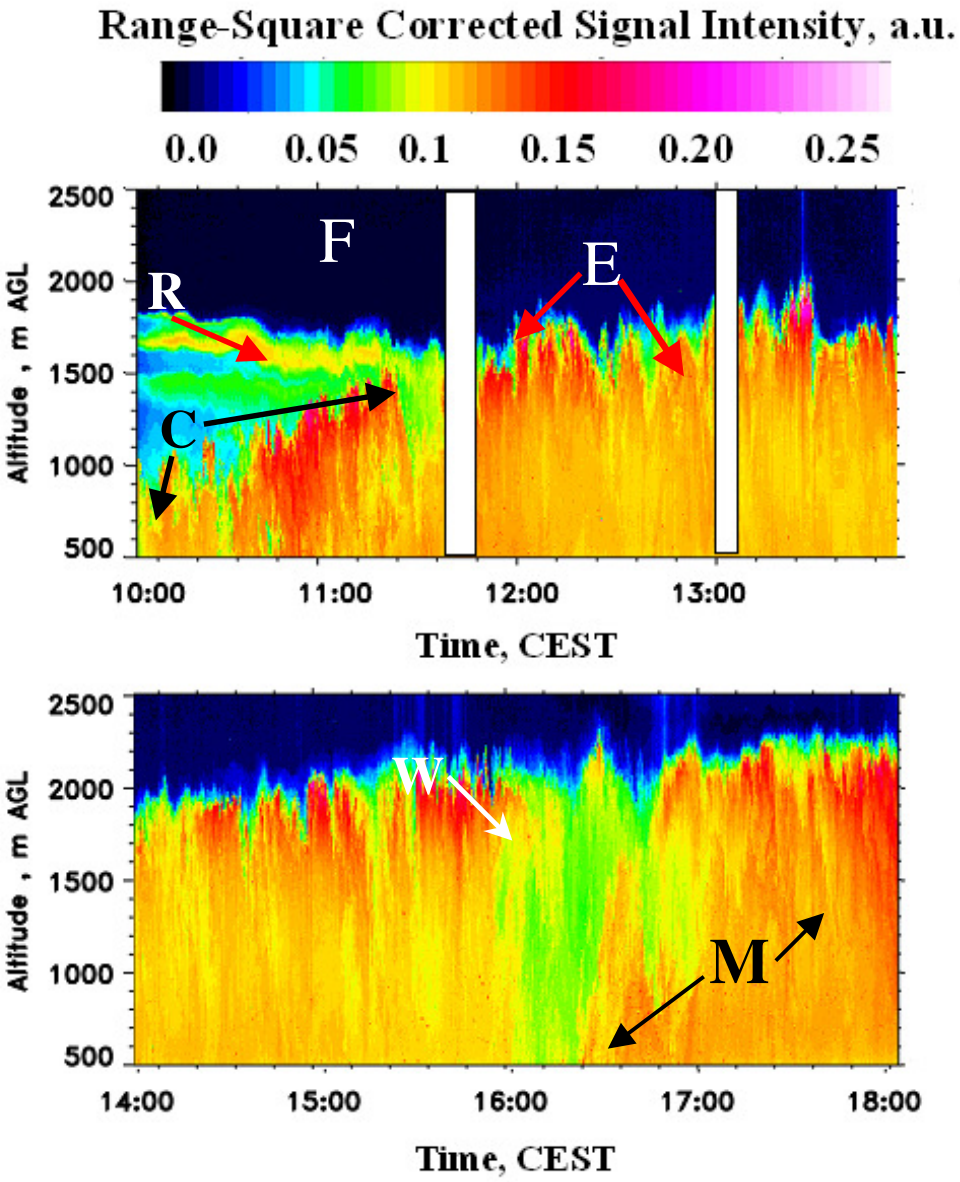

Figure 5.2: Time-height cross-section of the range-square-corrected backscatter signal, measured on 26 June 2004, from 0955 to 1810 CEST. The two white stripes mark the period where no data are available. The color scale is linear and goes from blue for weak backscattering to pink/white for strong backscattering. Temporal and spatial resolutions are 0.03 s and 3 m, respectively. The vertical axis is in meter, for altitude AGL and horizontal axis is time in CEST (UTC+2 h). R: a strong residual layer from previous day showed up around 1.8 km AGL, F: free atmospheric air with l very low aerosol load above 2.0 km, C: CBL growth during morning eroded nighttime stable layer, E: entrainment at the top of the CBL, W: wave-like activities, M: turbulent mixing inside the CBL.

A zoom-in-view of the lidar measurements collected between 1030 and 1033 CEST is shown in Figure 5.3. This figure demonstrates the UHOH lidar's capability to investigate the CBL with an ultra-high-resolution. With such data, variability of the instantaneous CBL height can be quantified and the EZT can be estimated (see, section 4.2 for the EZT determination). Obviously, high-resolution lidar measurements can resolve the changes in the instantaneous CBL height whereas the mean CBL height (based on several numbers of profiles) can cause a broadening of the entrainment-induced peak in the backscatter intensity due to the time evolution of the mean CBL.

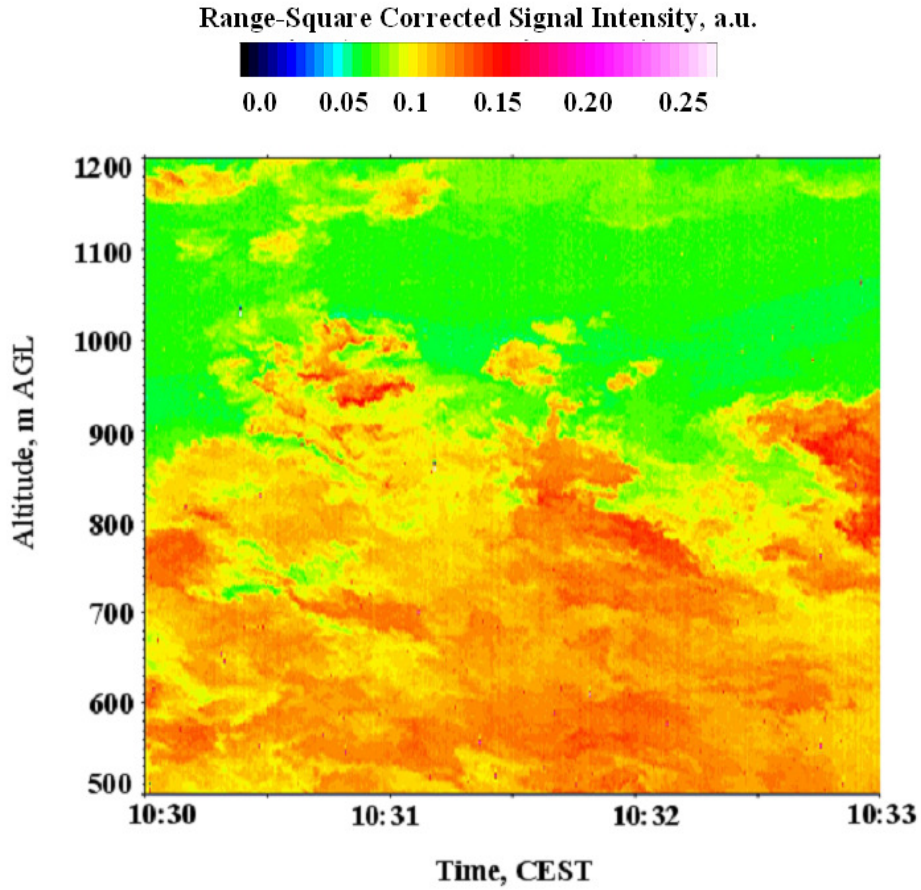

Figure 5.3: A zoom-in-view of the range-square corrected signal intensity collected between 1030 and 1033 UTC (extracted from Figure 5.2) showing the detailed vertical structure of the CBL during morning.

Such high-resolution lidar data can retrieve the entrainment-driven small-scale patterns, especially in the daytime CBL as can be seen in this figure.

Time-height cross-section presented in Figure 5.2 shows that a strong previous night residual layer (marked by 'R') was observed at an altitude of about 1.8 km AGL in the morning until 1120 CEST while the free-tropospheric air with very low aerosol load was present above 2.1 km altitude (marked by 'F'). Around 1130 CEST, the growing CBL (marked by 'C') contacted the base of the residual layer and eventually became indistinguishable. Also visible is that starting at 1120 CEST, the dust layer became trapped in the entrainment region. This interaction will be discussed in section 5.3.2.3. Influenced by this process, the CBL was grown in thickness and thus a one-way entrainment dominated. When laminar air from the free troposphere and capping inversion are introduced into the CBL, thickness of the CBL grows. On the contrary, none of the turbulent air is incorporated into the laminar air. These characteristics were clearly observed by the UHOH lidar measurements.

Figure 5.2 shows that from 1200 CEST onwards, a strong mixing of the aerosol particles in the entrainment zone near the top of the CBL (of about 2.0 km AGL) was observed arising due to a regime of well-mixed CBL (marked by 'E'). The depth of the CBL was remained nearly constant around 2.0 km until 1800 CEST. Some wave-like activities were observed around 1610 CEST (marked by 'W';

see, section 5.3.6.2). Inside the CBL, small-scale turbulence features were observed until 1800 CEST (marked by 'M').

The time-height cross-section (Figure 5.2) shows two different regimes of CBL evolution. One during the rapid growth of CBL and another in the afternoon with a regime of equilibrium entrainment i.e., when CBL evolution is in a quasi-steady state. Quasi-stationary CBL (case I) was first used to demonstrate the three techniques for CBL height determination. These analyses were then extended to study the CBL in the morning (case II).

5.3.1 Case I: Quasi-stationary convective boundary layer

5.3.1.1 Results obtained with logarithm gradient method, inflection point method, and Haar wavelet transform analysis

Figure 5.4 illustrates the retrieval of h_{LGM} and h_{IPM} for backscatter signal acquired at 1552 CEST on 26 June 2004. Before the LGM, IP, and HWT were applied on the lidar data, 10 consecutive lidar profiles were averaged which provided a time resolution of 0.3 s. In the following analysis for LGM and IP method, no further time averaging was performed but a gliding average with a Gaussian window of full width at half maximum of 30 m was applied in height on the raw data before $D(z)$ was calculated. This averaging was necessary to determine the minimum gradient peak. The influence of changing height difference ($dz = z_2 - z_1$) on $D(z)$ was tested. After performing this sensitivity test, the appropriate peak in the $D(z)$ profile related to the ABL top was found. For these data, dz of 30 m was found to be most appropriate for searching the minimum of $D(z)$. As expected Figure 5.4 clearly shows the minimum of the 2nd derivative (inflection point) appears below the height the minimum of the 1st derivative. So if the LGM correctly finds the transition zone between the mixed layer and the free troposphere, then IP method will mark the mid of the transition zone which is below the h_{LGM}. Depending upon the turbulent activity present in the ABL, the local discontinuity between mixed layer and free troposphere atop is defined as the transition zone here. This transition zone is also a means of determining the EZT in different atmospheric conditions (Flamant et al., 1997).

The HWT-based analysis (discussed in the section 4.1.4) was applied to the same data to retrieve the ABL height. The wavelet covariance transform $W_f(a,b)$ was computed for each profile and the altitude corresponding to its maximum was denoted as the ABL top. The crucial point for estimating ABL height following this approach is dependent on the choice of two parameters: the interval between upper (z_{max}) and lower (z_{min}) altitude where the HWT should be applied, and the value of the dilation (a) and translation (b). Following Davis et al. (2000), a sensitivity test was performed to obtain the characteristic differences of the $W_f(a,b)$ values for different dilations as shown in Figure 5.5. The location of the maximum covariance turned out to be at an altitude of 2030 m for all dilation values beyond 175 m. For the lower dilation values in this case, the function $W_f(a, b)$ exhibited two or three peaks and the procedure for determining h_{LGM} became ambiguous.

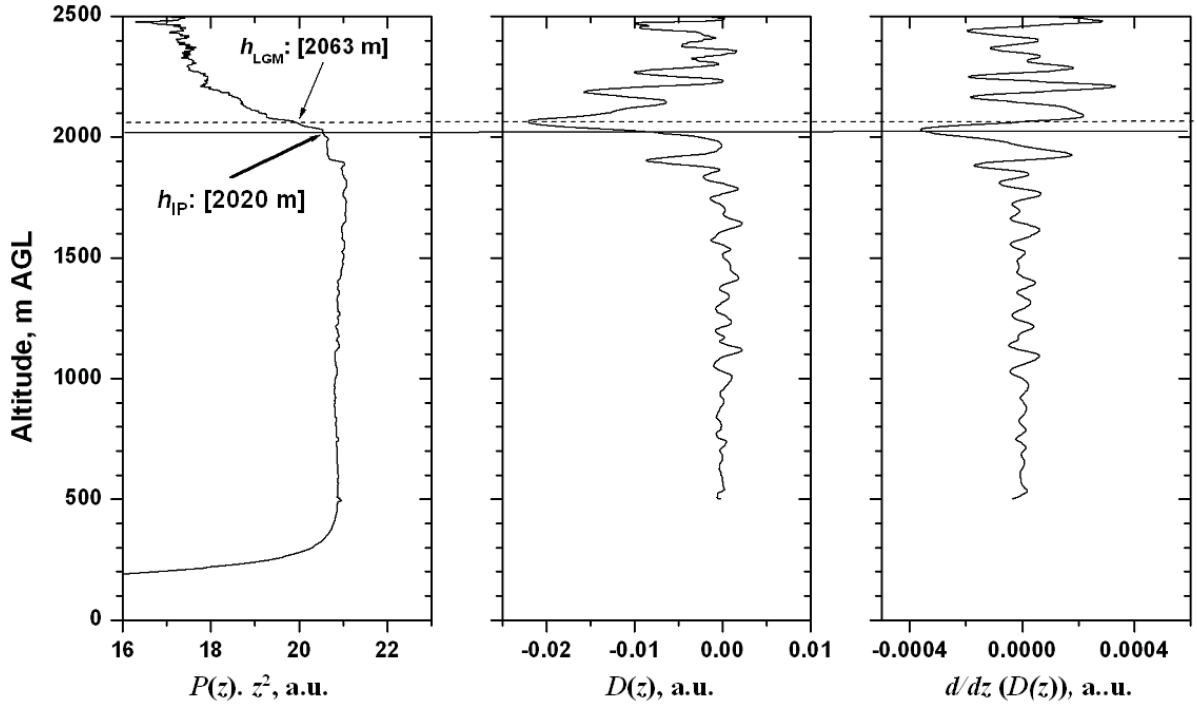

Figure 5.4: Determination of the instantaneous height of the CBL on 26 June 2004 at 1552 CEST using LGM and IP method. The plot represents in arbitrary units: the background-subtracted range-square corrected backscatter signal (left panel), 1st derivative (middle panel), and 2nd derivative (right panel) of the logarithm of range-square-corrected signal. The temporal and spatial resolution of the data is 0.3 s and 3 m. In height, a 30 m gliding average is applied. h_{LGM} and h_{IP} are found at 2063 m and 2020 m AGL, respectively.

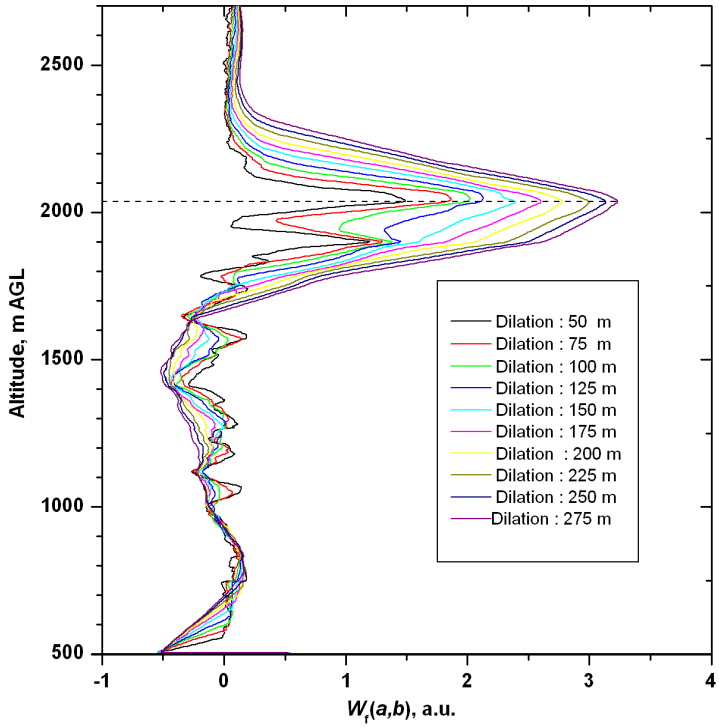

Figure 5.5: Wavelet covariance transform values $W_f\,(a,b)$ for different dilations from 50 m to 275 m. Except for dilation of 50 m, 75 m, 100 m, 125 m, 150 m, and 175 m all show a maximum value at 2030 m yielding the ABL top. This result is obtained after applying the HWT to the data collected on 26 June, at 1552 CEST as in Figure 5.4.

For obtaining h_{HWT}, the dilation value of 200 m was chosen for whole time series of case I. Unless otherwise stated the HWT analysis was constrained between 500 m and 3000 m altitude.

5.3.1.2 Intercomparison among the different techniques

Figure 5.6 presents the time-height cross-section of the range-square corrected signal intensity collected between 1430 and 1600 UTC (upper panel) the temporal evolution of h_{HWT}, h_{LGM}, and h_{IP} (upper panel). The two time series using the LGM and the HWT were found to be highly correlated (correlation coefficient of 0.85) and the linear trends in both cases were very similar. In general, h_{HWT} is smaller than h_{LGM}. This is a characteristic feature for the HWT. The HWT coefficient becomes maximum when the covariance between backscatter profile and the Haar function is a maximum. But this value is again related to the value of dilation. Brooks (2003) showed how the HWT method identifies a point close to the center of the transition zone, with a trend towards higher values with increasing dilation. The HWT method will thus tend to identify a point lower than the LGM, though the difference will vary both from profile to profile and with dilation for any given profile. The LGM identifies the location of the minimum in the vertical gradient of the backscatter, which tends to lie within the upper part of the transition zone.

It is important to mention here that the LGM and the HWT analysis are necessarily not different from each other, if dilation value of the range resolution (in this case 3 m) is applied during estimation of $W_f(a, b)$ in the HWT analysis. Furthermore, the advantage of the HWT method allows limiting the analysis to a chosen range of scales, so that small gradients (e.g., caused by noise) will be cancelled. The HWT coefficient is calculated at each height level; caused by this implicit smoothing, the technique does not require additional averaging of the signals in height as in the case of LGM.

The h_{IP} is always smaller than h_{LGM} because the 2nd derivative of the range-square-corrected signal has always a local log-minimum below the minimum of the 1st derivative (see, Figure 5.4). The IP method actually searches for the interface between the mixed layer and the free troposphere and therefore h_{IP} is defined as the middle of the transition zone. On the other hand, definition of h_{LGM} is different from h_{IP}. Since h_{LGM} is defined as the base of the transition zone, it becomes also the top of the mixed layer. This directly implies $h_{LGM} > h_{IP}$ (Figure 5.3).

Comparison of the mean CBL heights determined from the respective time series yielded a difference of 59 m between the LGM and the HWT-based analysis while a difference of 63 m was found between LGM and IP method. A difference of only 5 m was found when comparing the mean CBL heights estimated by the HWT and IP method. Correlation analyses among the three time series were performed. The resulting correlation coefficients between time series of h_{LGM} and h_{HWT}, h_{LGM} and h_{IP}, and h_{IP} and h_{HWT} are 0.815, 0.811, and 0.781, respectively. It can be stated that $h_{LGM} > h_{HWT} > h_{IP}$ for the case of 1.5-h lidar measurements of quasi-stationary CBL (Figure 5.6).

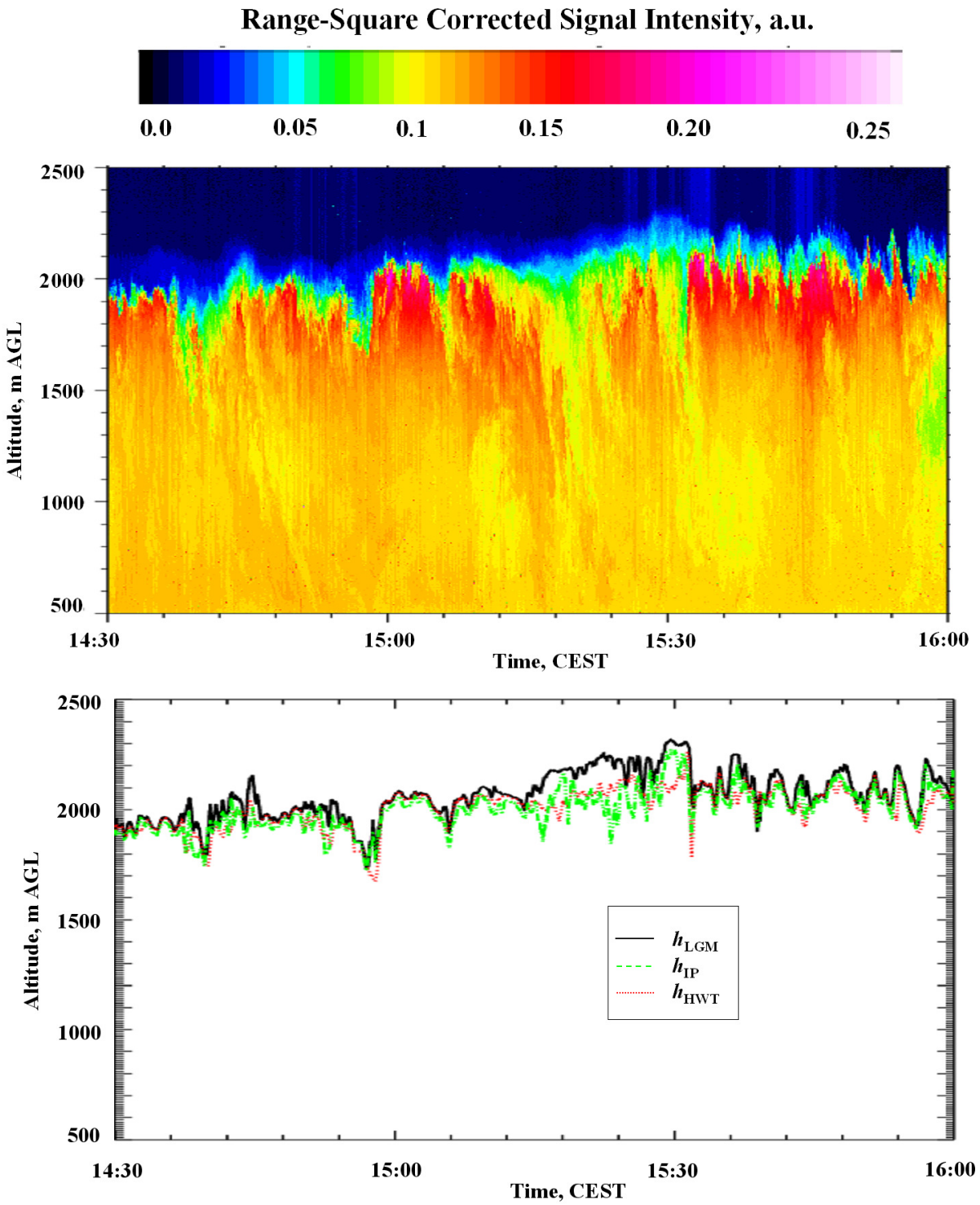

Figure 5.6: Time-height cross-section of range-square corrected signal intensity (upper panel) and the time series of h_{LGM}, h_{HWT}, and h_{IP} (lower panel) for case I.

Two important results were obtained concerning the accuracy of the results obtained with the HWT-based approach. The vertical distribution of the variance (section 5.3.1.4) of the fluctuation of the particle backscatter coefficients showed the maximum at 2022 m AGL. The vertical profiles of potential temperature and water vapor mixing ratio obtained with the radiosonde launch at 1200 UTC on this day from the near-by weather station manifested a strong signature of the temperature inversion and a sharp

gradient in the mixing ratio at an altitude of 2005 m AGL confirming the height of mean CBL (Figure 5.8). This was very close to the mean value of h_{HWT} (2008 m) during this time. On the contrary, the LGM-based results do not show such close similarity neither with the variance profile nor with the radiosonde-derived height.

The application of LGM often becomes quite complicated because the minimum cannot be well defined or several minima might exist over an extended height range. On the contrary, being a convolution the HWT-based approach does not show several peaks in the distribution of the HWT coefficient, as is the case for LGM, if an appropriate dilation value is selected. The dilation value of 200 m was chosen for the case I after a detailed sensitivity test of this value. The LGM does not offer such an opportunity. Previous studies (including very recently published one; Baars et al., 2008) on the application of the HWT method used relatively high values of dilation (of about 450 m in Baars et al., 2008; of about 1000 m in Cohn and Angevine, 2000;) for determining CBL top. Furthermore, Baars et al. (2008) also found the h_{LGM} to be higher than h_{HWT} in their study but they did not investigate in detail the reasons behind these characteristic differences between these two methods. High spatial resolution in the UHOH lidar data yielded the facility to use a relatively lower dilation value of 200 m while the high temporal resolution facilitated to obtain a close picture of the high temporal variability of CBL height. Indeed, a large dilatation, which comprises this first gradient and the second one (that represents the mixed layer top), will give a largest coefficient than a dilatation comprising only the first or the second gradient. This is an important source of bias with the wavelet method. A difference of around 100 m between the h_{LGM} and h_{HWT} are observed (Figure 5.6) around 1515 CEST for this reason. Presence of a large transition zone during this period is visible as yielded by the time-height cross-section. Furthermore, longer dilatations would require unnecessary computations and are more susceptible to errors from a varying backscatter profile above the CBL, particularly if there are various layers, as it will be discussed further (section 5.3.2.1).

On the other hand, IP method inherently uses the information from the profile obtained with the LGM, a series of criteria have to be fulfilled to use this result as a correct estimate of CBL height (see, Sicard et al., 2006; for a detailed discussion on these criteria).

It can be concluded that the HWT-based approach is the suitable or preferable technique for the automated determination of the instantaneous height of the CBL, even for lidar data collected in a temporally, vertically, and horizontally complex situations.

FFT-based spectral analysis was performed on the time series of h_{LGM} , h_{IP} , and h_{HWT} and the results obtained are shown in Figure 5.7. All of them show a power law dependency with a spectral exponent (slope value, γ) of about 1.0. The temporal resolution in the time series is 0.3 s. Therefore, the Nyquist frequency ($f_{max}/2$) for the FFT spectra is 1.66 Hz. None of the slopes confirm the –5/3-power law dependency. In this case, the time series created by the increments of a nonstationary signal has a spectral exponent of around 1, and so is a quasi-stationary signal. For such signals, DFA algorithm is not applicable (see, section 4.3).

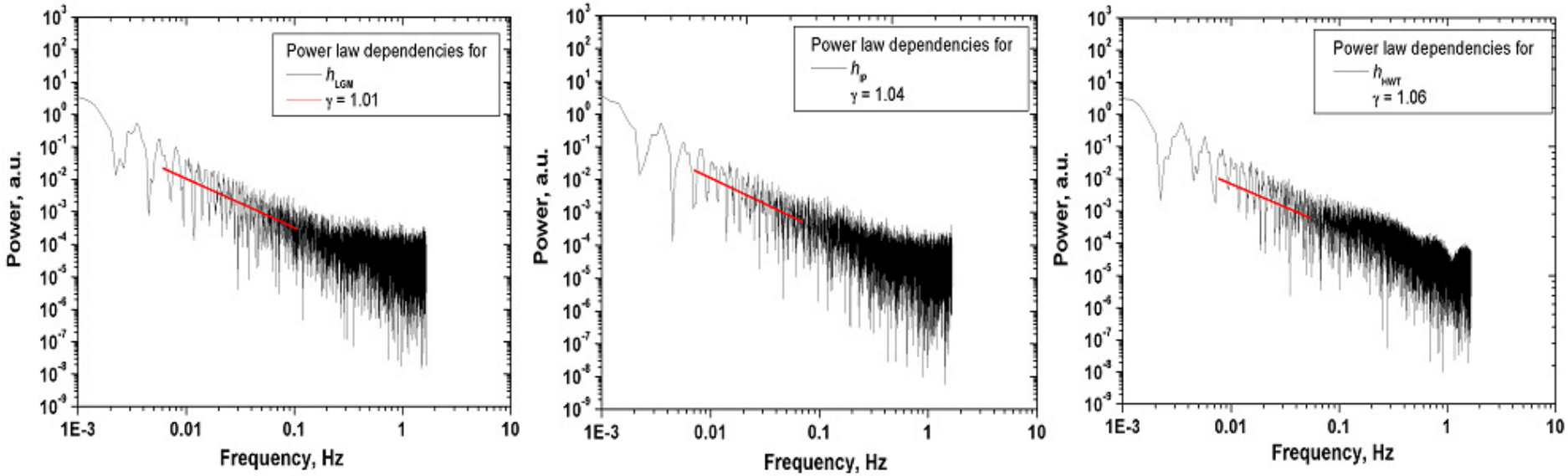

Figure 5.7: FFT power spectra for the three different time series: Left: Logarithm gradient method, middle: IP Method, right: Haar wavelet technique. Slope for each spectrum are also shown as straight red line on each panel.

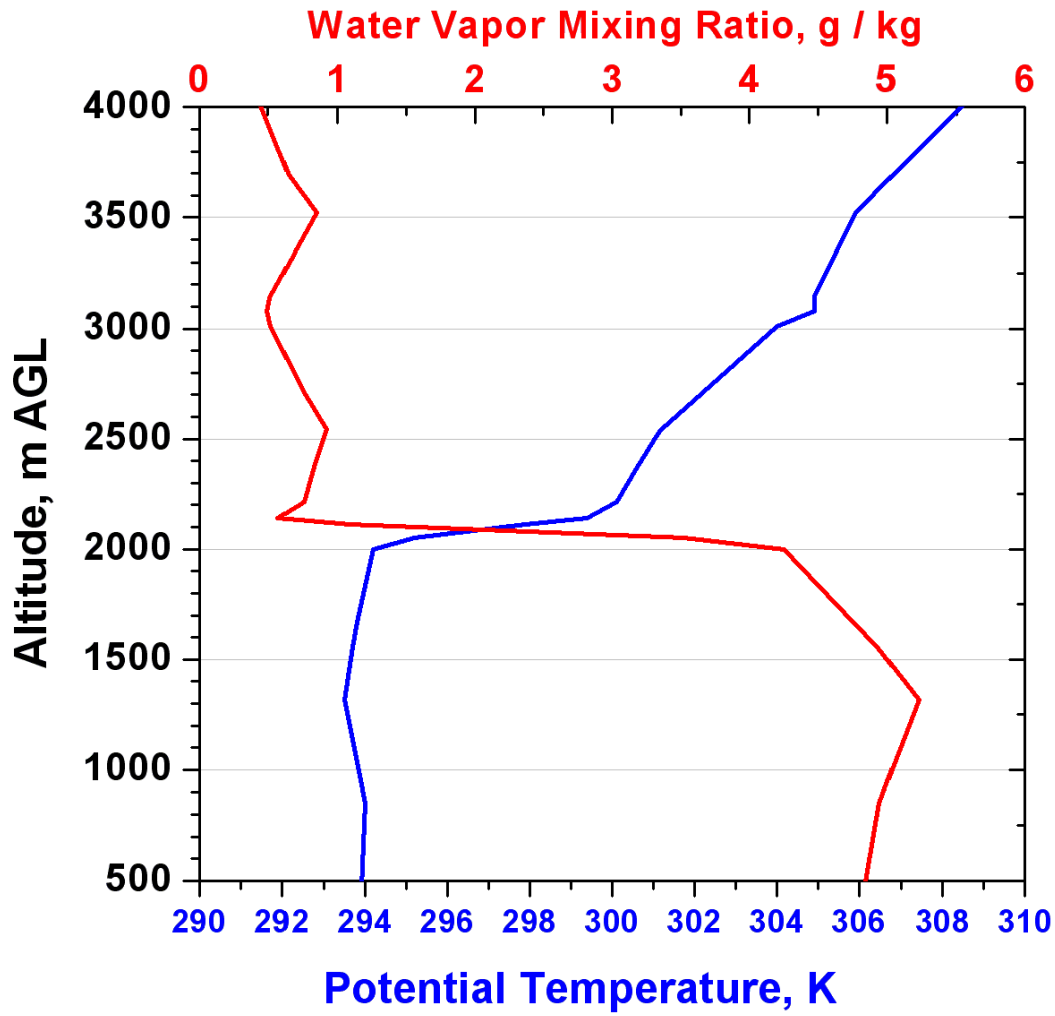

Figure 5.8: Profiles of the potential temperature (in K) and water vapor mixing ratio (in g/kg) obtained from the radiosonde launch at 1200 UTC from Stuttgart/Schnarrenberg (48.8333° N, 9.2000° E, 315 m ASL) station on 26 June 2004.

5.3.1.3 Entrainment zone thickness for case I

Two different approaches are applied for estimating the EZT from the time series of the instantaneous CBL height. The standard deviation of the CBL height time series yields the value of the EZT (e.g., Davis et al., 1997; Hägeli et al., 2000). This technique is assigned here to be the standard deviation technique. The EZT value obtained through this technique is 92 m using the time series of h_{HWT}. The frequency distribution of h_{HWT} shown in Figure 5.9 is nearly symmetrical. This distribution is peaked around 2050 m AGL and does not spread much which yields the fact that most of the observations showed the CBL height around 2.0 km AGL. Larger values are considered to be due to the most energetic thermals. The values around 1700 m AGL were arising most probably due to the strong entrainment of the free-tropospheric clean air.

Results obtained from cumulative frequency distribution method (discussed under section 4.2) are shown in Figure 5.10. This figure shows the evolution of the CBL height together with an illustration of the cumulative frequency distribution technique on the time series (upper panel).

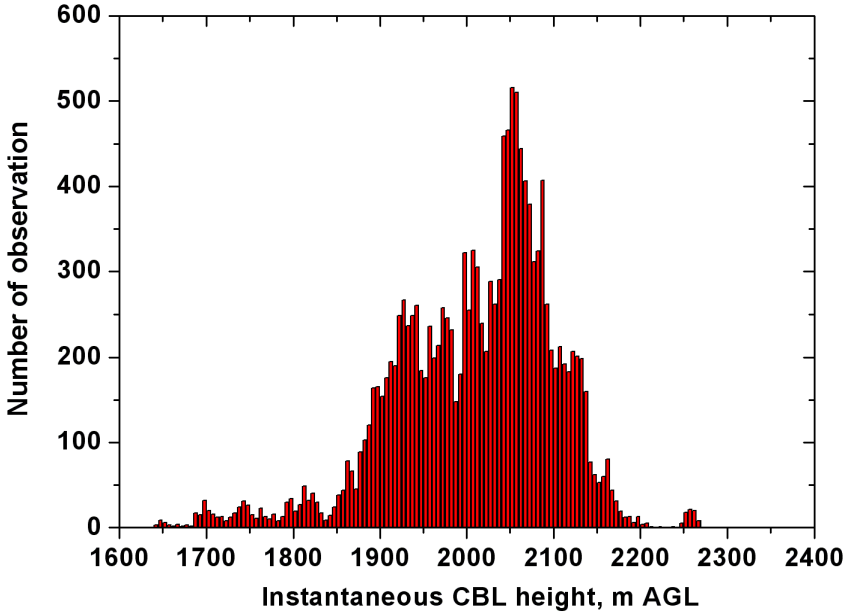

Figure 5.9: Frequency distribution of the instantaneous CBL height derived by the HWT-based method for case I.

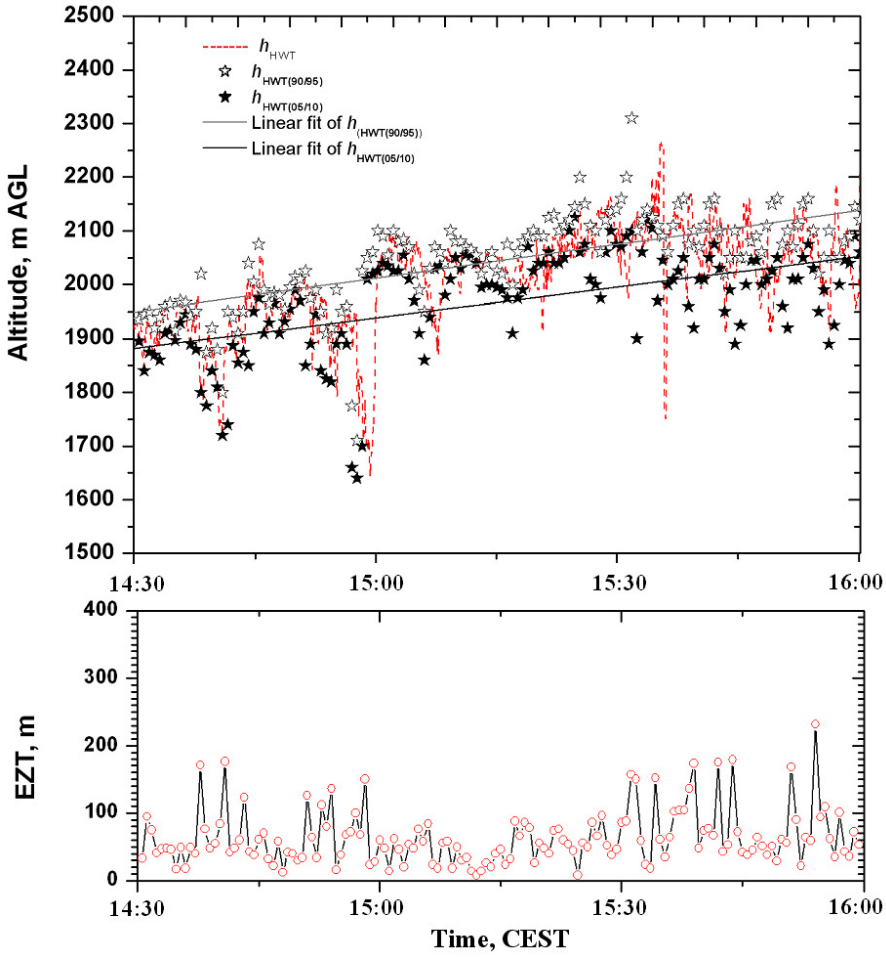

Figure 5.10: EZT estimation after cumulative frequency distribution of instantaneous CBL height time series (of same data as in Figure 5.12b), derived from 0.3 s resolution UHOH lidar data. Linear fits for both $h_{\mathrm{HWT\ 05/10}}$ (blue line) and $h_{\mathrm{HWT\ 90/95}}$ (red line) values of the cumulative frequency distributions are shown here. The lower panel shows the estimated EZT values for this case. For further details, see text.

The determination of the EZT is performed also using the time series of h_{HWT}. Lower and upper parts of the entrainment zone are denoted as $h_{HWT(05/10)}$ and $h_{HWT(90/95)}$, respectively, where the first one corresponds to the mean of the 5 %-10 % values of the cumulative frequency distribution and the second one corresponds to the mean of 90 %-95 % values. Subtraction of these values yields EZT. 30 s was the averaging time over which the EZT was calculated. Figure 5.10 also shows the evolution of the estimated EZT (lower panel). The values of EZT are ranged around 80 m while the mean value of EZT is 75 m. Some higher values of EZT around 200 m might be arising due to an enhanced convective activity and associated entrainment of the FT air. This mean value of EZT is of about 20 % smaller compared to the one from the standard deviation method.

Melfi et al. (1985) considered lower and upper limits of the cumulative frequency distribution to be 4 % and 98 %, respectively. On the contrary, Flamant et al. (1997) and Beyrich and Gryning (1998), mentioned in their study that these percentage values are author dependent and stated the choice of a fixed percentage value is rather complicated due to intense mixing in the entrainment zone (both horizontal and vertical). Therefore, the average values of the 5 %-10 % values were considered for minimizing the possible step effects in the frequency distribution. Time series-based technique following cumulative frequency distribution allows remarkable insights into the variability of CBL height and thus can provide a significant understanding of the nature and scale of the mixing processes. The evolution of EZT is appeared to be anticorrelated with the location of convective plume tops and EZT became very thick (of about 200 m) between actively rising plumes. Application of cumulative frequency distribution for computing EZT from a time series of vertically pointing lidar data is of first kind here.

5.3.1.4 Profiles of higher-order moments for case I

So far, the evolution of CBL top has been discussed only. To add further quantitative information, an attempt is made to estimate the turbulence processes for the entire 1.5-h observations (case I). A detailed description of turbulence processes inside the CBL can be achieved by the estimation of higher-order moments of particle backscatter coefficient fluctuations (β'_{par}) if the hygroscopic growth of the particles is neglected (see, section 4.4). These profiles were estimated up to an altitude of 2.7 km as it was found previously for this dataset that the CBL height was below 2.7 km AGL without presence of any significant growth rate, any CBL clouds and further aerosol layers above the CBL top. This kind of classical picture of well-mixed CBL regime can be assumed to be appropriate for investigating the turbulence features.

Using the noise error profiles by means of statistical error propagation, variance, skewness, and kurtosis profiles including error bars (with respect to statistical and sampling errors) were determined. Autocovariance analyses of the high-resolution time series or analyses of variance spectra were

performed for this purpose. Details of these methods are explained in Senff et al. (1994), Wulfmeyer (1999a), and Lenschow et al. (2000), so that only the major results are summarized here.

Figure 5.11 shows variance spectra of relative particle backscatter coefficients during the 1.5-h observations at eight different heights inside the CBL. Lidar data with time resolution of 10 s is used here. Log $S_F(f)$ is plotted here against log (f). The solid lines in all the plots show the decrease of the spectra as expected according to the –5/3-power law describing the inertial subrange of the spectra (Kolmogorov, 1941). Obviously, the inertial subrange was reached in all cases. This confirms the time resolution used here to be high enough to resolve the energy containing eddies and part of the inertial subrange. Recently, Engelmann et al. (2008) showed similar characteristics in the variance spectra of β'_{par} for a case of well-mixed CBL confirming $f^{-5/3}$ roll-off (inertial subrange) in the spectra. But they did not extend their results to investigate the vertical profiles of higher-order moments of β'_{par} as has been performed in this study. Furthermore, range resolution in their lidar data was relatively lower (75 m) than UHOH lidar data (3 m).

Following Lenschow et al. (2000), autocovaiance function (denoted as $m11$ in their paper) for each height level was calculated to determine variance of the particle backscatter and corresponding noise variance. The autocovariance function calculated for 100 lags for four selected heights (1000, 1350, 1750, 2000 m) in the CBL are shown in Figure 5.12. The increase of the total variance at zero lag at 2000 m was due to both the increase of the atmospheric variance and the noise variance.

Figure 5.13 plots the vertical distribution of the integral scale with and without noise correction. This profile including other higher-order moments profiles for this case were normalized with the mean CBL height of 2008 m estimated by averaging 1.5-h time series of h_{HWT}. This figure shows clearly that without noise correction the integral scale would be significantly underestimated. The standard error due to instrument noise is also shown on the 2/3-power law fit curve. The integral scale is in the range of 75 s inside the CBL but decreased to 30 s near z_i. A more detailed investigation yields that the values of the integral scale were between 50 s and 75 s within $0.2z_i$ and $0.9z_i$. But, a slight increase was observed at $1.1z_i$, which might be arising due to strong entrainment occurring near the CBL top. Nevertheless, the integral scale estimated is significantly larger than the time resolution. This means that roughly the first 5-7 lags of the autocovariance function fall within the inertial subrange. Therefore, the major part of turbulent fluctuations in the CBL can be resolved with the UHOH lidar data.

Vertical distributions of variance, skewness, and kurtosis of the β'_{par} including error bars with respect to statistical and sampling errors were determined (Figure 5.14). Vertical profiles of the

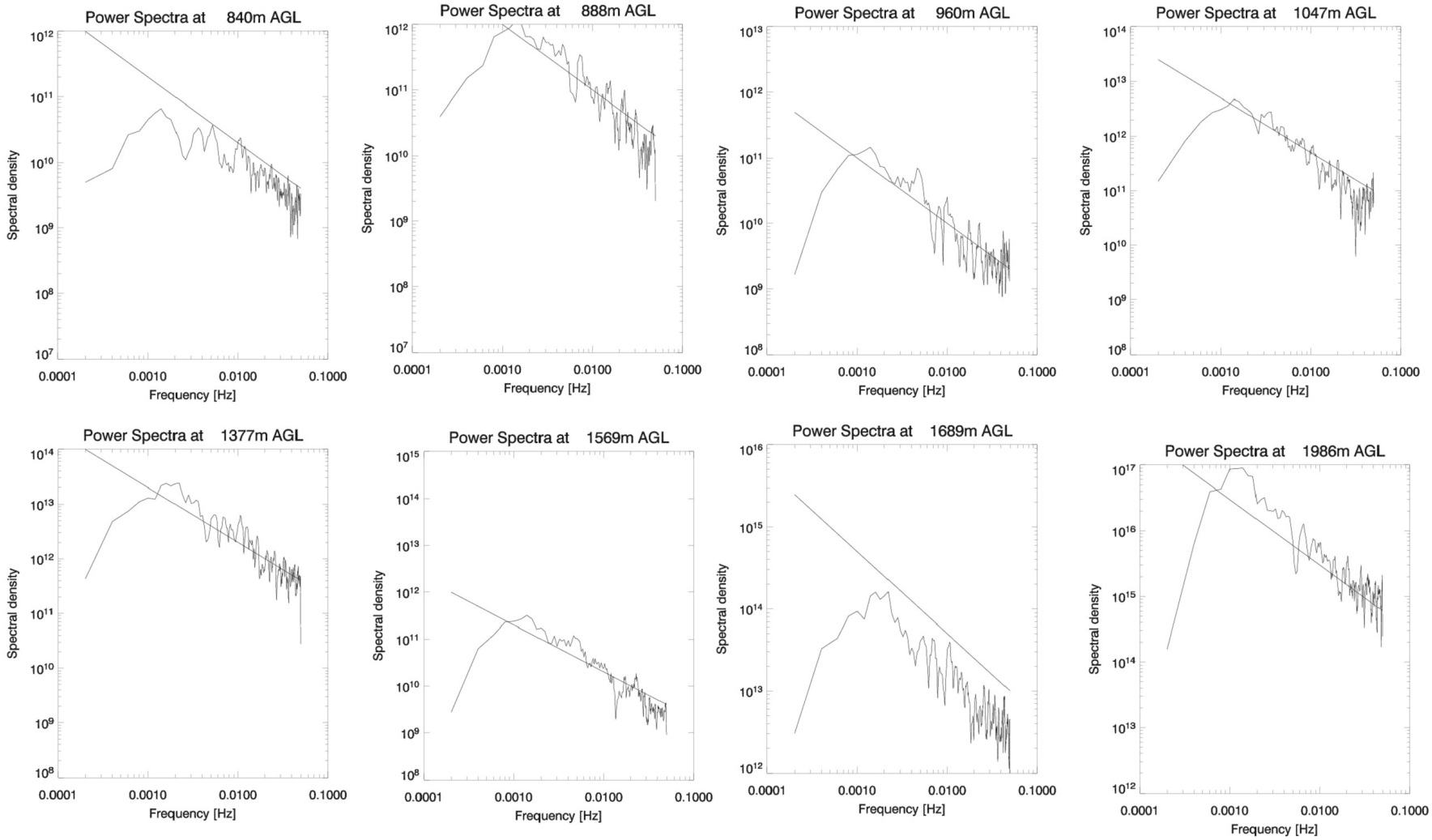

Figure 5.11: Spectra of relative particle backscatter coefficient at four different heights. –5/3-slope is shown in each panel to present the expected shape of the inertial subrange.

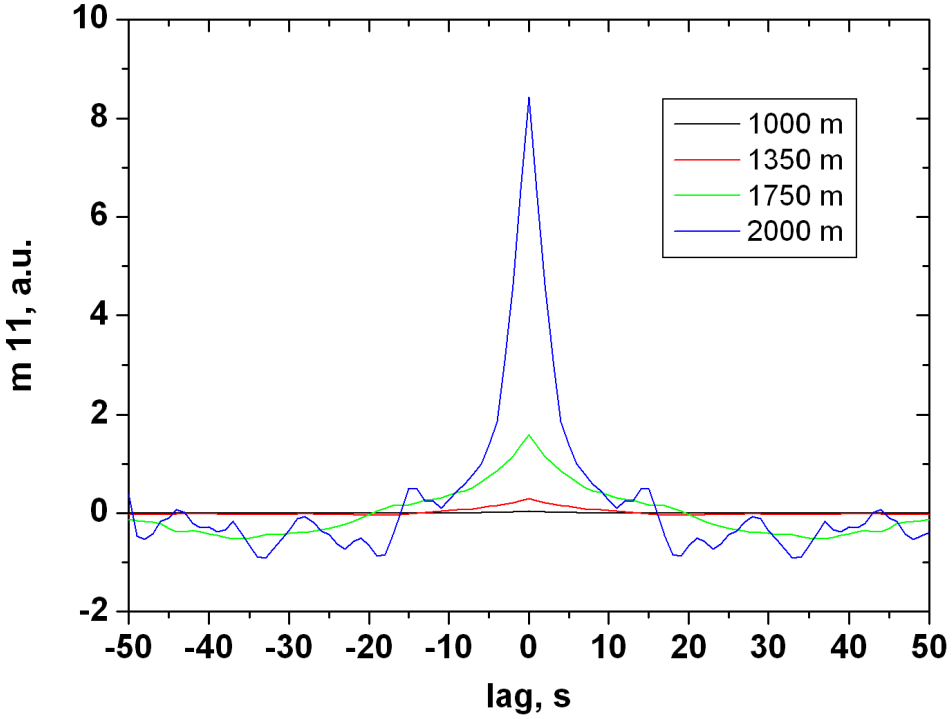

Figure 5.12: The $m11$ (t) for four different heights for case I. The inertial range is resolved by only 5-7 data points.

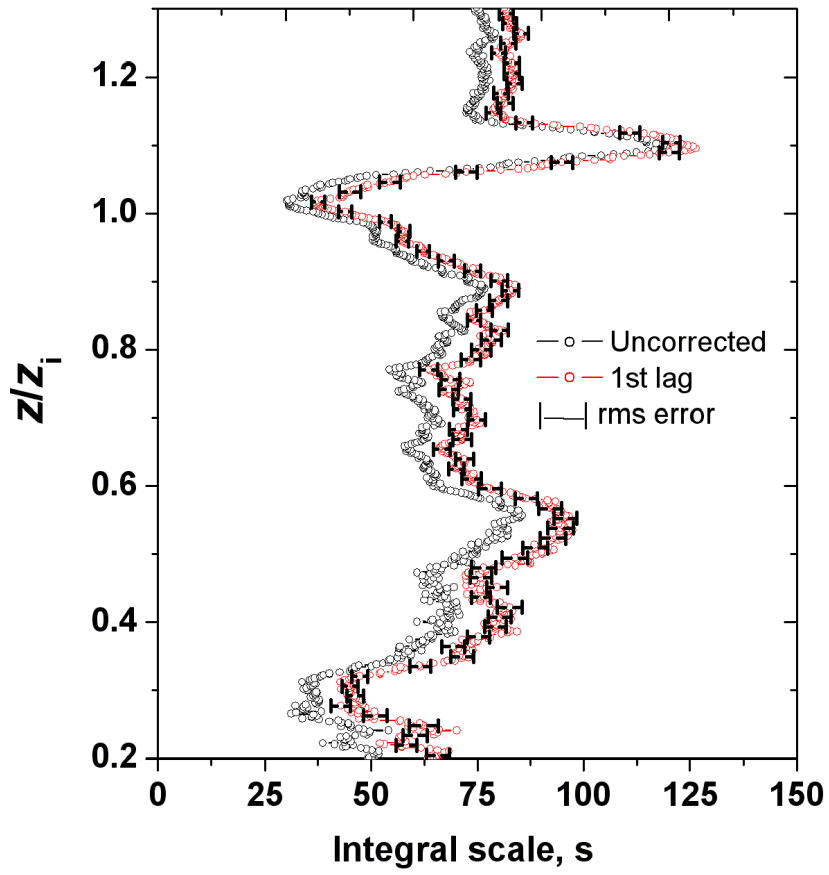

Figure 5.13: The integral scale of particle backscatter coefficient fluctuations retrieved with two different noise corrections and without correction. The bars on the linear fit curve denote the standard error due to instrument noise.

variance with and without noise corrections illustrate that noise correction is necessary for all altitudes. The variance shows a maximum near the entrainment zone (around 2022 m AGL), which was very close to the top of the mean CBL height. These properties of the variance profile are similar to that of the findings of Sullivan et al. (1998) and Wulfmeyer (1999b) concerning the humidity.

Figure 5.14 (middle panel) shows the skewness profile without any sort of correction for noise and with noise correction using a three-point linear extrapolation to zero lag. Noise error and the sampling error are also plotted here as error bar on the linear fit curve. Vertical variability of the skewness shows the presence of significant structures inside the CBL. The estimated noise error was small. But the sampling error was relatively high above the CBL top. A comprehensive description of convection up to the CBL height can be observed from the value of S_k. The negative S_k value inside the well-mixed CBL as obtained in the present case is not unexpected. A prominent peak and positive value was also observed in the region CBL top.

Figure 5.14 also presents (right panel) the kurtosis profile with and without noise correction. The sampling and noise errors are shown on the corrected kurtosis profile. First lag and linear fit approach provide here nearly similar results. Throughout the entire CBL the uncorrected profile shows a constant value around 4 with a slight increase at $0.6z_i$. But, at the top of the CBL, the profile shows a significantly higher value of K of about 12.

A brief summary of the quantitative results obtained for the present case is given in Table 5.1.

Table 5.1: Summary of the results obtained for Case I

	$h_{\mathbf{LGM}}$	$h_{\mathbf{IP}}$	$h_{\mathbf{HWT}}$	**From variance profile**
Slope (γ), from FFT power spectra of the time series	1.01 ± 0.06451	1.04 ± 0.0644	1.06 ± 0.0654	Not applicable
Mean CBL height	2068 m	2005 m	2008 m	2022 m
EZT from standard deviation method	118 m	77 m	92 m	Not applicable

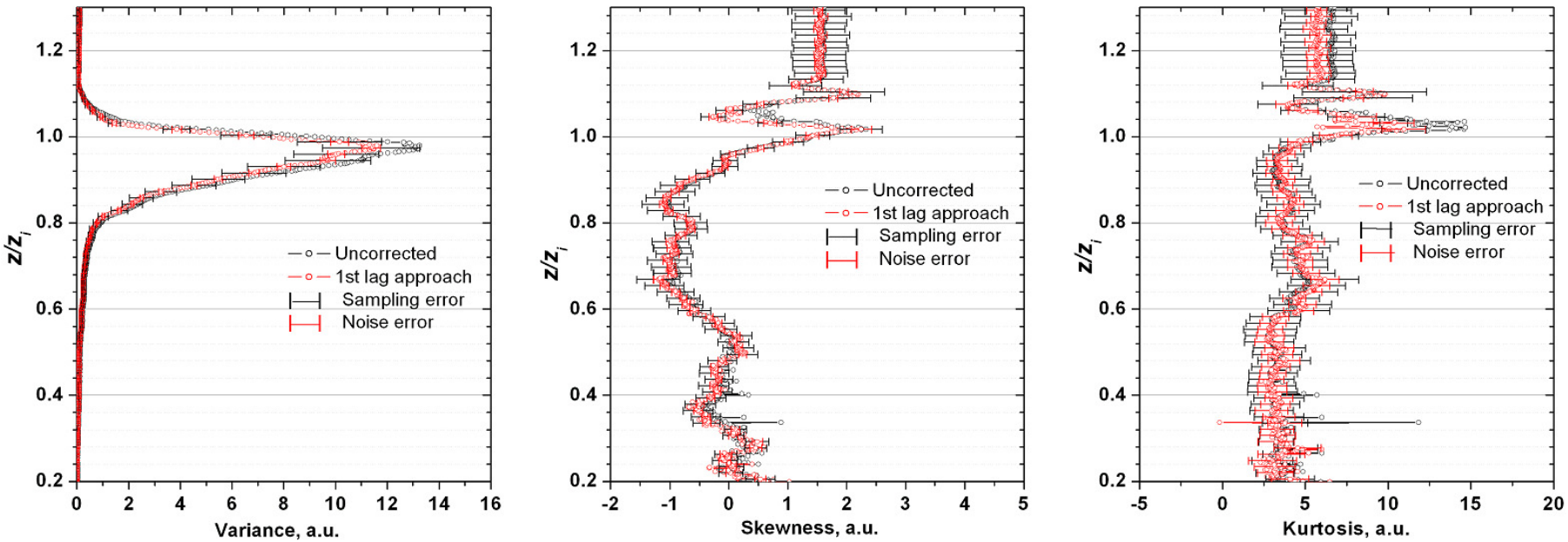

Figure 5.14: Vertical distributions of the variance (V), skewness (S_k), and kurtosis (K) for case I with two different noise corrections and without any correction. Statistical and sampling errors are also shown. See text, for further discussion.

5.3.2 Case II: Convective boundary layer during its rapid growth in morning

5.3.2.1 Retrieval of convective boundary layer height

This section deals with the investigation of the CBL evolution obtained with the UHOH lidar measurements between 0955 and 1115 CEST on the same day as in case I. During this time, the evolution of CBL confirmed an interesting regime transforming from a stratified structure in the morning to a well-mixed CBL toward noon. In general, the application of the HWT-based method as discussed in section 4.1.4 works well. But this algorithm can lead to significant problems when multiple aerosol layers exist. The other two methods also have these biases. Such a situation was observed during case II. Before the HWT was applied on the range-square-corrected signal, 10 consecutive lidar profiles were averaged which yielded a time resolution of 0.33 s. Figure 5.15a is the time-height plot of $D(z)$ values. The residual layers were confined within the altitudes from 1.6-2.1 km. This confinement was due to less turbulent motion in this region. The LGM picked the strongest gradient, which was not always at the top of the newly developing CBL but for many profiles was found in the RL. Thus a fully automated LGM routine failed in identifying the top of the CBL. The HWT was applied within the altitude from 500 m to 3000 m. A similar analysis was performed for the choice of dilation value as in case I and dilation value of 260 m was found suitable for this dataset. It was mentioned earlier that the value of most suitable dilation depends on the nature of backscatter profile. Figure 5.15a displays that the HWT sometime picked the top of the RL instead of the top of the convectively growing boundary layer.

The HWT analysis was modified then to find correctly the height of CBL top with the following procedure. At first, the aerosol layer was identified from the time-versus-altitude plot of $D(z)$ of the background corrected signal as displayed in Figure 5.15a. Then the upper altitude limit below the aerosol layer was selected and used as z_{max} (in Eqn.4.9) for calculating $W_f(a, b)$. The upper limit in the integration for obtaining the $W_f(a, b)$ is now not limited to a fixed altitude but differs in time owing to the presence of the RL. Although the approach is based on a subjective determination of the residual layer, this technique needs a very limited number of user-defined inputs. Following this approach, also used by Senff et al. (2002), and Cohn and Angevine (2000), difficulties arising due to the appearance of RL were eliminated.

Figure 5.15b shows the growth of CBL top (black-solid line) overlaid on the range-square-corrected backscatter intensity after the subjective approach was applied. This figure exhibits also the capability of the HWT-based approach to retrieve correctly the CBL height in the presence of multiple dust layers. The morning time convection is clear from both figures showing the growing CBL top from 0.8 to 1.3 km. The possible interaction between the convectively growing boundary layer and the RL can be observed at the end of the time series. This interaction is discussed in section 5.3.2.3.

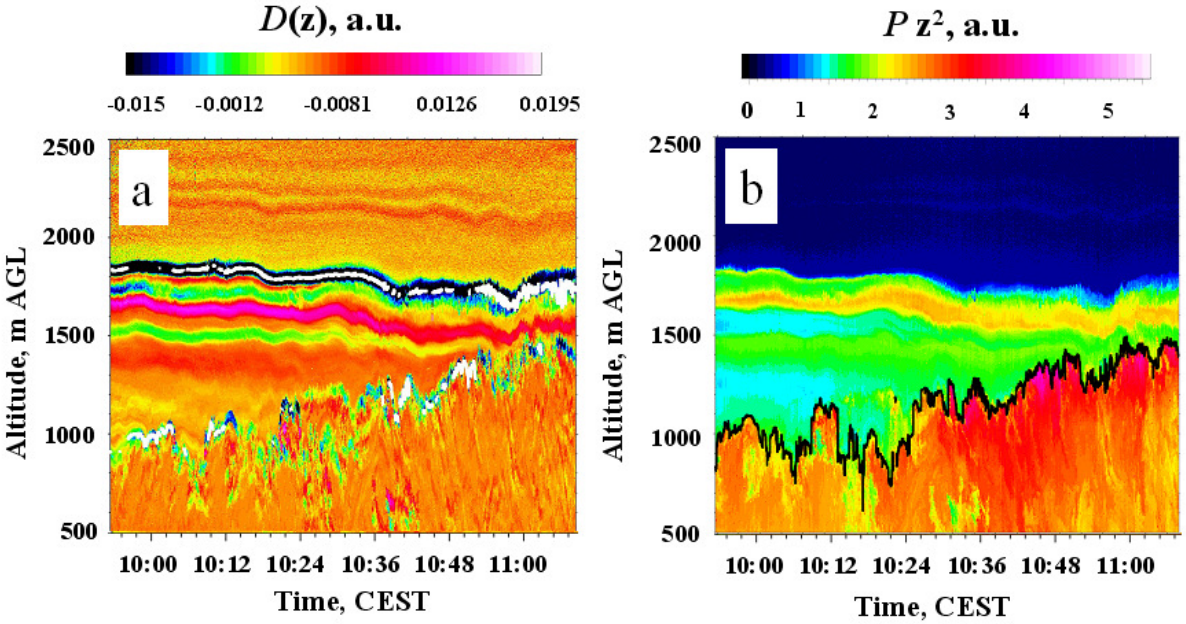

Figure 5.15: Retrieval of ABL top by the HWT method in the presence of several aerosol layers in the ABL. The HWT is applied in altitude range from 500 m to 3000 m with a dilation value of 260 m. (a) $D(z)$ values are plotted in time-versus-altitude frame. Clearly visible is that the HWT-based analysis mostly finds the previous-night aerosol layer height as ABL top as overlaid with the white line on the image. (b) The HWT is applied below a selected altitude by confirming the presence of the RL (see, text for further details about this subjective approach). Time series of convectively growing ABL top (h_{HWT}, solid black line) is superimposed on the range-square corrected lidar backscatter intensity.

5.3.2.2 Entrainment zone thickness for case II

Following the standard deviation method and cumulative frequency distribution method described in section 4.2, the EZT was determined for case II as was performed for case I. Figure 5.16a shows the normalized frequency distribution of h_{HWT} for case II. The standard deviation approach yielded a value of 140 m for the EZT. The frequency distribution is highly asymmetrical reflecting two different regimes of the CBL. The distribution around 900 m AGL is expected to be due to the entrainment and corresponding mixing process inside the CBL while the distribution around 1300 m AGL is due to the penetrative convection at the top of the CBL.

Results obtained from the cumulative frequency distribution method are shown in Figure 5.17. Temporal averaging for the cumulative frequency-based approach is also 30 s as in case I. The determination of the EZT was performed using cumulative frequency distribution of the time series of h_{HWT} . The upper panel shows the time evolution of the h_{HWT} together with the results obtained from cumulative frequency distribution. The $h_{HWT(05/10)}$ and $h_{HWT(90/95)}$, are also shown in the figure. The lower panel shows the 30-s interleaved EZT values. This technique yielded a mean EZT of 62 m.

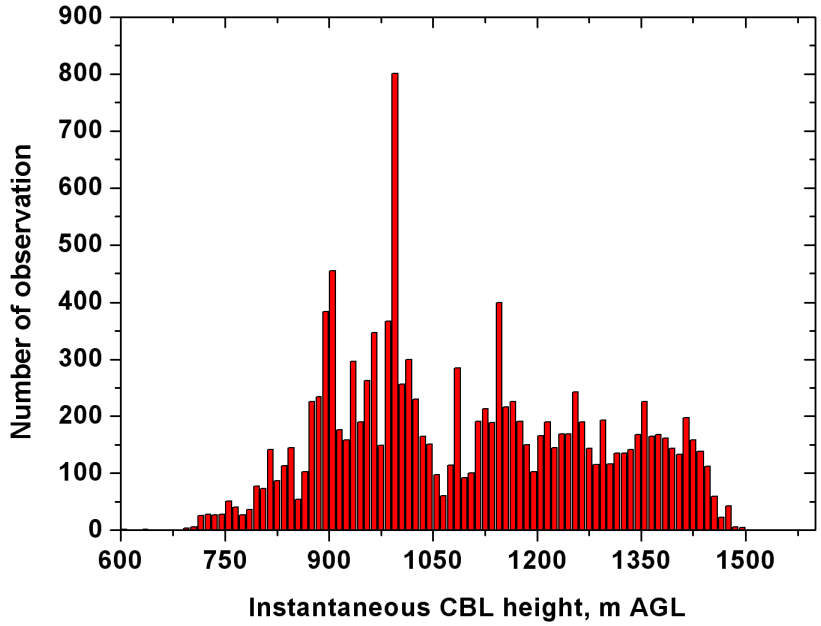

Figure 5.16: Frequency distribution of the instantaneous CBL height derived with the HWT for case II.

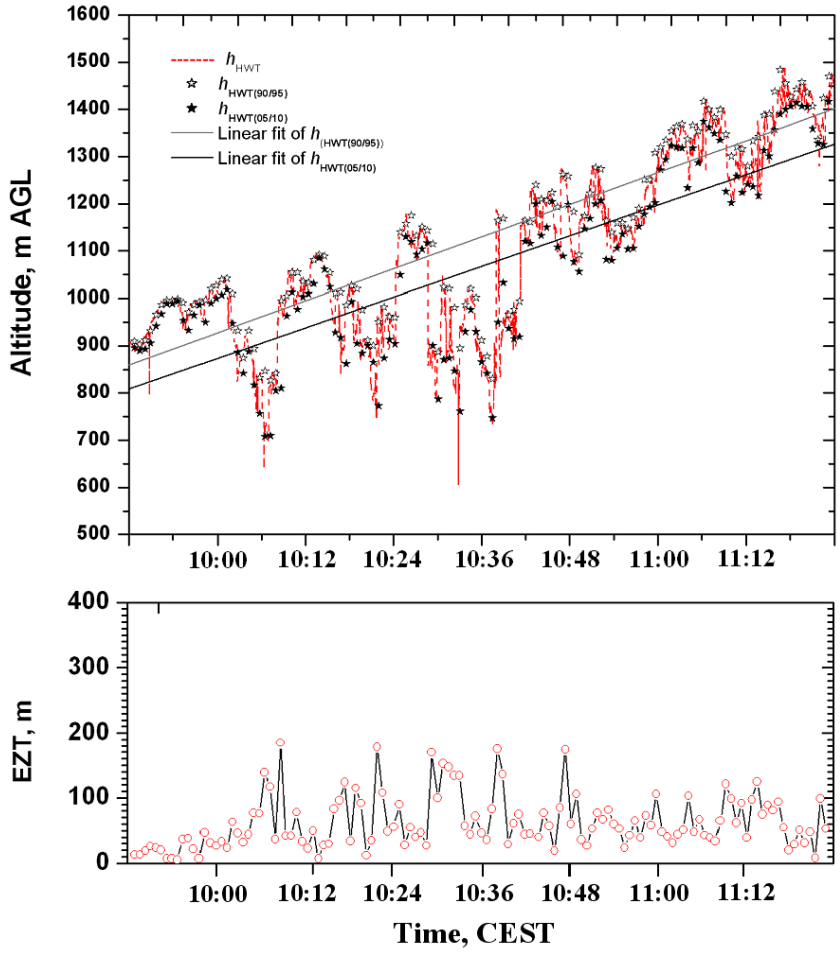

Figure 5.17: EZT estimation by cumulative frequency distribution of h_{HWT} for case II. Linear fits for both $h_{HWT\ 05/10}$ and $h_{HWT\ 90/95}$ values of the cumulative frequency distributions are shown here. Lower panel shows the EZT variability during this time period.

A large difference was found between the values of the EZT for these two methods. Both cases show that the EZT obtained with the standard deviation method is higher than that with the cumulative frequency distribution method. One probable reason for the discrepancies can be due to the presence of different intrinsic trends in the time series of the CBL height that cannot be easily determined. A detailed investigation of the differences found for the EZT (17 m for case I and 82 m for case II) needs further research. Nevertheless, this regime (case II) has rarely been considered in previous studies of the CBL entrainment zone characteristics though being an important aspect with respect to near-surface air pollution.

5.3.2.3 Penetrative convection in the convective boundary layer

The interaction between the CBL and the RL atop mentioned in the previous section is studied here. A similar study was performed by Pahlow et al. (2005) for the case of a forest fire smoke. In their paper, they studied the interaction between the top of the CBL and the bottom of the smoke layer.

It is clear from Figure 5.18 that the growing CBL (red line in figure) and the overlying RL (black line) were coupled at an altitude of 1.7 km AGL just after 1115 CEST. This figure shows that the height of the RL was found to be descending and the CBL height to be ascending (see, the linear trends overlaid on them). This is a clear indication to the absence of turbulence motion in the RL. The RL at 1.8 km AGL in the present case was also observed in the lidar data collected on the previous night (on 25 June around 2230 CEST; see, section 5.3.6.1)

To correlate the RL height and the top of the CBL, first the linear trends of both time series were subtracted and then the correlation coefficient was calculated. The value of the correlation coefficient was found to be 0.33. Such poor value of correlation coefficient confirms the different behaviors of the two time series. The minimum and maximum interval between the linear trends of the two time series was found to be 80 m and 820 m, respectively. This effect (dynamical coupling with very poor correlation) might have been occurred due to the wave activity in the lower troposphere. Indeed, it is visible from Figure 5.18 that the dynamic coupling between the two time series is an indication of gravity waves. After the CBL started to grow, the RL evinced ripple structure due to the overshooting thermals at the CBL top.

This is observed from the figure that the h_{HWT} reached the level of the dust layer merging into one another becoming indistinguishable. This is normally called penetrative convection (Deardorff et al., 1969). As a result of this activity, cleaner air from the free troposphere enters the CBL by downdraft.

Trapping of the pollutants in the CBL is a familiar phenomenon, which arises due to the reason that none of the turbulent CBL air mass can carry pollutants into the laminar air. After sunrise as time progresses, the CBL over land can be modified by different phenomena: morning or early afternoon penetrative convection, and encroachment or decay of the late afternoon convection. Sorbjan (1996) showed in his work that early morning penetrative convection often evolves to an encroachment

structure due to rapid growth. Encroachment processes in the CBL are possible when the atmosphere above the CBL consists of an RL from previous night. Stull (1988) showed that if the CBL development is completely dependent on the surface warming, then the CBL encroaches upward only as the CBL warms. Therefore, during this time, the growth of the CBL height is highly correlated with the rate of surface heating. This was exactly the situation during case II in this study (see section 5.3.4 for further discussion on the correlation between the surface temperature and CBL height evolution). Also this work showed the fast growth of the CBL in the morning in the presence of an RL and a comparatively slower growth in the later afternoon. However, the transition between the free encroachments to the penetrative convection is difficult to determine.

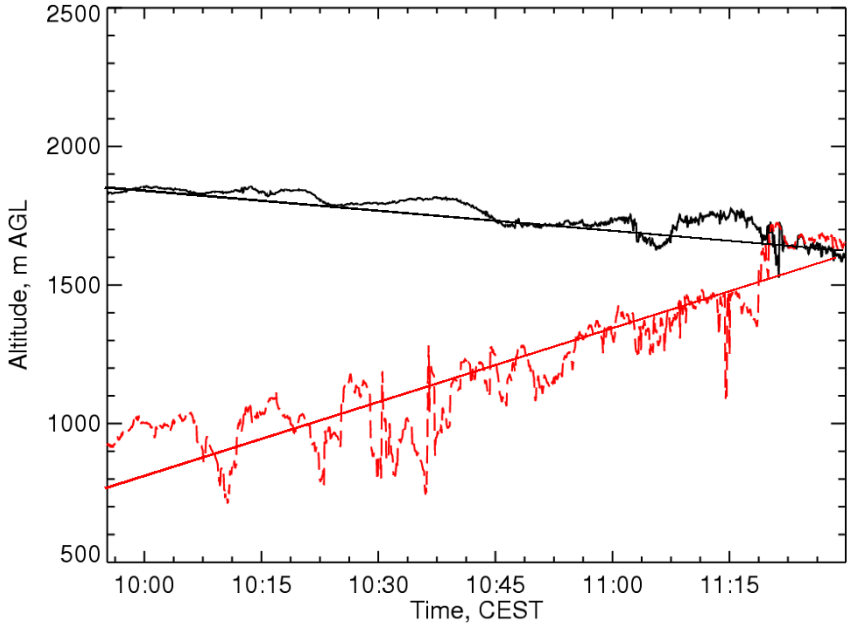

Figure 5.18: Evidence of penetrative convection in the CBL. The h_{HWT} (dashed-red curve) and the RL bottom (solid–black curve) are shown together with linear trends overlaid. Red solid and black solid lines are linear trend for h_{HWT} and residual layer bottom, respectively.

5.3.2.4 Profiles of higher-order moments for case II

Higher-order moments analysis was performed for case II in the similar fashion as was performed for case I aiming at the investigation of the turbulence profiles for this different regime where a rapidly growing CBL during morning eroded nighttime stable layer in presence of a strong residual layer above the CBL. The full time series of 1 hour 20 minutes (case II) of relative particle backscatter data are treated for this purpose. The calculation of the higher-order moments was restricted to the data obtained below 2.7 km AGL as a maximum value of instantaneous CBL height was found to be of about 1.7 km AGL.

Variance spectra of relative particle backscatter coefficient fluctuations at 8 selected height levels are shown in Figure 5.19. The –5/3-power law is also shown. This figure suggests that the inertial

subrange was achieved for some cases. There is considerable deviation in the higher altitude as can be seen from the spectra at 1755 m AGL. This is probably arising due to the presence of the residual layer at that height.

The autocovariance functions for 100 different lag values are shown in Figure 5.20 for four different heights (600, 800, 100, and 1200 m AGL). Similar to the case I, the integral scale for β'_{par} was of about 60-70 s inside the CBL as shown in Figure 5.21. For all higher-order moments profiles height is normalized with the mean CBL height (z_i, 1136 m) during this time calculated by averaging h_{HWT} values of this case. The integral scale value signifies that at a time resolution of 10 s that roughly the first 6-7 lags of the autocovariance function fall within the inertial subrange. Surprisingly, the vertical distributions of corrected and uncorrected profiles of the integral scales are nearly same except at the altitude above $1.4z_i$. There was a prominent drop of the integral scale value above $1.4z_i$, which might be arising due to the presence of the strong residual layer present at that height. Otherwise, above $1.1z_i$, an increasing trend was observed up to a high value of about 225 s at $1.5z_i$.

The vertical distributions of variance, skewness, and kurtosis with and without noise corrections are shown in Figure 5.22. Similar to the case I, the variance without the noise correction were observed to be overestimated in all heights. The sampling and noise errors as black and red error bars, respectively, are also shown for the corrected profile (i.e., variance obtained with the 1st lag approach). The variance below the altitude of about 500 m is not shown here as the data was affected by the partial overlap factor of the lidar system. Unlike case I, the distribution of V in height was not well defined. A sharp peak was observed at the mean CBL height. Additionally, some other peaks were also observed most probably due to the non-stationarities present in the CBL height evolution. But the influence of the different aerosol layers cannot be ignored while explaining the vertical distribution of the variance. There were secondary broad peaks between $1.3z_i$ and $1.4z_i$ with a local maximum. Most probably, above $1.4z_i$, high values corresponded to the residual layer at those heights. The rest of the large variance values most probably were observed due to turbulent activities present in the CBL. Above the RL, the variance profile decreased and reached nearly a value of zero. Further investigation of these characteristics needs detailed information on flux Richardson number (Sorbjan, 1990).

Similar to the results found by Mahrt et al. (1991), predominant negative skewness values up to the height of $0.8z_i$ were the result of rapid growth of the CBL height (see, Figure 5.22). But around an altitude of 900 m and higher, positive skewness was found. It is interesting to note that the S_k profile increased with height in two different altitude regimes: one from $0.8z_i$ and $1.1z_i$ and the other one from $1.2z_i$ to the RL bottom at $1.5z_i$. The first is representative of convective activity, which organized as height increased but the second one exhibited several peaks, which were arising most probably due to the presence of different scales of mixing. A marked and dramatic change in S_k with negative values at an altitude 1.6-1.7 km could be the result of the intrusion of free tropospheric air. This is consistent with the studies of Couvreux et al. (2005).

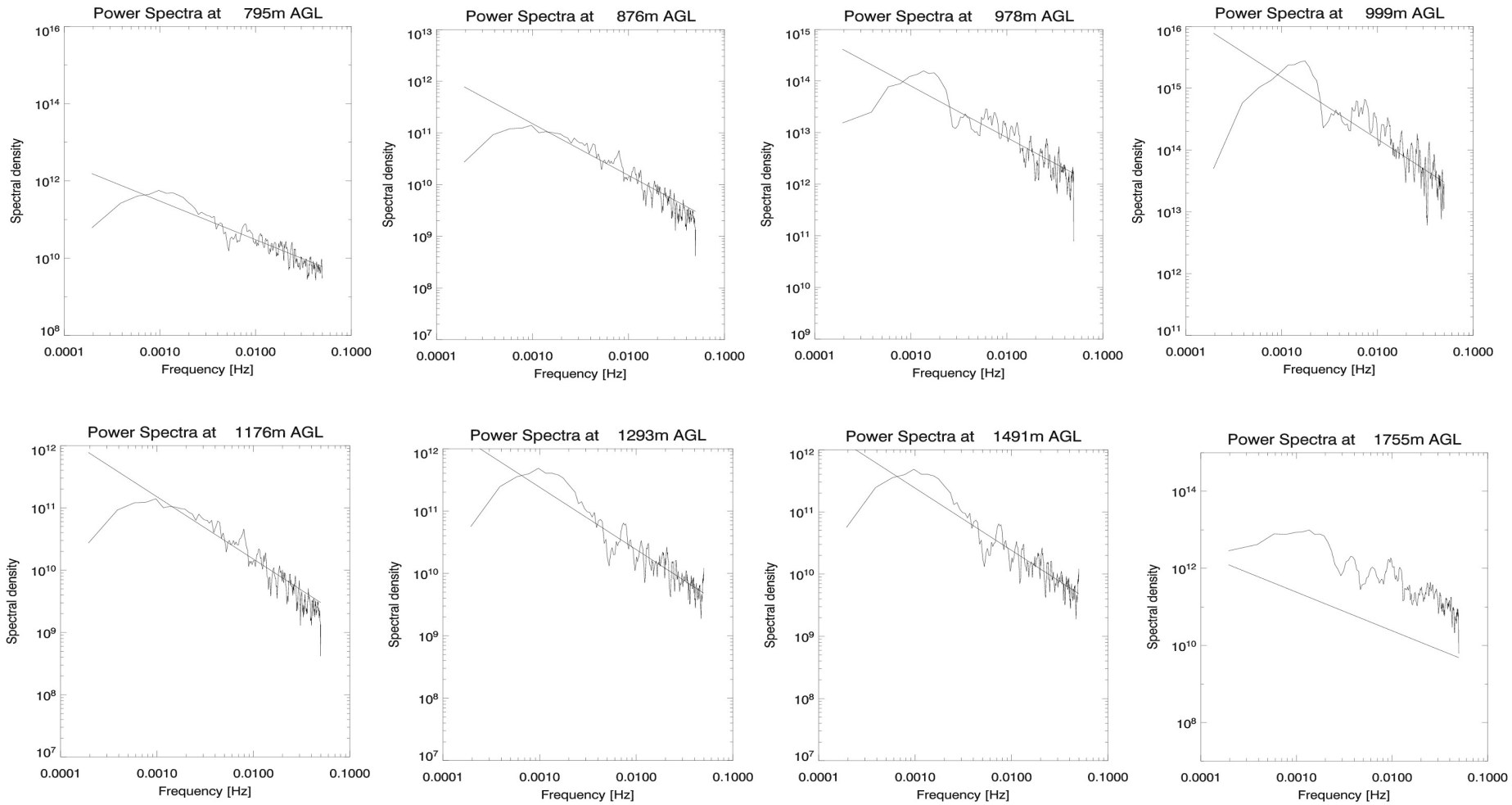

Figure 5.19: Spectra of particle backscatter coefficient at four different heights for case II. The –5/3-slopes are shown on each panel in order to present the expected shape of the inertial subrange.

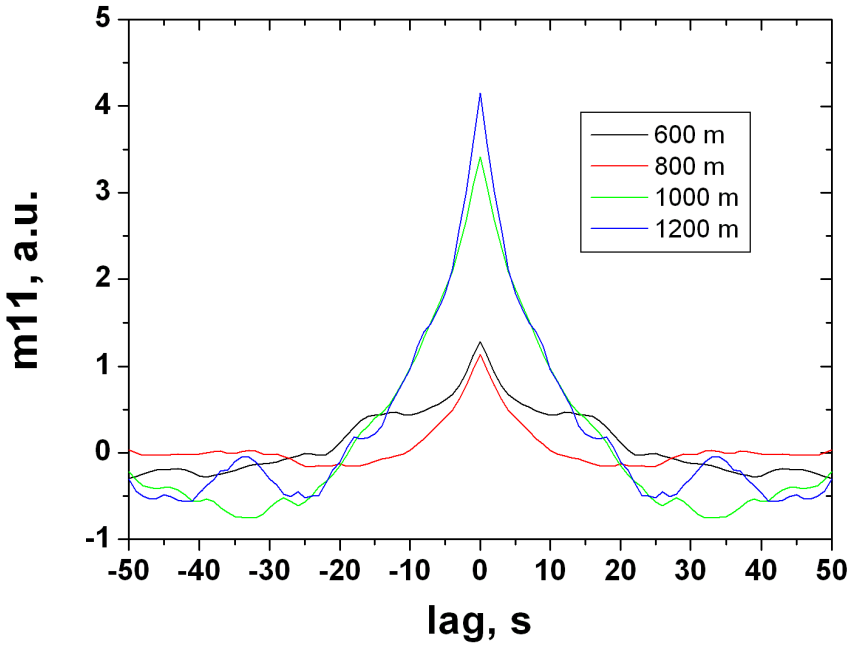

Figure 5.20: The autocovariance function at four different heights for case II.

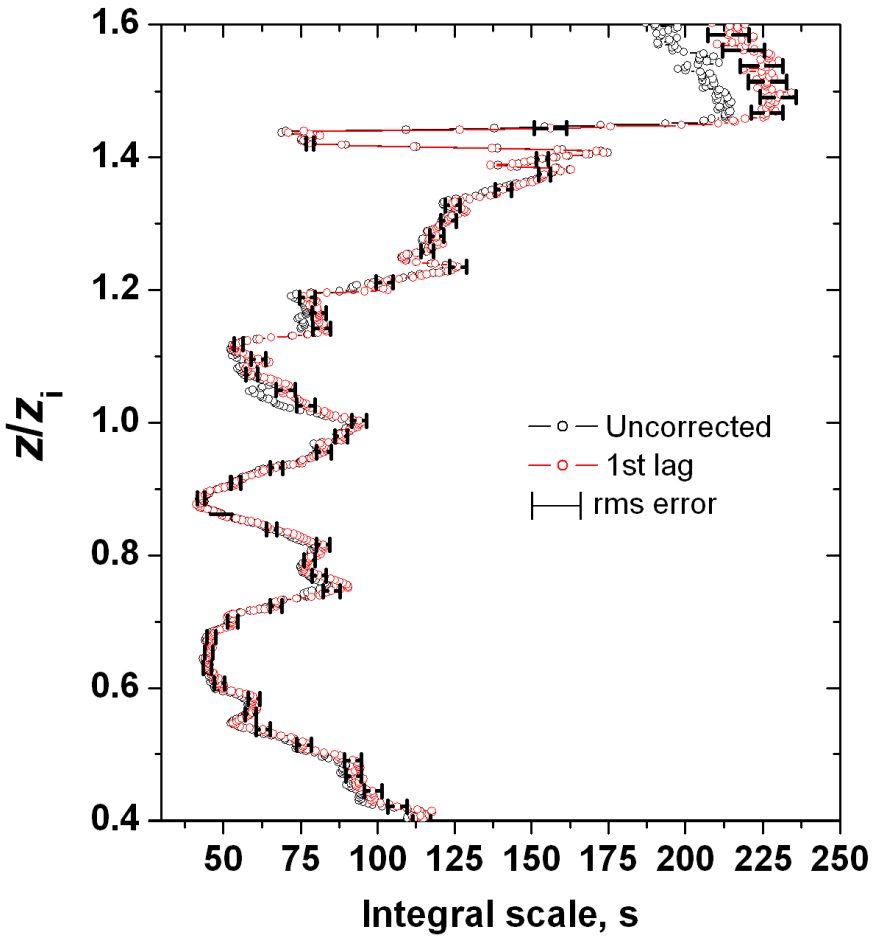

Figure 5.21: Integral scale for case II with and without noise correction. The standard error due to instrument noise is also shown as an error bar on the profile.

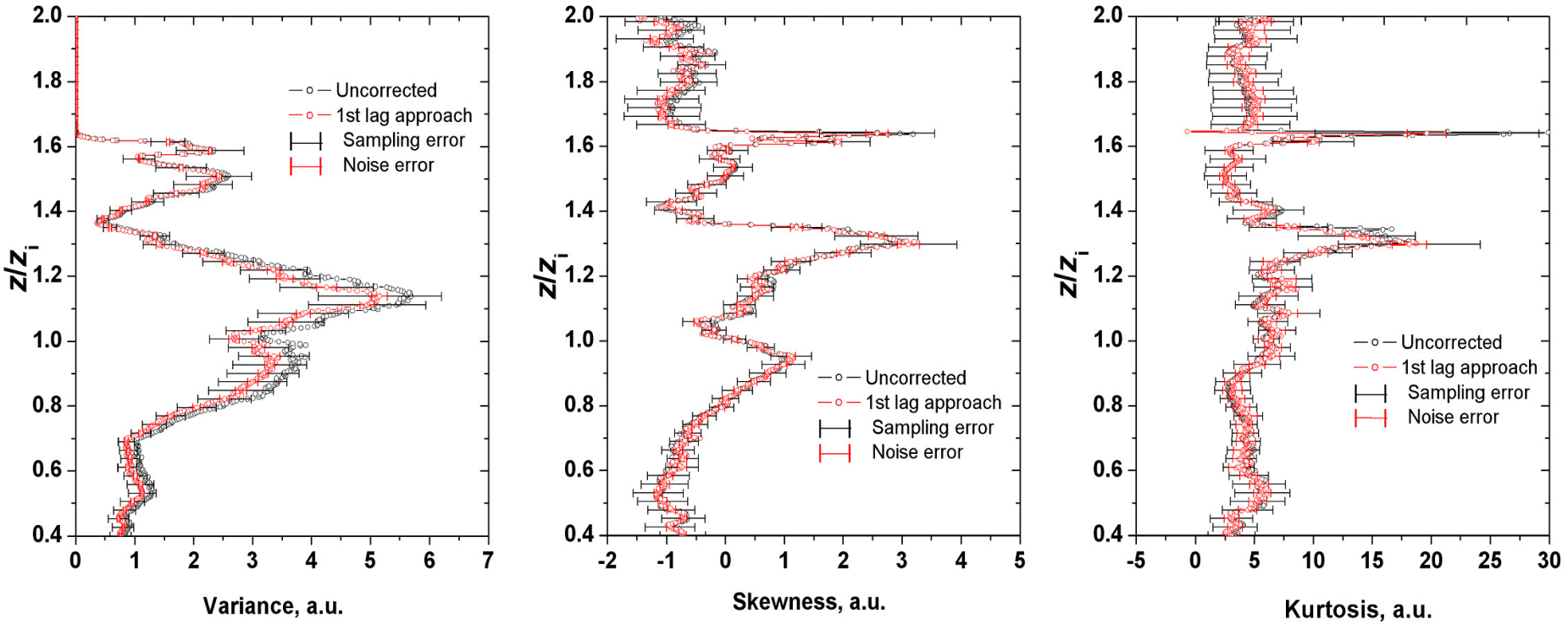

Figure 5.22: Profiles of variance (left panel, 2nd order moment), skewness, (middle panel, 3rd order moment), and kurtosis, (right panel, 4th order moment) obtained from the UHOH lidar backscatter intensity data from 0955 to 1115 CEST, 26 June 2004.

Above an altitude of $1.5z_i$, the S_k profile obtained a constant value close to 0 due to almost homogeneous aerosol distributions in the free troposphere. Kurtosis is shown in the right panel of the figure. The kurtosis increased with height from 3 to 8 in the region of ABL height. Again, K increased sharply to value of 16 due to the presence of RL.

Obviously the higher-order moments profiles are getting more complicated due to non-stationarities, rapid growth rate, and presence of the residual layers together with some other aerosol layers.

5.3.3 Comparison of case I and case II

Table 5.2 summarizes the qualititative and quantitative differences between two different CBL regimes. The key difference between the two cases is mainly arising due to two major reasons. Firstly, a rapid

Table 5.2: Comparison of the results obtained for case I and case II.

Features	**Case I (Time series 1430-1600 CEST)**	**Case II (Time series 0955-1120 CEST)**
Visual inspection of the time series of r-square corrected signal	Quasi-stationary CBL	CBL regime during its rapid growth
Residual layer	Not observed	Observed at an altitude around 1.8 km AGL, together with other multi-layered structure
CBL height growth rate	High, up to 5 m/minute	Very low (< 1 m/minute), nearly constant with time
Slope (γ), from FFT power spectra of the time series	1.0 ± 0.06	1.5 ± 0.038
Mean entrainment zone thickness	75 m while the a maximum value was 220 m	62 m while the maximum value was 200 m
Mean CBL height	Mean h_{LGM} of 2068 m with minimum of 1641 m and maximum of 2277 m	Mean h_{HWT} was found to be 1136 m with minimum of 678 m and maximum at 1545 m
Vertical profile of V	Classical picture of variance profile for a well-mixed CBL found. Maximum of variance found at 2022 m	Multimode distribution of V due to the presence of multiple aerosol layers. Highly affected by the rapid growth of CBL height. Maximum of variance was found at 1120 m AGL
Vertical profile of S_k	Mostly negatively skewed up to the top of the CBL and positive values found near the CBL top. Above $1.1z_{\mathrm{i}}$, free tropospheric air observed with constant skewness value	Highly complicated structure with both positive and negative skewness inside the CBL
Integral scale	Between 60 and 80 s up to the CBL top. Higher values are found in the entrainment zone.	Between 60 and 80 s up to the CBL top.
Power spectra of particle backscatter coefficient	Found to follow –5/3-power law inside the CBL	Found but, near the entrainment zone no such power law observed

growth of CBL height during the case II was observed with a rate of up to 5 m/minute while for case I, a very slow growth was found which could be considered as a quasi-stationary CBL. Secondly, unlike case II, no strong RL or any detached multiple aerosol layers were observed during the period of case I. The latter one resulted presence of penetrative convection at the top of the CBL during case II.

Similar behaviors were observed for both cases while demonstrating the CBL height estimation with LGM, IP method and the HWT-based analysis, i.e., the fundamental difference among the techniques providing $h_{LGM} > h_{HWT} > h_{IP}$. The mean EZT for case I and case II were found to be 75 m and 62 m, respectively. Mean CBL heights obtained with the HWT-based method were 2008 m and 1136 m for case I and case II, respectively. These differences are arising due to the enhanced entrainment processes prevailing during case I. An FFT-based power spectral analysis of the CBL height time series provided γ values of 1.0 and 1.5 for case I and case II, respectively. This is a confirmation of the implicit non-stationarity present during case II.

Some characteristic differences were observed in the vertical distributions of the higher-order moments. The vertical distribution of variance profile for case I provided a well-defined aerosol distribution due to turbulence inside the CBL. An expected peak was observed at the top of the CBL while variance profile for case II was found to consist of 2 to 3 different peaks in it. Most probably this was caused by the presence of overlying residual layers and a rapid growth during case II. Additionally, relatively large sampling errors were observed for all higher-order moment profiles for case II compared to case I.

The integral scale values for both cases inside the CBL (i.e., part of the CBL above the surface layer and below the entrainment zone) agree well with each other with a value of about 60-80 s. Additionally, a decrease of the integral scale was found for both cases near z_i. These findings are similar to the findings of Lenschow et al. (2000). But, the sharp drop of the integral scale at $1.4z_i$ for case II is most probably due to the heterogeneity induced by the RL aerosols present at that height. On the other hand, a larger value of integral scale was observed for case I (of about 120 s) near $1.1z_i$. Few more characteristic differences were observed for the third-order moments (skewness). Negative values of skewness were found inside the CBL while positive values were observed in the entrainment zone near the top of the CBL for case I. But for case II, skewness profile showed a high variability even inside the CBL with positive values.

Being the experimental area located in the region of Stuttgart downtown, an increased amount of anthropogenic activities during morning (case II) was not unexpected yielding diverse features in the turbulence profiles. Furthermore, UHOH lidar was operated at the bottom of a valley-like region so that aerosol distributions during case II are expected to be largely affected by different pollutants advected from surrounding regions in the morning. The estimation of the higher-order moments in this study solely used the aerosols to be the tracers of the CBL dynamics. Therefore, the observed structures in the aerosol distribution during case II most probably yielded such turbulence profiles in the CBL.

High resolution of the UHOH lidar measurements helped to make reliable evaluation of some turbulence parameters through the estimation of the higher-order moments. As found in other studies, the variance profile in present case also gave an indication to the variability inside the boundary layer. Obviously, the maximum variance value appeared at the mean CBL height. The normalized third-order moment or skewness value, obtained in this work showed a vertical variability in different height regimes. Free troposphere was found to be less skewed or without any asymmetry, with S_k value nearly equal to zero for both cases. Similar results concerning the vertical dependency of S_k value in CBL can be found in Mahrt et al. (1991), Couvreux et al. (2005), and Larson et al. (2001). Encroachment of free tropospheric air into the CBL was observed during the study of penetrative convection and the negative value of S_k near the RL is a confirmation. High positive values of K (in its vertical distribution) were obtained in the EZ, which agrees with the findings of Lenschow et al. (2000). In this intercomparison only qualititative aspects can be considered since different tracers have been used in those studies (water vapor mixing ratio, vertical velocity) and this one (aerosols). Furthermore, this should be noted that the results obtained are based on a technique, which uses an assumption considered to be true for a CBL regime where stationarity exist, and hygroscopic growth of the aerosol particles can be neglected. These assumptions are not considered to be true for the CBL regime during case II both due to the heterogeneity in the distributions of the aerosol particles influenced by a rapid growth of CBL, and the presence of the residual layers above.

5.3.4 Evolution of convective boundary layer height

Two different regimes of ABL growth were clearly observed from the full-day-time-series of the data, with respect to the estimated growth rate: one regime (from 0955 to 1115 CEST) with growth rate of 3-5 m/minute and another (1130 to 1800 CEST) with comparatively slower rate with 0.5–2 m/minute as evinced by Figure 5.23. This figure shows the time series of CBL height growth rate in m/minute (see, panel a) determined from the time series of the h_{HWT} estimated during 1000-1800 CEST (panel b). RH at ground is also shown in the figure (panel c). Increase of the surface temperature (panel d) and the growth of the CBL height were highly correlated to each other as seen from the figure. Rapid growth in the morning was caused by surface heating and associated convective activities while the decrease of the growth rate and then the persistence of a constant slower growth were due to interaction with the RL and resulting capping, subsidence, and advection. The afternoon boundary layer deepens slower than the morning one because it is thicker, and is therefore less heated by a similar surface heat flux. The CBL height reached its maximum (2250 m, obtained by the HWT method) around 1730 CEST. This suggests that the surface forcing was still present around this time. Sunset was at 2130 CEST on this day.

This should be noted that the encroachment at the top of the CBL mentioned in section 5.3.2.3 is most probably an outcome of the high correlation between the surface temperature and the CBL

height measured during this time. Surface temperature observed during 1000 and 1130 UTC showed a sharp increase from 18.2 °C to 20.2 °C while the CBL height developed from 678 m to 1545 m AGL. A correlation coefficient of 0.89 was found while comparing these two time series between 1000 and 1130 CEST. This is an indication to encroachment as the rapid growth of the CBL height is assumed to be highly dependent on the surface temperature while the RL atop remained more or less at the same altitude (around 1.8 km AGL) with a slightly decreasing trend.

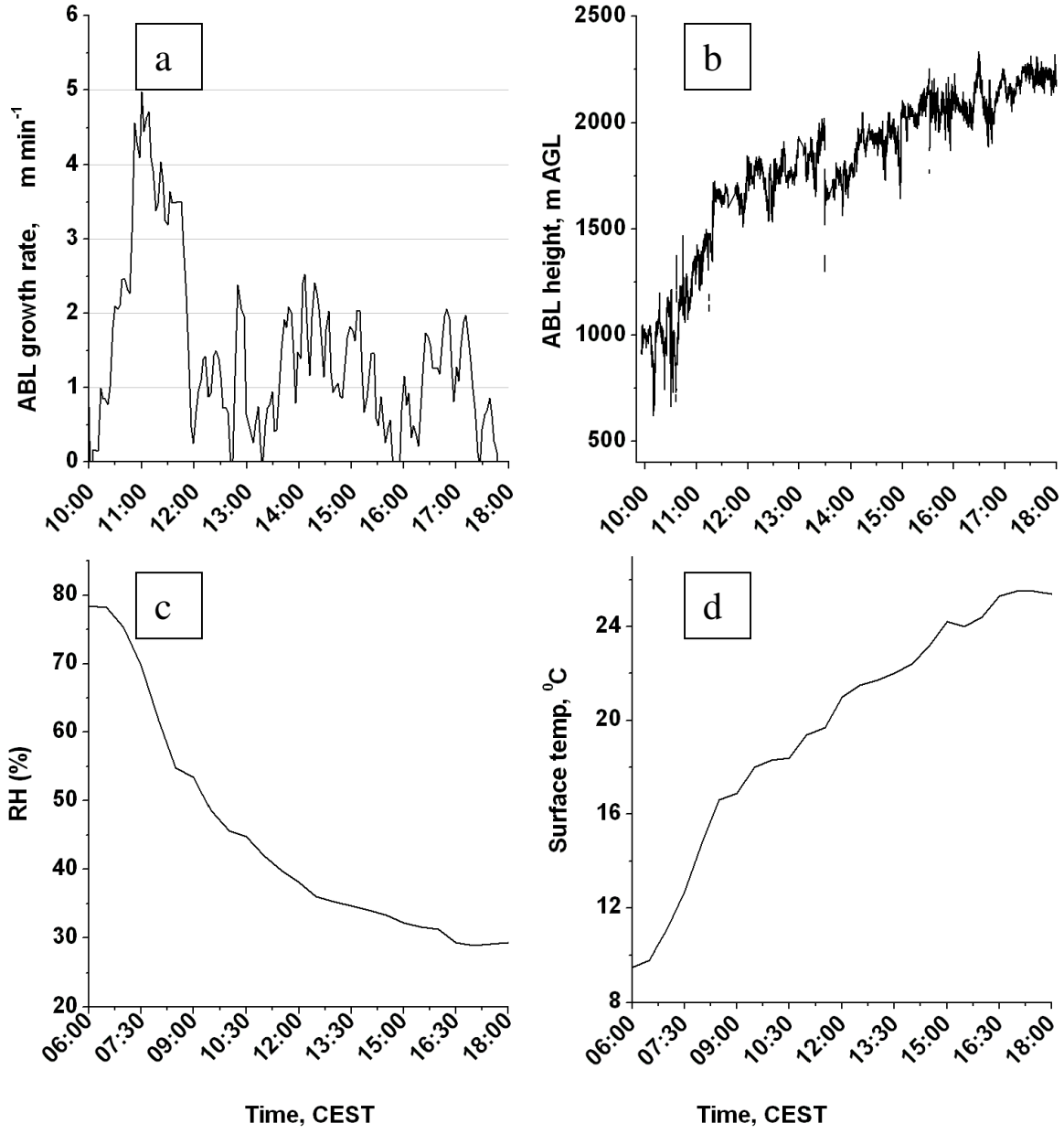

Figure 5.23: ABL growth rate is shown quantitatively (one regime with 3-4 m/min and another regime 0.5 to 2 m/min) and the surface temperature variation over whole day is also shown to illustrate how the surface heating affects the ABL evolution. Consequent effect of surface heating is revealed after 3 hours during 10:00 CEST. After comparison of the time series of ABL height and surface temperature following results are obtained: correlation coefficient: 0.87 if compared both CBL height and temperature from 0900 to 1800 CEST, Correlation coefficient: 0.97 if compared between CBL height (0900 to 1800 CEST) and temperature (0600 to 1800 CEST).

5.3.5 Statistical analyses of a convective boundary layer height time series: Non-stationarities

For the following statistical analyses, the Haar wavelet derived CBL height time series between 0955 and 1115 CEST of 26 June 2004 is used. The correlation embedded in the CBL top fluctuations can be investigated using DFA method as described in section 4.3.2. Figure 5.24 shows the local linear fits (blue solid line) for the CBL top time series divided into segments of length of 100 consecutive CBL heights. The vertical red lines indicate boxes of size 100. The bluew solid line segments represent the trend estimated in each box by polynomial fits (of order of 1 or 2). The same computation was repeated over various box sizes (n) to provide a relationship between $F(n)$ and n (see, Eqn. 4.13). The slope of the line relating log $F(n)$ to log (n) determines the scaling exponent (self-similarity parameter), α^* as mentioned before. Figure 5.25 presents the calculated value of alpha-exponent as obtained from the log-log plot of $F(n)$ and n for DFA method of polynomial of order 1 (upper panel) and order 2 (middle panel). Alpha-exponent values are 0.123 and 0.372 for DFA-1-and DFA-2, respectively.

For both DFA results, it is evident that long-range time correlations in the CBL top fluctuations were present with positive alpha value (< 0.5 here). Consequently, the spectral exponent values, (γ, 1.246 and 1.74 for DFA-1 and DFA-2, respectively) then was lying in the region $1< \gamma < 3$. It can be concluded that CBL height time series show a non-stationary process with stationary increments. Figure 5.25 (bottom panel) presents the FFT power spectra for the same time series following the method described in section 4.3.1. The value of γ obtained through FFT power spectral analysis is 1.502. This γ value denotes the similar characteristics concerning the non-stationarity in the CBL height time series. These parameters are the indicators of the dynamics of CBL.

The γ value here in any case is somewhat below the 5/3 resulting from Kolmogorov's theory for isotropic and homogeneous turbulence (Kolmogorov, 1941). This inconsistency prevents to relate the multifractal dimension to the spectral exponent value obtained. The CBL dynamic self-affinity with a roughness exponent of 0.37 is consistent with study of Pelletier (1997). Similar spectral analysis can be found in Melfi et al. (1985).

Figure 5.26 shows the hierarchy of the values of the generalized dimension $D_m(q)$ for the same time series. The straight line is drawn to enhance the value of q at which the $D_m(q)$ function starts to deviate from linear dependency. The $K(q)$ function defined by Eqn 4.18 indicates the intermittency of the signal. Thus the multi-fractal properties of the CBL height time series are expressed by two sets of scaling functions, $D_m(q)$ describing the roughness of the signal and $K(q)$ describing its intermittency. For the mono-fractal case $D_m(1)=0.75$, there is no intermittency in the signal at all, if $D_m(q) \equiv 1$. In the present case CBL height time series was found to be mostly fluctuating and with intermittency in it since the generalized dimension calculated lies between 0 and 1. Figure 5.22 yields that $K(q)$ function becomes almost linear in the region of higher q values, which implies that a single event was dominating in the statistics, i.e., non-stationarity embedded in the time series of the CBL heights.

These results show that the multifractal analysis yields a convenient framework for the description of different scaling regimes present in the convectively growing boundary layer. These analyses revealed the roughness of CBL top heights during the morning, non-stationarities in CBL height time series having anti-persistent signal with stationary increments. Generalized multifractal dimensions were found to be within 0 and 1. Main objectives of these analyses were achieved after characterizing the local correlations in the CBL top dynamics and by quantifying the multi-fractal behavior in it. The FFT analysis also revealed the fact that the CBL height evolution with time is expected to be a non-stationary process with stationary increments. The relationship between the spectral exponent (γ) and the Hurst exponent (α^*) for a self-affined time series was reasonably satisfied.

These results in general can help to achieve an understanding of the dynamical behavior of CBL depth especially when convective activity is a dominant feature. While comparing with the multifractal results of the previous studies it should be noted that it is not possible to make a straightforward and direct comparison since those studies deal with a purely spatial variations (as obtained with aircraft lidar data) of the tracers whereas the analysis performed is strictly for variations in time. Another key shortcoming may always arise in the multifractal results while using aerosols as tracers obtained with IR lidar systems: the lidar signal intensity is actually non-linearly linked to the particle backscatter coefficient and this is also true for the relation to the aerosol concentration.

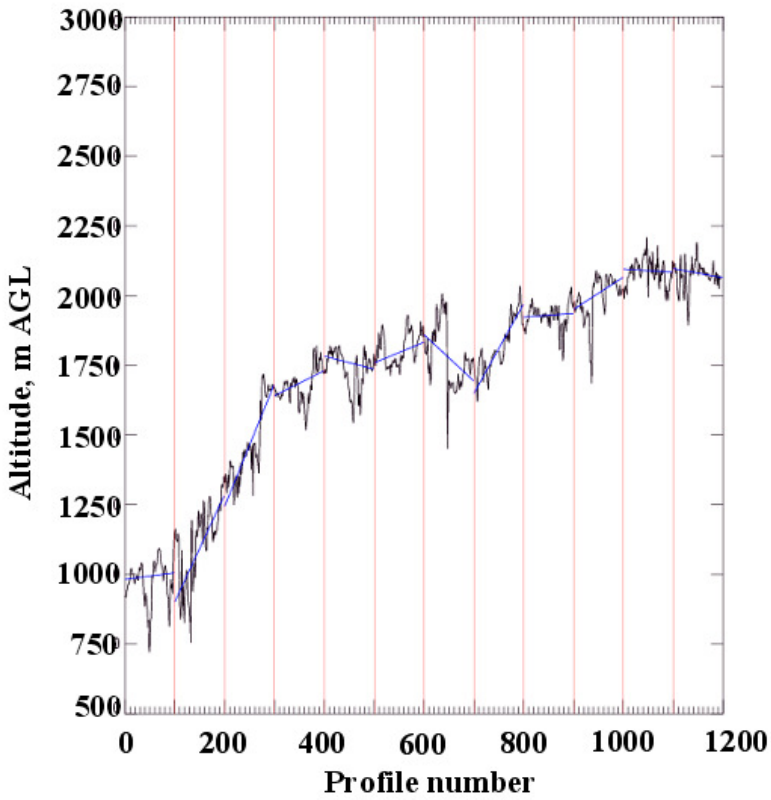

Figure 5.24: Local detrending in DFA algorithm using the CBL height time series obtained on 26 June 2004.

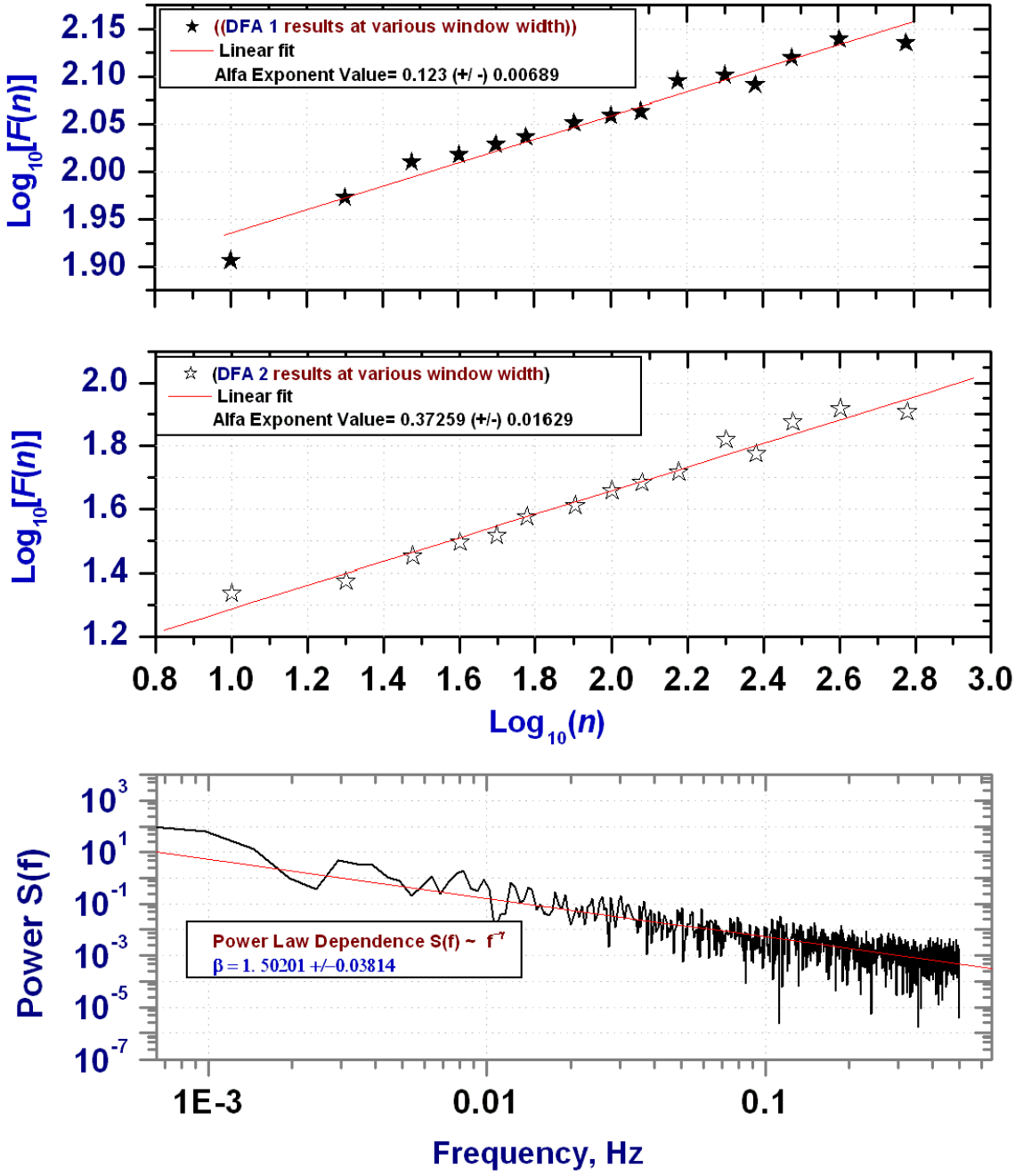

Figure 5.25: DFA results and FFT power spectral analysis. The bottom panel shows the power spectral of the CBL top height data. A spectral exponent value of $\gamma = 1.502$ characterizes the correlations of fluctuations (see, text for further details).

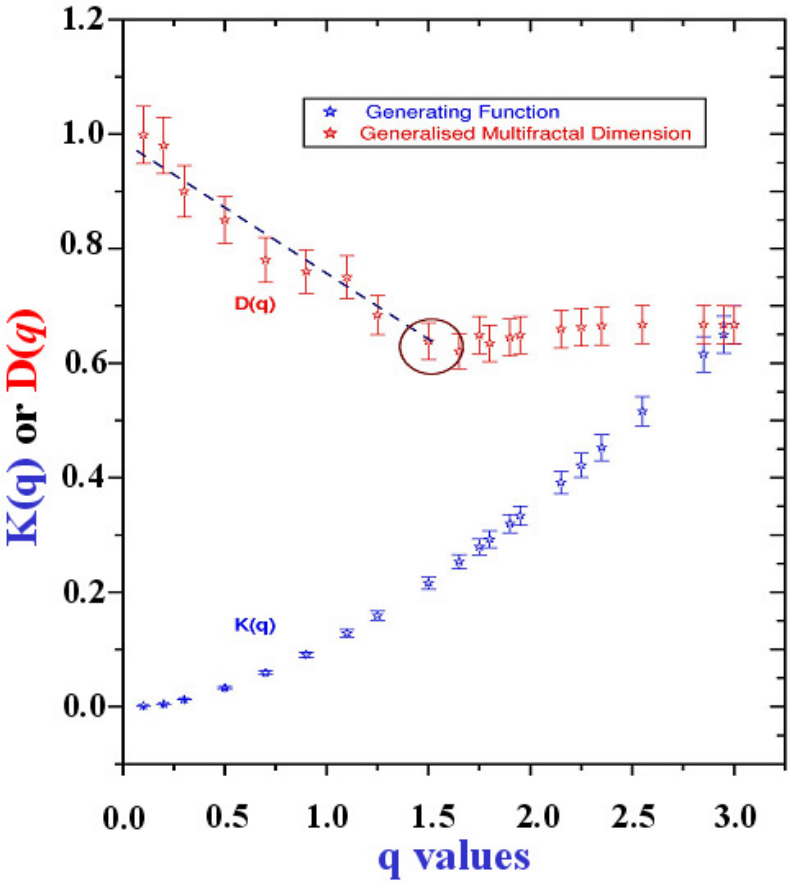

Figure 5.26: Generalized multifractal dimension, $D_m(q)$ and $K(q)$ for the CBL height time series presented in Figure 5.20. Deviation of $D_m(q)$ from the linear dependencies on q values is seen after the dashed line. $K(q)$ function determines the intermittency in the CBL height time series data.

5.3.6 Wave-like activities in the boundary layer

High-resolution lidar observations of wave activities in different atmospheric layers are another key issue in atmospheric science since these measurements can confirm waves with shorter periods. For instance, study of the internal gravity waves is important since they critically influence the energetic and dynamics of the region by momentum transfer (Holton, 1992). *A wave that propagates in density-stratified fluid under the influence of buoyancy forces is called internal gravity wave or internal wave* (Holton, 1992).

In the following section, two different events are described during which wave-like features were observed by the UHOH lidar during measurement period. A similar analysis on the structure and evolution of waves after the application of a high-resolution Doppler lidar can be found in Newsom and Banta (2003) and in Fritts et al. (2003). Both of the studies characterized the wave structures using lidar derived radial velocity field whereas the present work demonstrates the potential of an aerosol lidar system for investigating the wave-structures in a RL. There are different reasons behind the origin of gravity waves: the vertically shifting force induced by the terrain topography (McFarlane, 1987),

convection (Larsen et al., 1982), geostrophic adjustment (Uccellini and Koch, 1987), cold fronts (Gall et al., 1988), wind shear (Lalas and Einaudi, 1976).

Two different approaches were considered to characterize the oscillation observed during the measurement period: first by the conventional FFT analysis and second by the application of Morlet-based wavelet spectral analysis. The results show the existence of gravity waves and features similar to K-H waves.

5.3.6.1 Gravity waves

The UHOH lidar data acquired on 25 June 2004 revealed the atmosphere to possess a rich set of waves. Since the UHOH lidar samples backscattered data with a time resolution of 0.033 s and a spatial resolution of 3 m, relatively rapid phenomena in the atmosphere can be studied. Figure 5.27 reveals such evidence of oscillatory behavior in the particle backscatter field. Lidar data in the figure shows a residual layer with a top height of about 1.7 km, and a bottom height of 1.4 km showing an enormous mixing which is expected to be related to the presence of convectively driven internal gravity waves in the RL.

During evening when the heating of the earth surface by insolation starts to cease, a stable layer forms over the earth surface stopping the turbulence connection between surface and free troposphere. If the wind shear dominates over this stable-stratification, the turbulence may become an episodic event due to mixing and may give rise to some oscillatory behavior in the aerosol layer.

Although these sorts of waves are not generally of great importance for synoptic scale weather forecasting, they can be important in mesoscale motions. They are important mechanisms for transporting energy and momentum to high levels of the atmosphere. Additionally, this case served as an evidence of the appearance of the previous night aerosol layer present at the altitude of 1.6 km. This stayed around this constant altitude throughout the time series with oscillation. Obviously this layer was still present at the same height on the next day (26 June 2004) morning as was presented in section 5.3.2 (case II). Understanding the formation of residual layers above NBL, their evolution in the morning and their interaction with the growing CBL are some of the important components in the development of the more complete representation of aerosol dynamics in a complex valley-like location of Stuttgart city.

In order to better characterize the oscillation observed in the NBL, wavelet-based spectral analysis was applied to the time series of lidar signal intensity at eight equidistant altitudes between 1400 m and 2100 m. The application of wavelet spectral analysis to different altitudes rather than to a single altitude yields the advantage to extract the large amount of information content.

Figure 5.28 shows the scalograms (time/period) of the wavelet coefficient for the range-square-corrected signal intensity along the altitudes mentioned. In this plot each detailed coefficient is plotted

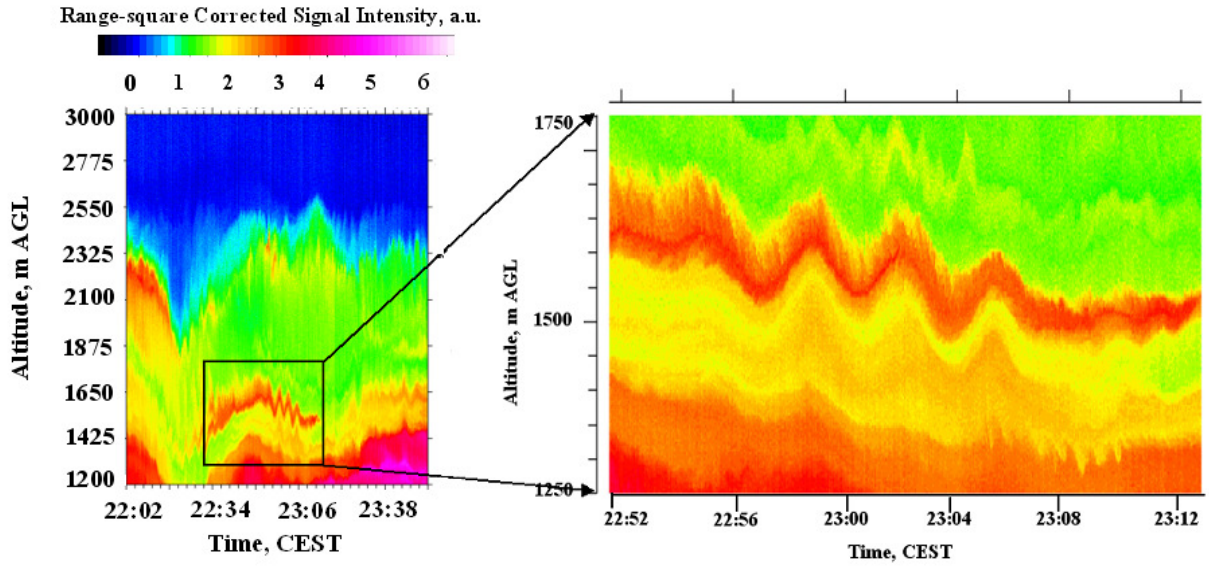

Figure 5.27: One set of UHOH lidar measurement acquired on 25 June 2004 (with time-resolution of 0.33 s) during lidar measurement at Stuttgart downtown revealed the atmosphere to posses a rich set of waves (convective gravity waves) in nocturnal boundary layer in the lidar backscattered intensity field.

as a pixel whose color corresponds to the magnitude of the wavelet coefficient. In addition to the scalograms each panel of the figure contains the time series of the signal amplitude at those altitudes (upper panel), and global wavelet spectral (right panel), which is equivalent to the power spectral from an FFT. Contours are overlaid on each scalogram. Localized wavelet spectrum indicates waves signature with a frequency of 0.0001 Hz. The global wavelet spectrum also shows a peak around this frequency. Figure 5.28 shows that the wavelet decomposed periods were present in all heights but at different times which indicates a propagation of the gravity waves. A defined structure of a frequency of 0.0004 Hz with a maximum around 2250 CEST can be seen in the figure. A weaker peak appeared at 2220 CEST but its period was slightly higher. These frequencies are not unexpected for gravity waves (Fritts et al., 2003).

In this figure, some more structures having frequencies lower than 0.0001 Hz are observed, however the significance of these structures are questionable due to edge effects. Edge effects arise due to finite length of time series. In the present analysis, the time series is padded with sufficient zeroes to bring the total length *N* up to the next-higher power of two, thus limiting the edge effects and speeding up the Fourier transformation during calculation. Padding with zeroes introduces discontinuities at the endpoints and as one goes to larger scales, decreases the amplitude near the edges as more zeroes enter the analysis. Some coherent small-scale structures (ripples) are also visible in the figure. Wavelet spectra at 1500 m AGL show the presence of coherence structure with a scale of 0.0004 Hz but the amplitude of these two structures is different in time. After 2230 CEST, the spectra show higher values of coefficient and evince that same feature is present but with prominent mode.

FFT-based spectral analyses are not able to show the location (in time) of the frequency present in the resultant spectra. Presence of the various frequencies in a time series can be evinced by FFT but

this is not sufficient information to characterize all the structures present. These results suggest that the wavelet spectral analysis is an efficient tool to provide information on the evolution of the different scales or periods that are involved with a wave event. So far, a very few studies have made a detailed investigation of the gravity waves induced aerosol structures by applying a very high-resolution dataset. It is demonstrated here that this sort of wavelet-based approach to a high-resolution lidar data can explore the wave-like phenomenon and their evolution in time. The tempo-spatial lidar data can explore

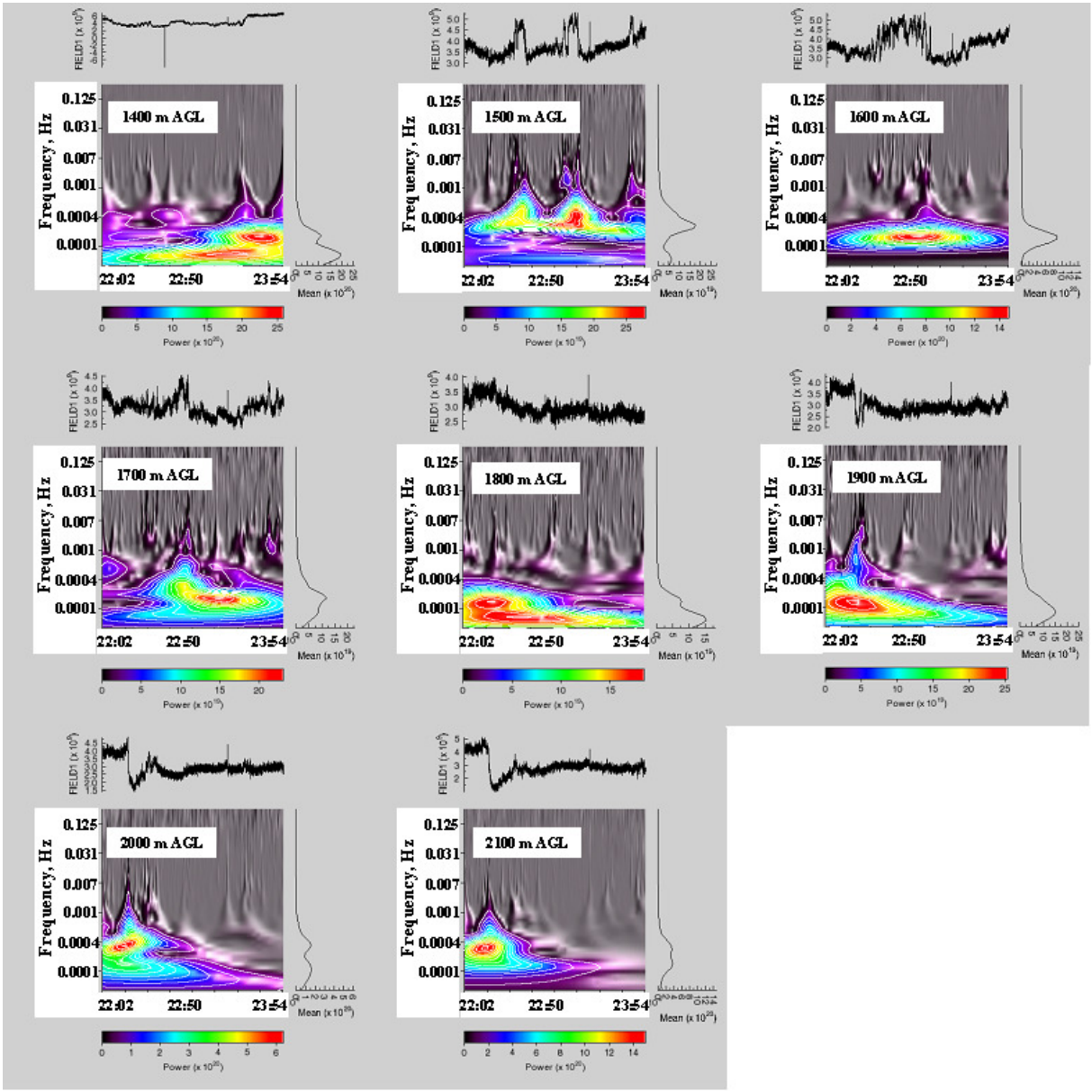

Figure 5.28: A detailed time-frequency representation of the range-square corrected lidar signal intensity at different altitudes AGL confirming different oscillatory structures present above NBL on 25 June 2004 by wavelet analysis. Morlet-based wavelet analysis power spectrum is shown here. Each panel shows the scalogram of lidar signal intensity at a particular height, time series of the signal intensity at that particular altitude together with the mean wavelet power spectra. Color scale increases from violet/black for minimum to red for maximum.

the wave-like phenomena in the RL (if present) and their dynamical mechanisms embedded in the NBL. Distribution of aerosols in the RL has a significant impact on local pollutant budgets at a variety of temporal and spatial scales and can improve the understanding of the structure of the lower troposphere and processes taking place in there.

5.3.6.2 Kelvin-Helmholtz activity

The K-H waves appear in the atmosphere mainly due to the presence of stratified shear flow instability (Fernando, 1991; Scorer, 1997). These waves act to mix across considerably vertical depths (up to around 1km) and dissipate energy. Estimation of this dissipated energy has a significant impact on atmospheric dynamics. Analytical, numerical and laboratory models (Esler and Polvani, 2003) have extensively studied the appearance and breakdown of such activities but it is not clear how these results can be applied to the waves in the real atmosphere.

High-resolution sounding of the CBL with the UHOH lidar revealed K-H structure in the CBL. The UHOH lidar data can be used to estimate the thickness of the K-H billow or the amplitude of these billows and the billow wavelength. During the measurement on 26 June 2004, one set of the UHOH lidar data as shown in Figure 5.29, captured a specific fine structure of the CBL. In an altitude between 1.75 and 2.23 km, displayed in the figure (see, square region in figure 5.29a), a wave-like instability was observed starting to grow at 1610 CEST. This type of activity is an implicative of K-H activity. Kelvin's cat's eye patterns embedded within step-like structures are shown in zoomed-in-view (Figure 5.29b). The K-H wave height (H) in the figure running along a step-like structure was of about 50 m deep. According to Turner (1973) the most probable K-H wavelength is 7.5 H, where H is the depth of the layer. This gives a wavelength of about 400 m, which is not unrealistic for a case of a well-mixed CBL (see, Stull, 1988). The structure started to break around 1624 CEST together with sudden onset of strong turbulence, associated with overturning and breaking of the waves into turbulence.

K-H waves as observed here are class of waves those forms at the top of the CBL along the overshooting thermals (Stull, 1988). The top of the CBL here is well marked by a sharp interface as can be seen from the figure. This figure also shows the breaking of the K-H structures and a rapid dilution of the aerosols in the CBL around 1620 CEST. Thermals were also observed. During such a situation, often rapidly evolving K-H waves are observed (Stull, 1988). The wavelength of the K-H waves implies that the feature might has been triggered by shear instability generated by strong vertical wind shear above the experimental site.

Lidar observations of these types of activities in the CBL may provide at least some qualitative insights into the instability and turbulent mixing processes in the CBL. Collocated radiosonde retrieved horizontal wind profile can reveal some more details of these K-H structures. Nevertheless, the lidar dataset presented exhibits the potential of the UHOH aerosol lidar system to detect the K-H wave activities in the ABL.

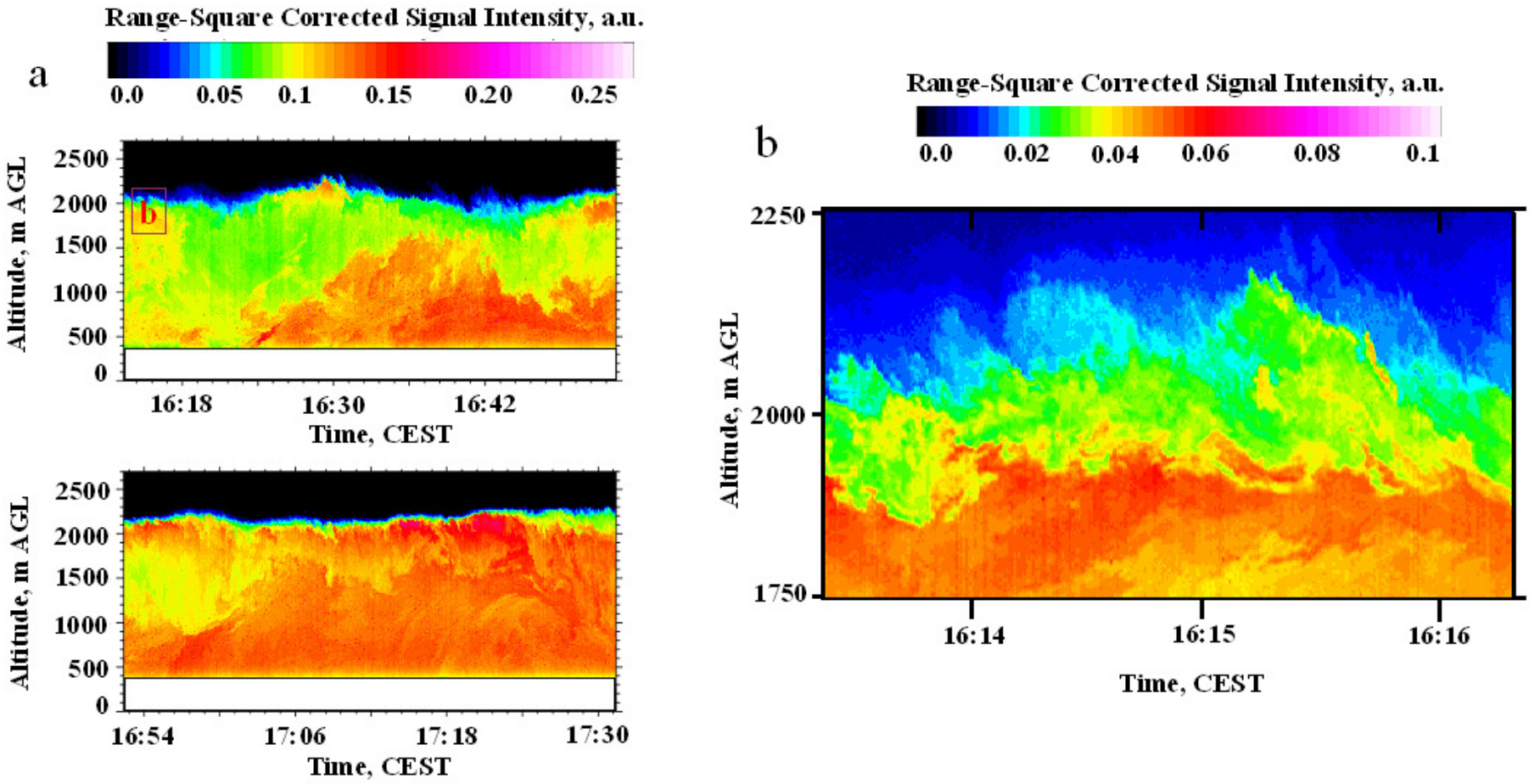

Figure 5.29: (a) Range resolved relative aerosol backscatter intensity (extracted from the data obtained on 26 June 2004) showing the presence of Kelvin-Helmholtz like wave activity in the ABL, (b) zoom-in-view of the K-H waves '(cat's-eye' patterns) extracted from the full time series of the lidar data. Partial overlap region up to of about 400 m AGL is blocked by a white stripe.

5.4 Summary and conclusions

Special emphasis was given to the results from a study of convective boundary layer and its evolution based on a ground-based upward looking lidar system. The results demonstrated that high-resolution lidar measurements could contribute to a clear description of the physical processes, taking place within the CBL, especially that one of the Stuttgart region having a valley-like location. For this study, data with range resolution of 3 m and time resolution of up to 0.033 s were used which were obtained with the UHOH lidar in a vertically pointing mode, using a wavelength of 1064 nm. In this work, the instantaneous CBL height, its growth rate and associated entrainment in the course of sunny days were investigated.

Various complex convective activity patterns were revealed in the analysis both during quasi-stationary CBL (case I) and a rapidly growing CBL (case II). Configuration of the system providing high-tempo-spatial resolution enabled to monitor the small-scale structures in detail. This work studied the variability of the instantaneous CBL height during morning and afternoon and facilitated to calculate the EZT from this variability. The altitudes of the CBL top over the city of Stuttgart were found to be within 1–2.3 km AGL. The aerosol distributions over Stuttgart downtown area during day and night exhibited highly variable aerosol load distributed over complex vertical structures.

A detailed intercomparison of the three advanced techniques (LGM, IP, and HWT) was performed with an aim to select a best suitable approach for the purpose of routine measurements of instantaneous CBL height. An FFT-based analysis also showed same value of spectral exponent ($\gamma = 1.0$). The Haar wavelet-based approach was selected to be suitable for the routine determination of instantaneous CBL height from the UHOH lidar data. During one case when atmosphere encountered a dense aerosol layer, the associated interaction between the RL and the underlying CBL is found to be an indicative of penetrative convection. Appearance of this sort of RL is considered to be due to the trapping of aerosols and other pollutants emitted at night in the valley-like location of Stuttgart city.

Evolution of h_{HWT} through the course of the day was studied. Two different growth rates were observed: a high growth rate of up to 5 m/minute in the morning and another with a very low value of around < 1 m/minute. The instantaneous CBL heights were varied between 0.6 and 1.5 km AGL during the rapid growth while the same were varied between 1.6 and 2.3 km AGL for the other case. The EZT in the morning was lower (62 m) than in the afternoon (75 m) as was confirmed by the results obtained with the cumulative frequency distribution method. Consequently, two different turbulence regimes were observed both inside and at the top of the CBL, as confirmed with the higher-order moments profiles of the aerosol backscatter fluctuations.

FFT power spectra of the instantaneous ABL height showed power-law dependency for the case of rapidly growing boundary layer. The spectral exponent value obtained in the energy spectrum, confirmed the non-stationary behavior. The γ value (1.502 ± 0.08314) obtained in this case does not agree well with that (1.6 ± 0.02) of the findings of Boers et al. (1995). In their case, the investigation of

boundary layer height was confined in a trade-wind cumulus regime. FFT analysis, DFA technique and multifractal analysis were found effective to study the non-stationarity behavior of CBL height evolution and the correlations in their fluctuations. For the selected case during the morning it is demonstrated that the CBL height evolution was a type of non-stationary anti-persistent process. Through this study one can identify the dynamic scaling in a CBL height time series. Nevertheless, these types of time series-based statistical analyses can give rise to a suitable approach for the CBL modeling which is still a challenge in atmospheric science (Pelletier, 1997). These analyses exhibited that the CBL height fluctuations could be characterized by simple statistical parameters like multifractal dimension, and roughness exponent that can be a good basis for the ABL modeling.

To date, for the first time, a high-resolution aerosol lidar measurements explored the benefits of the higher order moments estimation of the aerosol backscatter field identifying different CBL activities. These results show the capability of an aerosol lidar to resolve turbulent processes in a larger portion of the CBL and in the lower troposphere. Profiles of higher-order moments were derived including noise and sampling errors for two different CBL regimes as mentioned before. The accuracy of the measurement was mainly limited by the sampling errors involved due to the turbulent statistics. The variance profile for the quasi-stationary CBL provided well-defined aerosol distributions due to turbulence inside the CBL showing maximum value of the variance at the top of the mean CBL height while for a case during a rapid growth of CBL showed multiple peaks appeared in the vertical distribution of variance.

It was demonstrated that the major part of the inertial subrange was detected and that the integral scale (60-70 s) was significantly larger than the temporal resolution of the lidar system. Consequently, the major part of turbulent fluctuations was resolved. Negative values of skewness were found inside the CBL while positive values were observed in the entrainment zone near the top of the CBL for the quasi-stationary regime. Power spectrum analysis of the aerosol backscatter fluctuations at various heights inside the CBL showed a roll-off according to $f^{-5/3}$-power law which suggests that the inertial subrange was reached. Negative values of skewness were found inside the CBL while positive values were observed in the entrainment zone near the top of the CBL for the quasi-stationary regime. But for the case of a rapidly growing CBL, skewness profile showed a high variability even inside the CBL. Presence of different aerosol layers, a rapid growth of the CBL in the morning, a high non-stationarity make the distributions of the higher-order moments in the CBL rather complicated so that the interpretation of the results not at all was straightforward. A quasi-steady CBL is considered to be an appropriate for the estimation of higher-order moments for characterizing turbulence in the CBL. A detailed comprehensive description could be obtained after an intercomparison of these results with LES model results.

Chapter 6
Application of a scanning eye-safe aerosol lidar for investigating physical characteristics of aerosols emitted from a livestock farm

6.1 Introduction

Livestock farming have been found to be a major source of health-hazardous aerosol particles in the neighborhood around their locations. The transport processes of these aerosols and their distributions strongly depend on variable meteorological conditions, e.g., variability in the prevailing wind, temperature, and relative humidity and are often influenced by the obstacles outside the farm buildings, and physicochemical processes inside the ABL (Lammel et al., 2005).

Several studies have been performed to measure the aerosol source contribution of the livestock farming with various localized point measurement techniques around the facilities. Lammel et al. (2004) studied in detail the constituents of the aerosols emitted from such a facility in southern Germany (Talgut Lindenhof) with data collected from several point measurement techniques directly at the farm, downwind, and in an unaffected background region. Lee and Zhang (2006) studied the monitoring of the ammonia and odor emissions with a cylindrical dynamic chamber. Takai et al. (1998) made field surveys of indoor dust concentrations and dust emissions from various livestock buildings with cattle, poultry etc. Some other studies, which describe similar experiments, can be found elsewhere (Seedorf, 1998; Dong et al., 2007).

The computational fluid dynamics analysis (Bjerg et al., 2004), and numerical studies (Fraigneau et al., 1996) were also applied to problem concerning the emission from livestock facilities. Important results on the types, size distribution, and chemical constituents of the aerosol plumes emitted from such farms were obtained. In some cases the increase of aerosol loading at the downwind sites was observed (e.g., Lammel et al., 2004) yet leaving the optical properties, vertical extent, and transport range of the plume unresolved. Some of them provided the yearly or monthly amount of emission (Dong et al., 2007).

The most significant importance lies in devising effective remediation strategies to the problem of such emissions; these must be based on a comprehensive understanding of the actual phenomena. Application of three-dimensional scanning lidar technology needs to be demonstrated in this regard to provide both qualitative and quantitative description of the aerosol plume from livestock facilities over an extended region of the atmosphere as well as at closer vicinity.

Despite the need to characterize the aerosol emission from livestock farming and availability of the potential of scanning lidar technology, only few lidar studies have been reported to date. Hartung et al. (1998) made an effort in this concern to detect the strength of the aerosol emission from a farm. In their work, they only showed an increase of the lidar signal intensity (a single profile) for the aerosol plume, but they did not report the optical properties of the aerosols. Additionally, the study failed to yield details of aerosol transport by scanning measurement due to the restrictions given by the operation of non-eye-safe lidar. Recently, Prueger et al. (2008) studied the dispersion of the particulate matter outside an animal husbandry by means of eddy covariance towers. Additionally, they supported their findings with scanning elastic lidar measurements characterizing the dynamics of plume. But, they did not report the optical properties of those aerosols. In this concern it is worthwhile to mention that Holmén et al. (1998, 2001a,b) showed promising estimates of the emission factors from agricultural activities as obtained by an application of scanning lidar system.

It became quite clear that standalone application of the lidar technique for the measurements of aerosol optical properties will never be sufficient to investigate the problem of aerosol emission from livestock farms. Synergetic measurements with in-situ instruments and model validation are necessary. Therefore, a novel approach was developed within this work (see, section 6.2 for detailed discussion about the methodology).

To understand the significant importance of the aerosol processes, aerosol microphysical properties, and the impact of the anthropogenic aerosols emitted from livestock farms, a collaborative project (BW-PLUS, Baden-Württemberg Programm Lebensgrundlage Umwelt and ihre Sicherung) between University of Hohenheim and Max Planck Institute of Meteorology, MPI (M) was initiated by the ministry of the environment and transport of Baden Württemberg, Germany. The BW-PLUS field campaign (here after only PLUS1 campaign) was an important part of a project of the BW-PLUS program.

The advanced program BW-PLUS consists of different application oriented environmental research projects, including technical and methodological projects as well as development of instruments for the solution of environmental pollution issues.

The main objective of this work is to address a combination of high-resolved measurements and model simulations of aerosol properties in order to resolve the aerosol source and aerosol transportation on a small spatial and temporal scale. It can then help to achieve the microphysical properties of these anthropogenic aerosols.

The findings of this project work are an essential part of this dissertation. The key research issues which have been addressed in this chapter deal with:

- State of the research performed so far to detect the aerosol plume of a livestock facility, pointing at the gaps in those studies and proposing new approaches considered to close these gaps.
- Benefit of scanning lidar in the UV wavelength to quantify the optical properties of aerosol particles emitted from livestock farms.
- How do the physical/optical properties of the plume of the exhaust air from the farm change? What are the mechanisms involved?
- How important are the lidar scan strategies to capture the plume to understand the dynamics and evolution of aerosol properties close to a source? What is the instantaneous state of the aerosol structures at different distances from the source?
- Comparison with the lidar retrieved results with the results obtained from LES experiment. What are the advantages of the combination of lidar results, model results and in-situ measurements?

The computational tools of the LES model being extended to include aerosol optical properties (LES-AOP) were developed by Valdebenito (2008) in MPI (M) as a part of his doctoral thesis.

6.2 Methodology

The aerosol properties close to the source region change rapidly due to multitude of processes, e.g., diffusion, condensation, aggregation, chemical reactions, and deposition. As the number concentration, mass, particle phase, degree of mixing, and composition of the aerosol particles changes, eventually the PSD will be affected.

Physicochemical properties as well as climate and air pollution related characteristics of aerosols are pursued here with a new scheme: two or three-dimensional measurements and modeling of physical and chemical properties of aerosol particles. This was done with: (a) high-resolution measurements of aerosol optical properties by the UHOH scanning aerosol lidar system, (b) in-situ point measurements for the characterization of physical and chemical properties of aerosols surrounding source, and (c) a high-resolving atmosphere-microphysics-chemistry model. Figure 6.1 shows a schematic of the methodology to study the aerosol processes in concern. These processes include: changes of aerosol optical properties at close range of the source as well as at far ranges, wind driven aerosol transport in the neighborhood, and turbulence in the aerosol structures and associated lifting of the plume.

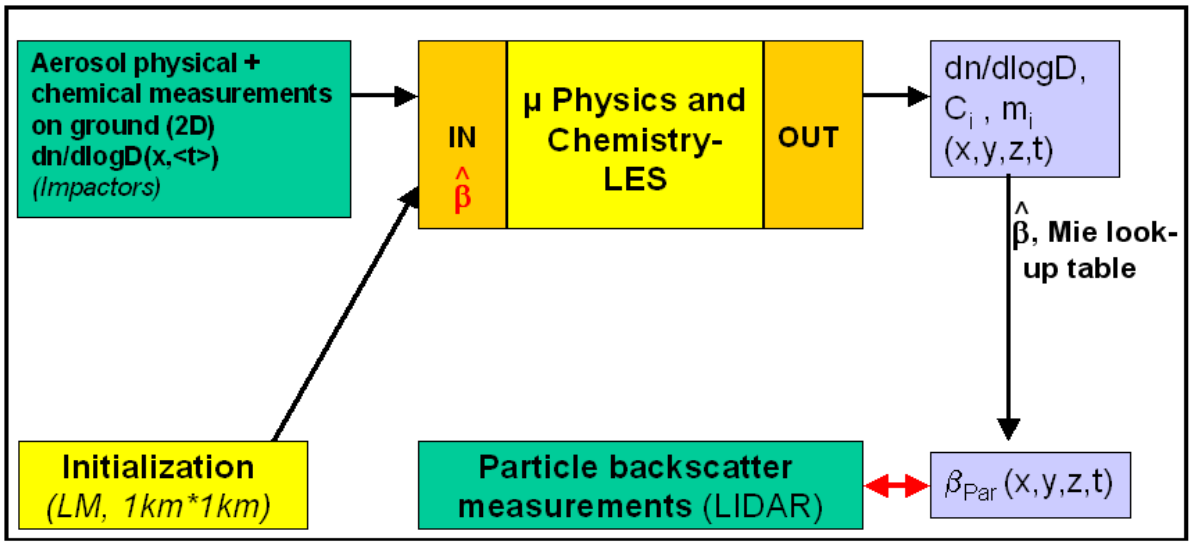

Figure 6.1: Schematic representation of the layout for investigating aerosol optical properties and mixing processes using new scanning high-resolution aerosol lidar system of UHOH and the high-resolving atmosphere-microphysics-chemistry model. For further details, see text.

Investigation of the aerosol mixing processes with this novel approach consists of the following steps (see, Figure 6.1):

1. **Initialization of the PSD:** On the basis of in-situ (e.g., impactor) field measurements of aerosol particles near the source, the LES-AOP produces a discretized size distribution of aerosol particles in 3-dimension for the model grid.
2. **Time evolution of the PSD:** Simulation of the microphysical processes in 3-dimensions (performed by the basic structure model)
3. **Aerosol optical properties:** Computation of the particle backscatter and extinction coefficient for each time step and grid point from the particle size distribution and the complex refractive index for different aerosol types.
4. **Intercomparison:** The common result, which is deliverable both from scanning lidar and LES-AOP, is the 2-dimensional field of optical properties of the aerosol plume. 2-dimensional fields of particle backscatter coefficients from the UHOH scanning lidar measurements are produced. A direct intercomparison is performed between the lidar measurements and the results obtained from LES-AOP simulations.

Aerosol processes are complex close to the source which will affect the distribution and composition of aerosols and consequently their optical properties (e.g., particle backscatter and extinction coefficients). Initialization and forcing for the model is derived from ground-based in-situ measurements of the precise size distribution and composition of aerosol particles. Local model output of the German weather service provides the meteorological variables for the initial state of the model.

In summary, a consistent description of the aerosol emission as well as its optical properties and thereafter better prediction of the aerosol characteristics in the vicinity of the livestock farm are aimed at. The model, once validated with the lidar measurements through performing a one-to-one

intercomparison, can be used to predict the optical properties and transport processes of the aerosols emitted from the livestock farms. Later, applications of this method can focus on the aerosol emissions from different livestock farms of various animal species.

The methodology developed is novel and unique for its attractive features and the important elements within. For instance, an eye-safe scanning aerosol lidar is an appropriate technology to this problem and therefore was explored during the PLUS1 campaign. Demonstration of the UHOH scanning aerosol lidar including its suitability to determine the optical properties of these aerosol particles was performed. Recognition of lidar relative (only) backscatter intensity and of the turbulence structure in the ABL is straightforward. Comparisons with LES results were previously performed by Mayor et al. (2003). Due to the presence of complicated and rapid aerosol processes near the source and close to the ground, the simulation of the optical properties of these particles becomes more challenging. Simultaneously, the lidar should be able to retrieve high-resolved two-three dimensional distributions of the aerosol optical properties instead of relative signal intensity if one is aiming at the accurate simulation and measurements of the aerosol optical properties together with the turbulent flow features. Furthermore, the LES-AOP model employs a more detailed description of the PSD and aerosol composition, which allows estimating the absolute value of the particle backscattering coefficient.

6.3 PLUS1 field campaign

The PLUS1 campaign was the first field deployment of the UHOH scanning aerosol lidar. The campaign took place during 11-21 September 2005 in close vicinity to a livestock farm. The farm is located in Mettingen (52°19.44´ N; 7°8.8´ E; 56 m ASL), Westphalia. The farm was selected for being located on a particularly flat terrain in northern Germany. It was an actively ventilated pig house hosting 1800 animals.

Lidar data were collected with high spatial and temporal resolution every day from morning to the early evening with the only exception of prohibitive weather condition arising from showers.

6.3.1 Selection and design of the experimental location

To understand complex processes close to the source and accomplish all their influences correctly in a LES model, a homogeneous terrain is always a better choice and so was in the case for PLUS1 campaign.

Both the deployments of the sensors for measuring aerosol properties in up wind and down wind, and the UHOH lidar scan strategies were optimized for the combination of experimental results and newly developed LES model results. The topography of the region as presented in Figure 6.2 shows

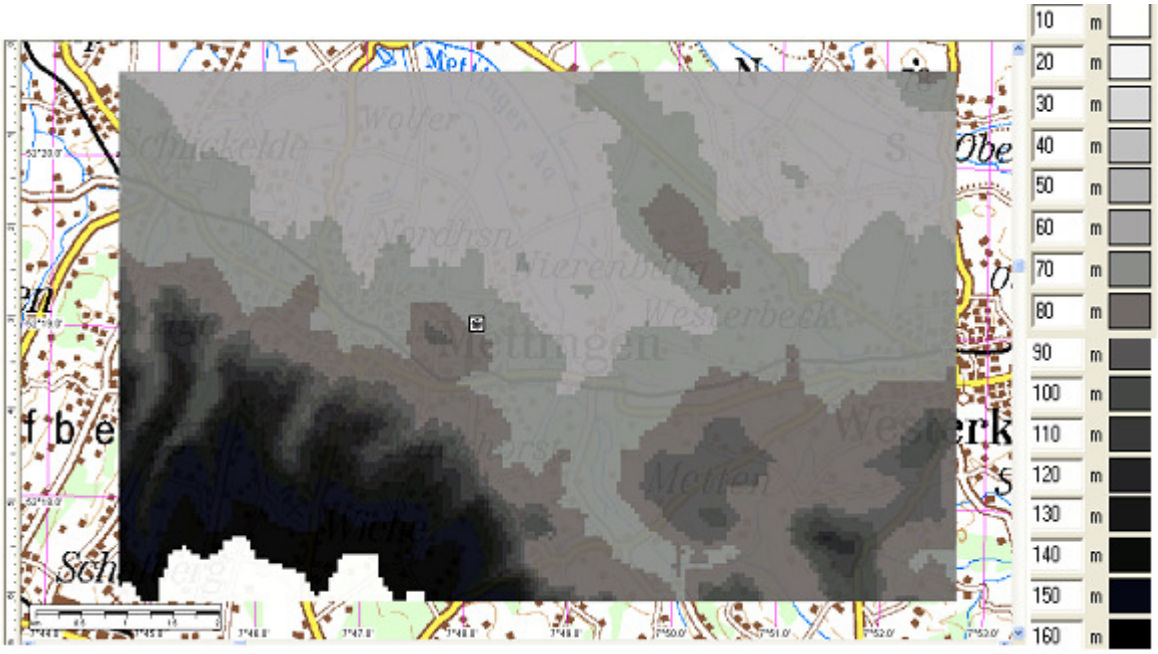

Figure 6.2: Topography of the measurement site showing the elevation variation (m, ASL) around the region of Mettingen with UHOH lidar site (square box). Source of the image: Top200 Viewer, © Geogrid-Viewer version 1.1.

the flatness of the experimental area while Figure 6.3 is an aerial view of the farm and its surrounding region.

In-situ sensors were placed in the field as shown in Figure 6.3 to investigate the transport and conversion processes (near the ground) of the emitted aerosols. The selection of the livestock farm in this location provided for several advantages to meet the goals of the BW-PLUS project. The major advantages are the following:

- large number of animals in the farm representing a source for particulate and gases.
- the farm building was large enough (25 m x 60m) to serve as a source of aerosol plume.
- the farm building was ventilated actively from one of the two chimneys (separated by of about 30m from each other) with output of 9 ± 2 m^3/s. Thus aerosol emission is in the order of magnitude of 100 g/h (related to PM_{10}; IIASA, 2001).
- no other similar sort of farms in the vicinity.
- flat terrain and observable from many sites together with good accessibility and working area.

The choice of the flat terrain arises due to the inherent limitations of the LES-AOP as to its incapability of mapping/simulating the aerosol flow regime in a complex topographical region. Measurements obtained during the nighttime and full cloud coverage were not suitable for the LES run. Furthermore, lidar measurements of aerosol flow over a flat terrain are more convenient than over a complex terrain due to the absence of orographical influence on the aerosol structures and transport so that the lidar results can be better interpreted. Therefore, episodes of dry and sunny weather conditions were selected aiming at predominantly occurring air mass mixing. As the chances are that water vapor

condensation takes place on the optics, the UHOH scanning lidar system was not operated in the evening and at night.

A detailed description of the UHOH scanning aerosol lidar system is found in section 3.2. The scan patterns were within the full hemisphere with the exception of the region around the sun for protecting the detector (a photomultiplier tube, PMT). Scan strategies were applied during PLUS1 campaign following the particular sun chart (available at http://cgi.stadtklima-stuttgart.de/mirror/sonnefre.exe) of the individual days. Such an example of the sun chart is shown in Figure 6.4.

The ground distance between the farm and lidar was 480 m as shown in Figure 6.3 and the farm was situated at an azimuth of 193.5°, measured from the geographical north. The outlet of the farm chimney is just 5-6 m higher compared to the horizontal lidar beam plane. There was a manure storage chamber in the close proximity of the building but was covered by a crust of dry material.

A hard target calibration of the scanner was performed at the beginning of the PLUS1 field campaign in order to adjust the scanner alignment so that lidar signal can be stored with correct spatial information with respect to the geographical location of the system (calculated from the elevation angle above the horizon and the azimuth angle measured from geographical north). Lidar signals from two chimneys of a power plant at a distance of about 6.4 km (Figure 6.5) were used for this purpose.

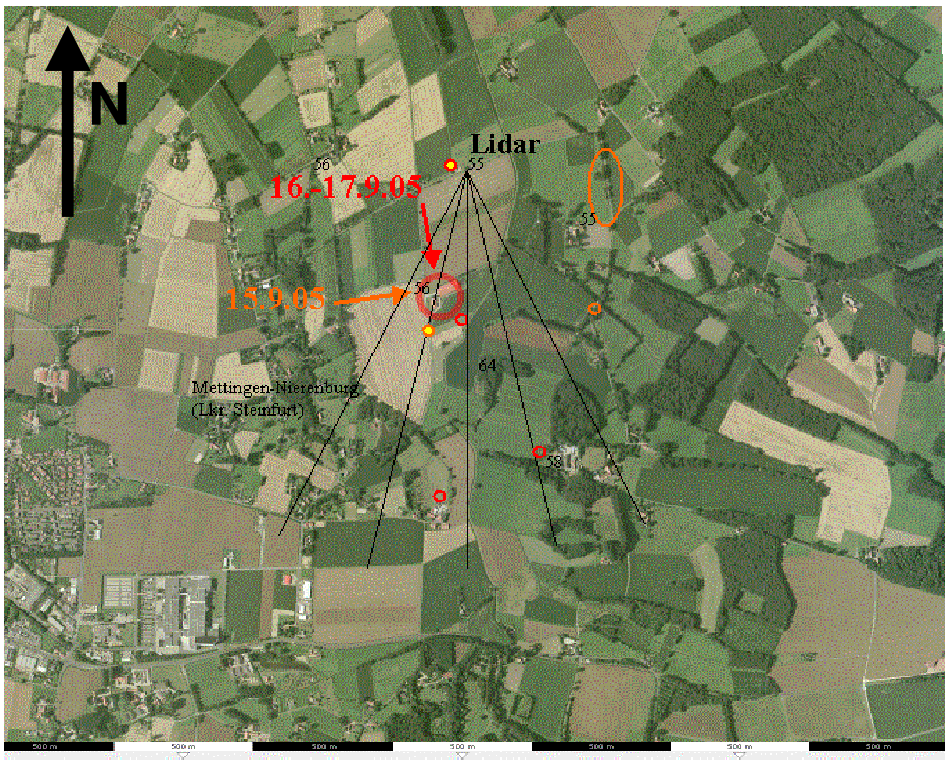

Figure 6.3: Wind directions (red arrow) and field experiment configuration with locations of the farm (large circle), the UHOH lidar system and sampling locations (upwind: yellow, downwind: red and orange) during measurement period in September 2005, close to Mettingen. The black radii denote a PPI sector scan performed with the lidar system. Source of the satellite picture: © GeoContent.

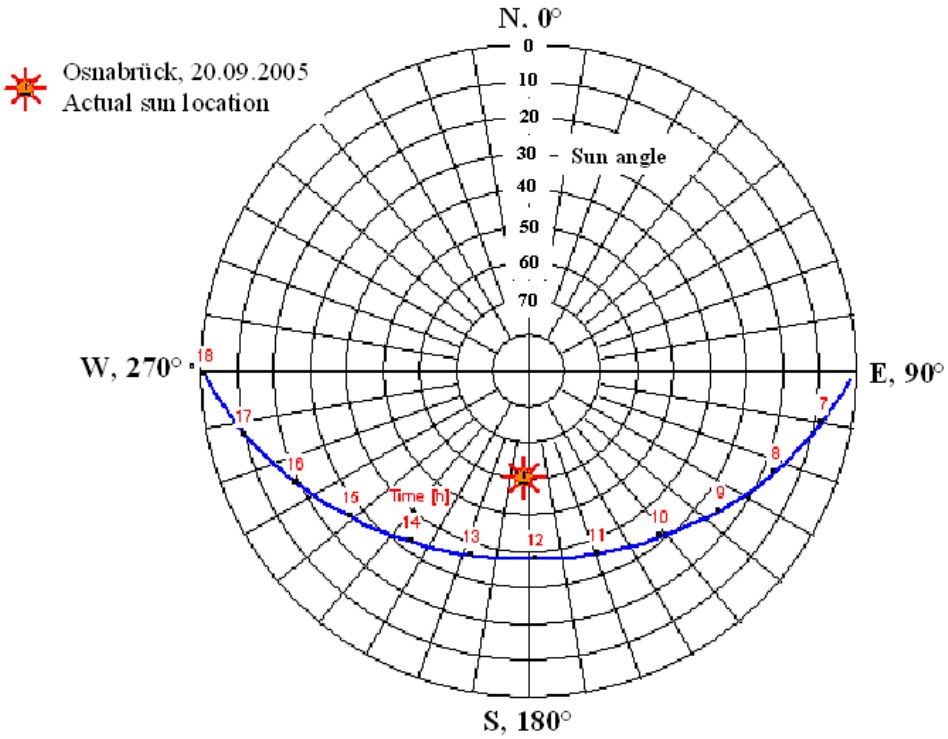

Figure 6.4: Elevation of the sun on 20 September 2005 on Osnabrück during the course of the day. Circles indicate the elevation and radial lines from the center of the plot the azimuth angle of the sun, respectively. Source of the chart: © (http://cgi.stadtklima-stuttgart.de/mirror/sonnefre.exe).

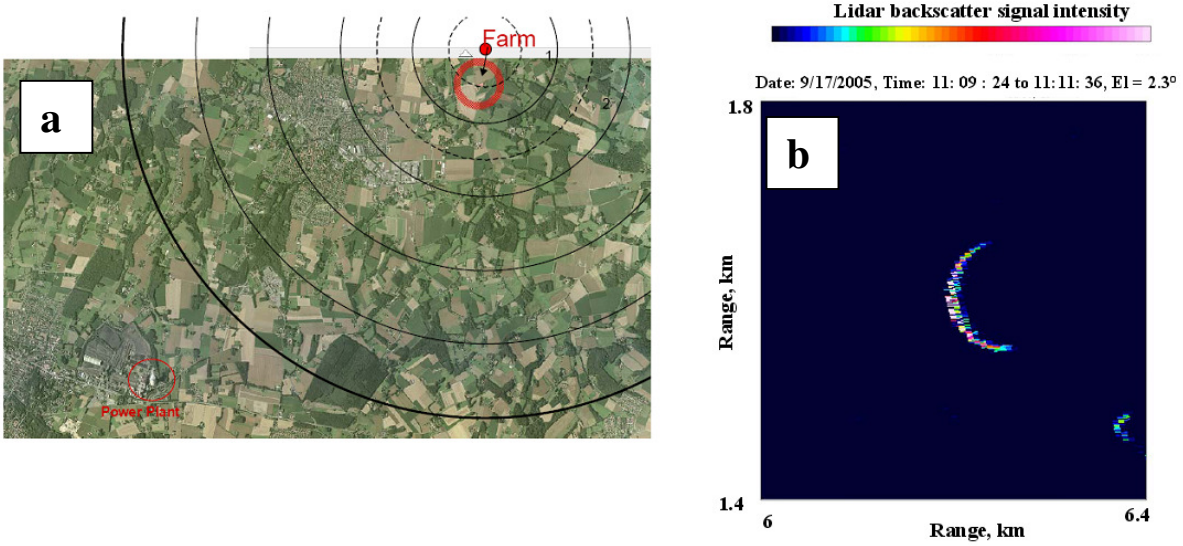

Figure 6.5: (a) Location of the power plant at Ibbenbueren together with the lidar near the livestock farm at Mettingen as a circle. (b) Calibration of the lidar alignment with hard-target measurement. This plot displays the extract of a PPI scanning measurement on 17 September 2005. PPI volume scan was performed at scan rate of 0.1° s^{-1} between azimuth angles of 73° and 79° within the elevation angle between 2° and 4° with an elevation step of 0.1°. One selected example PPI scan image is shown here. This yields time resolution of 0.033 s, range resolution of 3m and angular resolution of 0.003°. This image shows the lidar signature of the power plant chimney at a distance of 6.4 km from lidar. Source of the satellite image: © GeoContent.

The locations of the Chimneys were collected by a GPS receiver. The alignment of the lidar scanner was performed with an accuracy of better than 1 mrad. The range resolution of each lidar profile is 3 m; the azimuth-angle resolution is very high with only 0.0033° between consecutive

profiles. The backscatter signals of each laser shot emitted with a laser repetition rate of 30 Hz were recorded. Furthermore, this calibration demonstrates the high performance of the new lidar scanner, which combines high angular resolution with high stability.

6.3.2 Overview of the instruments deployed

In the presence of favorable weather conditions during the PLUS1 field campaign, different aerosol in-situ measurements were performed to characterize the source contribution of the livestock farm and the distribution and transport processes of aerosol plume in downwind. Furthermore, 8 meteorological radio soundings (Väisälä RS-92) were launched at different times of the day during the campaign. The radiosonde profiles of relative humidity and temperature are briefly discussed. In-situ aerosol and trace gas measurement instruments include the following:

- Trace gases samplers; $PM_{2.5}$ and PM_{10} filters.
- Optical Particle Counter (OPC), GRIMM 1108; 15 channels for aerodynamic diameter > 0.23 μm.
- Five stage mini cascade impactor; deposition of aerosol particles on platform covered electron microscopical grids for later laboratory analyses.

Results obtained from above instruments were directly or indirectly provided detailed qualitative and/or quantitative information to the LES-AOP model confirming the PSD, aerosol number density in downwind, aerosol constituents and properties.

6.3.3 Meteorological condition

During the PLUS1 campaign, air masses in two different synoptic situations were observed. The general situation is shown in the DWD (German weather service) surface chart in Figure 6.6. From 12-15 September 2005, contaminated air advected from west, under low pressure system “Takashi”, and from 16–20 September 2005, a maritime background air advected from north, dry and sunny under high-pressure system “Katja”. Radio-soundings during the campaign showed this fact confirming a difference in the humidity of the two air masses as shown in Table 6.1.

During the second situation, a strong upper level westerly current with wind velocities larger than 25 m s^{-1} passed over Europe (Figure 6.7). In this region, the main temperature contrast occurred between the air of arctic origin in the north and subtropical air in the south. At the southern edge of the current, a cyclonic vortex was formed which did not affect the weather in Central Europe. Within the next few days, the pressure in the middle troposphere over the Eastern Atlantic rose up. Thus the strong upper level westerly current and therefore the tracks of the following low-pressure systems were shifted to the north. Due to the strong upper tropospheric circulation the low "Takashi” moved rapidly eastward. It crossed Germany and continued eastward to Russia. Its surface front crossed Germany

from north to south during 16 September 2005. While ahead of the front, temperature over 20 °C was observed, it was significantly cooler behind the front with 10-15 °C.

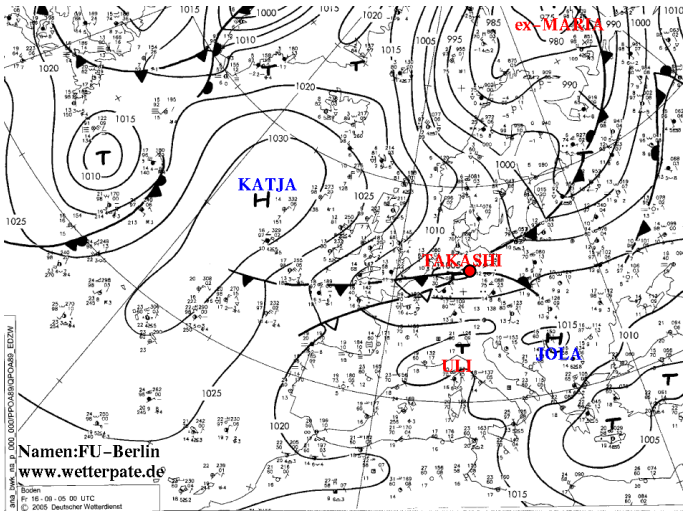

Figure 6.6: Surface chart showing the weather situation on 16 September 2005 at 00 UTC: replacement of cyclonic by anti-cyclonic influence ('Takashi' and 'Katja', respectively). Experimental location is marked by red circle on the image. Source: Freie Universität Berlin (2005).

Table 6.1: Results and observations of radio sonde launches during the intensive measurement period, 15-17 September 2005, in Mettingen (a.) near the ground (60 m height) and (b.) in 1000 m above ground.

a.

Start time (Date, UTC)	Pressure (hPa)	Temperature (°C)	Relative Humidity (%)	Wind-Direction (°)	Wind speed (m s^{-1})
15.9.05, 0906	1010.0	18.5	73	186	0.6
15.9.05, 1150	1008.5	18.0	72	290	2.3
15.9.05, 1412	1006.3	17.0	76	260	1.1
16.9.05, 1143	1002.4	14.5	61	290	2.9
16.9.05, 1510	1003.4	12.9	72	360	2.7
17.9.05, 0729	1013.2	9.8	75	260	1.4
17.9.05, 1141	1014.5	14.4	50	320	2.3
17.9.05, 1454	1015.0	13.3	63	290	2.0

b.

Start time (Date, UTC)	Pressure (hPa)	Temperature (°C)	Relative Humidity (%)	Wind-Direction (°)	Wind speed (m s^{-1})
15.9.05, 0906	895.9	8.9	96	272	14.7
15.9.05, 1150	895.0	10.1	84	269	13.6
15.9.05, 1412	892.9	9.2	97	281	13.6
16.9.05, 1143	888.1	4.6	73	344	10.7
16.9.05, 1510	888.7	4.7	79	349	12.9
17.9.05, 0729	896.6	3.0	75	344	7.0
17.9.05, 1141	898.5	3.8	89	327	4.6
17.9.05, 1454	899.3	4.6	79	340	4.4

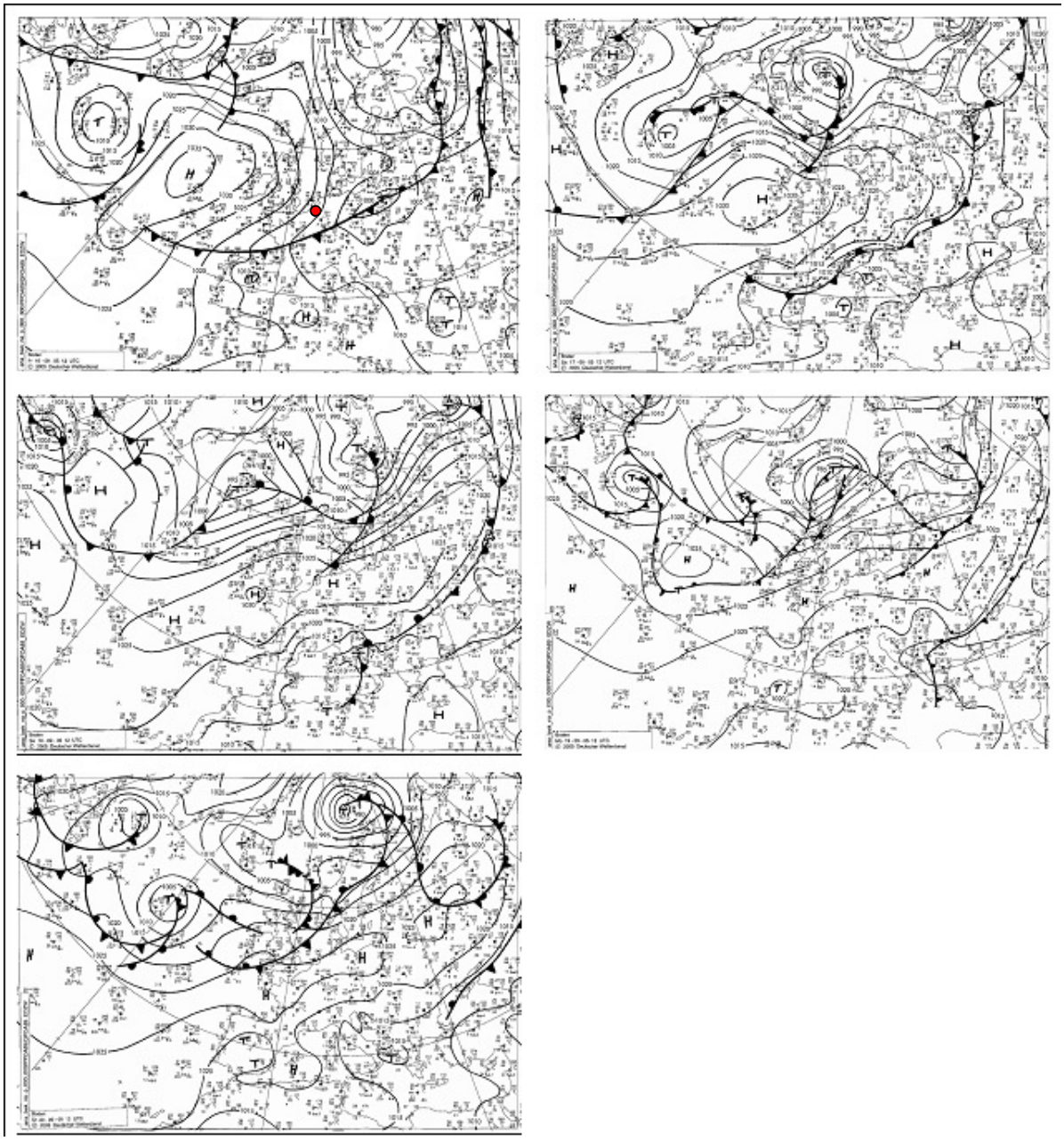

Figure 6.7: Surface chart obtained from the Deutscher Wetterdienst (DWD) from 16 to 20 September 2005 (from top left to bottom left) at 1200 UTC (in each case). Experimental location is marked by red circle on the image (top-left). Source: Freie Universität Berlin (2005).

Within the next few days, cooler air dominated in Germany. With increasing surface pressure a high-pressure zone with warm and sunny days and cool nights developed over Central Europe. Northeastern Germany was influenced by disturbances passing west to east over southern Scandinavia. They pushed low-level clouds from the Baltic Sea inland. In northwest Germany sunny conditions warmed up the incorporated cool maritime air up to 15-16 °C on 17 September 2005. At the night it became cold with lowest values slightly over the freezing point and ground frost occurred at some places. During the night to 18 September it again remained clear in many places in the range of the high-pressure zone. The high "Katja" reached the Baltic States with a core pressure of 1030 hPa. A

further high-pressure cell 'Lilo' formed over southwest England. In the core region of this elongated high-pressure zone it was again usually clear during the night to 19 September 2005. However it did not cool down as much as during the previous nights, since mild and humid air from the North Sea replaced the existing air of polar origin. The low-level Stratus cloud deck that swiped into north Germany from the Baltic Sea led to high temperature contrasts between the cloudy and cloud free areas both during the day and at night. The general weather situation did not change substantially during the next days, so that in Central Europe the anti-cyclonic weather persisted. This is true although the center of the high-pressure system is shifted to Eastern Europe.

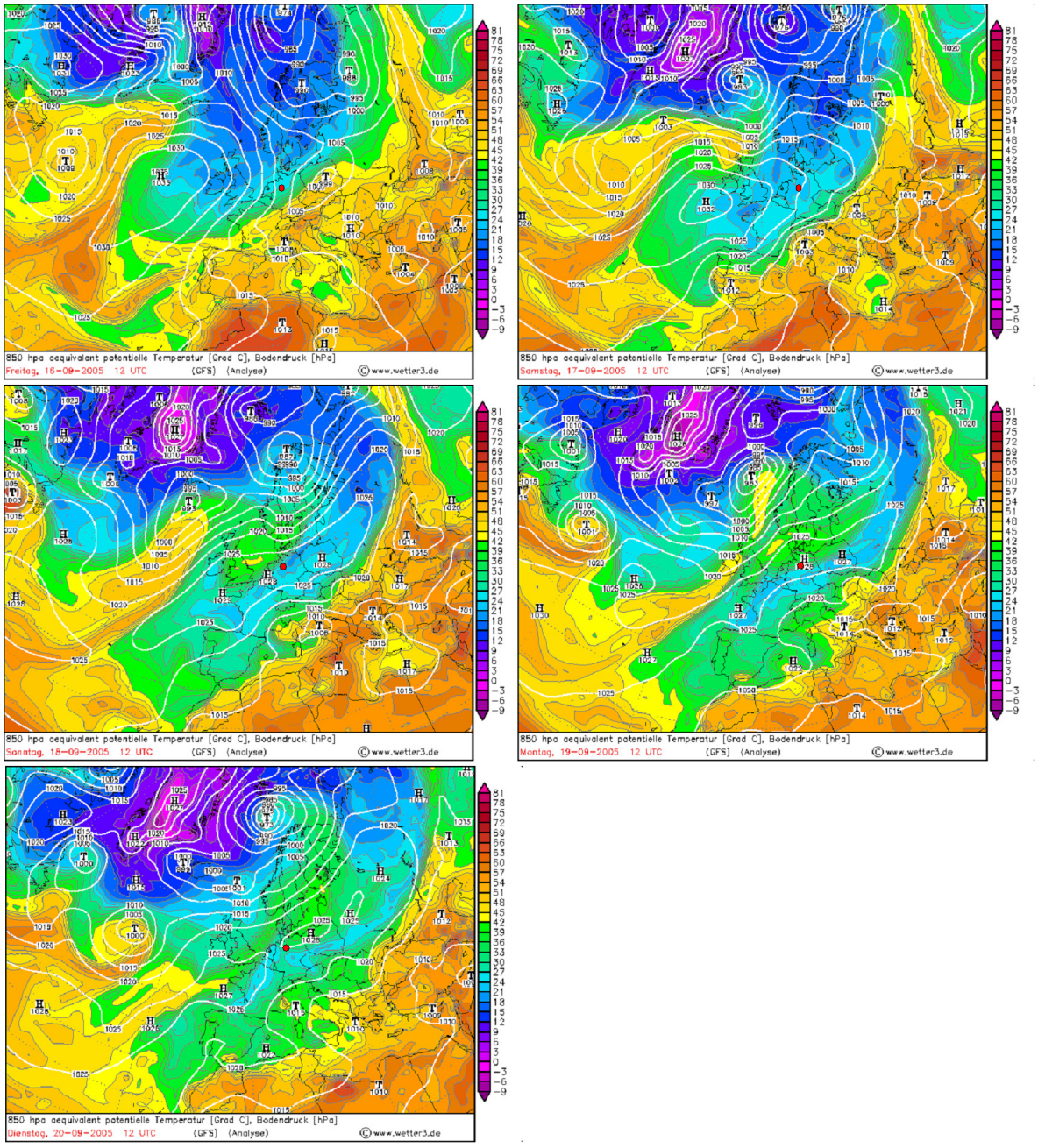

Figure 6.8: Field of equivalent potential temperature (in °C) at 850 hPa obtained from GFS 12 UTC analysis. Source: ©www.wetter3.de.

Figure 6.8 shows the field of equivalent potential temperature at 850-hPa level at 1200 UTC from 16-20 September 2005 (from top left to bottom left) obtained with the GFS analysis (available at http://www2.wetter3.de/Archiv/GFS/). Geopotential heights at the same level are also shown as contour on each panel. The region of the experimental area is marked by red circle. The cold front is well observed in the equivalent potential temperature field on 16 September (top left) arriving to northern Germany. A ridge extending from Southwest Europe to northeast as seen from 12 UTC analyses for 17 September influenced middle European region. In the following days, the whole middle European region was under the influence of a high-pressure system. In all the images, an arctic cold and dry air mass is observed (marked by the blue color on each image). In the south of this, a typical aged warm air mass (marked by green) was observed. During these days, wind was rather weak and was mainly flowing from north (not shown here).

Evolution of wind field at 10 m height at an interval of 6 hour (00, 06, 12, and 18 UTC, from top left to bottom right, respectively) on 20 September 2005 is shown in Figure 6.9. Wind direction over the experimental area on this day changed from southerly to northerly.

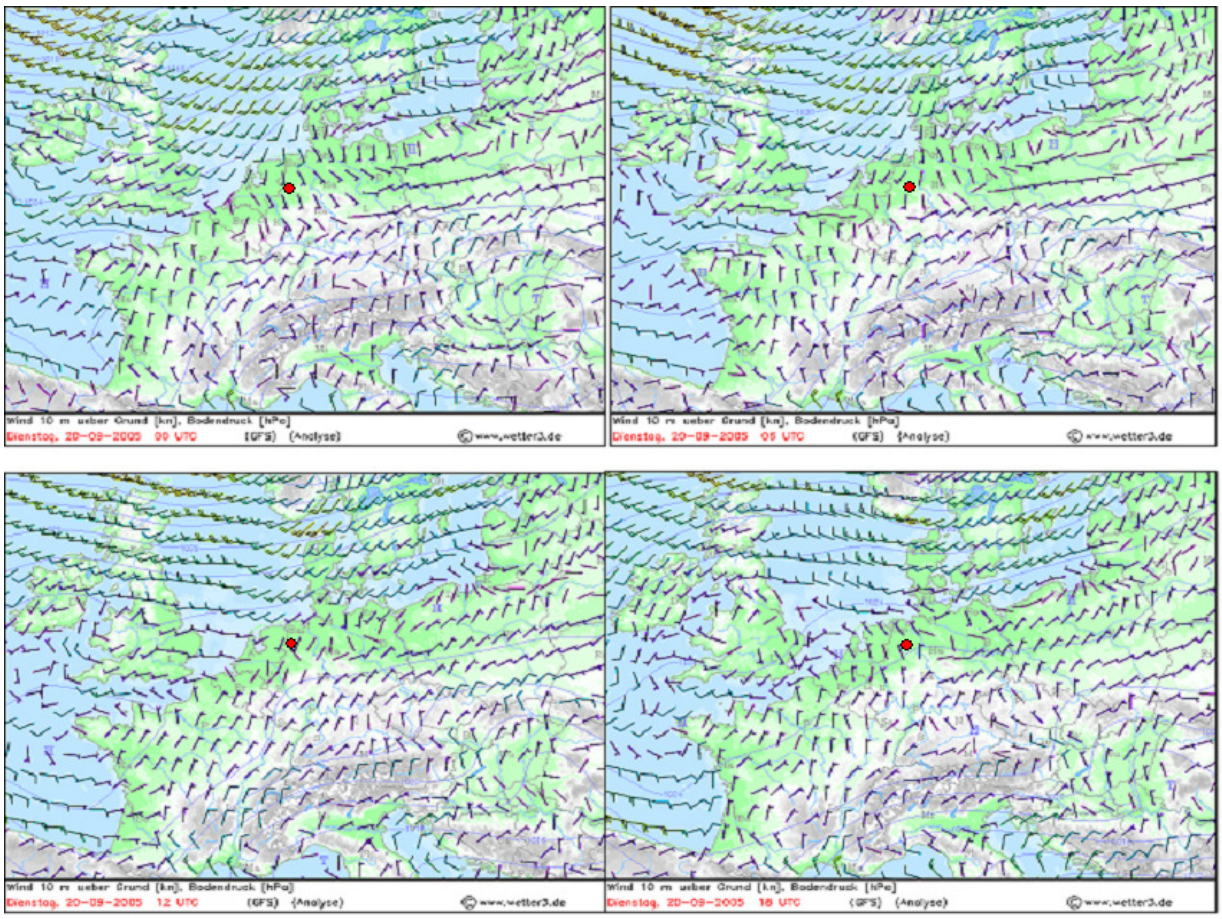

Figure 6.9: Wind field observed by the GFS analysis on 20 September from 00 UTC to 18 UTC (from top left to bottom right). Source: ©www.wetter3.de.

A strong contrast in the aerosol characteristics obtained with the in-situ measurements at ground was found during the two different meteorological situations during the campaign. The upwind particle mass concentration decreased from 120-220 gm^{-3} to 25-40 gm^{-3}, and the sea-salt increased strongly while the secondary aerosols decreased drastically (NH_4NO_3 and $(NH_4)_2SO_4$). The particle number concentration decreased from 160 cm^{-3} to 4–5 cm^{-3} (0.3 – 1 µm) and from 1.4 cm^{-3} to 0.4 cm^{-3} (> 1 µm). The background air was less polluted (e.g., < 10 ng m^{-3} of Pb compared with 10-25 ng m^{-3}). A high nitric acid concentration in the farm plume (4.5 ppb) in the afternoon of 16 September 2005 might indicate an upwind source of NO_x pollution. These experimental results are more detailed in Valdebenito (2008).

6.4 Results and discussion

6.4.1 High-resolution scans of smoke plume

With the aid of vertical scanning measurements, a 2-d image of the relative strength of aerosols can be produced from the individual lidar line-of-sight (LOS) signals. Figure 6.10 demonstrates the extremely high range and time resolution of the backscatter measurements of the UHOH scanning lidar. These data were collected on 19 September 2005, from 1740 to 1750 UTC. The RHI scans were obtained between the elevation angles of 2° and 20° towards north-west (azimuth of about 318°) from lidar system with a scan speed of 0.5° s^{-1} (recording time of 36 s for each scan). Range resolution is maximum with 3 m and so is the temporal resolution with 0.033 s, and angular resolution is 0.015° (in elevation). This figure displays total 9 sequential RHI scans of range-square-corrected backscatter signal intensity of a smoke plume, originating from the biomass burning near the lidar site at ground which was made by the local people for some agricultural waste removal purposes.

In all RHI panels, red to pink color shaded regions represent high signal intensities due to the plume being corrected for background and range-square dependencies. Plume motions and vertical extent both become visible from this sequence. This Figure shows that the dust plume extends in the ranges of 360-480 m and rises at heights between 10 and 40 m.

It is noteworthy, that the range of elevation angles, which were performed during the scan, was even larger than what would have been necessary to cover the size of the detected aerosol smoke streamer. Hiscox et al. (2006) made a quantitative study of the plume dispersion parameters with the use of high-resolution lidar scan images of smoke plume. They used RHI scan images of a plume to measure vertical dispersion parameters and vertical meander of the plume centerline. Future research can be planned for the application of this technique to UHOH lidar measurements to study dispersion. This may be performed by estimating the width, actual spread, and the vertical extent of the plume. Different dispersion models (e.g., Venkatram, 1988) can be used for intercomparison and validation.

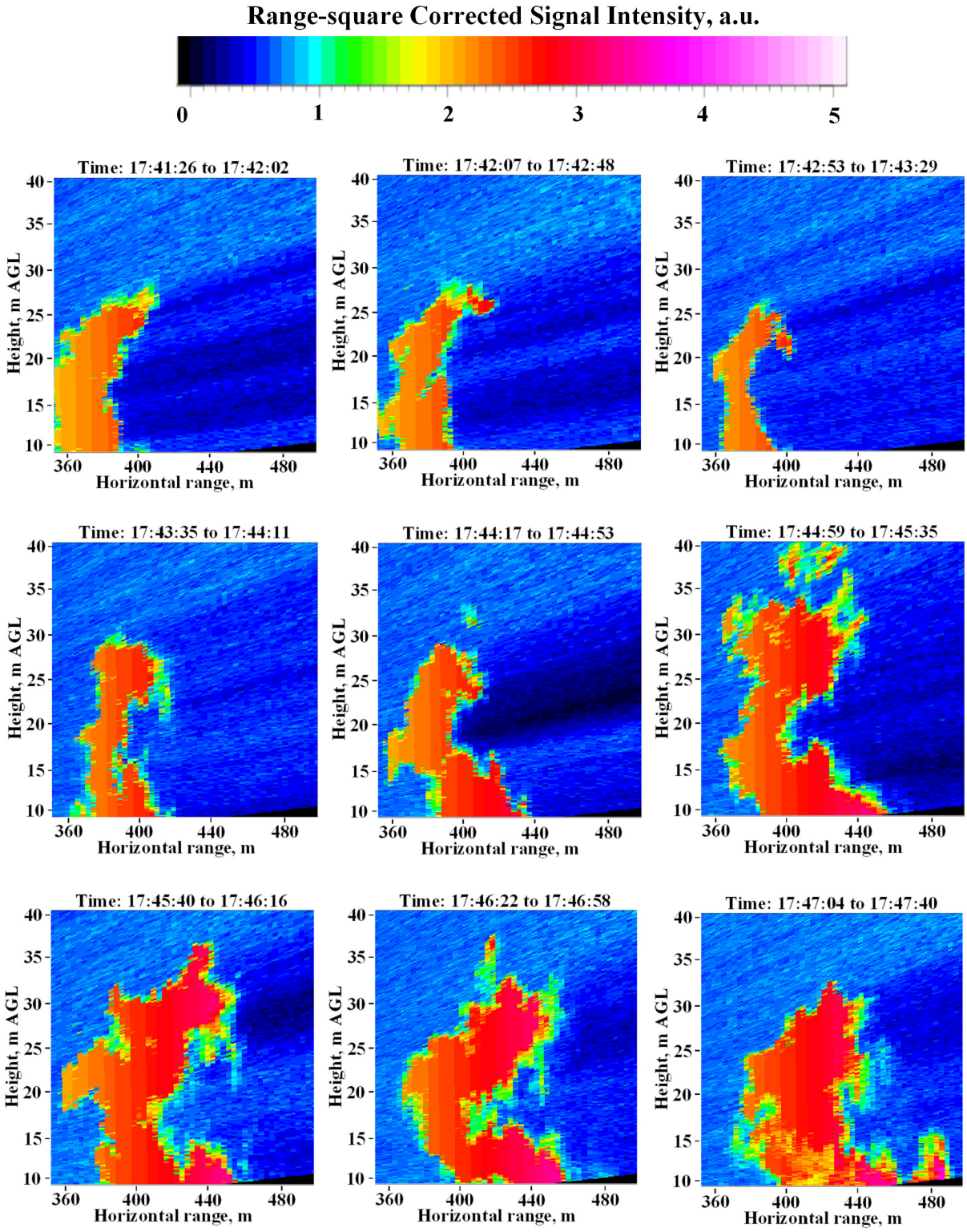

Figure 6.10: Sequence of RHI scans performed with the lidar in horizontal-range-to-height diagrams (from top left to bottom right) with vertical cross-sections of an aerosol structure due to biomass burning. Data was collected on 19 September 2005 from 1740-1750 UTC. Background-subtracted, range-corrected backscatter signals are plotted against horizontal range and height relative to the location of the lidar system. The plots show an extract of the data at constant locations: heights between 10 and 40 m, horizontal distance between 350 and 500 m. The azimuth angle (318°) was kept constant during these scans.

6.4.2 Aerosol optical properties in an RHI scan view

The UHOH lidar scan strategies (including type of scans, sector or volume of scan domain, scan speed) can be adapted in such a way that the ABL height and complexities arising in different ABL regime can be detected. Some sets of nearly hemispherical scans were performed on 20 September 2005 at about 1415 UTC. An RHI panel of the particle backscatter coefficient obtained (after applying the technique described in the section 4.6.2.2) is shown in Figure 6.11. This scan image reveals high variability of the aerosol particles in the ABL yielding clear signature of the ABL top at and around 1.2 km AGL over a distance of 3 km from north to south of the lidar system. Each scan started just above the horizon (5° elevation) to a scanning angle 175° and required approximately 6 minutes to be completed.

Above 1.2 km altitude, it was substantially cleaner air, so that inversion algorithm developed (section 4.6.2.2) for scanning lidar measurements could be applied in this case. Inside the boundary layer, variability of the particle backscatter coefficient was observed. No boundary layer clouds were present during these measurement periods.

Variation of the ABL heights over an extended region was arising due to the classical characteristics of ABL activities since surface forcing was not switched off at 1415 UTC. Scan speed was kept sufficiently low (0.5° s^{-1}) to provide high angular resolution of the aerosol distribution in the RHI field. A nearly constant ABL top over along the distance of 3 km is observed in the figure. This is

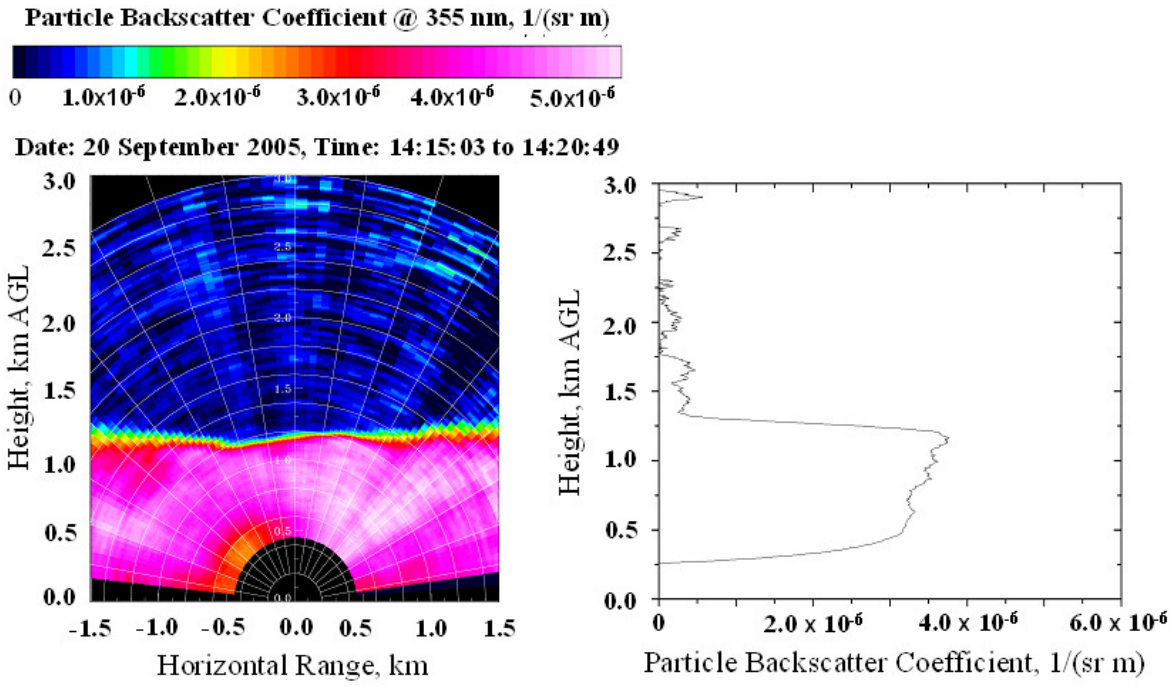

Figure 6.11: Left panel: Selected hemispherical RHI among 12 such scans collected on 20 September at 1415 UTC shows the high aerosol loading in the ABL. Scans were performed with a very low scan speed of 0.5° s^{-1} to acquire good resolution in range as well as in height. Scans were made in from south to north of the lidar system. ABL top variation at and around 1.2 km AGL over 3 km distance is visible. Right panel: Vertical profile (LOS at 90° elevation angle extracted from the RHI scan) of particle backscatter coefficient confirming the ABL top at a height about 1.2 km AGL.

not unexpected in a flat terrain-region like that of Mettingen. Entrainment-driven small-scale patterns are also visible.

The example presented is a selected scan among 12 such scans. Both temporal and spatial variability of the ABL aerosol field over the horizontal distance of 3 km can be observed by the animation of these scans (not shown here). Some wave-like structures at the top of the ABL have been revealed from the animation. These wave-like features are very similar to the features of convectively forced stationary gravity waves.

In the right panel of Figure 6.11, one example of the particle backscatter coefficient profile is chosen that represents the result when the lidar was pointing to the zenith. This profile confirms the top of the ABL at about 1.2 km AGL indicated by a sharp drop in $\beta_{\lambda,par}(R)$. A notable decrease in the backscattering profile up to a height of about 350 m AGL was caused by incomplete overlap function. Results up to this distance must be excluded from interpretation.

6.4.3 Investigation of aerosol plume from the farm

Near horizontal PPI scans at an elevation angle of 2.26° were performed on 20 September 2005 around 1615 UTC in an azimuth sector of 30° pointing towards the livestock farm (between azimuth angle 180° and 210°). Scan speed was 2° s^{-1} which corresponded to a duration of 15 s for each scan to be completed. During this time, wind was calm with a speed of about < 3 m s^{-1}. Temperature recorded during this time was 17 °C while maximum temperature of the day was 18.5 °C and RH was low (of about 45 %). Sun elevation angle was 15° and the end of the twilight was at 1807 UTC.

Data were collected with the maximum temporal (0.033 s) and spatial resolution (3 m) of the UHOH scanning lidar system. Before the particle backscatter coefficient is derived from the collected data, 10 consecutive profiles were averaged which yielded time resolution of 0.3 s and a gliding window average (width of 10 bins) in range was performed which provided 30 m effective range resolution. Then particle backscatter coefficient field was derived following the procedure described in section 4.6.2.2. A value for the lidar ratio at 355 nm, which can be considered as an average one for continental ABL aerosols, is 39 sr (Pappalardo et al., 2005). This value was used in the inversion technique to derive $\beta_{\lambda,par}(R)$.

Since these PPI scans took place inside the boundary layer, the procedure for the retrieval of the optical properties was not straightforward due to the absence of a constant calibration value in the far field. An advantage of the results obtained from hemispherical RHI scans (discussed in the previous section) was considered. First, the data of an RHI scan were analyzed and a calibration value above the boundary layer was made. The inversion technique resulted in a particle backscattering profile in the boundary layer. A vertical profile of $\beta_{\lambda,par}(R)$ yielded a clear indication of the ABL top over which the lidar signal could be easily calibrated. The selected zenith shooting profile was smoothed and

extrapolated. A calibration value was then obtained for the far field in the near horizontal PPI scans. In the literature extensive error considerations were accomplished to the inversion procedure (e.g., Bissonnette, 1986; Kunz, 1996). In general, it can be stated that the relative error of the particle backscattering coefficient corresponds for instance to the error of the calibration value in %. In this regard detailed sensitivity tests have been performed and discussed in Appendix- C.

Six out of 22 sequential PPI scans are shown in Figure 6.12. These scans show the near-horizontal (a slant plane at an elevation angle of 2.26°) distribution of the particle backscatter coefficient in range-range panel with the lidar system in the origin. Pseudo-color from black to white/pink corresponds to minimum and maximum particle backscatter coefficient in m^{-1} sr^{-1}, respectively. During this period wind was blowing nearly from north-northeast as shown by red arrow over the PPI scan (scan 1). Wind directions during all scans were same and therefore are not shown in all PPI panels. Location of the farm is overlaid as a square on the scan images.

Figure 6.12 clearly shows the emission of the aerosol plume from the livestock facility. Particle backscatter coefficient of the aerosol cloud emitted from the farm was of about 30 % higher than that of the background aerosol present in the atmosphere. The values of $\beta_{\lambda,par}(R)$ of the aerosols distributed in the region of 1.5-2.0 km were higher compared to the close region (region until 1.2 km) to the farm. This enhancement of the $\beta_{\lambda,par}(R)$ (up to 1.2 x 10^{-5} m^{-1} sr^{-1}) in the far distance most probably was caused by a humidity induced particle growth.

The aerosols emitted from this farm were found to be consisting of ammonium and nitrate salts on some other days during the campaign (Valdebenito, 2008). Increase in physical dimension of the plume might also be arising due to the effect of the dispersion. In light wind condition the dispersion of the aerosol plumes can be more rapid. Similar physical characteristics of the plume (originated from agricultural sources) and its dynamics were reported by Holmén et al. (1998). Blowing of the plume with the prevailing wind shows the aerosol transport with some effect of turbulence activities in the ABL. Emitted plume was lofted at a height of 20 m AGL near the source and of about 115 m at the extended region of 3.0 km. Very recently, Prueger et al. (2008) showed in their study that the vertical extent of the plume emitted from such a facility can be around 30-40 m in the close region. However, these values are critically dependent on many other factors. The results concerning the plume extension and maximum height agree well to the results obtained by Holmén et al. (2001) for an agricultural tilling. This case has been selected for the comparison with the LES-AOP results (see, section 6.4.6).

It can be stated that the Gaussian plume model will not be able to assess this type of plume emission. The farm is not a continuous source of aerosol. The emission necessarily depends on numerous factors, e.g., feeding rhythm, related movement of the animals inside the facility, ventilation system. In-situ point measurement techniques will underestimate/overestimate in such cases since they cannot provide high-resolution tracking of aerosol emission as possible with such scanning lidar technique. Sequential PPI scans during this period illustrate the evolution and transport of aerosol

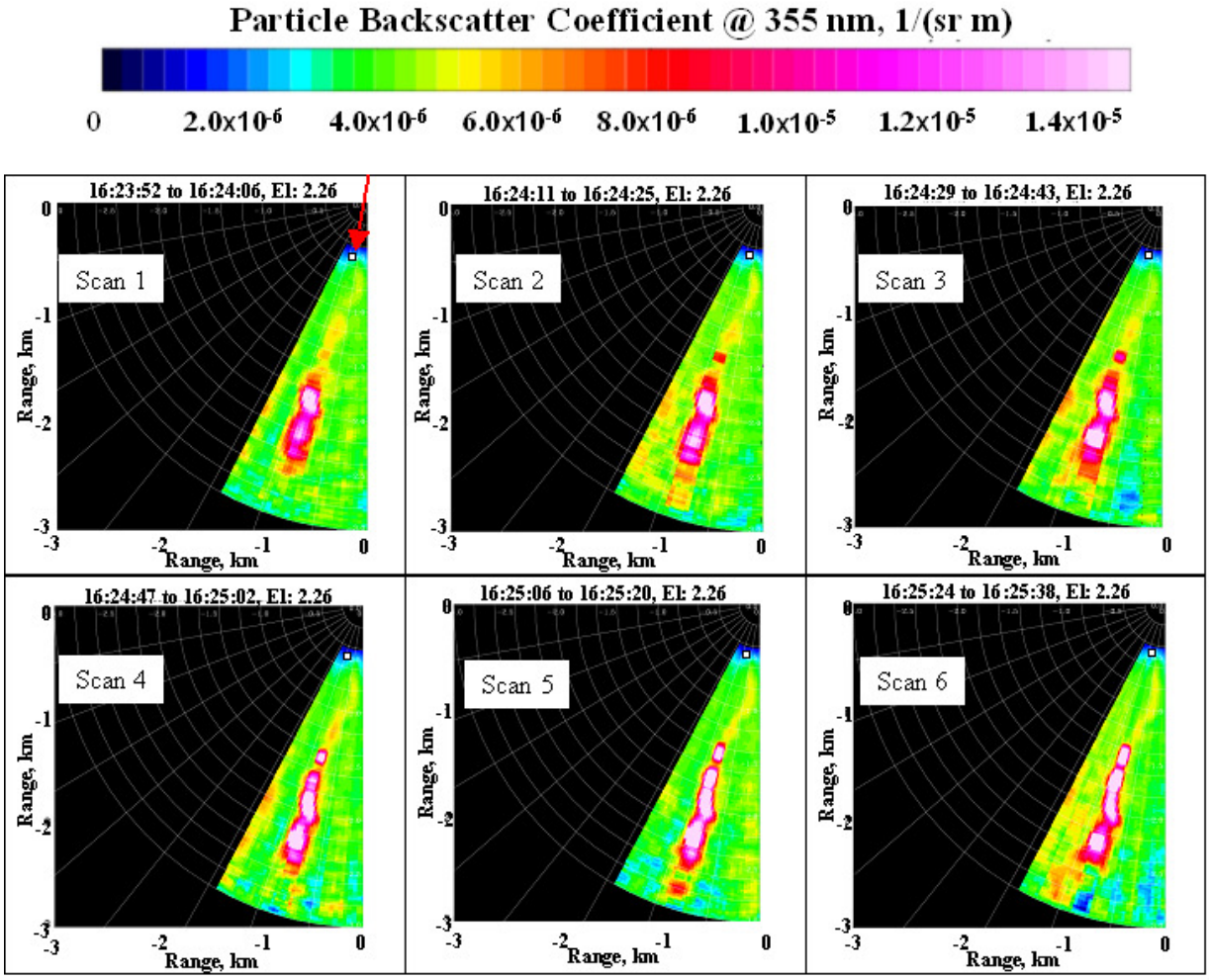

Figure 6.12: Near horizontal PPI scans (clockwise in the azimuth sector of 180° to 210° with a scan rate of 2° s^{-1}) collected at Mettingen, Germany, on 20 September 2005, around 1620 UTC. Sequence of six PPI scan images (among 22 such scans) showing optical properties, $\beta_{\lambda,par}(R)$ of the plume of the exhaust air form the livestock facility. Dynamics of the emitted plume in downwind is visible from the sequence. Each PPI sector scan took of about 15 s to be completed. The time gap between the end of one scan and the start of the next scan is of about 4 s when the system does not acquire data. Lidar is the located at the origin of the image and positive x-axis is in the direction of east. Range rings at each 200 m are displayed and azimuth sector at each 10° is shown. Aerosol plume from the farm (black-square on the image) with associated motion in downwind (red arrow: wind direction) and turbulence features are visible. The figure demonstrates the turbulent drifted structure of the aerosol plume. Note the increase of the plume dimension with distance from the lidar.

plumes. All the images are having similar characteristics in view of the contribution of the farm as an aerosol source although faint. Sequential PPI scan images also show the broadening of the plume and its downwind transport. If a time-lapse animation is made (not shown here) with 22 such PPI scan images through an avi file format, one can easily visualize the motion of the plume with the prevailing wind. These results provide a confirmation that plume emission from the facility obviously was not continuous and a Gaussian plume model cannot provide snapshots of such emissions. This kind of model has several limitations, e.g., in calm wind conditions, they have poor predictability.

It is important to mention here that the choice of PPI scans at a very low elevation angle detected the aerosol emission from the source. The illustration in Figure 6.13 shows that if the vertical

extent of the plume is very low, PPI scan at high elevation angle cannot detect the structure of plume in the scan domain. None of the PPI scans collected at high elevation angles (> 2.5°) were able to show the structures of the plume from the farm. This figure also gives an illustration of this fact showing resulting geometry of the exhaust aerosol plume, which can be pointed out due to the measurements accomplished with the lidar.

Another set of very low elevation (2.26°) PPI scans over the farm region yielded the structure of the emission of the aerosol plume. Figure 6.14 shows 3 out of a total of 52 PPI scans performed. Scans were performed with a low scan speed of 0.5°/ s. Time resolution and range resolution in the particle backscatter coefficient field were same as the previous case. In range, a gliding window average with a width of 30 m was performed. $\beta_{\lambda,par}(R)$ of the plume (of about 5.0 x 10^{-6} m^{-1} sr^{-1}) was similar as in the previous case. But the source contribution and transport with the prevailing wind is comparatively less clear as only a very narrow horizontal sector of the scan domain was obtained with the lidar measurements. However, these observations once again confirm the emission of the plume and downwind transport in the close as well as in far region of the farm.

None of the PPI scan measurements shown here is a part of a PPI volume scan. Therefore, all the available information about the vertical structure and extent of the farm plume is based on the fixed-elevation PPI-Scan. But, clear evidence was found regarding the lack of farm plume with a PPI scan at an elevation angle of 4.76° or more. The intercomparison results presented (see, section 6.4.6) confirm this fact.

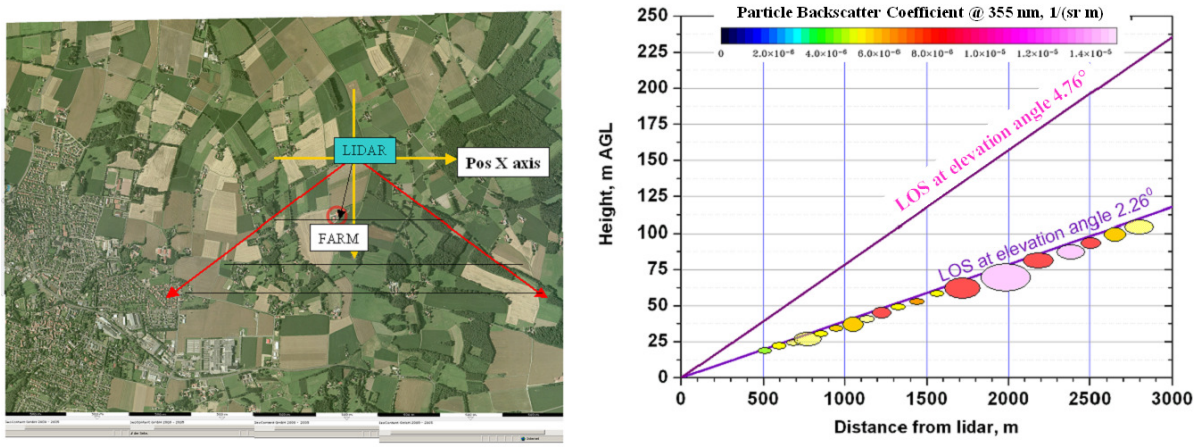

Figure 6.13: Schematic of the scan region and the location of the farm with respect to lidar. Left panel: Polar view of the scan region where lidar and the farm are shown. The farm is located at a distance of about 480 m from the lidar and at an azimuth angle 193.5°. Right panel: change in height with respect to the distance from the lidar at two different elevation angles, namely 2.26° and 4.76°. The height of the farm-chimney is 6 m higher than the horizontal lidar beam outlet. A schematic of the aerosol plume is shown with the color circles as a mimic of the plume. Color indicates the optical properties of the aerosol emitted. Diameter of the circles can be approximated as the plume dimension at different ranges. Please note that this is only a qualitative view of the emission to assess the extension of the plume.

During the PLUS1 campaign, RHI scan measurements showed in general only weak, if any, evidence of the farm plume. The PPI scans of 17 September were found to have too high elevation angle of about >4.5°, thus missing the farm plume (see, Valdebenito, 2008; and Lammel et al., 2007; for a brief overview on the lidar results and model simulations made for other days of the campaign).

Nevertheless, RHI scans over the farm area may confirm the vertical extent of the plume and can describe more insights into the aerosol transport processes. Very high-resolution rapid volume scan (both RHI and low elevation PPI) can yield 3-4 dimensional pictures of the plume emission in the future field experiments.

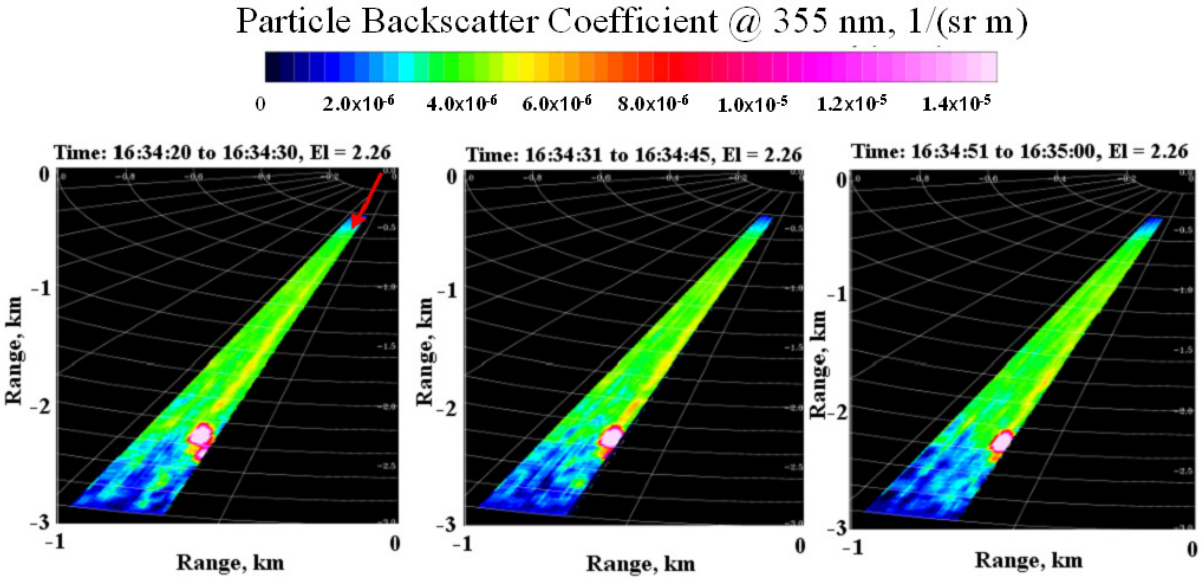

Figure 6.14: A set of three low elevations horizontal scans showing the emission of plume from the farm at 1631 UTC on 20 September 2005. Wind direction is shown as red arrow on one of the PPI scan (left panel).

6.4.4 Horizontal scans at different elevation angles

A comparison of three different PPI scans performed on 20 September is aimed here to assess the requirements of a suitable scan strategy for detecting emission from the farm and to illustrate the complexities involved in the aerosol emission and transport processes. Schematic of the scan region and the location of the farm with respect to lidar are shown in Figure 6.13 to support these results. Goal of this investigation is, however, not only the analysis of the natural variability of the aerosol particles emitted from the livestock facility; the determination of a suitable scan strategy is an important issue.

Figure 6.15 shows the PPI scan images of $\beta_{\lambda,par}(R)$ measured in the afternoon on 20 September 2005. There is a clear difference between the horizontal scan at 2.26° (panel B) and at 4.76° (panel A and C) elevation angle as shown in the figure. There was no significant increase of $\beta_{\lambda,par}(R)$ field when scan was performed at 4.76° elevation angle. On the contrary, near horizontal scan at an elevation angle of 2.26° showed the enhancement of the particle backscatter coefficient for the aerosol emitted (panel B). Quantitative analyses of these results are detailed in section 6.4.6 while

comparing the lidar-derived $\beta_{\lambda,par}(R)$ field with the LES-AOP simulations for PPI scans at different elevation angles.

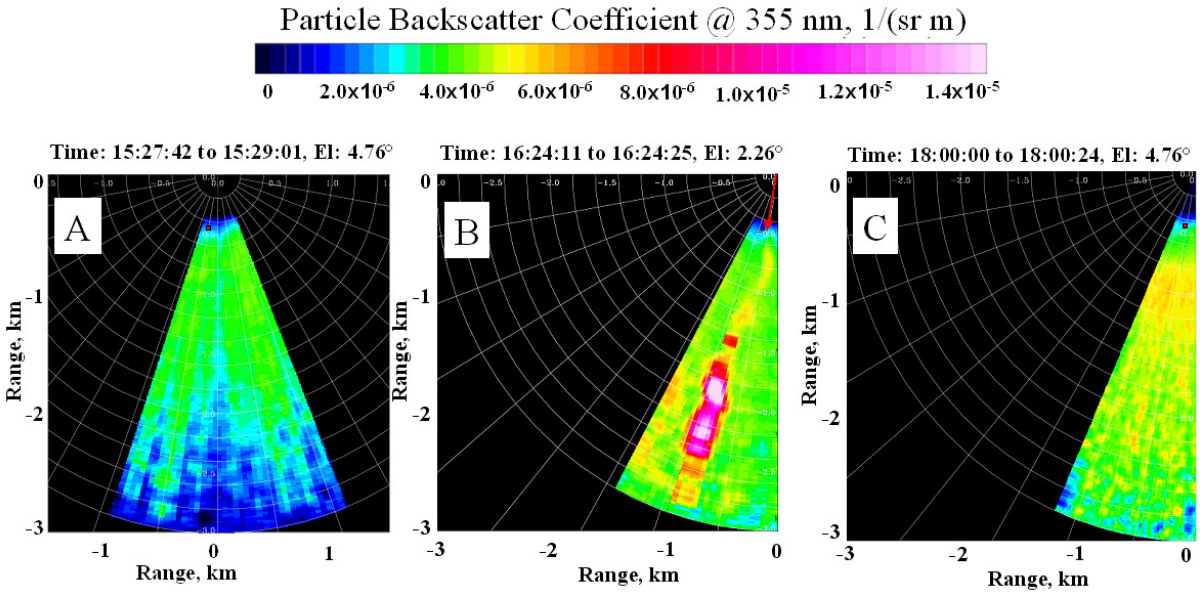

Figure 6.15: Three different PPI scans performed on 20 September 2005. Particle backscatter coefficient field at 4.76° elevation angle PPI scan around 1530 UTC and 1800 UTC (panel A and C, respectively), same as (panel A) but at 2.26° elevation angle around 1620 UTC (panel B). A clear evidence for the lack of the farm plume is observed in the PPI sector scan at an elevation angle of 4.76° (panel A and C). Wind direction is shown as a red arrow for the PPI scan at an elevation of 2.26° (Panel B) illustrating the downwind transport of the plume. The wind directions during other two scanning measurements were same.

6.4.5 In-situ measurements at ground

Apart from the LES-AOP simulation (Valdebenito, 2008) and the UHOH scanning lidar observations, in-situ point measurements of aerosol particles during PLUS1 campaign showed promising results to support this study. For instance, single particle analysis served for identification of the aerosol types, the degree of mixing, and supplied qualitative information concerning the aerosol chemical characteristics for improved initialization of the model.

Some of the experimental analyses of the collected particle samples were performed within this thesis in UHOH. The most important results regarding single particle analysis are shown in Figure 6.16 and 6.17. These figures show that on 17 September 2005, sub-micron carbon-containing particles (Figure 6.16) and super-micron particles (Figure 6.17) e.g., CaO and CaSO4 were present in the farm plume. The single particle analysis was performed by laser microprobe mass analyzer (LAMMA). A detailed description on the LAMMA technique is available in Wieser and Wurster (1986).

Selected results obtained with in-situ measurements are summarized here:

- Mass spectra of the single particle analysis evinced that the farm plume contained sub-micron (0.18 – 0.35 µm) carbon particles and super-micron (1.2- 3.5 µm) Ca, CaO and $CaSO_4$.

- Background aerosol was mainly consisting of Chlorides, possible oxides from Na, K, Ca as well as organic carbon (OC).
- Highly condensed carbonaceous matter, especially soot particle were not found in plume.
- The fine particulate matter ($PM_{2.5}$) content of S, Cl, Ca, K, Fe, and Ni showed a significant downwind/upwind increase.

During the measurement days (16 and 17 September, 2005) the background aerosol concentration was rather small containing sea salt, K and -oxides, hardly any secondary aerosol and no soot particles. The quantitative amounts of these particles were smaller on 17 September than on 16 September. The aerosol measurements at the ground showed an enrichment of organic particulate material. Ammonia was also present. A high ammonia concentration was found on 16 September (38 µg m^{-3}) compared to the other day (4.7 µg m^{-3}). These results and some other results obtained by in-situ point measurements were discussed in detail in Lammel et al. (2006, 2007) published as a part of annual reports of the BW-PLUS project.

Although, these results were not directly used for the lidar data analyses they provided a wealth of important information concerning

- identification of the aerosol particles
- the particle size distribution
- initialization of aerosol composition in model runs.
- qualitative information regarding the chemical aerosol characteristics.

These results facilitated the LES-AOP so that the key parameters for the initialization and forcing of the model were estimated from the in-situ measurements performed. The UHOH lidar cannot provide any kind of information on the PSD. Nevertheless, the results obtained with the lidar helped to evaluate the model results (see, intercomparison study in section 6.4.6), which were highly dependent on the in-situ measurements at ground.

All these results confirm that the livestock farm is an isolated aerosol source, and the aerosol barely influenced by other anthropogenic sources such as of agricultural or road traffic origin.

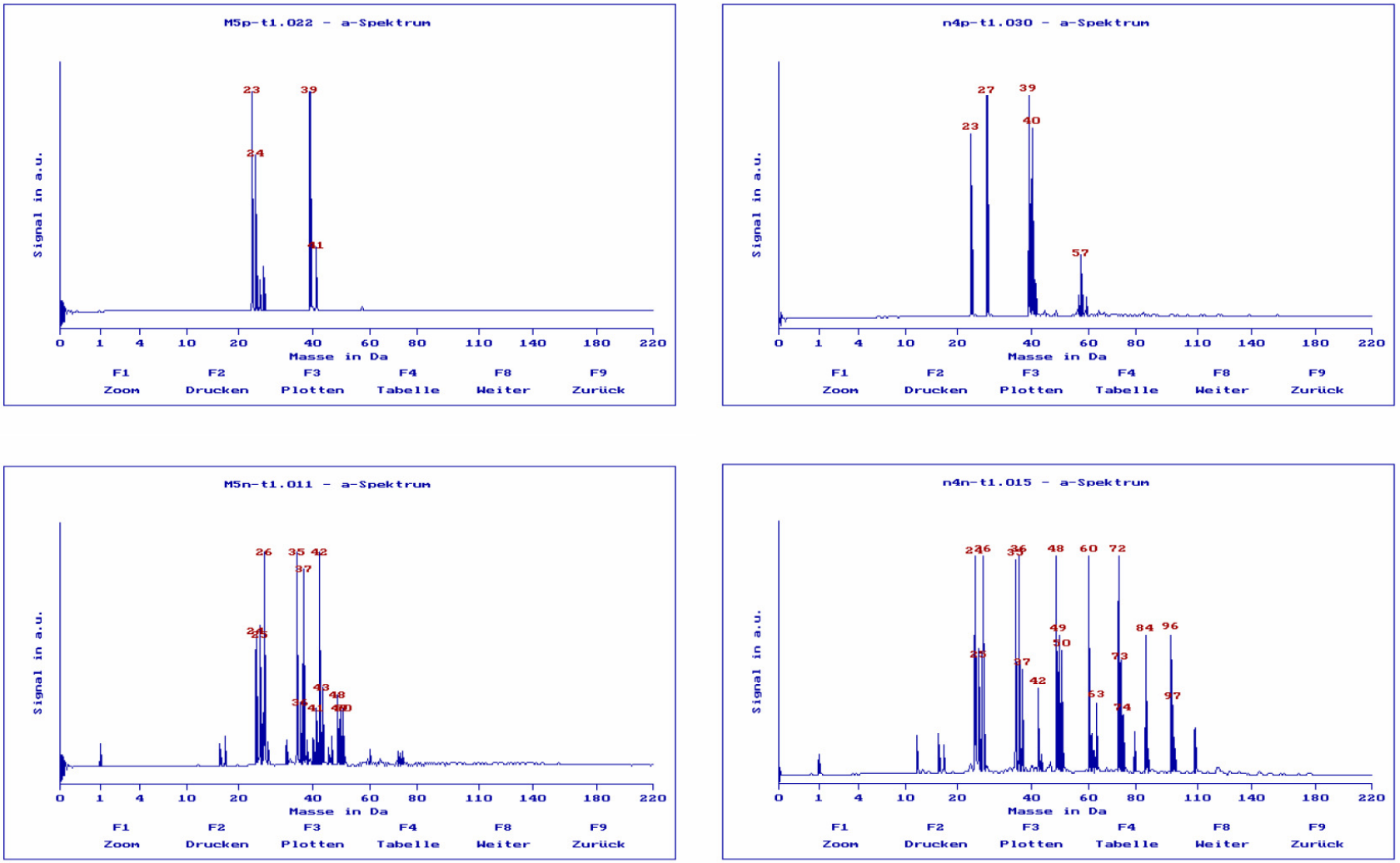

Figure 6.16: Comparison of typical positive (above) and negative (below) mass spectra of sub-µm (D = 0.18-0.35 µm particles upwind (left) and downwind (right) of the aerosol source collected near the farm (distance, Δs = 750 m) on 17 September 2005. Courtesy of: Prof. R. Wurtser, UHOH.

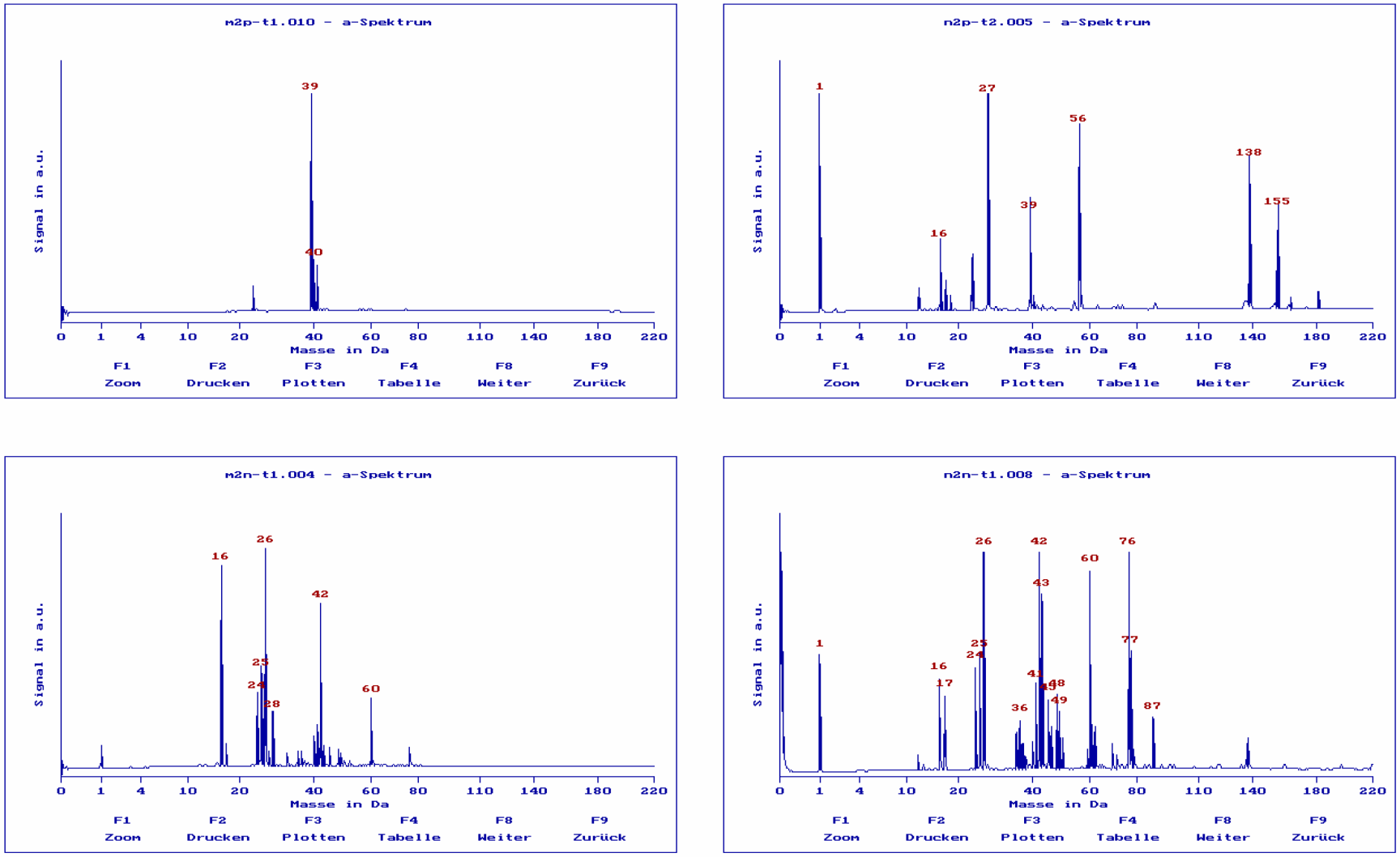

Figure 6.17: Same as Figure 6.16 but for super-micron (D = 1.2-3.5 μm) particles upwind (left) and downwind (right). Courtesy of: Prof. R. Wurtser, UHOH.

6.4.6 Intercomparison between lidar measurements and large-eddy simulation (LES) results

Intercomparison study is an important part of this work to demonstrate the novel technique. It allowed for better understanding the observed aerosol structures on the lidar scans by relating them with the simulated aerosol emission and transport near the source. The following section briefly describes the most essential part of the LES-AOP experiment while a detailed description of the model can be found in Valdebenito (2008).

6.4.6.1 High-resolving atmosphere-microphysics-chemistry model

There are two different approaches to the numerical simulation of turbulence: (1) direct numerical simulation where all relevant to dissipation scale of the flow are resolved, starting from the largest energy-producing eddies down to the small energy-dissipating eddies, and (2) LES, where a range of scales is resolved, from the largest eddies down to a defined cut off size, below which the dynamics are modeled. Resolving the flow implies that the equations of motion are integrated over a discrete mesh in time and space.

LES is a numerical approach that involves three-dimensional simulation of eddies and can resolve turbulence in the atmosphere. LESs are able to demonstrate two-three and/or three-four dimensional structures of turbulence (Wyngard and Brost, 1984; Stevens and Lenschow, 2001). LES results can be used as an efficient tool to analyze the time evolution of the coherent structures and their contribution to the turbulent transport. The LES can also be used to study cloud-free CBL (Sorbjan, 1995). Most of the LES experiments are based on the simulation of idealized ABL structures, followed up by the comparison with the turbulence statistical results obtained from in-situ measurements.

The high-resolving atmosphere-microphysics-chemistry model was developed (Valdebenito, 2008) on the basis of an existing atmosphere chemistry model, being a basic structure model with chemistry module (Chlond and Wolkau, 2000; Mueller and Chlond, 1996;). This LES was extended to a version so that it can simulate changes of the aerosol PSD in each grid point of the model domain for each time step. The PSD initialization, PSD evolution, and calculation of aerosol optical properties (AOP) are the key components of the LES-AOP. Aerosol processes in the LES-AOP included emission, transportation, sedimentation, and condensation. Due to the high computational demand of the LES approach, the LES-AOP model neglected the coagulation and nucleation processes.

The key features of the LES-AOP experiment, which are important for the intercomparison study, are:

1. Selected days (17 and 20 September 2005) were simulated between 0900 and 1800 UTC.
2. Model domain: 4 km x 4 km base and 2 km high.
3. Horizontal and vertical grid resolutions are 50 m and 20 m, respectively.
4. Temporal resolution was adjusted during simulation time (between 1 and 5 s).

5. Forcing and output time step: 15 minute.
6. The model produced instantaneous and time averaged fields of optical properties of aerosols.
7. The aerosol (from the farm) PSD was derived from measured $PM_{2.5}$ and PM_{10} (relative to upwind).

6.4.6.2 Intercomparison results

For intercomparison study, lidar measurements obtained on 20 September 2005 were selected because it contained only some sets of PPI scans with elevation angle below 3° among all the lidar measurements performed in PLUS1 campaign. The clear indication of the farm plume was obtained from these low elevations PPI scans. Furthermore, it was found that the particle backscatter coefficient for 20 September was consistently higher than for 17 September (Valdebenito, 2008). An intercomparison between the results obtained with the lidar and model simulation for 17 September is also discussed.

Lidar derived results of the optical properties of aerosols obtained from a single instantaneous PPI scan made in less than one minute cannot be compared directly with the LES-AOP results due to relatively large forcing and output time step of the model (15 minute). Therefore, for the intercomparison, an effort was made to average over 22 consecutive PPI scans obtained between 1615 and 1630 UTC on 20 September (described in the section 6.4.3). Profiles of $\beta_{\lambda,par}(R)$ lying on the same LOS of each PPI scan were averaged for this purpose. No further range averaging was performed. Figure 6.18 shows a direct comparison between PPI scan image of averaged $\beta_{\lambda,par}(R)$ field obtained with the UHOH lidar (left panel) and the LES-AOP results of 15-min averaged fields (right panel) around 1600 UTC on 20 September. The simulated $\beta_{\lambda,par}(R)$ values were interpolated to the PPI scan projection for 2.26° elevation angle as shown in the figure. Four different sorts of aerosol scenarios were simulated to achieve the intensity of the background fluctuations. The background values seemed to be better represented by the high aerosol scenario. The high aerosol load (HAER) was based on the total mass on the individual stages of the cascade impactor (determined by gravimetric analysis), which determined the background aerosol number size distribution. A detailed description of these aerosol scenarios is available in Valdebenito (2008).

This figure once again shows the structure and transport of the emitted plume. An averaged PPI scan fails to show the bending of the plume due to the turbulence effect and the influence of the small-scale features. This loss of information becomes evident if any of the PPI scans in Figure 6.12 are compared to Figure 6.18.

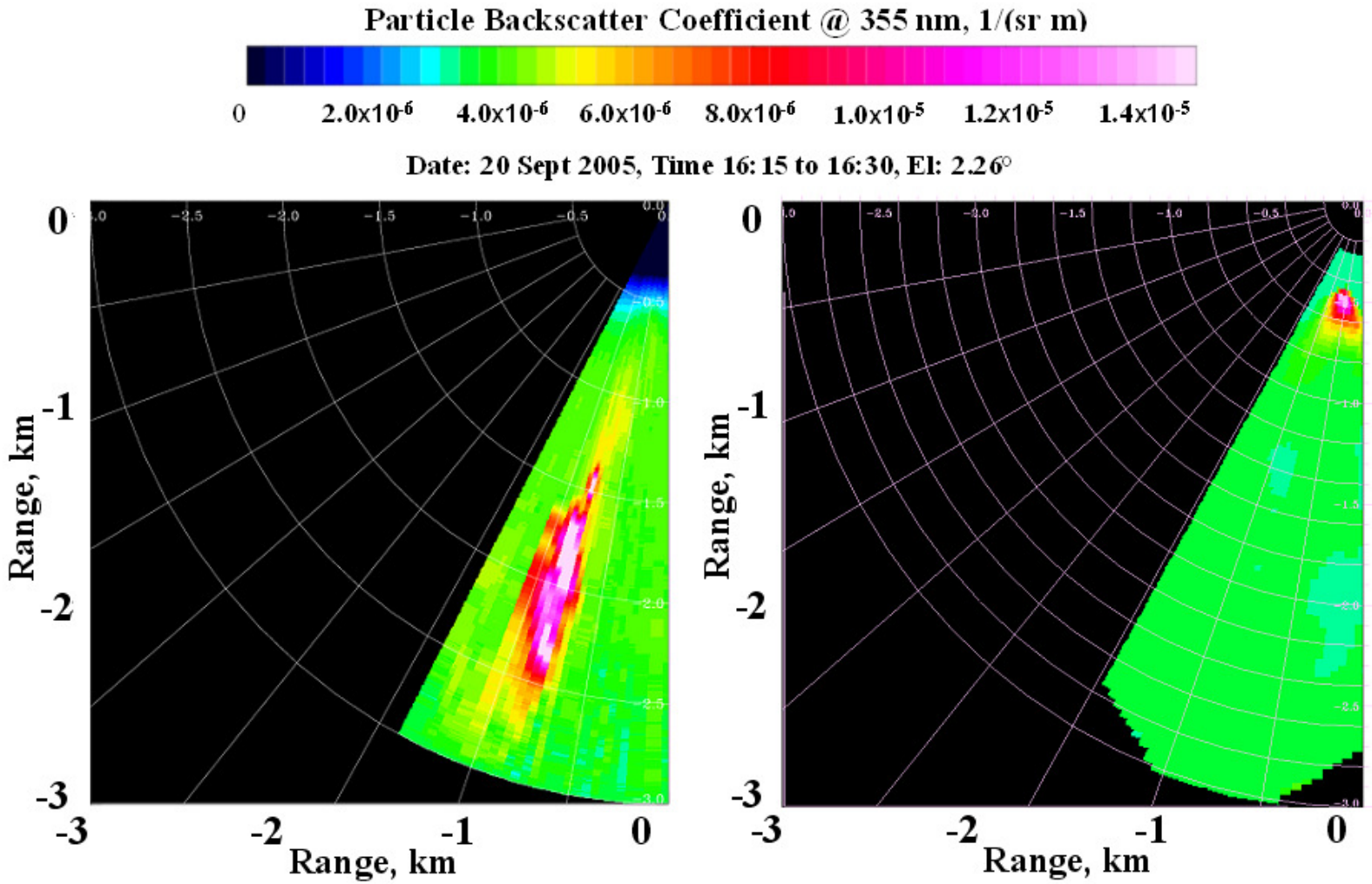

Figure 6.18: Intercomparison between measured and simulated PPI-scans between 1615 and 1630 UTC on 20 September 2005. Left: UHOH lidar estimated particle backscatter coefficient field, right: simulated particle backscatter coefficient field after LES-AOP. Source of the model results: Valdebenito (2008).

A detailed intercomparison was then performed to investigate the aerosol plumes during the whole day. For this purpose, data collected by the UHOH lidar and simulation results by LES-AOP between 1000 and 1800 UTC on 20 September are considered (Table 6.2). The table shows $\beta_{\lambda,par}(R)$ obtained both with the UHOH lidar and LES-AOP. In the Table, $\Delta\beta$ represents the contribution of the aerosol source i.e., the livestock farm. This value was calculated by the difference between total particle backscatter coefficients due to the farm-polluted fields (background and aerosol from farm) and the particle backscatter coefficient for the background aerosol contribution (β bckgrd). Furthermore, $\sigma_{ß}$ is the standard deviation of the farm polluted instantaneous field.

The PPI scans at two different elevation angles (2.26° and 4.76°) were considered for the intercomparison. As the UHOH lidar performed different scan patterns during this day including different PPI, RHI scans at different elevation and azimuth angles, respectively covering various scan domains, there are some gaps in the lidar results. Additionally, for the LES-AOP simulations, there were three different types of predicted $\beta_{\lambda,par}(R)$ for three different aerosol scenarios, namely, optical density low (ODL), optical density medium (ODM), and optical density high (ODH).

Table 6.2: Comparison of predicted (model, under 3 scenarios of aerosol properties, ODL, ODM and ODH, 1 s-means) and measured (lidar) ranges of the aerosol particle backscatter coefficient $\beta_{\lambda = 355\ nm}$ (10^{-6} m^{-1} sr^{-1}) in the plume (Δß, maximum value, 15 minute mean) and in the background (ß, mean ± standard deviation, 1 s-mean) for Mettingen, 20 September 2005, 1000-1800 UTC for conical (PPI) scans at two different elevation angles.

Time (UTC), tilt of PPI scan	**Measured (x 10^{-6} m^{-1} sr^{-1})**		**Predicted (x 10^{-6} m^{-1} sr^{-1})**					
			ODL (Optical density low)		**ODM (Optical density medium)**		**ODH (Optical density high)**	
	Δß	ß bckgrd	Δß	ß bckgrd	Δß	ß bckgrd	Δß	ß bckgrd
1000 (2.26°)			0.60	1.10±0.05	3.68	5.95±0.16	5.26	8.60±0.24
1000 (4.76°)	<0.25	2.5±0.12	0.16	1.07±0.05	0.93	5.70±0.29	1.42	8.31±0.37
1100 (2.26°)			0.27	1.02±0.05	1.38	5.65±0.12	2.00	8.13±0.23
1100 (4.76°)	<0.42	3.5±0.21	0.18	1.03±0.05	1.01	5.58±0.23	1.54	8.11±0.29
1200 (2.26°)			1.43	0.85±0.09	8.51	4.73±0.43	12.3	6.75±0.64
1200 (4.76°)	<1.0	1.5±0.51	0.33	0.93±0.09	1.94	5.02±0.37	2.80	7.27±0.61
1300 (2.26°)			1.67	0.80±0.06	10.1	4.36±0.31	14.6	6.25±0.46
1300 (4.76°)			0.59	0.83±0.06	3.58	4.48±0.30	5.19	6.46±0.49
1400 (2.26°)			1.17	0.79±0.06	7.26	4.19±0.34	10.6	6.14±0.50
1400 (4.76°)	<0.62	1.8±0.31	0.31	0.79±0.03	1.95	4.19±0.16	2.83	6.12±0.26
1500 (2.26°)			1.79	0.75±0.06	10.9	3.90±0.38	16.5	5.81±0.57
1500 (4.76°)	<0.22	1.8±0.11	0.31	0.75±0.02	1.89	3.90±0.13	2.85	5.79±0.20
1600 (2. 26°)	6.0±0.3	2.9±0.21	1.68	0.70±0.06	11.1	3.61±0.40	16.6	5.43±0.59
1600 (4.76°)			0.35	0.70±0.03	2.30	3.63±0.23	3.43	5.43±0.34
1700 (2. 26°)			1.61	0.66±0.07	10.3	3.42±0.44	15.8	5.18±0.68
1700 (4.76°)	<0.38	2.5±0.19	0.51	0.66±0.03	3.23	3.44±0.19	4.94	5.18±0.28
1800 (2. 26°)	<0.32	2.2±0.16	7.19	0.65±0.29	46.3	3.39±1.88	68.8	5.14±2.75
1800 (4.76°)	<0.31	3.1±0.15	1.12	0.64±0.13	7.18	3.34±0.81	10.6	5.04±1.19

Comparing these results of table 6.2, one should note that the LES-AOP results were based on the sensitivity study performed during the model simulation, showing some discrepancies due to uncertainties of the initialization of the model simulations. This was mainly due to the lack of aerosol composition data by in-situ instruments on this day. The measured values were smaller than those of the best guess simulation, but exceeded the ODL scenario. The upper estimate (scenario ODH) yielded values between 3.5 and 6.3 x 10^{-6} m^{-1} sr^{-1}. Therefore, the uncertainty of the model forecast for the particle backscattering coefficient, being averaged over several square kilometers could be up to ± 50/70 %. Furthermore, the aerosol load scenarios reflect the uncertainty on the ground measurements. There is approx. a 70 % discrepancy between the background PSD estimated from the gravimetric analysis and the one estimated from the ion chromatography. There were no ground in-situ measurements available on 20 September; the model simulations were based on the in-situ measurements on 17 September.

The intercomparison between the measured and simulated particle backscatter coefficient field was also performed for 17 September 2005. Table 6.3 shows the aerosol contribution due to the farm at different times of the day on 17 September for PPI scan at two different elevation angles. The model simulations performed on this day showed that the heterogeneity on the background fields (caused mainly by turbulence) were much larger than the farm plume signal at 4.76°, which made the detection

Table 6.3: Comparison of predicted and measured (lidar) values of the aerosol particle backscatter coefficient $\beta_{\lambda = 355\ nm}$ (10^{-6} m^{-1} sr^{-1}) in the plume (Δß, maximum value, 15 min mean) and in the background (ß,mean ± standard deviation, 1 s-mean) for Mettingen, on 17 September, from 1000-1800 UTC conical (PPI) scans.

Time (UTC), tilt of PPI scan	**Measured (x 10^{-6} m^{-1} sr^{-1})**		**Predicted (x 10^{-6} m^{-1} sr^{-1})**	
	Δß	ß bckgrd	Δß	ß bckgrd
1000 (2.26°)			0.30	4.08±0.24
1000 (4.76°)	<0.22	2.0±0.11	0.02	4.28±0.25
1100 (2.26°)			0.81	3.37±0.22
1100 (4.76°)			0.05	3.62±0.30
1200 (2.26°)			0.64	3.38±0.21
1200 (4.76°)	<0.62	1.25±0.31	0.07	3.48±0.18
1300 (2.26°)			0.68	3.15±0.17
1300 (4.76°)	<0.54	1.2±0.27	0.10	3.22±0.16
1400 (2.26°)			1.05	2.94±0.15
1400 (4.76°)			0.09	2.99±0.13
1500 (2.26°)			1.16	2.73±0.10
1500 (4.76°)	<0.26	1.8±0.13	0.08	2.78±0.09
1600 (2.26°)			2.66	2.55±0.12
1600 (4.76°)			0.39	2.58±0.07
1700 (2.26°)			3.23	2.39±0.15
1700 (4.76°)	<0.20	1.0±0.1	0.39	2.42±0.08
1800 (2.26°)			3.29	2.25±0.10
1800 (4.76°)			0.55	2.27±0.07

of the farm plume on the PPI scans on this elevation practically impossible. For the 2.26° PPI scans the case is the opposite, the simulated heterogeneity on the background fields was much smaller than the farm plume signal. Detection with near horizontal scan at an elevation angle of 2.26° should have been possible at least after 1400 UTC. During this time, the model simulation showed sufficiently high values of particle backscatter coefficient of up to 1-3 x 10^{-6} m^{-1} sr^{-1} (see, table). However, lidar measurements, on this day, were performed at the larger elevation angle (e.g., PPI scan at an elevation of 4.76° or higher). The line of sight corresponding to this elevation angle (see, Figure 6.13) obviously misses the volume affected by the aerosol emission, so that the plume was no longer detectable by the UHOH lidar. This should be noted that the background aerosol scenario was inherently constrained by the uncertainties involved in the initialization of the model simulations.

A one-to-one direct intercomparison between two different days for continuous measurements cannot be presented since the scan pattern and the temporal coverage of the lidar datasets were changed from day to day and even sometimes within a single day. However, the LES-AOP model was capable to simulate the results on each day with the same model configuration with a defined grid resolution in the same domain.

Furthermore, there is a relatively small intersection between the lidar scan region and model domain due to very high resolution of the UHOH lidar (3 m in range) in comparison with the model (50 m in horizontal and 30 m in vertical). Consequently, this yields a difference (although small) between the lidar derived background aerosol strength and the model defined background aerosol field. Another reason is that the lidar scan is limited in a particular scan domain. Therefore, the definition of optical properties of background aerosol is not exactly the same as in model domain. Furthermore, although the observed range of values of $\beta_{\lambda,par}(R)$ lies between the simulated values under the various scenarios, but no single simulation scenario seems to match all the observations (Valdebenito, 2008).

The intercomparison results show that

- Observed range of values for the backscattering lies between the aerosol simulation scenarios
- The model simulation managed to represent the intensity of the farm contribution

But, the LES-AOP results fail to capture the shape of the farm plume and intensity of the background fluctuations. Uncertainties in the combined effort are arising probably due to the following reasons.

- Vertical resolution of the model domain is 20 m starting at 10 m height
- LES performance is poor at the lowest grid point (10 m), which arises due to the presence of the surface. This is an inherent property of LES models (Khanna and Brasseur, 1997)
- Design of the LES-AOP for producing very small-scale structure as can be detected by the UHOH lidar is limited by very high computational demand.
- The horizontal heterogeneities of smaller size than the resolution of the LES-AOP model were not captured

- Vertical variability in detail is missing due to lack of volume scan. Unavailability of low-elevation (of about 2°) PPI/RHI scan on 17 September reduced the number of possible cases for the intercomparison between the observation and simulation of the farm plume.
- In-situ measurements were incomplete during the field experiment on 20 September 2005. The aerosol compositions were assumed to be that of 17 September suggesting no change of the aerosol hygroscopic properties.
- No RHI volume scan was performed below an elevation angle of 4.76° and no PPI volume scan was available covering very low elevation to a high elevation performed with small elevation steps (< 2°).

The intercomparison results for the 17 September case showed that the LES-AOP could easily detect the aerosol emission from the farm by discriminating the farm contribution from the background in most of the cases when the scan was performed at an elevation angle of 2.26° and in some cases for the elevation angle of 4.76°. This is consistent with the results obtained with the UHOH lidar measurements both on 17 and 20 September. Both the LES-AOP simulated and UHOH lidar derived aerosol field for the PPI scans at an elevation of 4.76° did not show any clear signatures of farm plume. This suggests that the rise of the farm plume was very low (see, Figure 6.13, for further explanation on the scan geometry). Both the model and lidar results confirm that the shape of the farm plume in the instantaneous PPI scan is strongly influenced by the turbulence while the time averaged field shows an approximately Gaussian shape. This once again confirms the requirements for high-resolution scanning lidar measurements.

The intercomparison results show that the representation of the aerosol transport around the livestock facilities can be obtained with the combination of the state-of-the-art eye-safe scanning lidar technique, in-situ point measurements and the LES-AOP simulations, as was performed within the BW-PLUS project.

6.5 Summary and conclusions

A mobile eye-safe scanning aerosol lidar at 355 nm (UV) was developed. With 300 mJ pulse energy and a pulse repetition rate of 30 Hz, it was possible to observe the 2-dimensional structure of the particle backscatter coefficient in the ABL and the lower free troposphere with high resolution. The eye safety made the system useful so that it could be operated without restrictions. A modified approach to the lidar inversion technique was introduced and applied to scanning lidar measurements obtained during PLUS1 campaign. This system demonstrated for the first time the application of a UV scanning aerosol lidar technique for investigating the optical properties and spatial distribution of the aerosol plume from a livestock facility. It was the first field deployment of the system. Tracking of the aerosol features yielded possible investigation of the boundary layer depth, and a clear recognition of a faint aerosol source (livestock farm) including both emissions and transportation processes.

A novel approach was introduced for the determination of the optical properties of aerosols by means of spatially and temporally high-resolution lidar measurements in combination with numerical simulations of aerosol optical properties with a high-resolving atmosphere-microphysics-chemistry model. During PLUS1 campaign near a livestock farm in Mettingen, Westphalia, Germany, from 11-21 September 2005, data for the novel approach were collected.

Lidar measurements and aerosol in-situ measurements were performed. The investigated aerosol source was weak, i.e., not visible with the eye; it caused an increase of the aerosol number density downwind of up to 5 % in the lowermost 50 m of the atmosphere. The primary particulate matter emission flux was estimated from model results to be 100-500 g/h. Particle backscatter coefficient values of the aerosol plume were of about 30 % higher than that of the background aerosol contribution. With the aid of the scan strategy, it was possible to investigate aerosol transport arising mainly due to the prevailing winds close to the source and up to a distance of more than 3.0 km. The lifting height of the investigated plume was found to be of about 20 m AGL near the source and of about 115 m AGL in the extended region at 3.0 km. An averaging over longer time periods (of about 15 minute) showed a roughly Gaussian-resembling aerosol plume.

Downwind diffusion and associated expansion of the plume became clear from the results. The aerosol structures presented through the PPI scan images showed very high particle backscatter coefficient of 1.0×10^{-5} m^{-1} sr^{-1} at a distance of about 1.5 - 2 km from the source. Longer time series of such scan patterns will yield more insight into the emission and transport of the plume during different episodes of ABL regimes. Due to the lack of in-situ measurements on this day, investigation of aerosol composition was not possible.

Intercomparison study shows that the there are certainly some differences in the particle backscatter coefficient field obtained with the UHOH lidar and the LES-AOP simulation. The model was capable to represent the intensity of the farm contribution with some uncertainties. As for this day (20 September 2005) no in-situ aerosol data were available to initialize the model; the lidar measurements and model results could not be compared directly. This also yielded a limitation in the model simulation to set the upper and lower emission scenarios that largely depends on the uncertainty coming from the ground measurements. The results agree in backscatter coefficient and shape of the plume with the measurements.

The combination of eye-safe scanning lidar system and the high-resolving atmosphere-microphysics-chemistry model will be able to investigate the aerosol emission of diverse sources like motor traffic, power station emission, and emissions from various agricultural sources. Therefore, the methodology developed, has an extraordinary future potential for studying the emission of health-hazardous particles to assess the health related risk and evaluate the environmental policies on such issues. The uncertainties in the results can be reduced in future field experiments by improved in-situ and lidar measurements. The optical aerosol characteristics could be predicted only with a substantial uncertainty, ±50/70 % for the particle backscattering coefficient. This uncertainty comes from

inconsistency between the results from different techniques (gravimetric analysis and ion chromatography) applied even to the same measurements. Furthermore, in-situ measurements were incomplete during the field experiment. The experiences suggest that the forecast quality of the model could be improved by modification in-situ measurement strategy. The time resolution and the error of the mass regulation of the particle size-resolved measurement of the background aerosol could be improved by deployment of impactors with higher flow.

Very high-resolution and fast RHI/PPI volume scans can improve this study by an accurate investigation of the vertical extent of the plume. In future, the accuracy of the LES-AOP model can be increased by the use of aerosol optical properties derived from lidar observations in the estimation of the model initial values.

Chapter 7
Characterization of the convective boundary layer structure in a highly complex orographical region during PRINCE-2006

7.1 Introduction

Aerosol distribution over inhomogeneous low mountainous regions is a complex issue due to a variety of reasons. For instance, observations in hilly and mountainous terrain show that while the CBL structure in the early morning is highly inhomogeneous, the afternoon CBL structure tends to be horizontally homogeneous (Lenschow et al., 1979). Dayan et al. (1988) concluded that orography is a major factor determining the CBL height variability, rather than differences in synoptic conditions or land use. De Wekker et al. (1997) and Kossmann et al. (1998) investigated radiosonde profiles and aircraft data from field study in the Black Forest region of south-west Germany and showed two different behaviors of the CBL: evolution of a CBL that follows the underlying terrain towards a CBL which seems to be unaffected by the terrain in homogeneity.

Advection plays an important role in the CBL structure over hilly regions (Kossmann et al., 1998). Very few research studies have focused on the application of the state-of-the-art scanning lidar system for investigating the spatio-temporal variability of aerosol optical properties in complex mountainous regions.

In contrast to the lidar measurement from aircraft for estimating the spatial variability of the aerosol flow, scanning lidar measurement at ground from a single point is relatively inexpensive and needs comparatively less effort to change the measurement strategies. Hence, the purpose of the present study is to demonstrate the temporal and spatial variations of the aerosol flows in the CBL in association with the relevant dynamical processes over complex terrain. Prior to this campaign, the UHOH scanning aerosol lidar was transformed to a scanning rotational Raman lidar system. A brief description of the RRL is given in chapter 3. Procedures for the determining the aerosol optical properties are described in chapter 4.

Following critical issues have been addressed and resolved with the aid of scanning and vertical lidar measurements performed during the PRINCE campaign.

- How far is the scanning lidar technique capable of characterizing the complexities involved in the mountain induced flow and aerosol flow in the neighbor valley?
- How are the optical properties of CBL aerosols and their dynamics modified in a pre-convective environment over mountains?
- What are the major effects of irregular terrain on the classical CBL structures?
- How are the transport processes over the mountains modified during different times of the CBL evolution?

7.2 Brief overview of the PRINCE campaign

The present section deals with the observation and characterization of aerosol optical properties and aerosol transport in a highly complex orographical region during the PRINCE campaign (Groenemeijer et al., 2008) that took place in the northern Black Forest in southwest Germany in July 2006. The PRINCE campaign was aimed at the measurement of the atmospheric temperature and dynamics prior to orographically induced deep convection. To date, there is a large gap in the knowledge concerning when and where convective cells in the course of the day develops and what are the necessary elements of a field program concerning the measurement strategies.

This field campaign was part of a project COSI^{TRACKS}, which aimed at reliable statistical assessments of the frequency of convective storms, their damage potential and regional distributions. The major goal of the PRINCE campaign was to demonstrate the multi-sensor-based observations of the pre-convective processes in the mountainous region. Figure 7.1 shows the complex topography of the PRINCE campaign region with the location of the UHOH RRL system at the summit of the Hornisgrinde mountain (48°36´12.9´´ N, 8°12´3.5´´ E, elevation of 1161 m ASL). The campaign area covers the northern Black Forest as well as the eastern upper Rhine valley. The lowest elevation of the Rhine valley floor is around 120 m ASL and the highest elevation is the lidar site itself.

The UHOH scanning rotational Raman lidar was one of the many active and passive remote-sensing instruments, which were operational during the field campaign. Figure 7.2 shows a photograph of the UHOH RRL, the IMK (Institut für Meteorologie und Klimaforschung) Doppler lidar, and the IMK cloud radar on the Hornisgrinde mountain peak during the campaign. Additionally, the deployment of mobile teams releasing radiosondes was performed. The locations for the RS launches were adapted to the developing weather situations following PRINCE Operations center. Moreover, the added value of equipping a research aircraft with real-time satellite information and data from ground-based operational radars were evaluated.

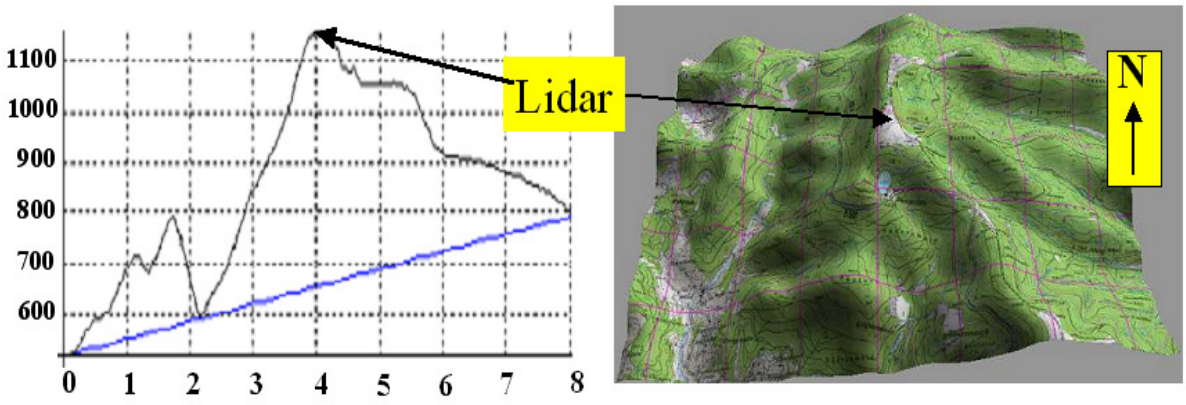

Figure 7.1: Location of the UHOH RRL at Hornisgrinde mountain during the PRINCE campaign together with the surrounding inhomogeneous orography (right). East west transect line over a distance of 8 km (keeping lidar at the middle) showing the change of elevation in m ASL (left).

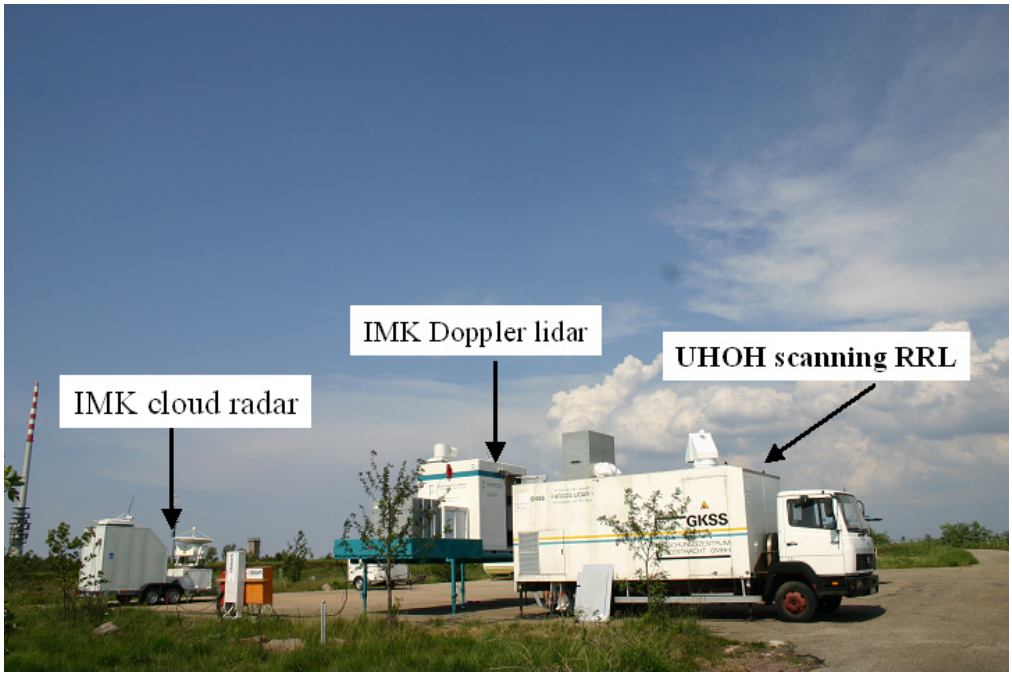

Figure 7.2: Photograph showing three remote sensing instruments deployed during PRINCE campaign on the summit of Hornisgrinde mountain.

7.3 Results and discussion

In the following, three different case studies are presented: (1) the first one concerns the data obtained on 12 July 2006 (case I) when the atmosphere encountered a convective storm cluster, (2) the second case highlights the complex aerosol dynamics in a CBL on 15 July (case II), and (3) the third case delineates the strong heterogeneity of the aerosol distribution during the daytime CBL evolution on 9 July (case III) arising due to the presence of RL, cumulus clouds, and orographical flow modification. The UHOH RRL detected how various layers of enhanced particle backscatter were influenced by turbulence resulting from solar heating and, possibly, developing convective storms.

7.3.1 Case I

Investigation of the range-resolved distribution of the optical properties of aerosol particles and their distribution during the pre-convective weather situation as well as after the passage of the convective cells are the main objectives of this case study. Recently, Groenemeijer et al. (2008) studied in detail this case demonstrating the application of multi-sensor measurement strategy while Trentmann et al. (2008) investigated the variability of the convective precipitation during this case on the basis of multi-model simulations.

A detailed description of synoptic weather situation during this case can be found in Groenemeijer et al. (2008). In the early morning of 12 July, storm systems were formed over the Rhine Valley about 30 km to the west-northwest of Hornisgrinde at around 0330 UTC. The first convective clouds were visually observed across the western and eastern slopes of the Murg Valley. Figure 7.3 shows two visible satellite images at 1200 and 1500 UTC on this day. It can be seen that at 1200 UTC, the cluster in the PRINCE region was one of the first storm clusters to develop, together with larger clusters in the southeast that developed over the Swabian Jura. Three hours later, the storm cluster was dissipated leaving some remnant cirrus fields over the Black Forest.

High-resolution fields of $\beta_{\lambda,par}(R)$ obtained (applying the RRL technique) with the UHOH RRL in vertically pointing mode is shown for two observation times: before the convection was initiated (Figure 7.4a and 7.4b) and after the cell passed by and convection broke down (Figure 7.4c and 7.4d). The temporal and spatial resolutions are 10 s and 7.5 m, respectively. Time series of CBL heights obtained with the HWT-based method are also overlaid on the time height cross-sections.

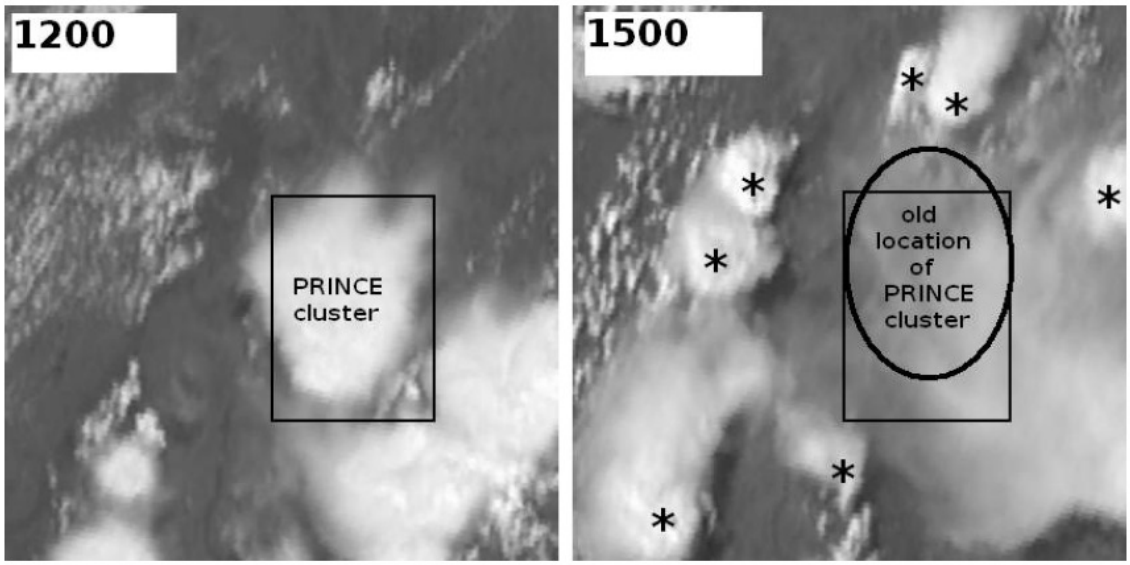

Figure 7.3: The "PRINCE" convective cluster observed by Meteosat 8 (VIS) at 1200 UTC (left) and the new convective development around the original cluster location at 1500 UTC on 12 July 2006 (right) marked by a star. The rectangle corresponds to the PRINCE region. Source: FZK / EUMETSAT.

It is important to note that the HWT-based analysis was applied on the vertical profiles of $\beta_{\lambda,par}(R)$ rather than on the range-square corrected lidar signal intensity. A well-mixed CBL was present over the experimental region in the morning of 12 July shortly after 0800 UTC. On this day, sunrise was at 0338 UTC and sunset was at 1928 UTC.

It is important to mention here that with the application of RRL technique, it has been possible to estimate the aerosol optical properties from an altitude of 200 m AGL. This new-overlap region could only be achieved due to the RRL technique.

Several radiosondes were launched at an interval of 2-3 hours during the day. They were launched from the radiosonde site on the western slope of Hornisgrinde at Brandmatt (of about 700 m ASL), approximately 3.0 km west of the mountain peak. Profiles of relative humidity and potential temperature for four-selected sonde (0700, 0900, 1300, and 1500 UTC) on this day are shown in Figure 7.5.

Figure 7.4a shows the presence of neutrally stratified elevated aerosol layers in the early morning over the lidar site at different altitudes between ground and 3.0 km AGL. The CBL height during this time was observed to be nearly constant at an altitude around 0.9 km AGL. No thermals were present. An aerosol layer with thickness around 200 m above an altitude of 1.0 km was detached having slight undulations throughout this measurement period.

A highly complex stratification within the lower 2.5 km AGL over the lidar site was present on this day. High backscatter coefficients at around 1 km AGL mark the boundary layer top as shown in Figure 7.4b. But the detailed investigation of the evolution of CBL top height is not possible since boundary layer cumulus clouds were present at the CBL top. Just below the cloud, $\beta_{\lambda,par}(R)$ was relatively high due to increasing RH causing growth of the cloud particles.

Due to the higher extinction inside these optically thick clouds, the lidar signal disappeared and no retrieval was possible. These regions are colored black as shown in Figure 7.4b. A second layer, which was probably related to an advected RL, was delimited in approximately at 1.4 km AGL. The 200 m thick layer with weak $\beta_{\lambda,par}(R)$ of about 1.0-2.0 x 10^{-6} m^{-1} sr^{-1} was still present. It was relatively dry and warm as was confirmed by the relative humidity and temperature profile obtained by 0900 UTC sonde (see, Figure 7.5b). Clouds observed by the lidar were developing at the CBL top in the crest of waves, which were probably excited by the mountain range.

An aerosol-clear layer at about 1.4-1.5 km AGL (Figure 7.4b) was associated with the temperature lid until 0930 UTC as was confirmed by the simultaneous temperature measurement by the UHOH RRL. Profiles of potential temperature obtained with the UHOH RRL for four selected times (of 0635, 0930, 1435, and 1710 UTC) on this IOP day are shown in Figure 7.6. At this time (around 0930 UTC), the earlier stratified aerosol layers were more and more mixed by turbulence. It is important to mention that the convection to the east of the mountain became organized after 0930 UTC, which

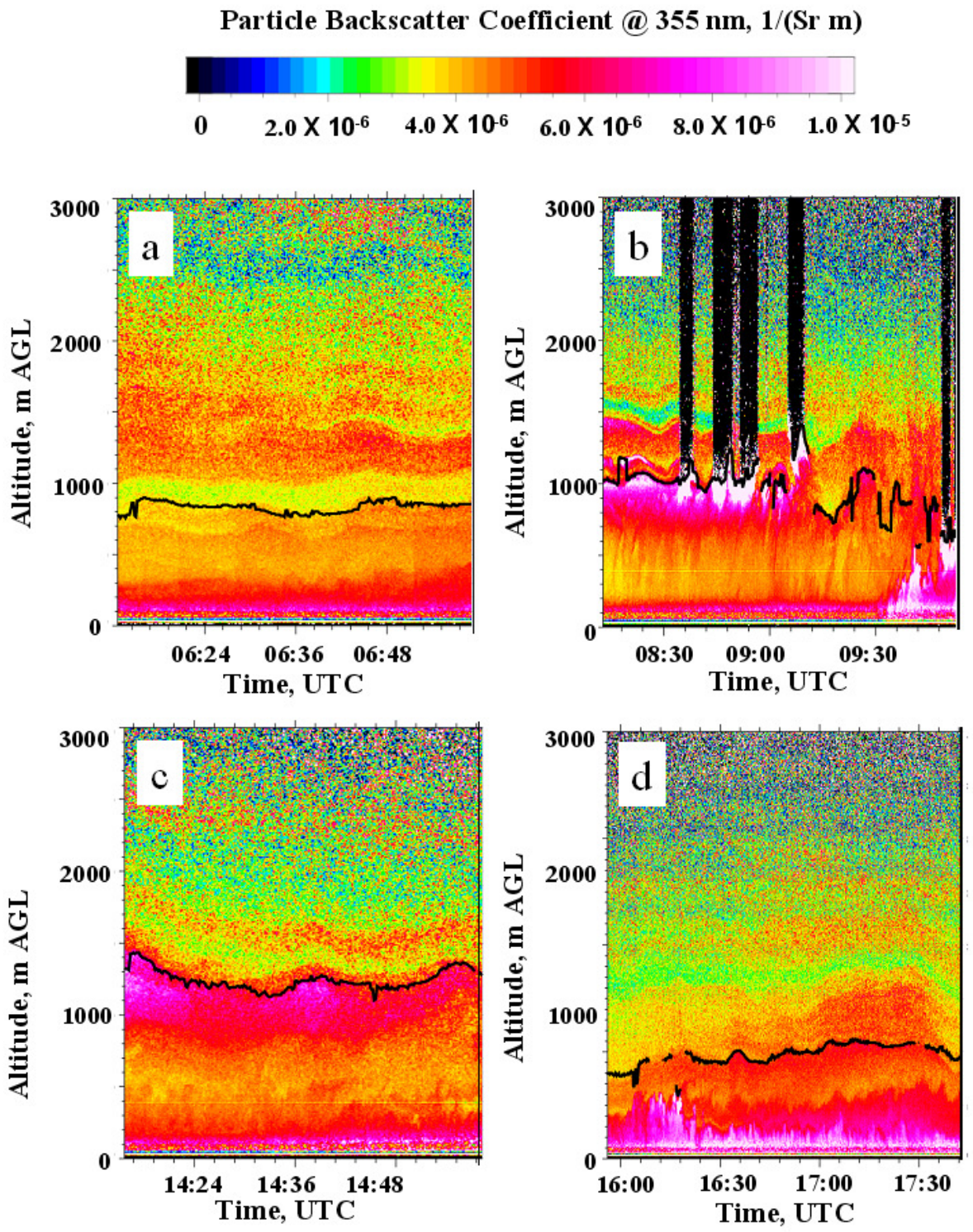

Figure 7.4: Time-versus-height display of $\beta_{\lambda,par}(R)$ field during four different regimes [a-d] of the ABL on an intensive observation period on 12 July 2006 during PRINCE campaign. The temporal and spatial resolutions are 10 s and 7.5 m, respectively. Clear air is indicated by blue. High value of $\beta_{\lambda,par}(R)$ is indicated by red to pink while clouds are marked by white. Evolution of CBL heights (black solid curve) is overlaid on each panel.

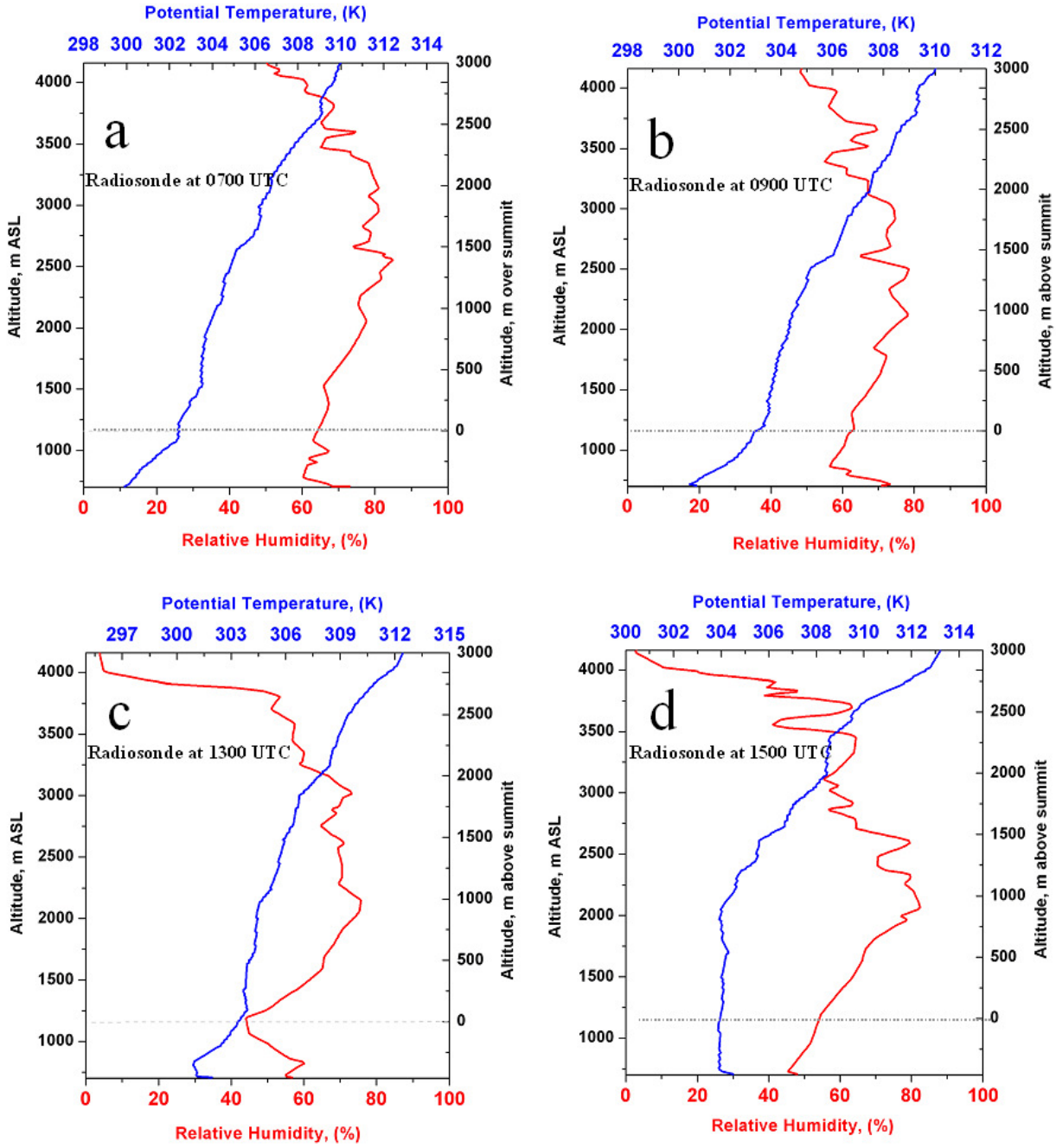

Figure 7.5: Radiosonde profiles of potential temperature (in K, blue curve) and relative humidity (in %, red curve) on 12 July 2006 during four different times (0700, 0900, 1300, and 1500 UTC) of the day, launched from Brandmatt. Vertical axis at the right side on each panel shows the altitude above the lidar site.

might have influenced the observed aerosol structure above Hornisgrinde. This might have been caused by advection rather than by insolation as the cirrus-shield remnants prevailed until late afternoon. At this time the heating of the surface was already low due to the low elevation of the sun, which was also seen in the fact that the well-mixed CBL was delimited to heights below 1 km AGL. Figure 7.4 depicts the complexities of the aerosol layers present during different times on this day. CIN and CAPE for a 50 hPa mixed parcel at Brandmatt calculated from the radiosonde profile at 0702 UTC were 62 and 994 (J/kg), respectively.

Collocated Doppler lidar measurement of radial velocity field obtained by an RHI scan (west to east) around 0933 UTC is shown in Figure 7.7. In color scale, the radial velocity values are plotted in the RHI panel. This figure confirms the presence of different aerosol layers those were observed by the UHOH RRL (see, Figure 7.4a and b). Easterly wind components of 1-2 ms^{-1} were observed throughout most of the layers to the east of the Hornisgrinde mountain. On the west of the mountain peak, a flow pattern with a bottom layer of winds with 1 ms^{-1} westerly component with a thickness of 700 m was observed. This corresponds to an upslope branch of mountain breeze.

Figure 7.4c shows that the CBL between 1410 and 1500 UTC was rather stratified with various separated aerosol layer present between 0.5 and 2.5 km with different particle backscatter coefficients. An aerosol layer above the CBL top (marked by the black solid line) was observed at altitudes between 1.7 and 1.8 km with relatively high $\beta_{\lambda,par}(R)$ of about 6.0 x 10^{-6} m^{-1} sr^{-1} compared to surrounding layers. The RH was high (of about 80 %) at these altitudes as can be seen from the 1300 UTC RS profile (see, Figure 7.5c).

Figure 7.4d shows a slightly elevated evolution of the CBL around 1700 UTC. The CBL height was dropped by 0.5 km during this time as compared to the case in Figure 7.4c. This is not surprising due to the decrease of the convective activities. The CBL was then stabilized around 1730 UTC but the aerosol layers above the CBL top were still present. During this period, a thick cirrus-deck was present at altitude of around 10 km AGL (not shown here). The presence of this cloud deck stabilized the CBL significantly reducing the insolation. Wave-like structures were prominent as can be seen from the field of $\beta_{\lambda,par}(R)$.

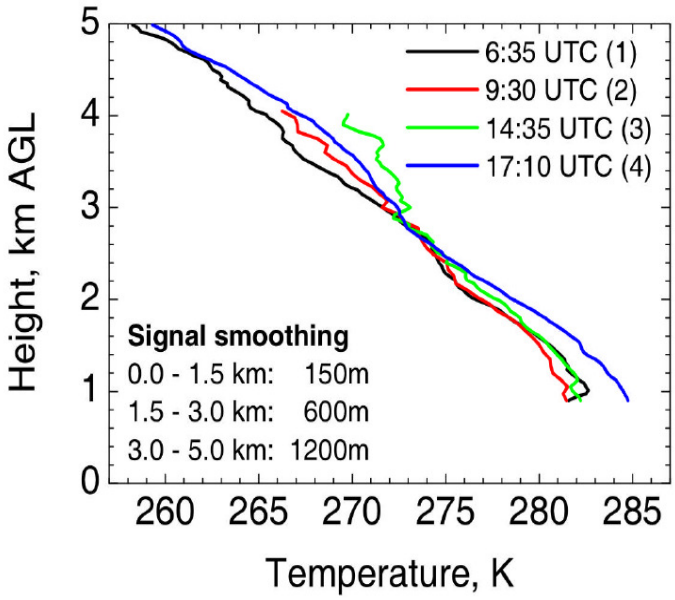

Figure 7.6: Temperature measurements with the rotational Raman lidar: profiles measured on 12 July 2006 at Hornisgrinde (1161m ASL). Lidar data were acquired around the indicated time during (1) 40 minutes, (2) 30 minutes, (3) 40 minutes and (4) 60 minutes, respectively. The spatial resolution is 37.5 m (profile 1, 3 and 4) and 75 m (profile 2). Lidar signals are smoothed with the indicated window lengths. The data error increases with altitude from approximately 0.2 K at 1 km to 1 K at 5 km AGL. Source: Groenemeijer et al. (2008).

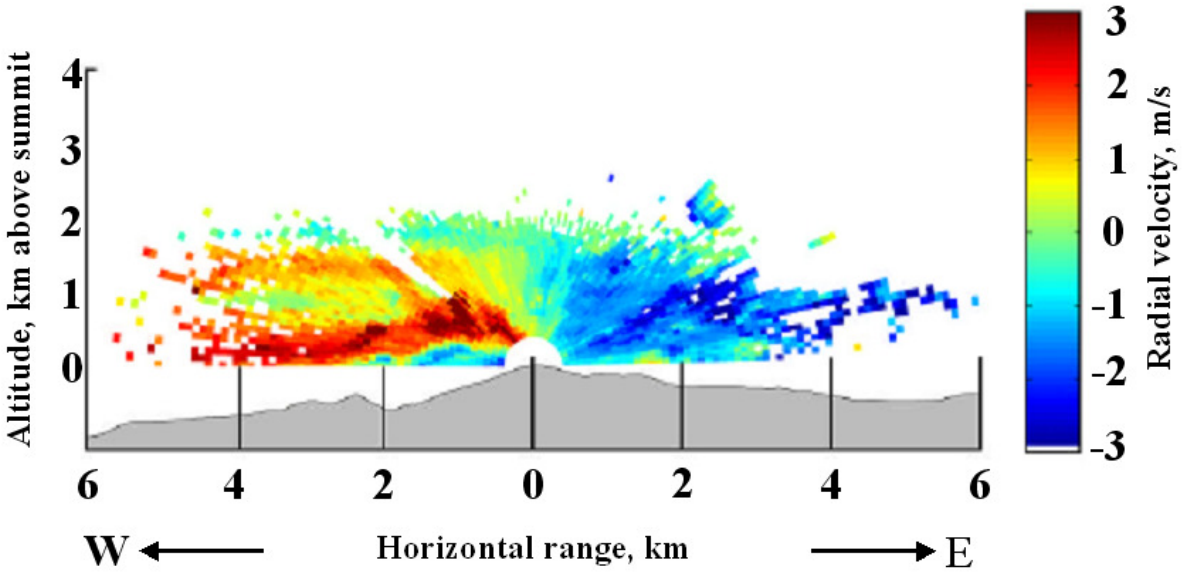

Figure 7.7: Field of radial wind velocity obtained with the IMK Doppler lidar around 0933 UTC on 12 July 2006. Scan was performed from west to east. Blue color represents a velocity component towards the system and red corresponds to the away from the system. Source: Groenemeijer et al. (2008).

After the convection broke down in the early evening, a pronounced temperature lid was present at height around 1.4 km AGL during the course of the day as evinced from the temperature measurements with RRL. Temperature measurements as shown in Figure 7.6 confirm that a lower tropospheric warming was occurred at Hornisgrinde. A comparison of the profiles of 0635, 0930 and 1435 UTC revealed a warming of the air above 2.7 km altitude. For example, at 3.8 km the temperature increased by 5 K in this period, most of it after 0930 UTC. Between 0930 and 1435 some warming also occurred down to 1.8 km AGL. Between 1435 and 1710 UTC, after the decay of the convective system, the air above 2.7 km was cooled again by approximately 2 K. This might be the main reason why there was no convection initiated at the lidar site.

7.3.2 Case II

During PRINCE, the UHOH RRL collected extensive sets of data with RHI scanning measurements. A subset of 6 selected consecutive RHI scans of 90 scans performed on 15 July 2006 towards east of Hornisgrinde is displayed in Figure 7.8. The images (a-f) show the vertical scan results from an elevation of 5° to 90° yielding a well-mixed CBL. By linking the scan frames through an animated gif, time-lapse animations of the atmospheric aerosol dynamics from few meters above ground can be investigated. This figure evinces the aerosol flow from east to west, which was governed by the wind driven transport. Each scan required of about 90 s to be completed. Scan speed was set to low (1.0° s^{-1})

to provide high angular resolution in the RHI field of $\beta_{\lambda,par}(R)$. Range rings at each 200 m are shown in the figures. Temporal and spatial resolutions are 10 s and 3.75 m, respectively.

A sharp decrease in the field of $\beta_{\lambda,par}(R)$ was observed at an altitude of about 800 m AGL along the horizontal distance of about 2.0 km indicating the presence of relatively cleaner air above. In pseudo-color scale, blue corresponds to the relatively aerosol free air and the red-to-pink region corresponds to the high particle backscatter coefficient. Migration of this structure in the lower CBL could be investigated in detail through the animation if the gravitational settling of the aerosol particles is ignored. A turbulent convective motion is visible from ground to an altitude of about 900 m. This is an indicative of the CBL top at that height. An entrainment zone is visible in the altitudes between 800 and 900 m AGL with highly variable $\beta_{\lambda,par}(R)$ field. Unlike case I, no stable residual layers were observed during this case. The CBL aerosol regime present in this case is strictly due to enhanced mixing process. The CBL top was present at around 800 m AGL most probably due to a temperature inversion

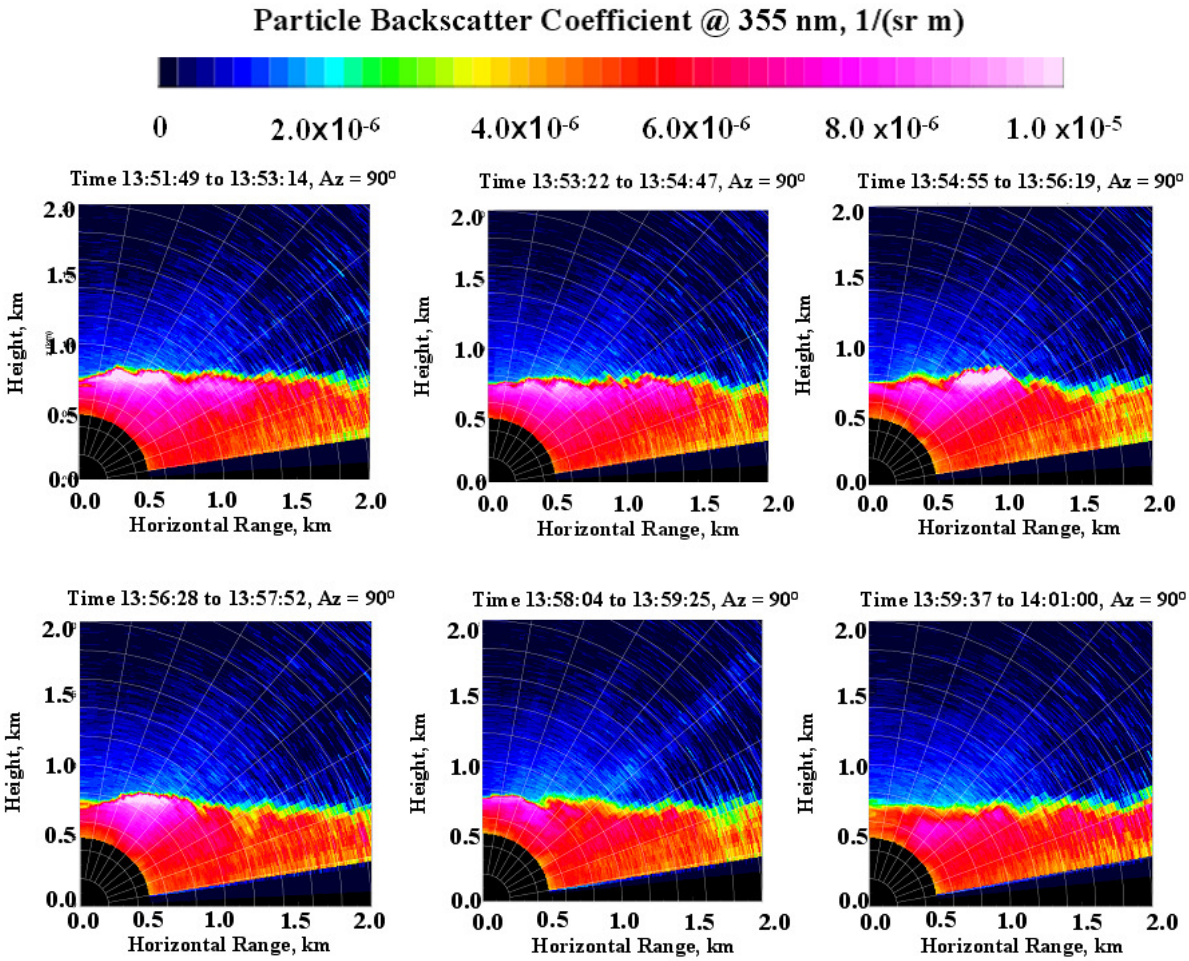

Figure 7.8: Eastward RHI sector scans from elevation 5° to 90° with temporal and spatial resolution of 1 s and 3.75 m, respectively. The scan speed was 1° s^{-1} thus the angular resolution is 1°, collected at Hornisgrinde on 15 July 2006 during PRINCE campaign. Selected 6 RHI scans of 90 such scans are presented here.

at this altitude that forced the aerosols to remain within the CBL. This case demonstrates the requirement of the sequential relatively long time RHI scans to study the CBL aerosol field, the CBL height and it spatial variability, and the associated entrainment inside the CBL in a complex topographical region like Black Forest.

7.3.3 Case III

Figure 7.9 shows the evolution of the aerosol field over the lidar site from 1000 to 1700 UTC on 9 July 2006. Temporal and spatial resolutions are same as in case II. Vertical axis is extended up to 2 km AGL to highlight the CBL portion in which convective mixing processes are visible. This figure shows the structure of the convective boundary layer over the mountain region during the course of the day. The Black solid line overlaid on the time-height cross-section represents the top of the CBL evolution determined by the HWT-based analysis. Only exception lies during the presence of low-level convective clouds over the measurement site.

A residual layer was present (green and yellow colored region up to an altitude of 1 km) during the early noon (until 1130 UTC) and became indistinguishable with the growing CBL. The $\beta_{\lambda,par}(R)$ values are nearly constant in the lowest part of the CBL, indicating the existence of a well-mixed boundary layer. The CBL height reached a maximum value of 1.0 km in the late afternoon. An undulation of the aerosol-laden CBL could be observed from the time series. Sharp rises of the CBL height from time to time were arising probably due to the presence of the Hornisgrinde mountain, which led to enhanced turbulence and drag, and then deepening of the boundary layer. Thermals were also present. Switching off or decaying of the surface forcing is considered to be the major reason behind the decaying of the CBL top around 1700 UTC.

The UHOH RRL lidar has one advantage so that the particle extinction-to-backscatter ratio (lidar ratio) can be directly measured from the two RRL signals as described in section 4.7. Lidar ratio profiles obtained at five different times (1115, 1245, 1430, 1530 and 1700 UTC) for case III are shown in Figure 7.10. The aim is to confirm the presence of different types of aerosol particles present inside and above the CBL on this day.

Lidar ratio profile at 1115 UTC yields a vertical variability with a value around 40 sr until an altitude of 1.6 km AGL. There is a sharp peak in the lidar ratio around 1.7 km AGL suggesting a very high extinction value as the time-height cross-section already evinced a relatively lower value of backscatter coefficients at this altitude.

Lidar ratios were found mostly between 35 and 45 sr with some vertical variability within for the aerosol measurements until 1300 UTC as can be seen from the profile at 1115 UTC and 1245 UTC. The $S(R)$ profile at 1245 UTC showed rather less variability in height with a value around 35 sr. The $S(R)$ profile at 1430 showed a sharp increase at 1.2 km AGL from 25 sr to 40 sr in the region of lofted dust (see, Figure 7.9) and decreased with height to 10 sr. A similar peak was observed in $S(R)$ at 1.8 km

AGL. Such similar values of lidar ratio confirm the presence of same type of aerosol particles in those heights indicating a pronounced effect of relatively large particles on the optical properties. Unexpectedly low lidar ratios (< 10 sr) were observed both inside and above the CBL during the late afternoon as can be seen from the $S(R)$ profiles at 1530 UTC and 1700 UTC. This is consistent with the field of $\beta_{\lambda,par}(R)$ as presented in the time-height cross-section in Figure 7.9. This confirms the presence of similar types of aerosol particles during the late afternoon.

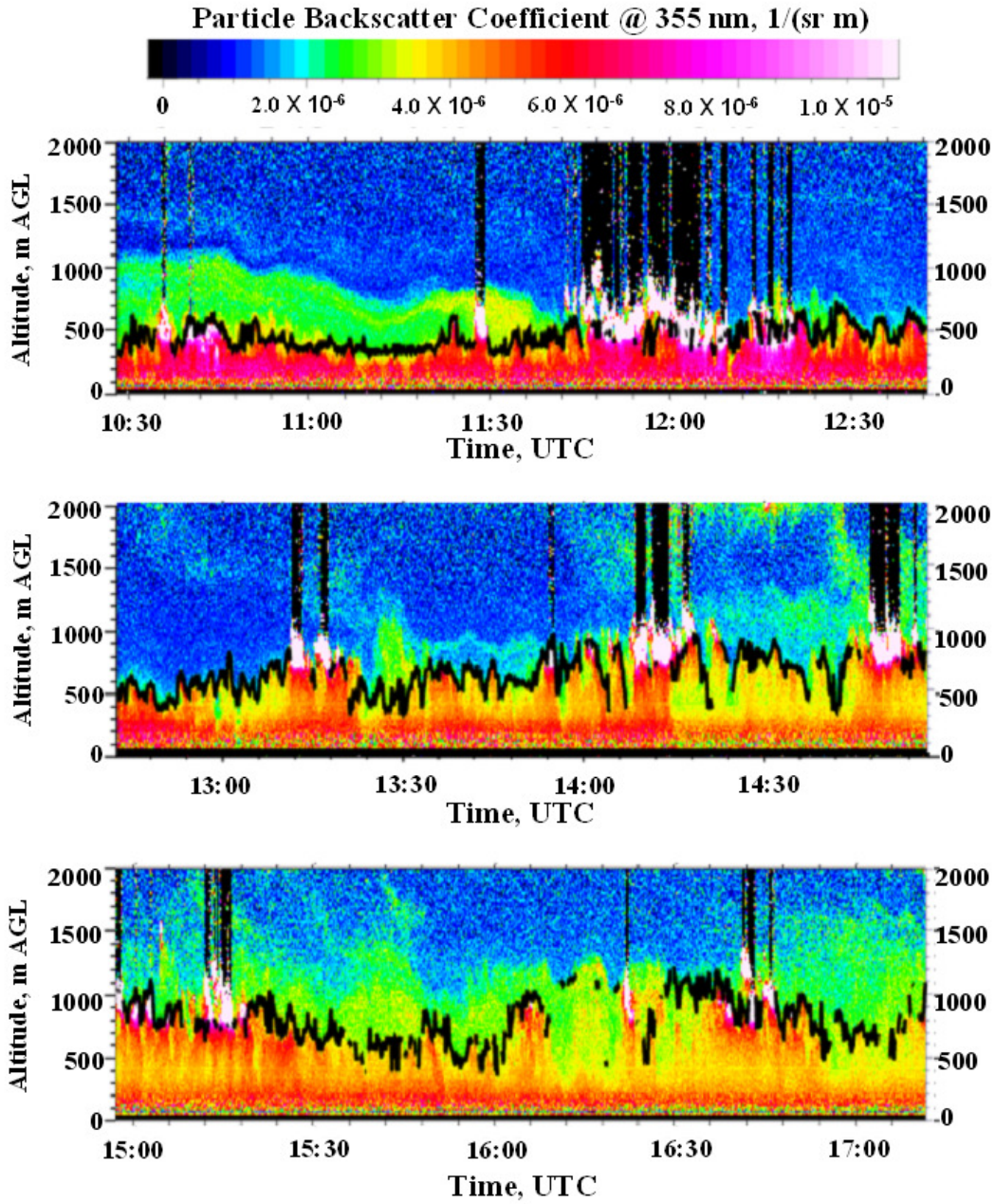

Figure 7.9: Lidar time series of particle backscatter coefficient from 1015 to 1715 UTC in three panels (from up to down) measured on 9 July 2006 during PRINCE campaign showing the well-mixed CBL. CBL top are marked by black-solid line on the time-height cross-section.

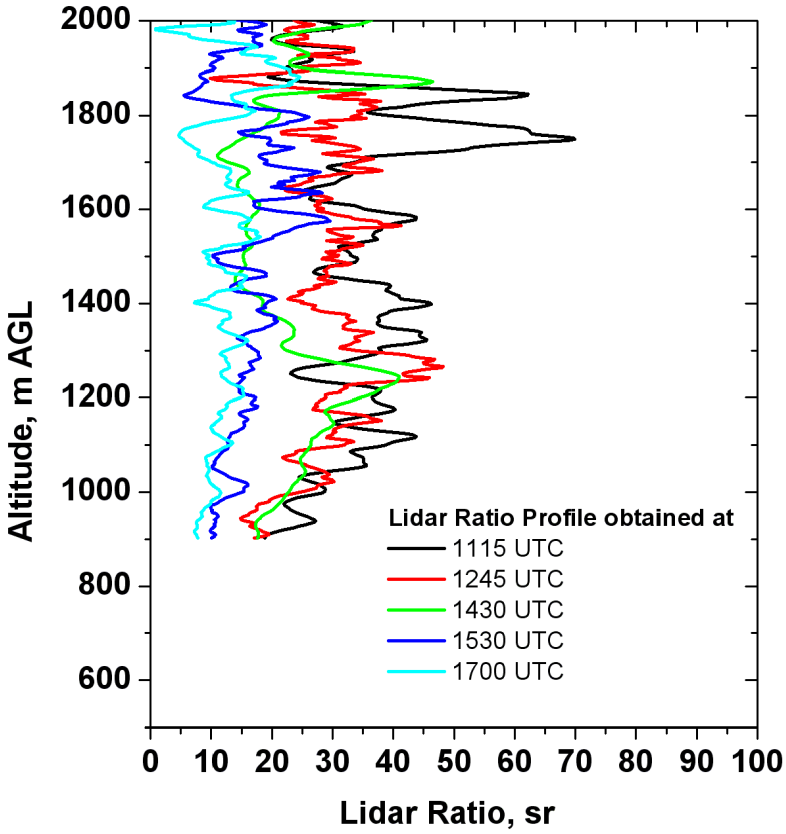

Figure 7.10: Measurements of the lidar ratio taken in and above the CBL during five different times of the day on 9 July 2006.

Through the analyses of the vertical profiles of lidar ratio, a key difference in the aerosol load and aerosol type were observed between noon (with high lidar ratios) and the afternoon (with relatively lidar ratios).

Figure 7.9 illustrates the presence of wavy aerosol layers during the first one hour of the measurement period (1030 to 1130 UTC) within the altitude between 0.5 and 1.0 km AGL. But the shallow CBL below was affected to a larger extent by the local orography and was more inhomogeneous than the aerosol layer above. This Figure shows the down mixing of the aerosol layer towards the growing CBL around 1130 UTC. These types of processes are largely responsible for the increase of surface pollution concentration (McKendry et al., 1997).

This case study yielded a frequent transportation of aerosols above the CBL height especially during the afternoon (after 1400 UTC). Also visible is that during these times, thermals became more vigorous. The venting of the pollutants above the CBL heights are referred to as “mixing-layer-venting”.

It is probably difficult to discuss the correlation between aerosols and the development of the cumulus clouds in the mountainous regions. However, it can be seen that aerosol layers above the boundary layer were observed only when $\beta_{\lambda,par}(R)$ in the boundary layer was high. Around 12 UTC, the cumulus activity was high and aerosol backscatter was high in the CBL but $\beta_{\lambda,par}(R)$ was low

above the CBL. On the contrary, around 1630 UTC $\beta_{\lambda,par}(R)$ was observed relatively high above the CBL height in the presence of cumulus clouds. This indicates that aerosols in the upper layer were transported from the boundary layer probably with the cumulus activity. The mechanism of the transportation and the effect of aerosols on the cumulus characteristics can be a very interesting topic for future study. Nevertheless, this type of characterization of CBL height evolution over mountain peaks is of particular importance for the better prediction of the dispersion of air pollutants over these regions, which is a poorly understood part of the CBL over complex terrain.

An FFT-based power spectral analysis (see, section 4.3.1) is performed on the instantaneous CBL height time series obtained between 1220 and 1320 UTC. During this time, CBL was well-mixed and no further aerosol layers were observed above the CBL height. Figure 7.11 shows the log-log plot of the normalized power spectra and frequency. The curve resulted a spectral exponent value of 0.9. The –5/3-power law is also shown in the figure (blue line). This value of γ suggests the CBL regime to be quasi-stationary. Similar results were obtained for a case of well-mixed CBL regime described in chapter 5.

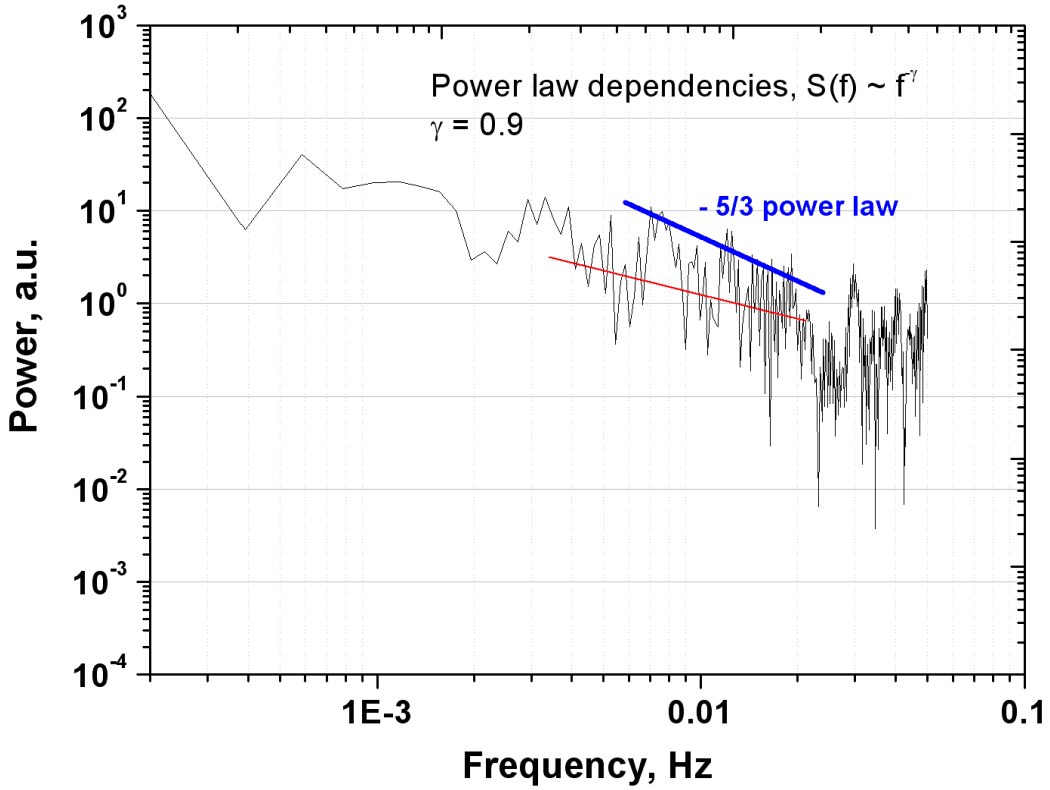

Figure 7.11: FFT power spectra for the CBL height obtained between 1220 and 1320 UTC on 9 July 2006 (case III). The blue line corresponds to –5/3-power law curve.

7.4 Summary and conclusions

The first scanning aerosol measurements with the rotational Raman lidar technique were realized during the PRINCE campaign in 2006. Within this campaign the influence of complex mountainous region on the CBL and the optical properties of aerosols and their transport and mixing under convective weather conditions were investigated. With both the vertically pointing and scanning measurements, multi-sensor measurement strategies from a complex mountainous region were demonstrated. Lidar observations showed single-layered aerosol structures, well-mixed boundary layer, multi-layered aerosol distributions, and oscillation in the aerosol layers during different days of the campaign. The CBL heights were found to vary between 800 m (1900 m ASL) and 1200 m AGL (2300 m ASL) during most of the campaign days.

During one IOP day (case I) in the PRINCE campaign, combined high-resolution measurements of aerosol optical properties and temperature field with the UHOH RRL revealed undulating aerosol-rich layers in the preconvective environment and a gradual warming trend of the lower troposphere as the nearby storm system evolved. The lower clouds inside the CBL were associated with the developing storm system, but the exact influence of these features on the convective initiation is not much clear.

Collocated Doppler lidar measurements of radial wind velocity confirmed the complexities in the various aerosol structures and their dynamics inside the CBL above the mountain. For instance, the case I showed that the top of the elevated easterly flow was approximately at the same altitude as the top of the boundary layer. This supports the idea that the air within the upslope flow out of the valley (here Rhine Valley) rose near the mountain top (Hornisgrinde) and returned towards the valley as part of this elevated easterly flow. The observations of the different aerosol layers at various altitudes over the Hornisgrinde mountain on this day showed that the height of these layers was rather constant but with slightly different $\beta_{\lambda,par}(R)$ values. These aerosol layers were found up to an altitude of about 3.0 km AGL. These results suggest that the aerosol layers over the mountainous regions are often very high than the CBL height.

Furthermore, the results obtained with the Doppler lidar confirming the upslope flow (from valley to mountain) and the return flow (as a part of a elevated easterly) suggest a consistent picture of the dynamics of these aerosol layers over the mountain as was observed by the UHOH RRL. These results illustrate that such transport are often efficient in the morning above the low mountain regions under relatively low wind speed, implying that aerosols in the higher layers during the morning or even during the noon are not necessarily remnants of residual layers, as it is commonly defined.

Time height cross-sections of the $\beta_{\lambda,par}(R)$ field on 9 July (case II) in this study showed significant variation in CBL height over timescales of tens of seconds. This was associated with very high variability of the aerosol distribution inside and above the CBL.

Independent measurements of vertical distributions of the particle extinction and backscatter coefficients were presented. The resulting lidar ratios indicated strongly variable aerosol layers. Even

on a same day, two different types of vertical variability of the lidar ratios were observed implying the presence of two different types of aerosol particles.

The CBL height varied between 0.5 and 1.1 km above the mountain and a residual layer above the height of the CBL persisted until the early afternoon. Unlike case I, no other aerosol layers at higher altitudes were observed. This suggests that the observed residual layers might have been remnants of the aerosols from the surrounding valleys. Whether this is the case requires further research. During this time, CBL growth rate was low enough. But the detailed investigation of the interaction between the RL and CBL was not possible as the CBL cumuli were developed at the same time when the CBL and the RL height became indistinguishable. An FFT-based spectral analysis of the time series of the height of a well-mixed CBL case yielded a spectral exponent value of 0.9 confirming a quasi-steady regime of CBL.

The results illustrated that the mixing and transport processes over mountain regions not only influence the CBL development and its modification but also enhance the vertical transport of the pollutants unlike over the flat and horizontally homogeneous terrain.

High-resolution RHI scanning measurements yielded spatial variation of the ABL structures with a significant aerosol plume with $\beta_{\lambda,par}(R)$ of 6- – 8 x 10^{-6} m^{-1} sr^{-1}. The CBL height during this case was found to be of about 0.8 km AGL with very small spatial variability over an extended region of 2 km. Time-lapse animations of the RHI scan images of the aerosol optical properties are an important data product obtained but unfortunately cannot be presented in a thesis.

Chapter 8
Investigation of temperature field and aerosol optical properties during COPS

8.1 Brief overview of the Convective and Orographically-induced Precipitation Study

COPS is a Research and Development Project (RDP) of the World Weather Research Project (WWRP) aimed at studying and advancing the quality of forecasts of orographically-induced precipitation in complex terrain. The overarching goal of COPS is to "**advance the quality of forecasts of orographically-induced convective precipitation by four-dimensional observations and modeling of its life cycle"** (Wulfmeyer et al., 2008). COPS focused at the identifications of the physical and chemical processes responsible for the deficiencies in quantitative precipitation forecast over low-mountain regions with the goal to improve their model representation.

A better understanding of the triggering mechanisms for convection caused by orographic effects is of immense importance. Therefore, the results containing the aerosol processes inside the CBL in the low mountain region is an important element to fulfill the overarching goals of COPS. Barthlott et al. (2006) confirmed in their study that the better representation of the flow patterns in mountainous areas improves the forecasting in these regions.

Within COPS, a dense network of state-of-the-art active and passive remote sensing systems was deployed during the three months long (June-Aug, 2007) field campaign in south-western Germany/eastern France region to observe atmospheric variables in three dimensions. Figure 8.1 depicts the locations of the COPS supersites over the complex orography in the Black Forest region.

A detailed description of the COPS field campaign (see, www.uni-hohenheim.de/cops/), research activities during the campaign (see, http://www.cops2007.de/), and the first results obtained are described in Wulfmeyer et al. (2008a), the COPS scientific overview document, and in the COPS field report, respectively.

The overarching goals and the detailed descriptions of the COPS campaign are beyond the scope of this dissertation. COPS was a unique opportunity to study numerous CBL processes in a complex terrain in diverse meteorological conditions during three months long period. Therefore, an extensive research is carried out within this dissertation using the data collected with UHOH scanning

RRL (Radlach et al., 2008a, b) to study various ABL processes. These include observation of aerosol optical properties in different times of the day and during different synoptic situations, the effect of orography on aerosol flow, aerosol transport, and aerosol turbulence processes. Combined and time synchronous synergic measurements of different lidar systems provided for the first time an unique potential to demonstrate aerosol process in ABL (e.g., distribution and dependencies of aerosol optical properties on relative humidity and temperature) and finally to demonstrate the application of sensor synergy.

For the first time the RRL technique is applied for RHI scanning measurement to determine aerosol optical properties (both particle backscatter and extinction coefficient and then corresponding lidar ratio) in 2-3 dimensions together with high temporal and spatial resolutions. This brings a new element to the lidar application for the ABL research.

The key ABL research issues addressed in this concern are:

- A detailed investigation of ABL over low mountain regions both during day and night.
- Demonstration of advanced scan strategies and potential benefit of multi-instrument dataset obtained during COPS.

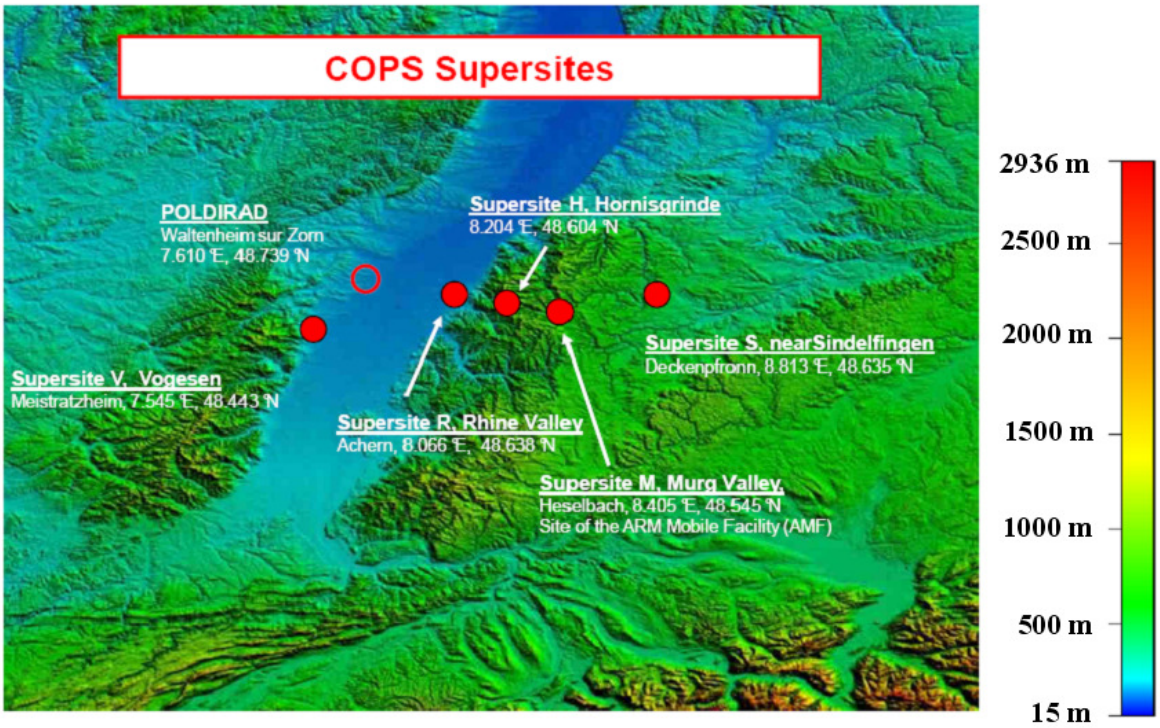

Figure 8.1: Set up of the COPS supersites overlaid on the orography. Color bar represents height above mean sea level. Source: COPS field report.

8.2 Instruments

In particular, two novel ground-based mobile scanning lidar systems were developed by the UHOH lidar group: a scanning rotational Raman lidar (RRL) which provides combined measurement of 3-d field of atmospheric temperature and aerosol optical properties with unprecedented accuracy, and a high-resolution water vapor differential absorption lidar (DIAL), which yields accurate measurement of water vapor fields and particle backscatter field at the near-IR wavelength. Differential absorption lidar is a technique which measures the water vapor number density with very high resolution in space and time by alternate emission of short laser pulses which are absorbed strongly by water vapor in the atmosphere (online) and which are weakly absorbed (offline) and by time-resolved detection of the atmospheric backscatter signals (Schotland, 1966).

During COPS, both lidar systems were located at the peak of Hornisgrinde mountain together with a large suite of remote sensing systems. The new scanning water vapor DIAL that was developed within three interlinked projects funded by the German Research Foundation (Deutsche Forschungsgemeinschaft, DFG) was deployed for the first time in the field during COPS. For brevity, this system is named here as UHOH DIAL in the following (see Schiller, 2009; for a detailed description of the UHOH scanning DIAL system). First results obtained with the UHOH DIAL system during COPS can be found in Pal et al. (2008).

Application of the UHOH DIAL system to estimate the water vapor mixing ratio is described in detail in Schiller (2009) while the synergetic measurements of different lidar systems (including UHOH RRL and UHOH DIAL) during COPS are discussed in Behrendt et al. (2008) and Wulfmeyer et al. (2008b).

8.3 Results and discussion

The RRL observations of selected profiles of the particle extinction and backscatter coefficients and then extinction-to-backscatter ratio at 355 nm wavelength (lidar ratio) under various meteorological conditions during the COPS field campaign are presented. Different scan patterns were performed during this campaign. These include:

- Continuous vertical measurements.
- Continuous RHI scanning measurements with an increment of 5° within the upper hemisphere.
- Combinations of time-synchronous RHI scan measurements and vertical measurements.

8.3.1 Examples of vertical measurements

Figure 8.2 shows an example of time-height cross-section of $\beta_{\lambda,par}(R)$ at 355 nm as derived from zenith-shooting RRL measurements between 1930 and 2045 UTC on 12 August 2007. This figure

shows the field of $\beta_{\lambda,par}(R)$ up to an altitude of 12 km AGL including cirrus cloud structures at an altitude of 10 km AGL. The right panel shows a zoom-in-view of the region (altitude between ground and 4.0 km AGL) marked by the rectangle in the left panel. This image yields the presence of the gravity wave structures in the residual layers. Wind was relatively calm in the boundary layer and was blowing from southwest at the mountain height while it changed slightly to westerly at an altitude above 600 m. Cirrus cloud layer showed an enhanced $\beta_{\lambda,par}(R)$ of >1.5 x 10^{-5} m^{-1} sr^{-1} due to the cirrus crystals.

High values of $\beta_{\lambda,par}(R)$ up to 4 – 5 x 10^{-6} m^{-1} sr^{-1} in the residual layer and a sharp drop of this value to 1 x 10^{-6} (m^{-1} sr^{-1}) above 2.2 km were due to high RH (of about 80 %) and the presence of dry layer (with RH of about 40 %), respectively. Collocated radiosonde retrieved RH profile as shown in Figure 8.3 confirms the high variability of the moisture structures present during this time. The zoom-in-view shows relatively high $\beta_{\lambda,par}(R)$ at 3 km height AGL and corresponds to the peak in the RH profile (increase up to 80 % RH).

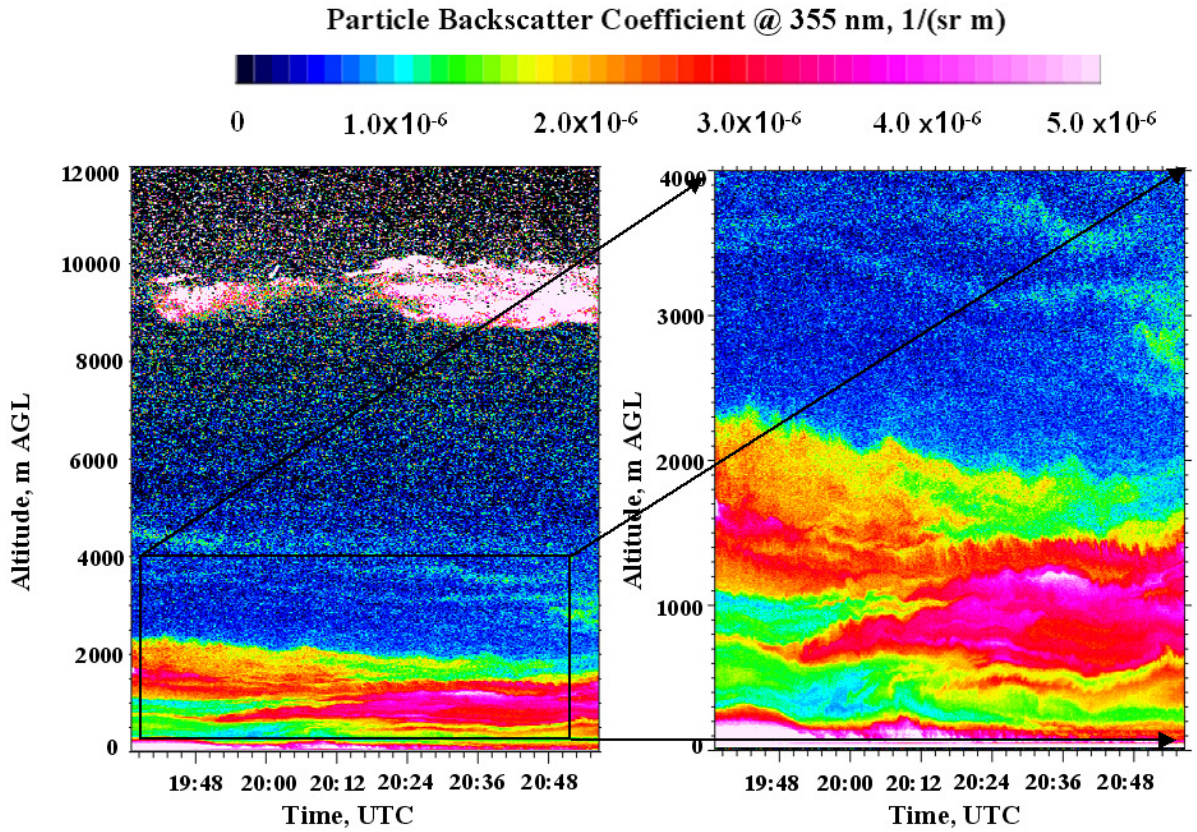

Figure 8.2: 13-s resolution time-height cross-sections of particle backscatter coefficient during night on 12 August 2007 showing the aerosol structure influenced by the local orography. A zoom-in-view of the field of $\beta_{\lambda,par}(R)$ is shown in right panel.

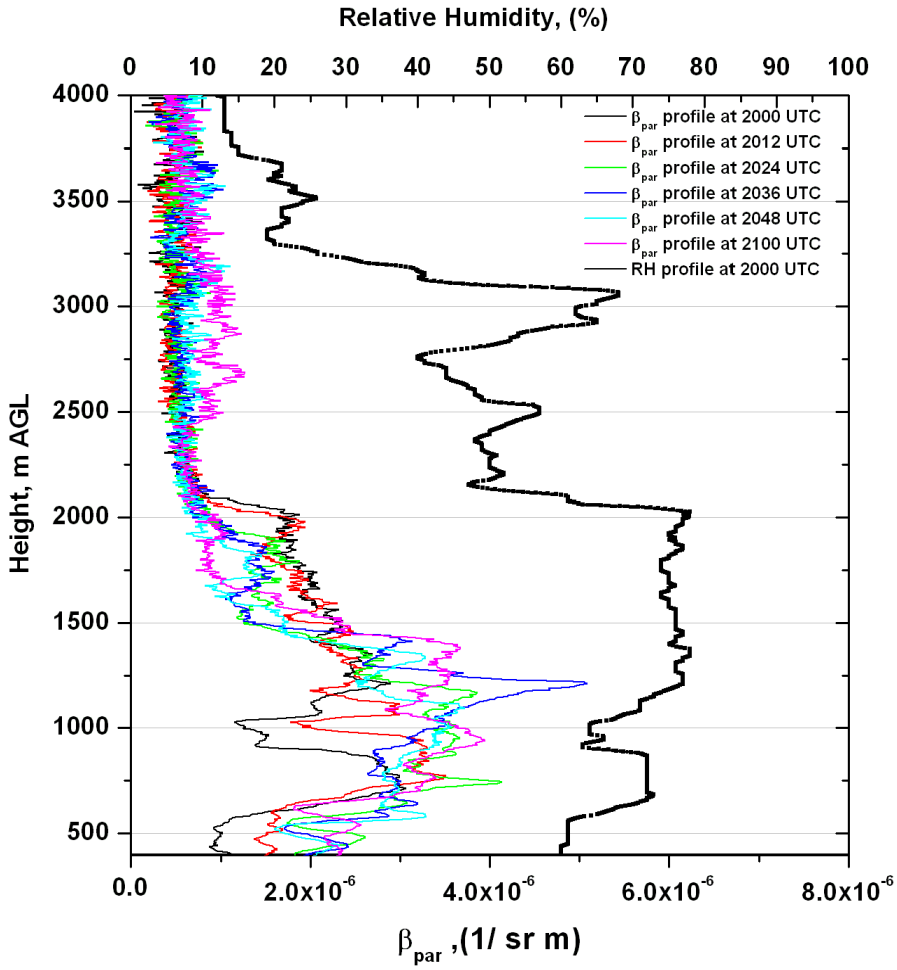

Figure 8.3: Vertical profile of particle backscatter coefficient at different times during the measurement period around 2000 UTC on 12 Aug 2007. Relative humidity profile obtained from collocated radiosonde is shown as black solid curve.

12-minutes interleaved vertical profiles of $\beta_{\lambda,par}(R)$ (at different times during the measurement as shown in Figure 8.2) from 0.4-4.0 km are shown in Figure 8.3 together with RH profile obtained from radiosonde launched at 2000 UTC from the lidar site. The dependencies of the particle backscatter coefficient on the RH values are higher in the lower altitude (between 0.4 and 2.0 km) due to the higher values of RH (of about 80 %). Relatively lower dependencies of the particle backscatter coefficient on RH in the higher height are arising due to the larger drift of the RS from the measurement site.

It can be seen from Figure 8.2 and Figure 8.3 that the structure of aerosol distribution is closely related to the structure of relative humidity. The structures of aerosol distributions in the ABL up to 2.2 km height and very thin aerosol layers above the boundary layer are observed up to about 2 km height coincide with high humidity values in those regions. As there is a similarity in distribution patterns of aerosols and relative humidity, a very simple relationship between the value of backscatter coefficient and RH is feasible.

8.3.2 Two-dimensional field of aerosol optical properties

During COPS, the UHOH RRL performed RHI scan in steps of 5° with a predefined start and end elevation angle. This is called discrete scan pattern (explained in detail in Appendix- B). Such hemispherical RHI scan patterns give an advantage to study the 2-d structure of both particle backscatter and extinction coefficients and therefore the comprehensive representation of the aerosol optical properties.

Figure 8.4 shows a sequence of three such RHI scans detailing the fields of $\beta_{\lambda,par}(R)$ (upper panel) and $\alpha_{\lambda,par}(R)$ (lower panel). These figures show a complex structure with a superposition of several aerosol layers between the surface and 4 km altitude and in different directions or elevations. Presence of layers with relatively lower aerosol loading at 0.9 km, 1.2 km, and at 3.5 km AGL suggests that the aerosol layers are decoupled. The origin of the relatively strong particle backscatter coefficient in the west is considered to be the aerosol layers trapped over the valley (see, Figure 8.1 for a detailed picture of the orography). These are basically the residual layers from the previous night stable boundary layer over these regions. The structures present in all scan images are consistent with the collocated RS profile of RH and temperature (not shown here). The increase in $\beta_{\lambda,par}(R)$ up to 5.0×10^{-6} m^{-1} sr^{-1} around 3.0 km AGL is due to the increase in RH at those altitudes.

Two different inversion layers observed in the 2-dimensional aerosol structures in RHI scan images are confirmed by the RS retrieved temperature inversions at 1.3 km and 3.0 km. These strong inversions are associated with the RL aerosols.

A key advantage of the UHOH RRL system is the independent determination of the ratio of the particle extinction-to-backscatter coefficients (denoted as $S(z)$). For investigating the physical properties of the aerosols observations presented in Figure 8.4, six selected vertical profiles of lidar ratio are shown in Figure 8.5. These profiles are determined from the RRL profiles collected at LOS of 90°. Temporal and spatial resolutions are 10 s and 37.5 m, respectively.

Figure 8.5 shows that the vertical distribution of the lidar ratio was approximately independent of height up to 2.5 km AGL. In this region, lidar ratios were between 20 and 25 sr. Few peaks were present as can be seen in the 0602 and 0608 UTC profiles. The sudden lofting of the lidar ratios is due to the thin aerosol layers at those levels. But there is step-like increase in $S(z)$ up to 60 sr around 3.5 km AGL. This implies that the aerosol below the height of 2.5 km AGL was of same origin while the aerosols in the altitude between 3.0 and 3.5 km AGL were certainly of different origin.

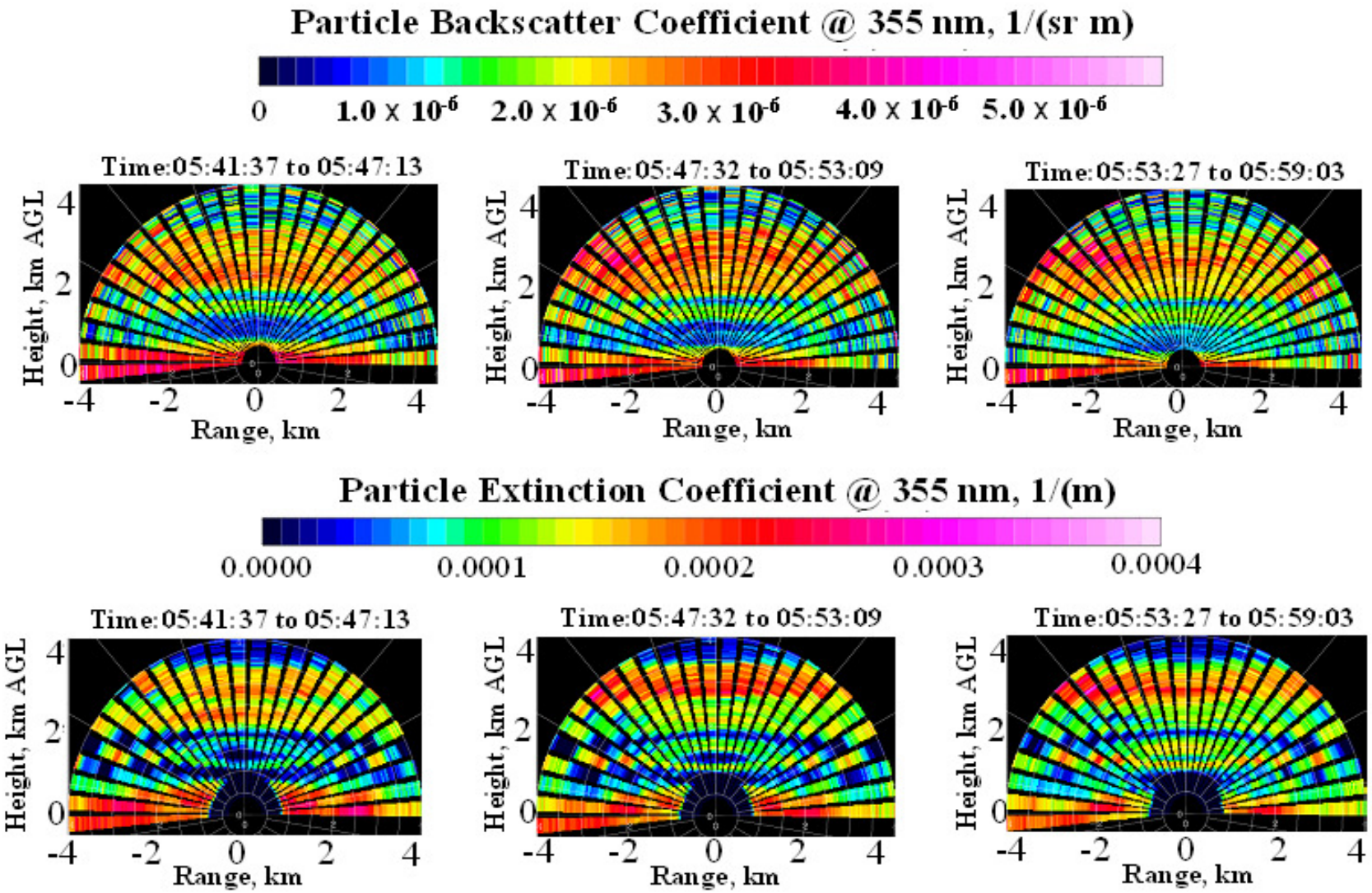

Figure 8.4: 3 consecutive hemispherical RHI scans from west-to-east showing particle backscatter (top panel) and extinction coefficient (bottom panel) field. Clearly visible is the presence of multiple aerosol layers in the early morning on 14 June 2007.

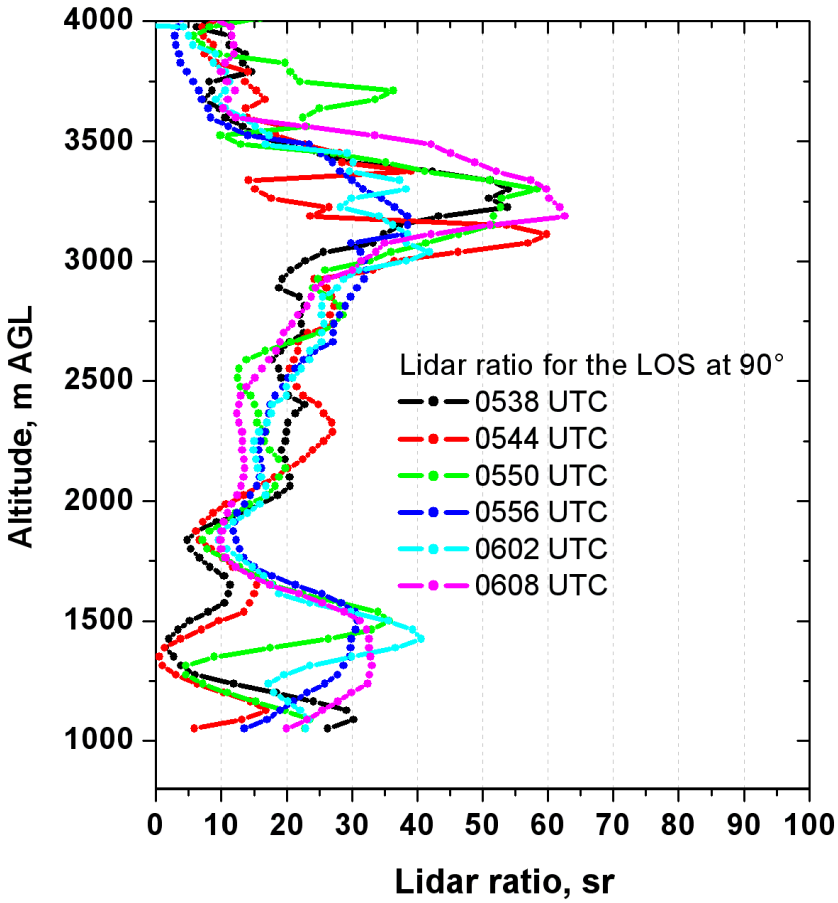

Figure 8.5: Six selected profiles of lidar ratio measured with the UHOH RRL during the RHI scan measurement presented in Figure 8.4. Lidar ratio profiles for the LOS at 90° are only shown.

RHI scan measurements of the aerosol optical field (see, Figure 8.4) and the vertical profiles of the lidar ratio presented confirms that the thick aerosol layers between 3.0 and 3.5 km were not originated from the ABL activities but advected from somewhere else. In general it can be stated that the lidar ratio in the lower altitude is rather low (< 30 sr) which is lower than for the aerosol types purely caused by anthropogenic pollutions. Whether these are due to the recirculation of local emissions or long-range transport can be confirmed by the backtrajectory analyses by locating the origin of these aerosols in higher altitudes.

8.3.3 Combined measurements of aerosol optical properties and temperature

On 25 August 2007 during IOP 18b (see, COPS Field Report, for a brief overview on the COPS IOPs), UHOH RRL performed a continuous RHI scan pattern as a part of supersite cross-section scan scenario. The aim of this scan pattern was to collect atmospheric variables in 2-dimensions in an extended region so that data collected from various supersites can be linked together to investigate the atmospheric flow patterns without any gap. Furthermore, this is a unique way to demonstrate the application of sensor synergy, which is a key research goal of COPS.

Figure 8.6 shows six consecutive hemispherical RHI scans performed on this IOP day between 1556 and 1629 UTC. Each scan took of about 5 minutes while RRL averages 650 shots in each LOS. The plane in which the RHI scan was performed was oriented towards the neighboring COPS supersites (azimuth of 291°). Temporal and spatial resolutions are 13 s and 37.5 m (10 range bins averaged), respectively in the particle backscatter coefficient field. Wind was blowing from southwest of the measurement site. Distinctly visible is that aerosol layers between 1.5 and 2.5 km were present. These layers were observed more or less at constant altitude throughout the one hour scanning measurement (not shown here). Steep temperature inversion at this altitude triggered such high $\beta_{\lambda,par}(R)$ followed by trapping of the pollutants.

Figure 8.6 shows that at the beginning (scan 1), two different aerosol layers were observed which started to couple as time progressed (scan 3 onwards). Orographically-induced aerosol flow dynamics is visible near the altitude of lidar location. This is likely to be due to the rise of aerosol-rich air masses from the valley to the height of nearest mountain peak (here Hornisgrinde) followed by the enhanced vertical transport on the steep slopes. These types of vertical transport process arising due to the presence of mountain peaks are referred to as “mountain venting”. In the boundary layer, the horizontal wind speed observed by the collocated radiosonde (see, wind barbs in Figure 8.8) was found to be of about 5 m s^{-1}. During this time, wind was mostly westerly.

The Rhine valley region (west of lidar site) consists of enhanced industrial activities where higher emissions of anthropogenic aerosols are not unexpected. High aerosol loading in the LOS at an azimuth of 291° towards Rhine valley (within 500 m above the lidar height) was most probably due to the trapping of the pollutants over this valley. This is observed from the figure that the vertical structures of the ABL over the valley region were composed of successive aerosol layers. The layers at the lower height are expected to be due to the valley emission and the higher layers are likely to be due to the combined emission, advection, and mixing. These results are also suggestive of the presence of the exchange processes over mountainous regions.

Figure 8.6 yields a situation of non-horizontal ABL top generated by differences in the terrain elevations. To date, such a high tempo-spatially resolved description of the exchange processes over complex terrain is rare in the literature. The high $\beta_{\lambda,par}(R)$ near the lidar site can be explained by the presence of humid air mass. The aerosol layers with high backscatter coefficient between 1.5 and 2.5 km AGL can also be explained by the profiles of the temperature and dew point temperature obtained with the collocated radiosonde profile (Figure 8.7) at 1654 UTC launched from the supersite Hornisgrinde. A relatively low particle backscatter coefficient field in the region between 0.7 and 1.5 km heights in all scans is arising due to the less humid air as observed in the RH profile obtained with the radiosonde launches.

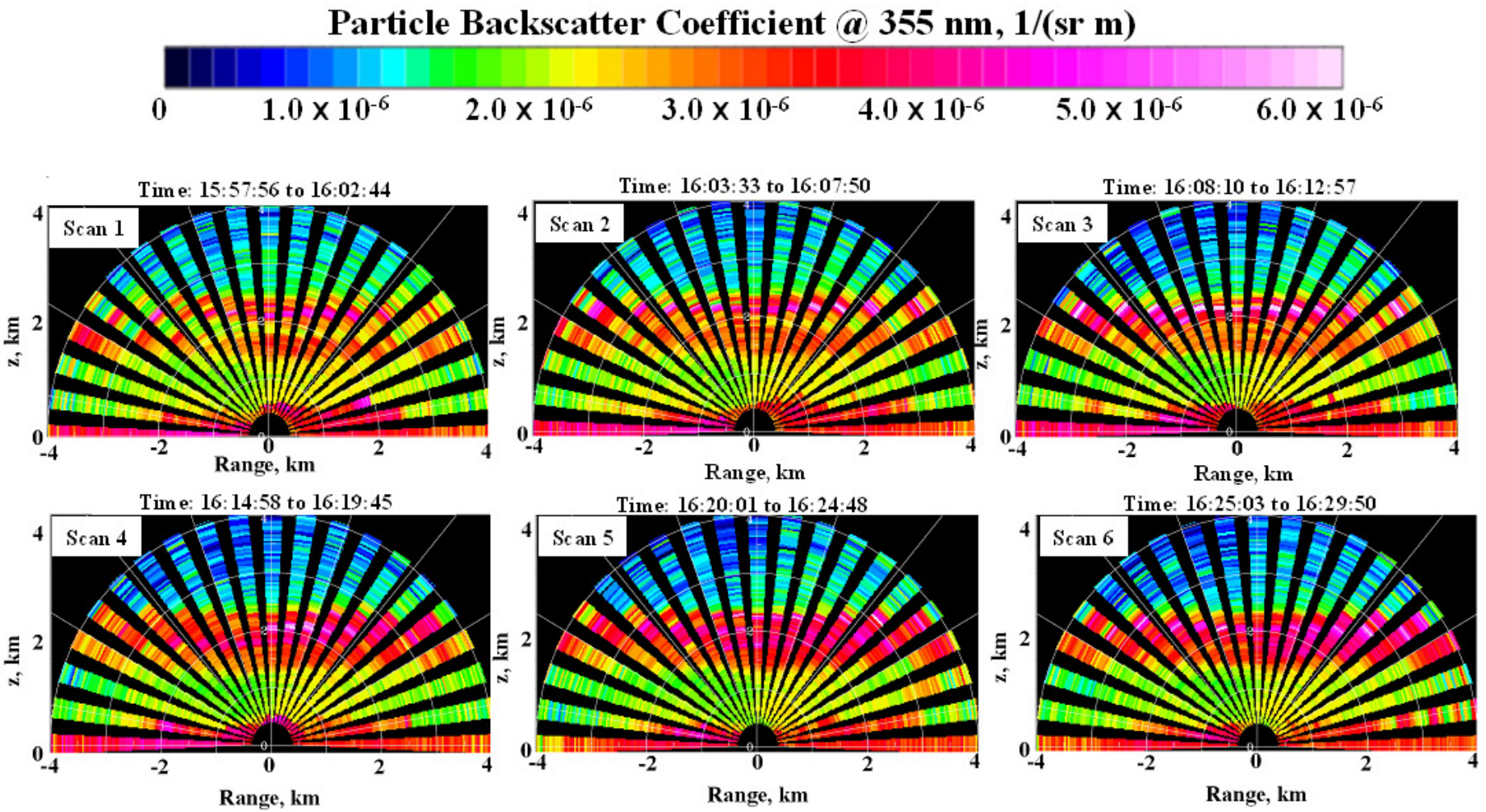

Figure 8.6: Sequence of six consecutive hemispherical RHI scans images (from top left to bottom right) of particle backscatter coefficient field around 1600 UTC on 25 August 2007. The plane in which the RHI-scan was performed was orientated towards the neighboring COPS Supersites (azimuth = 291°). Temporal and spatial resolutions are 13 s and 37.5 m (10 range bins averaged), respectively.

The field of potential temperature (commonly denoted as θ) derived from simultaneously measured temperature field with the RRL between 1600 and 1700 is presented in Figure 8.8 (see, Radlach, 2008c; for the method to calculate this variable). Potential temperature is defined as the temperature that a parcel of dry air would have if it were compressed to a standard pressure of 1000 mb. Since potential temperature is conserved for dry-adiabatic motion in the atmosphere, θ is kept constant within well-mixed layers and for descending (ascending) air parcels that are undergoing dry-adiabatic warming (cooling). At this time the elevation of the sun ranged from 20° to 10°. As can be seen from the wind barbs in Figure 8.8, the airflow was mainly westerly in lower heights (<2000 m ASL or of about <900 m AGL) and in the free troposphere (>3000 m ASL or of about >1900 m AGL). In between the wind was southwesterly orientated. Figure 8.8 shows some features that are consistent with ascending air motion due to overflow over the ridge as for rising air constant θ is expected. A warm θ-tounge was stretching downward just east of the mountain peak. This supports a process, which is mixing down air from aloft to the ground layer. $\beta_{\lambda,par}(R)$ was slightly increased (as shown in figure 8.6) within this θ-tounge.

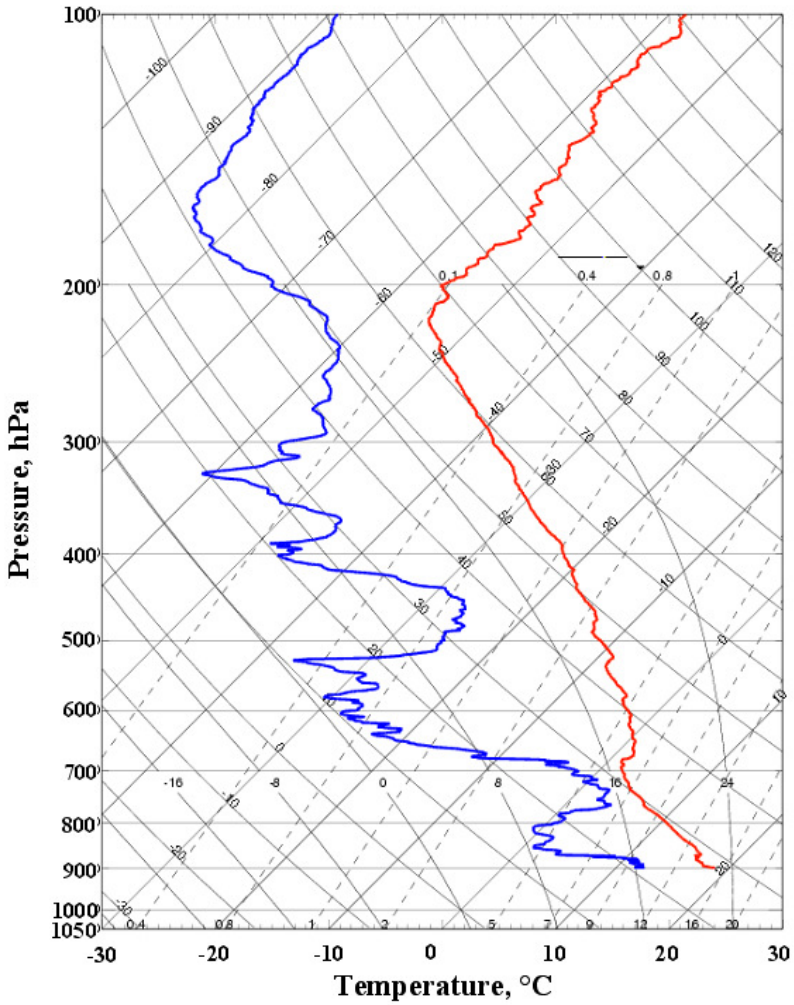

Figure 8.7: Skew-T Log-P diagram showing radiosonde ascent from supersite Hornisgrinde at 1654 UTC on 25 August 2007. Blue solid line is the dew point temperature and the red solid line represents the temperature.

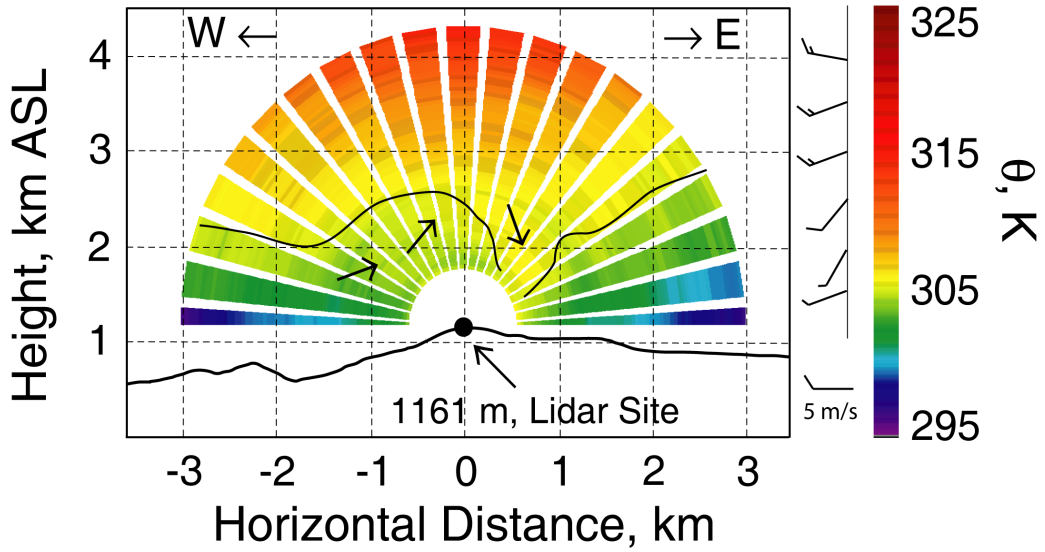

Figure 8.8: Field of potential temperature obtained with the scanning RRL for the same data presented in Figure 8.6. For this field 13 consecutive raw-data scans were averaged giving an averaging time of 3 minutes for each profile. The range resolution is 37.5 m. A gliding average of 300 m was applied. The wind barbs show horizontal wind data measured by the radiosonde launched at the lidar site at 17 UTC. The black line marks the potential temperature of 305 K. Source: Radlach et al. (2008b).

This case presents a brief summary of characterization of the dynamics of aerosol stratification containing mixed and detached (accumulation) aerosol layers over complex terrain and valleys. Similar phenomena have been extensively observed during different IOP days of COPS field campaign and offer a detailed description of the aerosol dynamics (as in this case) over mountainous region using the state-of-the-art lidar technology.

8.3.4 Optical properties and dynamics of cirrus cloud

The UHOH RRL lidar measurements in the early morning on 1 July 2007 yielded an interesting episode with the presence of a strong residual layer up to 2.0 km AGL and a 2.5 km thick cirrus cloud layer in between 5.2 and 7.7 km AGL. The left panel of Figure 8.9 presents the time-height cross-section of the range-square corrected signal intensity for the data obtained at the elastic channel of the RRL from 0400-0800 UTC. Investigations of the transmission and reflection properties of the cirrus particles and wavelet-based spectral analysis for determining various scales of turbulent motions present in them are aimed here.

Particle backscatter coefficient field obtained for this dataset is shown in the right panel of Figure 8.9 in the altitudes between ground and 4.0 km AGL. This figure shows high aerosol loading

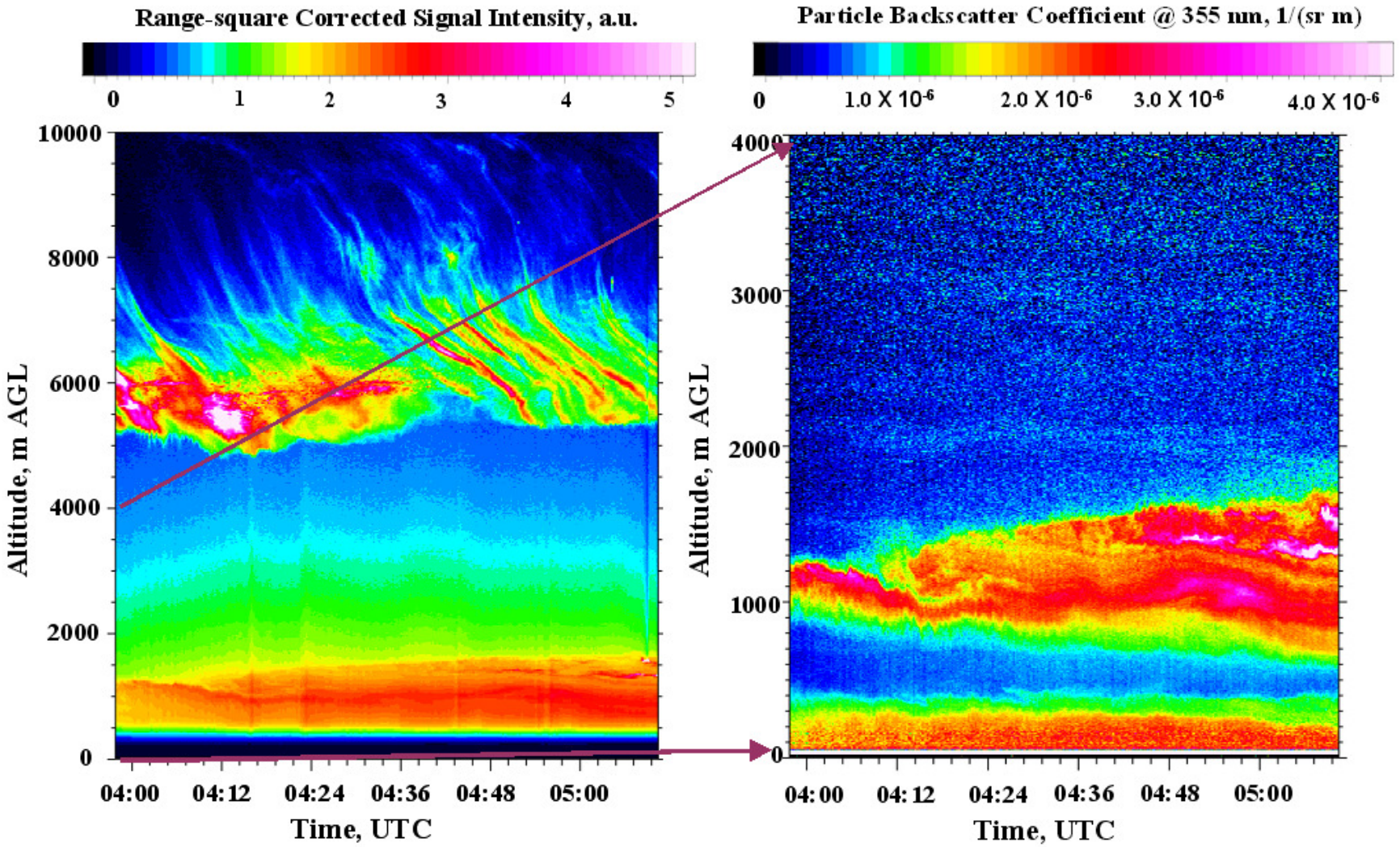

Figure 8.9: Range square corrected signal intensity of the elastic channel of RRL showing early morning stable boundary layer together with cirrus cloud at an altitude around 6 km AGL (left) and particle backscatter coefficient field between 200 and 4000 m AGL obtained from 0400-0500 UTC on 1 July 2007 (right).

between the ground and 2.0 km AGL. Obviously this is a stable RL with high backscatter coefficient of around 3.5 x 10^{-6}, m^{-1} sr^{-1}. A very low $\beta_{\lambda,par}(R)$ field between 0.5 and 1.0 km is arising due to a dry layer present in this region as confirmed by the collocated radiosonde derived RH profile. This feature is again confirmed after comparing the potential temperature profile obtained from the collocated RS profile.

Figure 8.10 presents an example of time-height cross-section of particle backscatter and extinction coefficients in the altitude of cirrus cloud layers (from 5.0-8.0 km) for the same time period as in Figure 8.9 showing the variability of the optical properties of the cirrus. Collocated sounding at 0500 UTC showed that the temperature in this cirrus layer varied from –20 °C at cloud bottom (of about 5.2 km AGL) to –36 °C at the cloud top (of about 8.0 km AGL) while the RH was fairly constant with a value from 60 – 65 %. The tropopause height was observed at 11.7 km during this time. Figure 8.11 shows 15 minute interleaved vertical profiles of lidar ratio belonging to this observation.

In general, in cirrus clouds, the extinction and backscatter and hence the lidar ratio can vary if layers of falling ice crystals are present. Lidar ratio profile in Figure 8.11 shows variability of lidar ratios in heights between 5.2 and 7.5 km from 3 - 25 sr. This large variability in the lidar ratio profile suggests that the observed cirrus cloud layer contained both horizontally oriented ice particles (for lidar ratio of about 3 sr) and ice crystals with considerable amounts of particles (for lidar ratios > 20 sr) larger than 300 µm (Takano and Liou, 1989). Platt (1978) showed that few oriented crystals could produce strongly enhanced backscattering and unrealistic low lidar ratios. The present case also showed a very high particle backscatter coefficient (> 2.5 x 10^{-5}, m^{-1} sr^{-1}) in the altitudes from 5.5 – 6.0 km AGL. Furthermore, dependencies of the lidar ratios on the cirrus thickness were investigated (not shown here) for the entire time period but no clear tendency was found.

Very often, to characterize cirrus layer properties, the lidar ratio corresponding to the ratio of the cirrus optical depth to the backscatter coefficient integrated over the cirrus layers is determined and is interpreted as the cirrus-layer “mean” lidar ratio (Seifart et al., 2007). For the present case, a value of 11 sr is obtained. It should be mentioned here that until now multiple scattering correction (Weinman, 1976) and effect of specular reflection (if present) are not taken into account for determining lidar ratios. However, the RRL technique used in this work has the potential to provide a reliable description of the cirrus optical properties, which is not achievable with elastic backscatter lidar technique. The cirrus layer showed both temporal and vertical variability of the lidar ratio. It implies that the inversion algorithm used to derive the extinction coefficients under the assumption of a height-independent lidar ratio will definitely yield erroneous results in such cases.

Optical properties of the cirrus clouds and their structures are necessarily influenced by small-scale features at high altitudes where turbulence is patchy or intermittent (Demoz, 1997). Smith and Jonas (1997) demonstrated the wavelet analysis to be an efficient tool to investigate turbulence characteristics in cirrus cloud. High-resolution lidar data is considered here to be an appropriate time

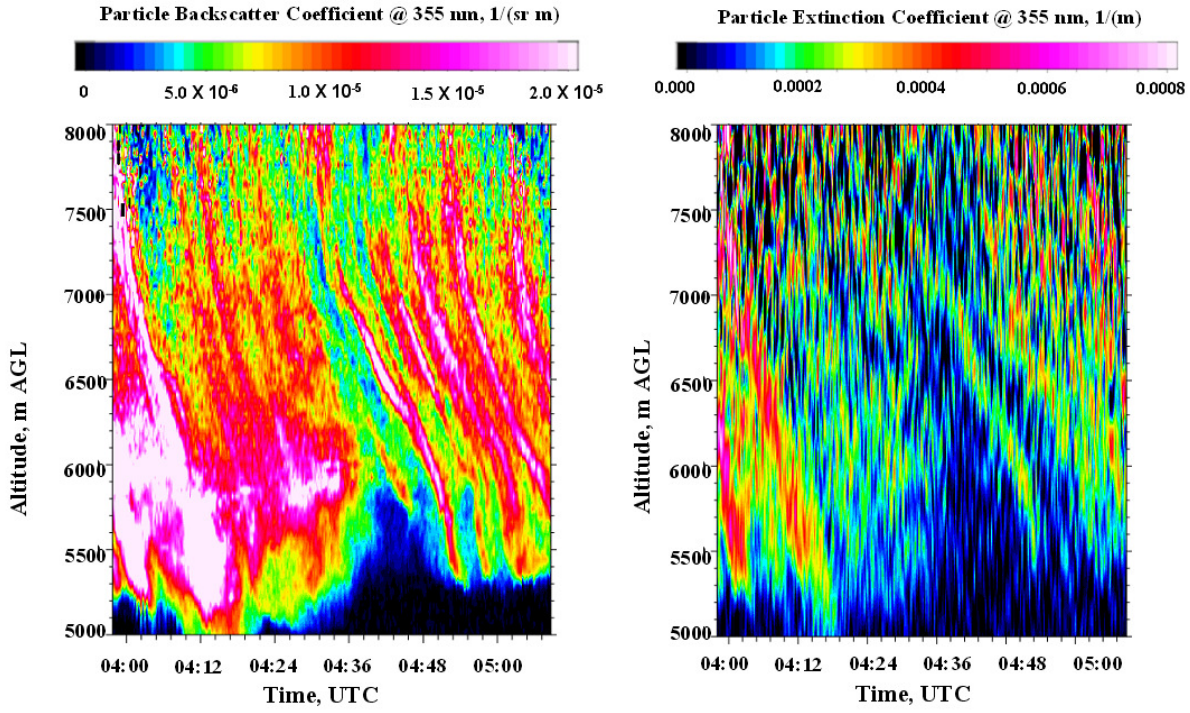

Figure 8.10: Time-height panel showing the particle backscatter coefficients (left) and particle extinction coefficients (right) in the region of thick cirrus cloud between 5.0 and 8.0 km on 1 July 2007.

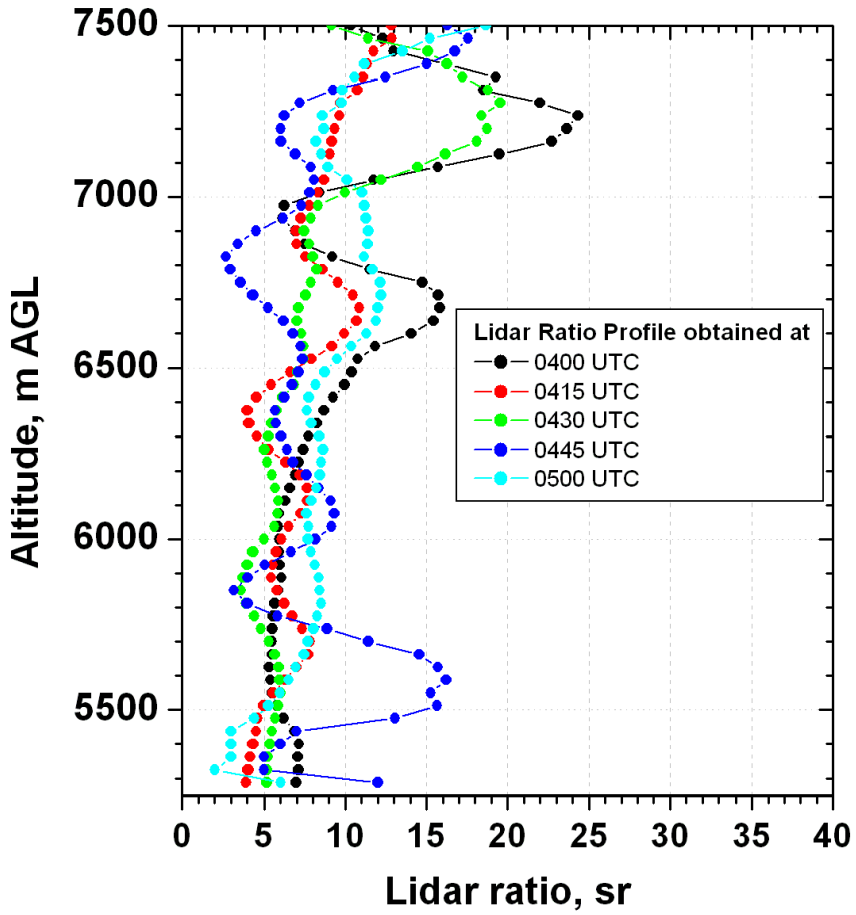

Figure 8.11: 15 minutes interleaved vertical profiles of lidar ratios for the cirrus layer observed on 1 July 2007.

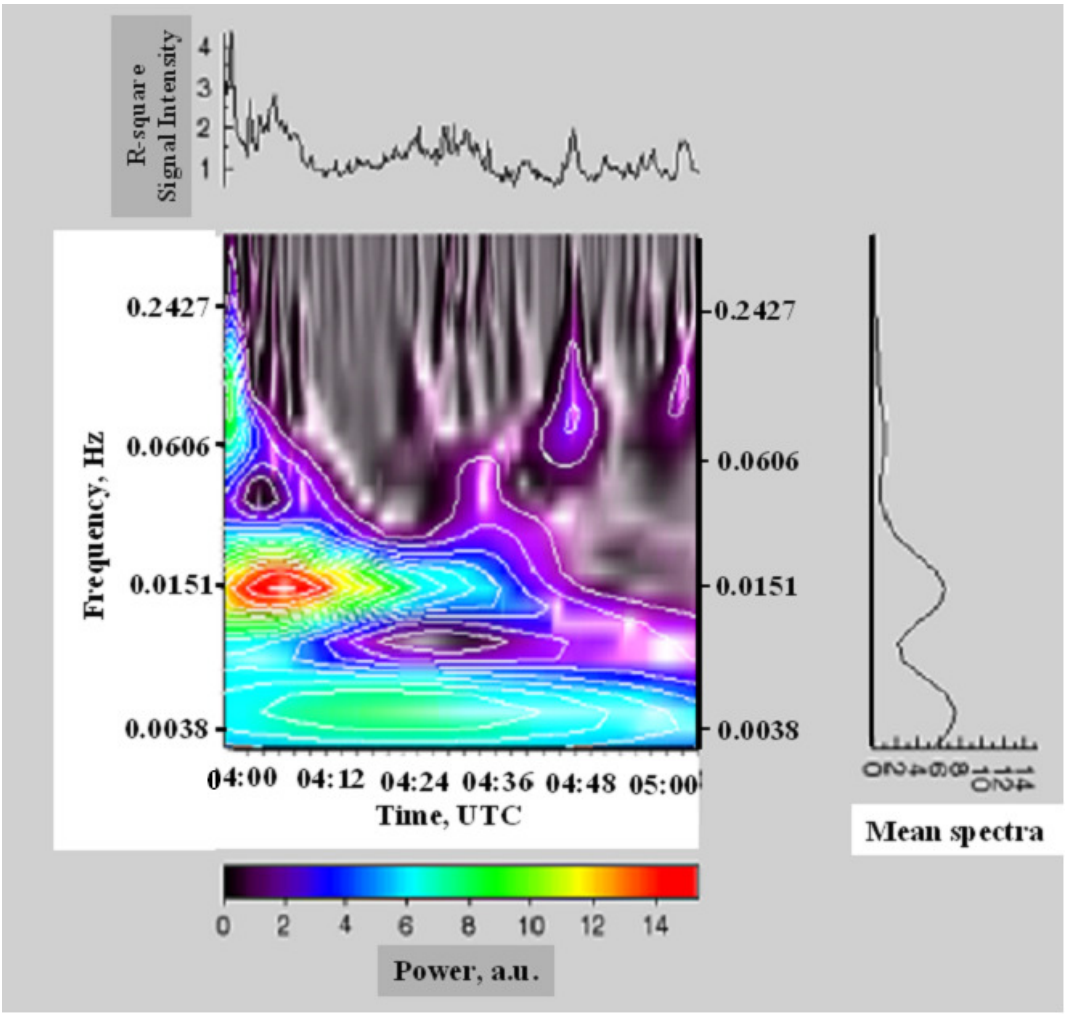

Figure 8.12: Wavelet scalogram for the time series of lidar signal intensity at an altitude of 6.0 km presenting the appearance of different scales in the wavelet spectra. This figure identifies the dominant frequencies present in the cirrus layer using wavelet analysis of an 80-min time series of lidar data. Contour lines are also plotted. Time series of the signal intensity (upper panel) and averaged global spectra (right) are shown (see text for further explanation).

series for applying wavelet transform to investigate the turbulence features present in the cirrus layer. Small-scale turbulence has an important influence on the cirrus structure. To extract small-scale turbulence features present in these layers, time series of range-corrected lidar signal intensity is treated here for the wavelet-based spectral analysis. Furthermore, the large vertical extension (up to 3.4-4.0 km) of the cirrus cloud layer presents an advantage to study the internal variability within them.

Some features have been obtained after the Morlet-based WT analysis (discussed in chapter 4) of the time series of range-corrected lidar signal intensities at 5.0 km altitude where the cirrus clouds showed maximum variability. This example case was selected to illustrate the type of the results that is expected from the localized space-scale analysis. The wavelet-based techniques fortunately are able to extract and analyze multi-scale features hidden in the time series and therefore is applied here.

Two to three different frequencies were found to be dominant after the wavelet analyses. Figure 8.12 shows the scalograms (time/period) of the time series of lidar signal intensity at 6.0 km where the

wavelet power spectra (average of absolute wavelength coefficient squared) are represented with pseudo-color scale increasing from black through green to red. Contours are overlaid for a better description of the wavelet spectra. It is important to note that the Morlet wavelet yields $\lambda = 1.03s$, where λ is the Fourier period, indicating that for the Morlet, the wavelet scale is almost equal to the Fourier period (Torrence and Compo, 1998). Time series of the signal amplitude at the selected height is also shown in the upper panel of the Figure 8.12. An interesting result deduced from the wavelet scalograms is that the different scales of 0.015 Hz are embedded inside the cirrus layers.

Two other peaks at 0436 and 0450 UTC indicate that the prominent contribution in variations is due to two scales centered about 0.06 Hz. Another small-scale structure was present in the scalograms at the beginning of the time series with a frequency of around 0.25 Hz.

Wavelet coefficients from the continuous analysis have been used to calculate global power spectra at the selected altitude and are shown in the right panel of Figure 8.12. The first peak in the averaged spectra is questionable since at this higher scale the edge effect is dominant and results are not reliable in this region. But the other scale corresponding to a value of 0.01 Hz with higher value of wavelet coefficient (red-color in the color bar) significantly demonstrates the presence of the corresponding frequency between 0400 and 0430 UTC.

8.3.5 Scanning lidar measurements of aerosol field

The UHOH DIAL system performed various scan patterns during the COPS IOPs. Two examples of RHI scan measurements of background-subtracted and range-square corrected offline signal intensity collected on 25 August 2007 (IOP 18 b) are shown in Figure 8.13. An aerosol plume is observed in this region colored in red against the green/yellow background. This shows how fast the aerosol particles can be lifted up to higher altitudes (towards the CBL top) triggered by the orography-induced convective activities.

Wind was blowing from west-southwest as was observed by the collocated radiosonde profile (see, wind barbs in Figure 8.8).

Continuous RHI scans were performed in such a way that each scan took of about 48 s both in forward (from elevation angle of 2° to 25°) and backward (from elevation angle of 25° to 2°) direction. The scan speed was set low enough ($0.5° \ s^{-1}$) in both directions to provide high angular resolution. The high laser power of the UHOH DIAL system allowed capturing the aerosol structure up to a distance of more than 12 km.

Figure 8.13 shows diverse aerosol structures around a Cumulus mediocris (Cu med) cloud. This cloud attenuated the signals beyond it. A thick aerosol layer was present at an altitude of 2.0 km AGL throughout the measurement period as has been seen in the time-lapse animation of 30 such consecutive RHI scans (not shown here). The animation reveals that two detached aerosol layers existed which were coupled as time progressed. Enhanced convective activity and the associated dynamics of the aerosol

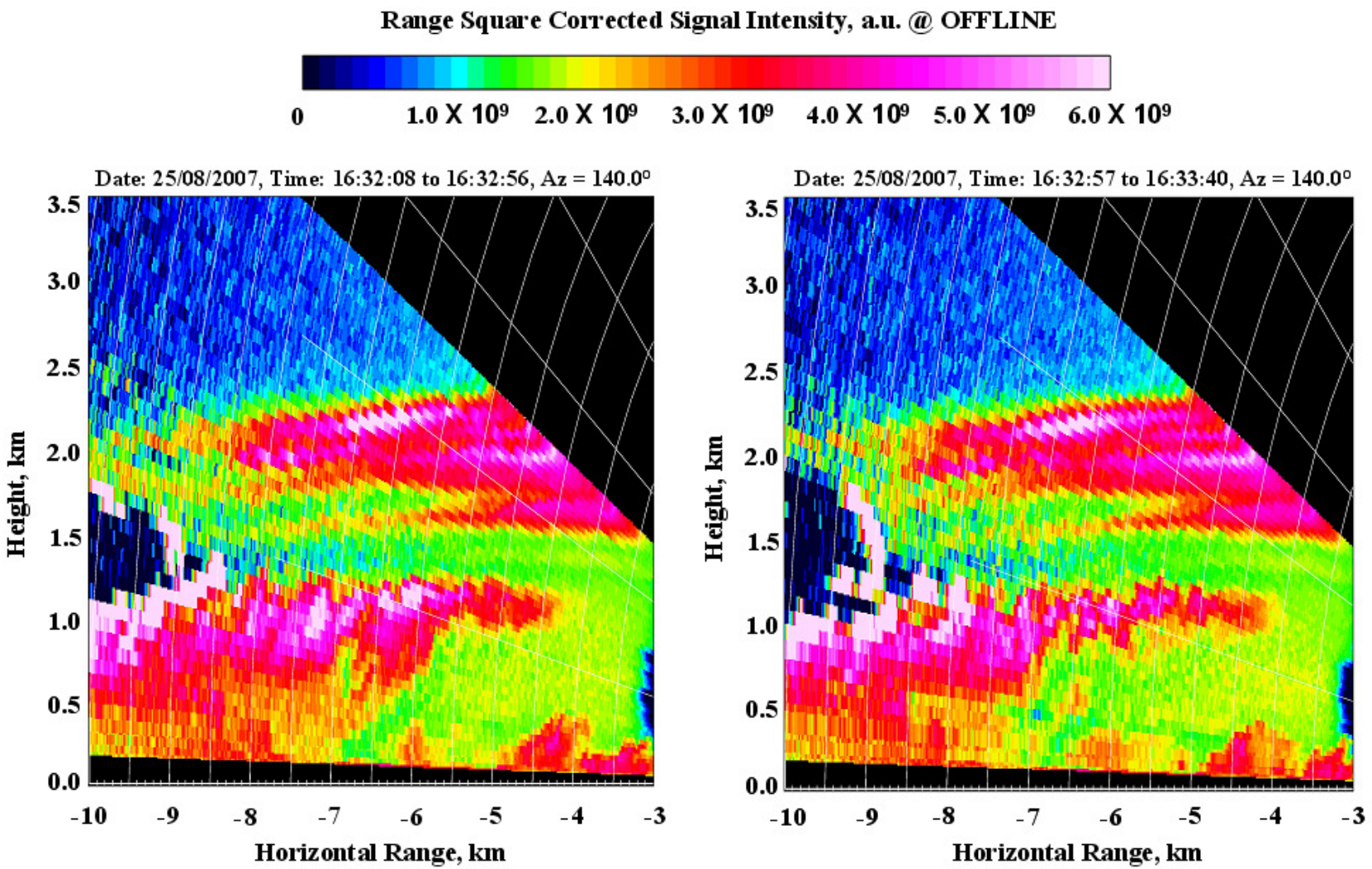

Figure 8.13: Example of RHI scans with the UHOH DIAL: range-corrected backscatter intensities showing the aerosol field around a Cumulus mediocris (Cu med) cloud. The scan speed was 0.5° s^{-1}, each profile is with 1-s average giving an angular resolution of 0.5°. Elevation angles of 2 to 25° are covered. The range resolution is 15 m. The horizontal scale gives the distance to the lidar in km. The scan direction was towards southeast.

plume in the height between 0.2 and 0.6 km are visible. Wind driven aerosol dynamics at a height of 1.0 km AGL can also be seen in the animation. The retrieval of the humidity field from such scanning measurements is in progress.

8.4 Summary and conclusions

High-resolution measurements of aerosol optical properties for some selected cases have been presented from the data obtained during the COPS field campaign in summer 2007. These results provide an important contribution to the CBL processes over low mountain regions like Black Forest. Orographically-induced flow modification has been studied in detail.

To best of my knowledge, for the first time 2-dimensional field of aerosol optical properties are determined after applying the rotational Raman lidar technique. This modified approach can give a better confidence towards the application of the scanning Raman lidars for studying the atmospheric aerosol processes with high accuracy. Measurement of aerosol optical properties during daytime with sufficiently high resolution is found to be an attractive feature of the UHOH RRL system.

The UHOH RRL measurement of aerosol optical properties during one case showed the presence of a thick aerosol layer up to an altitude of 3.0 km with a very high value of particle backscatter coefficient of about 6.0 x 10^{-6} $sr^{-1}m^{-1}$. This aerosol layer showed wave-like features over the mountains. The vertical distribution of aerosols yielded high $\beta_{\lambda,par}(R)$ up to 6.0 x 10^{-6} sr^{-1} m^{-1} which were highly correlated with the high values of RH of about 85 % derived from the collocated soundings. Some other aerosol layers with relatively low $\beta_{\lambda,par}(R)$ of 1.0 – 2.0 x 10^{-6} sr^{-1} m^{-1} were also present. In these layers, lower RH (of about 50 %) was observed. These results concerning the relationship between relative humidity and particle backscatter coefficient can help to obtain a better estimate of the hygroscopic factor. This is foreseen that these results can be improved by a combination of the simultaneous measurements of aerosol optical properties by UHOH RRL and the water vapor mixing ratio by UHOH DIAL system.

Independent measurements of particle extinction and backscatter coefficients, and the respective lidar ratio for the RHI scans confirmed two different types of the aerosol particles in the layers observed above the lidar site: one with a high lidar ratio of about 50 – 60 sr in the altitudes between 3.0 and 3.5 km and another with a relatively low values of lidar ratio of 20 – 30 sr below 2.0 km altitude. These results are of unique importance for obtaining valuable information on the different types of aerosols and their extent and structure inside and above the ABL over the mountain and surrounding valleys.

Combined measurements of 2-dimensional field of aerosol optical properties and temperature by RRL showed presence of different stability regimes over the mountain peak and their effect on the surrounding aerosol field. The RHI scan measurements presented for this case investigated some features that were consistent with ascending air motion due to overflow over the ridge. The distribution

of the aerosol layers over the experimental site showed the terrain following flow features. The particle backscatter coefficient was slightly increased within a potential temperature tongue. These results, once complemented with the collocated remote sensing instruments, will allow making use of synergetic data products to investigate and understand important processes that inhibit or support convection in low mountain regions.

Observation of optical properties of aerosols, and dynamics in the cirrus cloud structures were derived from RRL technique and wavelet spectral analysis of lidar backscattering, respectively. Lidar ratios between the cirrus cloud base (5.2 km) and top (8 km) showed both high vertical variability with minimum and maximum values of 3 sr and 25 sr, respectively. Furthermore, a temporal variability was also observed while comparing the lidar ratio profiles during one-hour measurements. Small-scale wave structures were determined from the Morlet-based WT spectra. The results obtained from this analysis are promising and could be extended to three months time period (whenever present) of the COPS field experiment. The main disadvantage of this technique is that only octave frequency bands are resolved.

It should be noted that the interpretation of lidar observation of only lidar ratios of cirrus clouds in terms of properties of the cloud particles is not a straightforward task. This arises due to the complexities involved in the scattering processes in the cirrus layers and the presence of various sizes and shapes. To make general comments on the cirrus particles observed in the present case, it needs further case studies. COPS will give an opportunity to get more insights using multi-instrument datasets (in this regard) for calculating depolarization ratio, optical depth, emissivity, height, and cloud height for different sorts of cirrus layers like sub-visual, thin and opaque cirrus clouds observed during three month period.

Various time-synchronous scan strategies during the COPS campaign were found to be an efficient technique to study the atmospheric variables in 3-dimensions. Simultaneous scanning measurements of temperature field and aerosol optical properties are other key findings for ABL process studies during COPS. The relative particle backscatter field observed during an RHI scanning measurement with UHOH scanning DIAL system helped to investigate aerosol transport up to a distance larger than 10 km. Simultaneously measured water vapor field will no doubt be a treasure on the lidar application for atmospheric remote sensing as well as a big step forward in enhancing our knowledge about atmospheric science.

Chapter 9
Summary, conclusions, and outlook

9.1 Summary and conclusions

Within this dissertation, a mobile, scanning eye-safe aerosol lidar system in the UV wavelength was developed and applied for investigating aerosol optical properties and transport processes in the lower troposphere, especially in the ABL. This work summarizes some of the most salient results of four different field campaigns/measurements and obviously adds some yet unpublished materials, which are based on the lidar application for studying atmospheric aerosols and the CBL processes. Here, main focus is to present recommendations for future work after briefly highlighting the key research findings.

From lidar measurements at IR wavelength

Within the first part of the thesis, the potential benefit of a vertically pointing lidar system operating at IR wavelength was demonstrated for a vivid representation of the daytime CBL over a complex terrain-induced urban region. Ultra-high-resolution lidar sounding during measurements in Stuttgart downtown explored detailed insights into two different regimes of CBL on a same day: a quasi-stationary well-mixed cloud free CBL (case I) and a rapidly growing CBL in the morning in presence of a strong residual layer above the CBL top (case II). For both cases, the instantaneous CBL height, its growth rate and associated entrainment were studied. Three different advanced approaches (LGM, IP, and HWT) were demonstrated for precise determination of the instantaneous CBL height and the associated EZT. The HWT-based analysis was found be a robust technique for this purpose. Additionally, the wavelet-based approach was qualified to detect CBL height in complex situation like in case II. This yielded an advantage to explore the interaction between the RL and the growing sCBL.

A rapidly developing instantaneous CBL height with a growth rate of 5 m/minute was observed in the morning when the CBL was growing from 700 m AGL to the height of a residual layer at 1545 m AGL. The mean EZT was found to be 62 m. Interaction between the CBL and the RL above in this case is found to be suggestive of penetrative convection at the top of the CBL. But the CBL was found to be well-mixed in the afternoon. The evolution of the instantaneous CBL height at around 2.0 km AGL was found to be quasi-stationary. An FFT-based power spectrum analysis confirmed this stationarity with a spectral exponent value of 1.0.

For the first time a high-resolution aerosol lidar measurements explored the benefits of the higher-order moments estimation of the aerosol backscatter field identifying different CBL activities. Application of the method introduced is so far valid for the well-mixed CBL regime where the fluctuations of aerosol microphysical properties can be neglected. The profiles of the higher-order moments of particle backscatter coefficient fluctuations in the CBL yielded a comprehensive picture of the CBL processes. It was demonstrated that the major part of the inertial subrange was detected and that the integral scale value (60-70 s) was significantly larger than the temporal resolution in the lidar data. Consequently, the major part of turbulent fluctuations was resolved. Vertical distribution of the variance, skewness, and kurtosis investigated the turbulence features in the CBL aerosol field and complex convective activity patterns with an accuracy that was mainly limited by sampling errors due to turbulence statistics. Furthermore, it was demonstrated that without noise correction, the values of integral scale, variance, skewness, and kurtosis in the CBL were either underestimated or overestimated.

Vertical distribution of variance showed a well-defined structure with a maximum value at the top of the CBL without further peaks confirming an aerosol distribution in a regime of well-mixed CBL. But the variance profile for the other case was found to consist of several peaks including the one at the mean CBL height. A negatively skewed structure of the aerosol distribution was found up to the top of the CBL and positive values of skewness were found in the entrainment zone for the case of well-mixed CBL. On the contrary, a high vertical variability with both positive and negative skewness inside the CBL was observed for the other case.

A detailed intercomparison study was performed between the two cases concerning the characteristics features of the higher-order moments profiles. This demonstrated the quasi-stationary CBL regime to be a better choice for investigating turbulence in the CBL. A non-stationary CBL regime may often provide erroneous profiling of higher-order moments. For instance, the integral scale value in the region of residual layer showed a drop of 100 s at $1.4z_i$ and an exceptional high value of 230 s at $1.5z_i$, most probably due to the heterogeneity induced by the aerosol particles in the RL.

An FFT-based spectral analysis, the DFA technique, and the multifractal analysis have been found to be effective to study the non-stationary behavior of the CBL height evolution and the correlations in their fluctuations. The power spectra obtained with FFT-based analysis of the instantaneous CBL height time series during its rapid growth showed power-law dependency. The resultant γ value (1.502 ± 0.08314) confirmed non-stationary behavior. This value of γ was found to be closely similar to that from the DFA methods. The values of generalized dimension were found to be between 0 and 1. The CBL dynamic self-affinity with a roughness exponent of 0.37 was obtained which is consistent with the previous studies.

Both the qualitative and quantitative description of gravity waves in a RL in the evening and detection of the K-H filaments in daytime CBL are two important parts of this work. Wavelet-based extraction of spectral characteristics of a wave-like event in a residual layer yielded scale dependencies

of various structures and confirmed a wave signature with a frequency of 0.0001 Hz. The global wavelet spectrum also showed a peak around this frequency. Such multi-scale feature recognition (as presented with the scalograms) cannot be obtained with the standard FFT-based analysis. The wavelength of the K-H filament was found to be of about 400 m, which is not unrealistic for a case of a well-mixed CBL.

From scanning lidar measurements at UV wavelength over flat terrain

Second part of the thesis emphasized on the development and application of a mobile eye-safe scanning aerosol lidar system for the study of aerosol processes inside the ABL. The lidar system was operated at a wavelength of 355 nm with an average power of 9 W in combination with a 40-cm scanner with a speed of up to 10° s^{-1}. The capability of eye-safe operation made the system useful so that it could be operated without restrictions. A modified version of the inversion algorithm was introduced for determining aerosol optical properties from scanning lidar measurements. The capability of estimating optical properties of the aerosol particles and facility of the high-resolution scanning are two of the most important features of the UHOH scanning aerosol lidar system developed within this work.

First eye-safe scanning UV-lidar tracking of the optical properties of aerosol plume from an agricultural facility (located in flat terrain) was realized. A detailed picture of the transport of the plume was obtained. The physical and chemical properties of these aerosols were determined by means of spatially and temporally high-resolved scanning lidar measurements in combination with a high-resolving atmosphere-microphysics-chemistry model and in-situ aerosol measurements at ground. Aerosol optical properties were predicted by the model and the results were compared with scanning lidar measurements.

Both model and lidar results yielded the particle backscatter coefficient of the plume to be of about 30 % higher than that of the background aerosol load near the facility. The aerosol structures presented through the PPI scan images showed very high particle backscatter coefficient up to 1.0×10^{-5} m^{-1} sr^{-1} in the far region of about 2 km. A series of PPI scans demonstrated that the movements of the plume near the livestock facility were complex and were highly influenced by the turbulence inside the lower ABL. Longer averaging (~ 15 minutes) in PPI scanning measurements showed an approximately Gaussian-shaped aerosol plume missing the turbulence driven structures within it. Ground-based in-situ measurements during the campaign showed an increase of the aerosol number density downwind of up to 5 % in the lowermost 50 m of the atmosphere.

High-resolution scanning around the farm explored diverse physical features of the emitted plume e.g., the coverage area and rising, turbulence diffusion, spatial and temporal variability, and transportation in downwind over long distances up to 3 km. The lofted height of the plume was found to be of about 20 m AGL near the farm and of about 115 m AGL in an extended region of 3.0 km.

Intercomparison results show that the LES-AOP detected observed range of values for the particle backscattering for different aerosol simulation scenarios. The model simulation managed to represent the intensity of the farm contribution.

In contrast to the conventional in-situ measurement techniques, combination scanning lidar system, in-situ aerosol measurements and LES modeling towards a study of the physical/optical characteristics of aerosol flows close to a livestock facility was found to be a unique technique and highly synergetic. The uncertainty can be reduced in future field experiments by improved and precise in-situ measurements and lidar scanning.

With the aid of novel technique developed within this work, following major key research issues concerning lidar application were achieved:

- Scanning aerosol lidar at UV wavelength is capable of estimating the optical properties of aerosol plume from a faint source.
- High-resolution scanning lidar measurements are required to investigate the spatial and temporal variability of the plume and their transport in downwind.
- An appropriate scan strategy was found so that the aerosol emission could be observed. Through this, a clear scan strategy for the improvements of the results is envisioned for future scanning lidar applications.

From the scanning rotational Raman lidar measurement over complex terrain

Scanning RRL measurement from the top of the Black Forest mountain investigated some of the CBL dynamical features, which were mainly driven by the local orography of the region. The RRL technique was modified to allow the retrieval of particle backscatter coefficient and particle extinction coefficient and then the corresponding lidar ratio from the scanning RRL measurements. This yielded another benchmark for the application of the RRL technique to determine the aerosol optical properties in 2-dimension which can be considered to be the most efficient way-out to investigate the aerosol processes in the ABL.

The first scanning aerosol measurements with the rotational Raman lidar technique were realized during the PRINCE campaign in 2006. The CBL height was found to vary between 800 m (1900 m ASL) and 1300 m AGL (2400 m ASL) over Hornisgrinde mountain during most of the campaign days. An FFT-based spectral analysis of a time series of the height of a well-mixed CBL case yielded a spectral exponent value of 1.0 confirming the stationarity in the time series.

A strong vertical variability of lidar ratios between 30 and 50 sr was observed in presence of different aerosol layers. Even on a same day, two different types of vertical variability of the lidar ratios were observed: one with 30 sr in the morning and another with 10 sr in the late afternoon confirming presence of two different types of aerosol particles.

During one IOP day (case I) in PRINCE campaign, combined high-resolution measurements of aerosol optical properties and temperature field obtained with the UHOH RRL revealed undulating aerosol-rich layers in the preconvective environment and a gradual warming trend of the lower troposphere as the nearby storm system evolved.

Results obtained with the collocated Doppler lidar measurements of radial wind velocity confirming the upslope flow (from valley to mountain) and the return flow (as a part of a elevated easterly) suggested a consistent picture of the transport of the aerosol layers over the mountain. Presence of these layers was confirmed by the UHOH scanning RRL while investigating the optical properties of the aerosols in those layers.

Some selected measurement examples were presented from the data obtained during COPS field campaign to show a unique importance for obtaining valuable information on the different types of aerosols, and their extent and structure inside and above the ABL over the mountain and surrounding valleys which is closely related to COPS.

Combined measurements of 2-dimensional field of aerosol optical properties and temperature showed presence of different stability regimes over the mountain peak and their effect on the surrounding aerosol field. These results once complemented with the collocated remote sensing instruments will allow using synergetic data products to investigate and understand important processes that inhibit or support convection in a low mountain range.

Independent measurements of particle extinction and backscatter coefficients, and the respective lidar ratio obtained from RHI scans confirmed two different origin of the aerosol layers observed above the lidar site: one with a high lidar ratios between 50 and 60 sr in the altitudes between 3.0 and 3.5 km and another with a relatively low values of lidar ratios between 20 and 30 sr up to 2.0 km AGL. These results are of unique importance for studying advection of different aerosol layers over the mountainous regions.

Observation of aerosol optical properties and turbulence driven features in the cirrus cloud structures were derived from wavelet-based spectral analysis. On using Morlet as the mother wavelet, the wavelet spectra of the time series of lidar signal intensity in the cirrus layer yielded different frequencies around 0.151 Hz, which were confirmed by the FFT power spectra. Presence of different frequencies during different times in the cirrus layer was most probably arising due to patchy turbulence in this region. Lidar ratios between the altitudes of cirrus cloud base (5.2 km) and top (8 km) showed high vertical variability with a minimum and maximum values of 3 sr and 25 sr, respectively.

9.2 Outlook

Three different advanced techniques for the determination of the instantaneous CBL height were demonstrated for the first time for ultra-high-resolution aerosol lidar measurements. The Haar wavelet-based approach can be applied for an automated detection of the CBL height on a routine basis. Future research can be directed towards estimation of the CBL height from high-resolution lidar measurements in real time for an immediate interpretation of the CBL aerosol processes.

The EZT can also be estimated routine basis in real time. Application of cumulative frequency distribution technique to the high-resolution time series of instantaneous CBL height to calculate EZT yields immense confidence for future lidar applications. Multi-instruments dataset will definitely help to demonstrate this in detail. Furthermore, the LES modeling of the entrainment processes is an essential issue for atmospheric applications (Otte and Wyngaard, 2001). Thus, several entrainment law formulations have been derived to date, which relate the entrainment velocity, namely the velocity at which the interface rises, to measurable parameters of the mixed and interfacial layers. Results presented with two different techniques could be related to these parameters.

Higher-order moments were calculated with respect to fluctuations of the particle backscatter coefficient at different heights. This highlights that aerosol lidar data can yield potential benefit to estimate turbulence features in the CBL. The application of these analyses for the CBL turbulence is an important aspect of atmospheric science, which has not been possible earlier applying developed techniques to aerosol backscatter lidar measurements. A deeper insight into the dependence of the variance of a scalar on scaling parameters in the convective boundary layer can be explored with the aid of results obtained from LES models (Wyngaard and Brost 1984; Moeng and Wyngaard 1984; Moeng and Wyngaard 1989).

The wavelet-based spectral analysis could be a good basis for aerosol lidar application towards estimating the multi-scale processes present during wave events.

Multifractal analysis exhibited that the CBL height fluctuation can be characterized by simple statistical parameters like generalized multifractal dimension, roughness exponent. More cases need to be studied, however, in order to provide a more precise interpretation of these results. The aim of this next step could be to classify CBL height time series according to their statistical properties and to relate these properties to the underlying dynamics in different meteorological situations. Another important aspect of this study could be in the direction of the application of these techniques to time series of other relevant physical parameters like pressure, temperature, humidity, and horizontal wind at the CBL height.

The eye-safe scanning aerosol lidar system operating at UV wavelength developed within this dissertation is found to be an important candidate for future lidar application for studying aerosol processes in the lower troposphere, especially inside the ABL. The novel approach developed within the BW-PLUS project has an extraordinary future potential for studying the emission of health-

hazardous particles to assess the risk they possibly pose, a prerequisite for mitigation measures. The key future research may include the following:

- The combination of observations and modeling approach could be used for an improved representation of aerosol sources in large-scale atmospheric modeling.
- Assimilation of the lidar derived aerosol optical properties by developing an aerosol operator can yield a better initial state of the field of optical properties in the LES-AOP simulation.
- A fast volume scan with very high speed is recommended to accomplish the detection of the plume from livestock farm so that aerosol structures and transport can be observed at multiple altitudes simultaneously, to yield a 4-dimensional description of the field of the aerosol optical properties.
- More powerful lidar systems with even greater dynamic ranges and sensitivity are technically feasible. This lidar system could be improved to a version to achieve longer range, high sensitivity and less maintenance facility. An important research effort could be made in making the system fully automated and unattended.
- Deployment of scanning rotational Raman lidar so that the independent aerosol optical properties and temperature can be derived.
- A surface meteorological station with frequent radiosonde launching facility can give more reliable information about the prevailing meteorological condition near the farm.

This is convinced that longer time series of lidar measurements can improve this study through an accurate investigation of the vertical extent yielding more insight into the plume emissions and transport during different episodes of ABL activities.

The resolution of the scanning RRL data will allow the analysis of turbulent structures within the boundary layer and sensible heat flux estimation by combination with the data of collocated Doppler lidar measurements during COPS. The results presented is a starting point in this concern to demonstrate the complex orography induced flow modification, evolution of CBL, role of residual layer or aerosol layer, mountain induced waves, and stable NBL processes. During COPS at the supersite Hornisgrinde, meteorological surface-based measurements including frequent radiosonde launches and state-of-the-art remote sensing instruments like scanning Doppler lidar, water vapor DIAL, cloud radar, scanning micro wave radiometer were performed. Combination of the data products from these instruments will provide a unique dataset for boundary layer characterization, convection initiation, and evaluation of the meteorological models, and for studying aerosol-cloud microphysics.

The analyses of the COPS dataset are still ongoing. Intensive research efforts have been initiated to connect all the data products from the different ground-based and airborne, active and passive remote sensing instruments to each other and to study the chain of processes leading to convective precipitation. Near-future research will be a big step forward concerning the 4-dimensional remote sensing based on COPS for studying convective initiation in complex terrain.

Appendix

A. Lidar data, data control, scan strategies, and analysis

A1. Overview of the lidar data structure and codes used

The UHOH aerosol lidar system stores data in a special binary format called Bscan format. This is achieved with the Labview codes developed (detailed in appendix-B) in UHOH within the part of this dissertation. Bscan is a program that runs from the PV-WAVE or IDL command line. Therefore, the format used for the data is called Bscan format. Within this work, the procedure for writing lidar data with this format was achieved. This format yields the user a number of advantages to analyze and visualize scanning and non-scanning lidar data.

Bscan reads fixed-length binary records. Each record in such a file contains a 30-word header followed by a profile of predefined length. All header words and profile elements are real*4 values and the first element of the profile is the value closest to the instrument. Several lidar data analysis and visualization tools were developed in IDL. With the help of Bscan format, one can produce two-dimensional, time-versus-range or time-versus-altitude, color images of any lidar dataset. Data obtained from any ground-based or airborne (nadir or zenith) lidar can be analyzed as long as the data are written in the required format. The format used for the UHOH aerosol lidar system contains the header information in each data file as shown in Appendix- A2. IDL codes made it possible to provide near-real time automated analysis and displays of the stored lidar data. Therefore, the UHOH lidar data structure is developed in such a fashion so that the basic information about the lidar run: the acquisition start time, the total number of lidar events inside the file the number of operational digitizer modules, the PMT voltages, the laser power, and some remarks can be achieved fast for the purpose of post processing.

Special emphasis was given for the retrieval of aerosol optical properties for vertical measurements and scanning measurements after two different techniques i.e., Fernald algorithm, rotational Raman lidar technique. An excellent graphical tool was designed to produce animation of the scan images for better understanding of the dynamical processes taking place in the atmosphere.

A2. Lidar data format

LIDAR DATA HEADER (Bscan) FORMAT
at UHOH as 25/05/2004

0	hour (0. - 23.): 18	[From GPS]
1	minute (0. - 59.): 39.000	[From GPS]
2	second (0.00 -59.999): 10.38	[From GPS]
3	GPS altitude (meters above mean sea level): 0	[From GPS]
4	alternative altitude (i.e. pressure altitude, not decided yet): 0	[Arbitrary]
5	alternative altitude (i.e. radar altimeter, not decided yet): 0	[Arbitrary]
6	beam azimuth (forward is 0, right wing is 90, aft is 180, left wing is 270, etc.): 0	[From Scanner]
7	beam elevation (0 is level with horizontal plane of platform, +90 is zenith, -90 is nadir): 90	[From Scanner]
8	platform roll (left-right angle in degrees off earth's horizon): 0	[Not used]
9	platform pitch (nose-tail angle in degrees off earth's horizon): 0	[Not used]
10	platform heading: 0	[Not used]
11	month (1. - 12., Please note that this variable will be used to test byte-order.): 11	[From Computer]
12	day (1. - 31.): 24	[From Computer]
13	year (please use full year; i.e. 1995 not 95.): 2004	[From Computer]
14	pulse repetition frequency (PRF) of lidar in Hz: 30	[Arbitrary]
15	number of shots that were not included (from intention) in this profile: 0	[Arbitrary]
16	data type identifier (please see addendum 1) : 260	[Arbitrary]
17	number of hours to adjust header time to get to UTC (positive or negative): 0	[From GPS]
18	platform latitude (north pole = +90, equator = 0., south pole = -90.)	[From GPS]
19	platform longitude (degrees east of Greenwich.): 0	[From GPS]
20	range from lidar of the first word in the profile in meters: 0	[Arbitrary]
21	range resolution of data in meters (i.e. 15 m per word if using 10 MHz digitizer): 3	[CS14100]
22	platform identifier : 9.0015	[Arbitrary]
23	number of words in header (currently 30.): 30	[Arbitrary]
24	no data flag (what you put in the profile if data is not available for a particular word): 0	[Arbitrary]
25	scan style (0 =VAD, 1=RHI, 2=FIXED, 3=OTHER): 0	[From Scanner]
26	number of laser shots actually used to derive this profile (header 28 minus header 16): 10	[Arbitrary]
27	number of laser shots intended to use to derive this profile (header 16 plus header 27): 0	[Arbitrary]
28	number of words in the profile (word in the data part of the record, not the header): 4096	[CS14100]
29	transect number or scan number (increases by 1 for each scan or transact): 0	[From Scanner]

A3. Data control and scan strategies

In principle there are two different types of scan strategies that have been followed during the lidar measurements during the four field campaigns performed from 2004-2007. First one concerns the continuous vertical measurement and/or PPI/RHI sector/volume scans and the other one is the discrete scan strategy, where a defined number of LOS data are collected covering a region of azimuth/elevation. In all cases, the amount of stored data is a trade-off between the time resolution/range resolutions and scans speed/number of scans/number of sectors. The data store policies have been followed in such way that the real-time displays during data acquisition are not hampered and/or the time necessary for post-processing is not large enough. The scan strategies largely depend on the aim to achieve with the lidar experiment and varied during the field campaigns performed.

B. Data acquisition codes in LabView

B1. Overview of the data acquisition codes

A number of dedicated data acquisition and evaluation programs have been developed within this research with an aim of providing near-real-time quick looks of the lidar data products. An accurate high speed DAC system was developed in LabView. LabView is a graphical programming language developed by National Instruments (http://www.ni.com). Several user-friendly programs were written in LabView 7.1 as a part of DAC providing excellent user interface design, scanner motion control, input/out file report, and real time display of lidar signals. The flow diagram showing the major steps involved in the DAC during lidar measurement is shown in Figure B1.

Three different versions of the DAC were developed. These are

(I) DAC for the vertically pointing lidar system at IR: This DAC was specially made for the controlling of the lidar data acquisition build with an ADC card CS14100 and storage of the lidar data in Bscan format on a PC. One screen shot of this version is displayed in Figure B2.

(II) DAC for the scanning eye-safe aerosol lidar system at 355 nm: This DAC is in contrast to the previous version of the DAC providing a unique capability of scanner motion control and process ADC signal only in single channel mode. Figure B3 shows one screen shot of this DAC during the lidar measurement yielding three major panels of the graphical interface namely initialization of the Gage card (right panel), display of the lidar data (central panel), and initialization of the scanner (left panel).

(III) DAC for the scanning rotational Raman lidar at 355 nm: A 3-channel Licel transient recorder was used in the data acquisition system. A stare-and-step scan strategy was optimized in the DAC. This DAC provides the user the possibility of (1) Choice of the scanning sector, scan type, scan step resolution, number of scan steps, time resolution, range resolution, option for time-synchronized scan. (2) User can put the above values through a batch file and run the code

continuously unless it is stopped. (3) Continuous display of GPS time, scanner location both in azimuth and elevation, (4) Time-synchronized scan with complicated scan pattern. A screen shot during lidar measurement is displayed in Figure B4.

B2. Implementation of scanning operation

The operator needs to define/fill the following fields before the scanning operation starts:

- Choice of the scanning type; i.e. either fixed PPI or RHI or volume scan (PPI/ RHI)
- PPI offset angle the scanner is deviating from the geographical north. This is called "Hall to North offset"
- RHI offset: angle the scanner is deviating from the geographical horizon. This is called Hall to Horizon offset.
- Stare angle: angle showing the direction (azimuth /elevation) the scanner mirror should look
- Start angle: Sector scan start angle
- End angle: Sector scan end angle.
- Scan speed: Maximum $10° s^{-1}$
- Number of scan: The default value is "infinity". The scanning movement is stopped when the main STOP button is pressed.

While initializing, the scanner always goes to the 0 angle of the motor processor and then it initializes to the selected offset angle. When it starts scanning then it always gives a feedback value (as it is asked for) of the position in degrees measured from the initialized position (from north for PPI and from horizon for RHI).

In summary, the scanning programme adds the following information to the vertically pointing lidar programme: (i) raw instantaneous elevation or azimuth angle value replied from the scanner processor, (ii) stare angle (fixed elevation or azimuth), (iii) scan number, and (iv) scanning type. Most important governing factor is the forward movement indicator, which takes care that the lidar data are stored only when the scanner is in the forward moving stage. This code takes care about the scanner motion control.

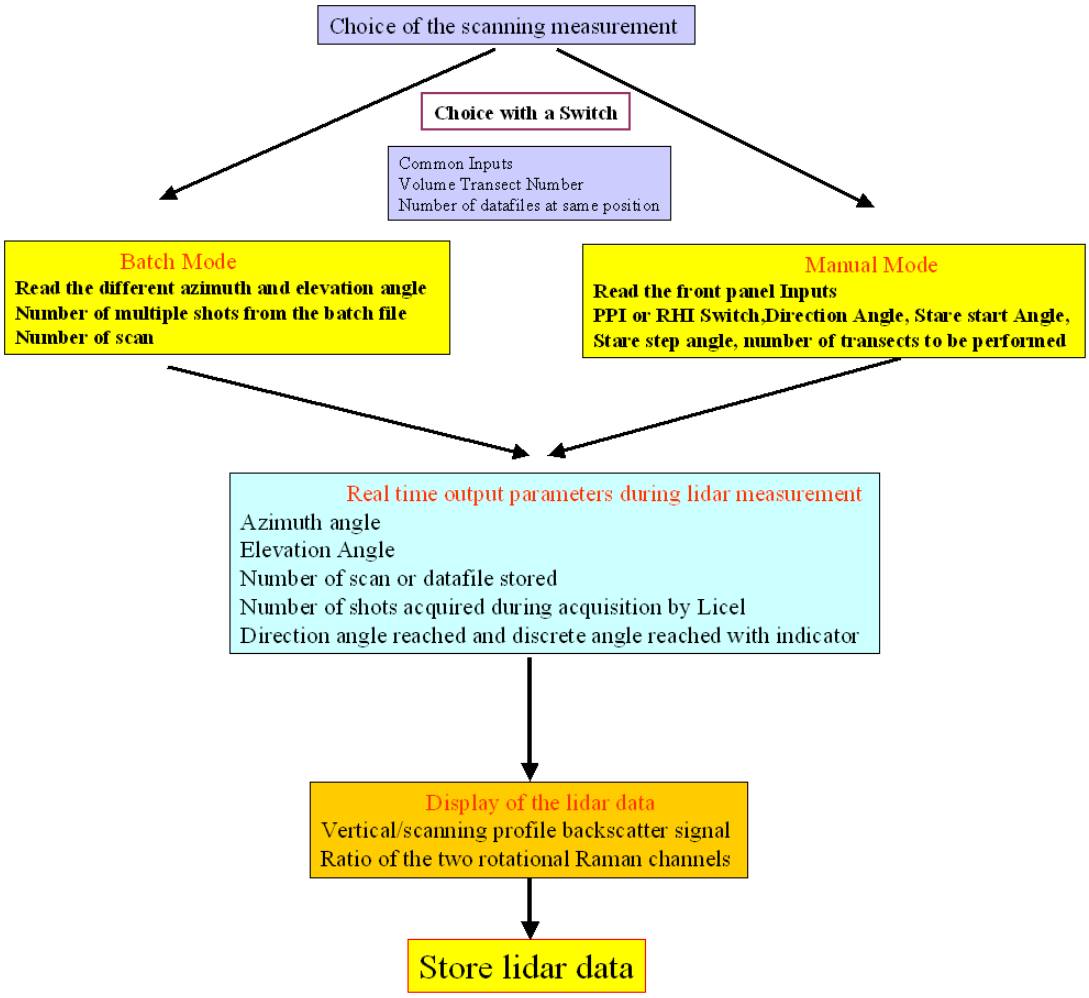

Figure B1: Flow chart showing the major steps involved in the of data acquisition software developed.

Visualization of the lidar signal intensity in real time (during measurement) is a significant issue in the field of active remote sensing technology. The processed lidar data in real-time are displayed in the front panel of the DAC. One example is shown in Figure B3. The plot shows the range-corrected backscatter signal versus number of emitted laser shots since the start of the measurement and versus range. The profiles were recorded with elevation angles between 30 and 90° with 0.033 s temporal resolutions and 3 m range resolution (which corresponds to about 180 profiles per scan). The top of the boundary layer in about 1.4 km height is characterized by lidar backscatter signal intensity. Vertical profiles are generally larger in intensity in this plot because the data are not corrected for atmospheric extinction here.

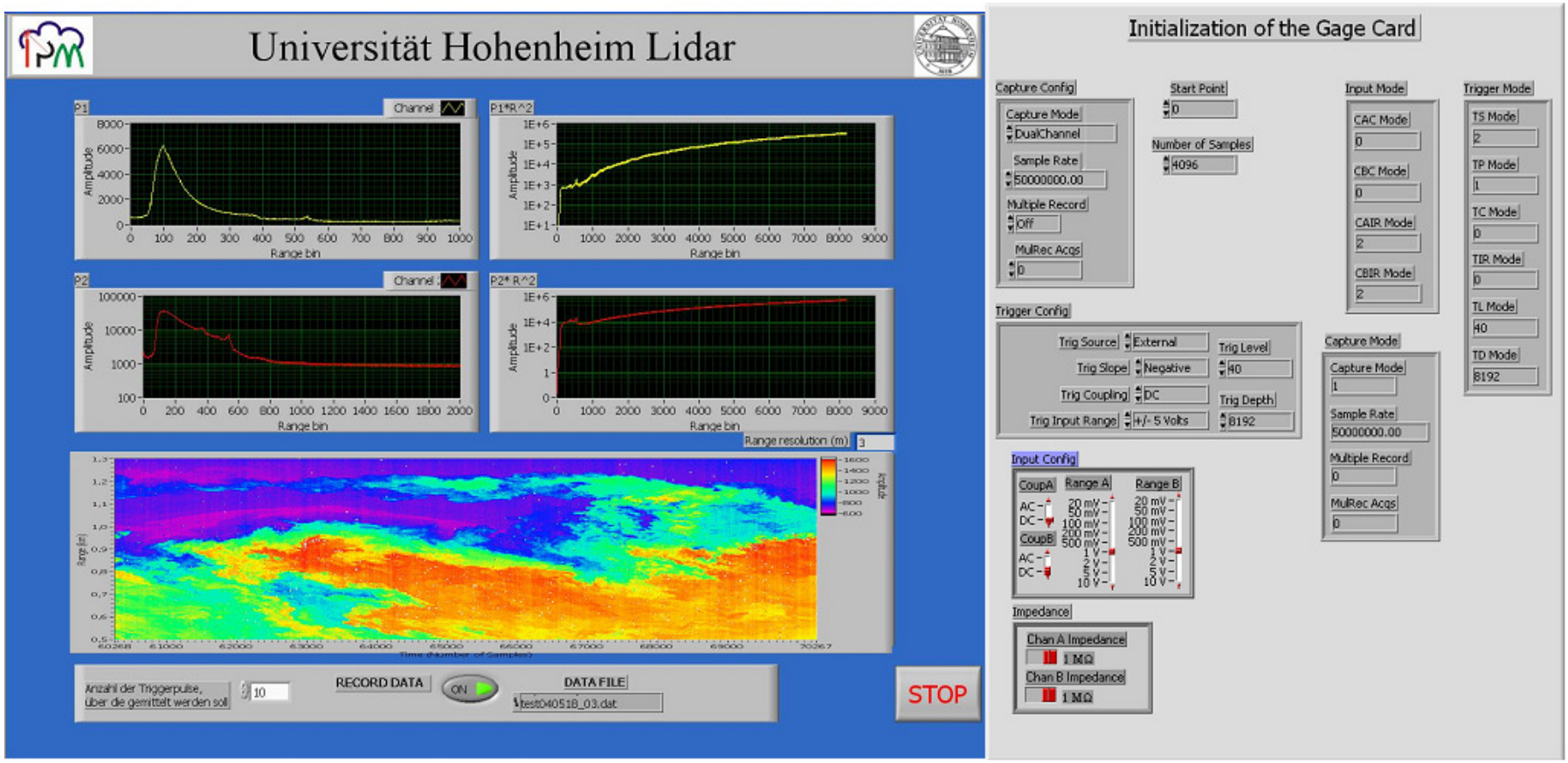

Figure B2: Front panel of the DAC of UHOH aerosol lidar during the measurement at Stuttgart downtown in 2004. The Full panel includes the panel containing the initialization of the Gage card CS14100 and a display panel containing the raw lidar signal for the wavelength 532 nm (left panel) and 1064 nm (right panel), and range-time indicator panel showing the evolution of the atmospheric aerosols structures.

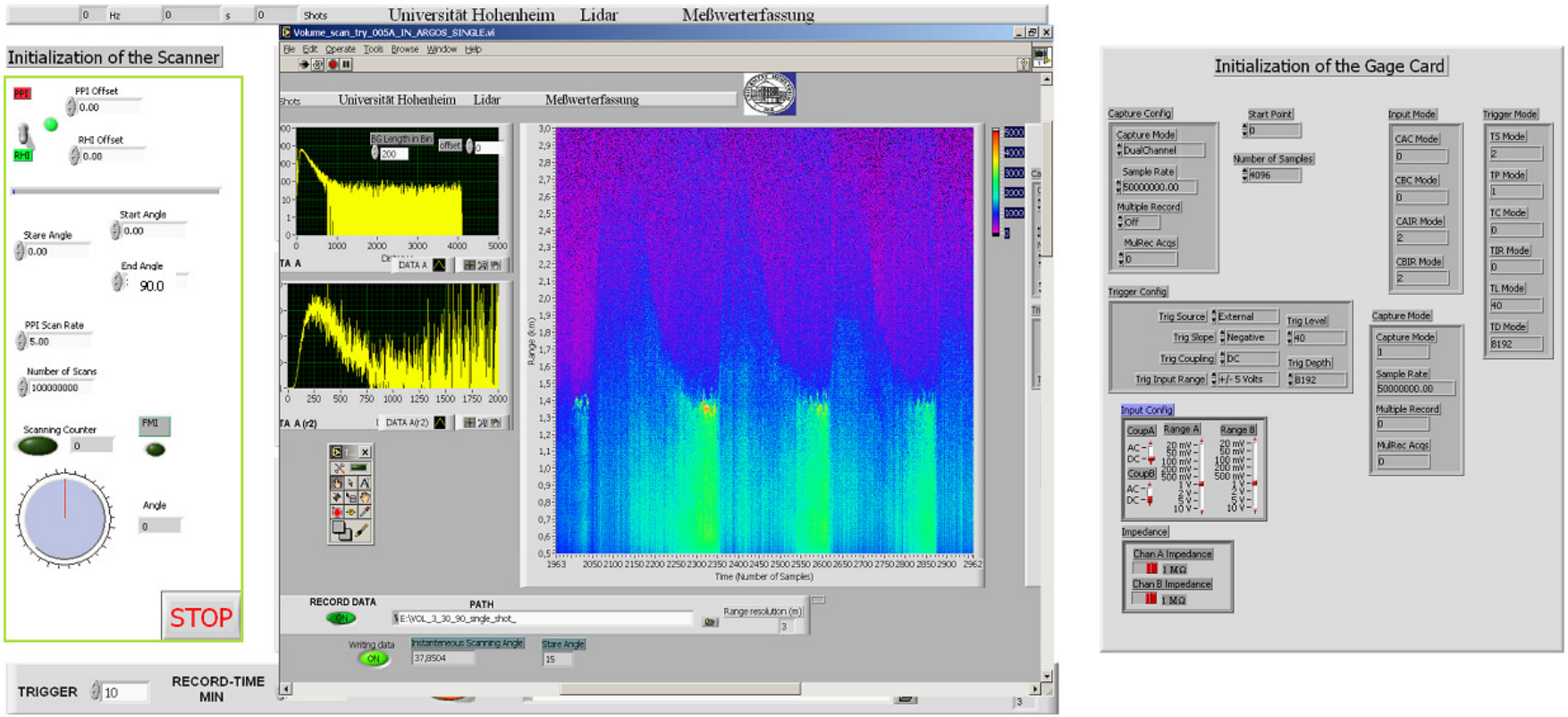

Figure B3: A real time display of an RHI scan in time-range panel during data acquisition obtained after a screen shot from the lidar data acquisition computer during test measurement at UHOH on 1 September 2005.

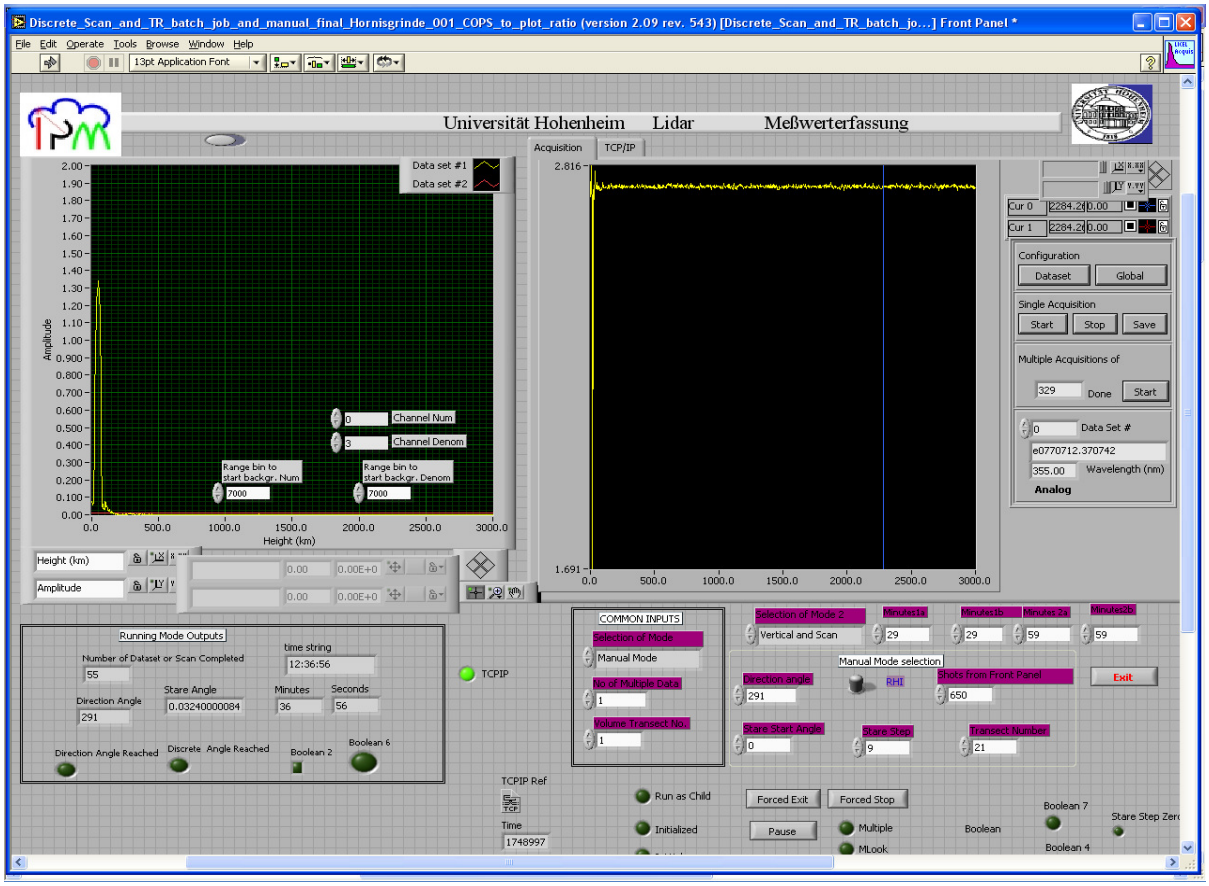

Figure B4: Latest version of the DAC of UHOH scanning temperature and aerosol lidar system during the field campaign COPS in 2007. Left panel (profile plot, abscissa is distance from lidar and vertical axis is value of the ratio) shows the ratio of the two rotational Raman lidar channel, which is an indicative of the atmospheric temperature profile in real time. Right panel shows the received backscatter signal intensity (mV) in the same fashion as left panel.

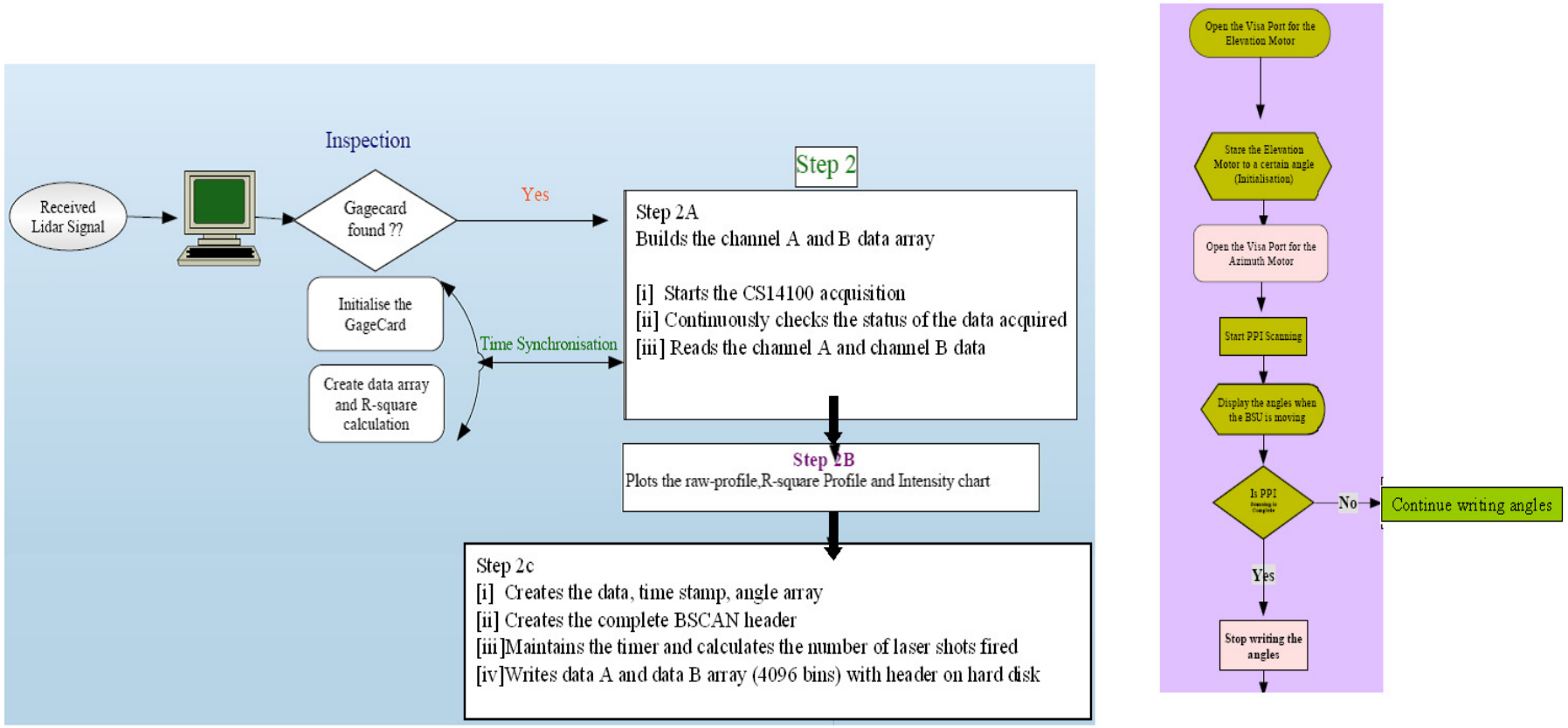

Figure B5: Flowchart showing the steps involved in the DAC. Data flow during acquisition (left) and scanner control (right)

C. Sensitivity tests for the inversion algorithm

The analytical inversion technique for determining aerosol optical properties from data obtained with the elastic backscatter lidar system is being used and discussed in the literature (e.g., Kunj, 1996; Fernald, 1984; Sasano et al., 1985; Klett, 1986; Bissonnette, 1986; among others) for approximately three decades and is still under discussion.

It has been mentioned in chapter 3 that the two-component monostatic lidar equation takes into consideration the scattering due to air molecules and aerosols under the assumption of a constant lidar ratio. Additionally, inversion method depends upon the specification of a boundary condition of a certain value for the backscatter coefficient at a designated range, so called calibration range.

Fernald (1984) showed in his paper that the boundary conditions at the far range give a better convergence when integration is made toward the near range. This is called backward integration scheme in the analytical inversion. Since the backscatter coefficient value at the boundary is usually unknown, it is often assumed that an aerosol-free layer exists at a certain level, which is called the matching method to calibrate the lidar signal.

As mentioned before the solution for $\beta_{\lambda,par}(R)$ with the inversion technique inherently uses some assumptions. Therefore, following sensitivity tests are of immense importance and have been performed:

- Dependencies of the retrieved $\beta_{\lambda,par}(R)$ on the assumed aerosol lidar ratio
- Behavior of the solution with forward and backward integration scheme
- Changes in the calibration height and the assumed $\beta_{\lambda,par}(R)$ value at that height
- Impact of the error in the Rayleigh scattering cross-section on the retrieved $\beta_{\lambda,par}(R)$ field

The Inversion algorithm is sensitive to the assumed value of the calibration range/height and the $\beta_{\lambda,par}(R)$ value at that calibration range. This raises another question concerning the sensitivity of the inversion scheme (forward or backward) in dependence of the calibration range. The assumption of the calibration range is therefore related to the integration scheme to be applied in the inversion algorithm. It has been shown in numerous literatures including the Fernald's paper on the inversion technique that the backward integration or so called far end solution is most appropriate as the corrupted (not accurate) $\beta_{\lambda,par}(R)$ value converges to the true value in the case when backward integration is used. A parametric sensitivity test of the two main inversion algorithms (inversion solution from near-end and far-end boundary conditions) was performed to demonstrate the stability of the inversion scheme applied. These two solutions are basically identical in theoretical point-of-view but they differ in practice because of the stability problems arising from the non-linearity of the monostatic lidar equation as shown in Figure C1. In this Figure the calibration range is considered at 4 km. Clearly shown is that

the analytical solution for $\beta_{\lambda,par}(R)$ at a range of 5 km has high instability for the forward integration scheme while in case of the backward integration scheme, the solution looks comprehensive. The lidar ratio confirms the relationship between the extinction to the backscatter ratio as mentioned in chapter 3. This ratio is not necessarily constant with height. Under most circumstances, the vertical distribution of the lidar ratio is not known.

Fernald (1984) assumed in his paper aerosol lidar ratio is constant in height. This essentially assumes that the size distribution and compositions are not changing with height and the variation in $\beta_{\lambda,par}(R)$ is due to the changes in the number density. Sasano et al. (1985) showed that a constant lidar ratio value can lead to errors in the $\beta_{\lambda,par}(R)$. This theoretical analysis suggested that the investigation of the retrieved $\beta_{\lambda,par}(R)$ solution needs detailed sensitivity tests. This is clear from Eqn. 4.32 that when a constant value is assumed for aerosol lidar ratio, solution is definitely affected by the molecular extinction coefficient. Present section investigates this after using UHOH lidar data rather than theoretical analysis. Figure C2 depicts the particle backscatter coefficient field obtained after applying

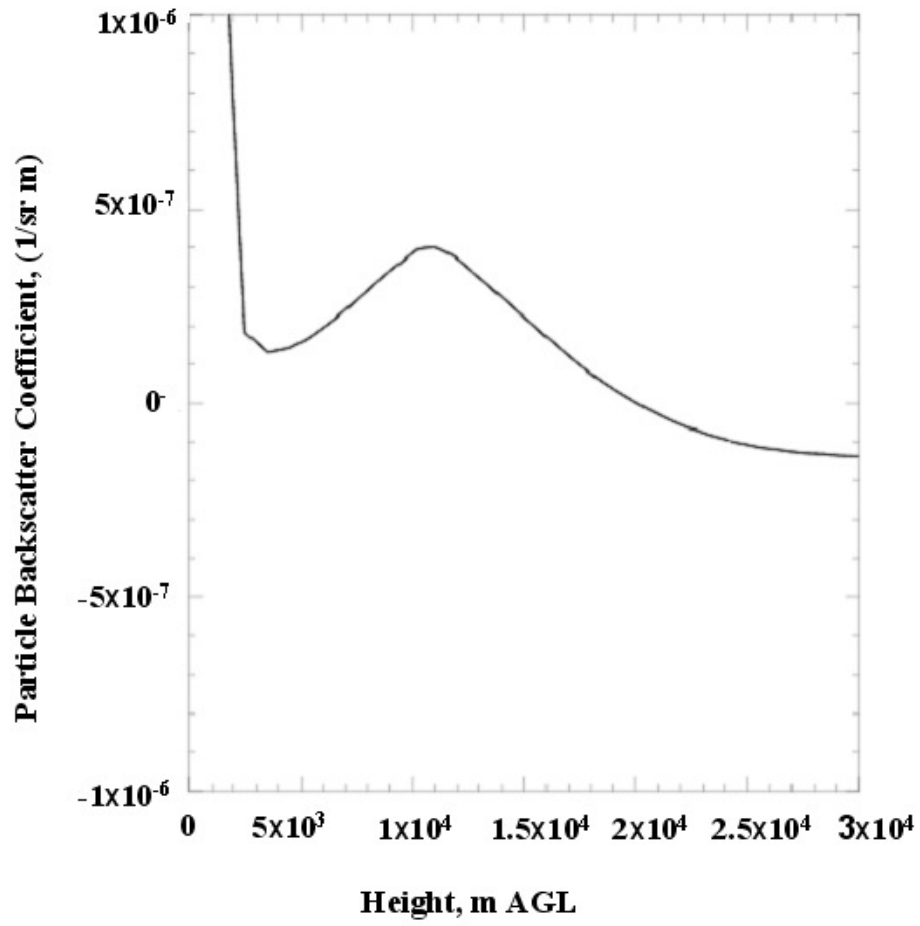

Figure C1: Demonstration of the instability present in the particle backscatter coefficient during forward integration scheme applied in the inversion algorithm.

different lidar ratio value (constant in height) during the inversion technique applied to the lidar signal. This Figure shows the effect of assuming constant lidar ratios during $\beta_{\lambda,par}(R)$ calculation. There is no chance to accurately estimate the aerosol lidar ratio value for this case. This value is assumed to be 39, a frequently used value for the aerosols for the European region (Pappalardo et al., 2005). Kovalev (1995) showed in his paper that the distortions of the aerosol extinction profiles are in general larger if the assumed lidar ratio is overestimated. The findings here are similar to that obtained by Kovalev (1995) if one assumes that the lidar ratio value used here is correct.

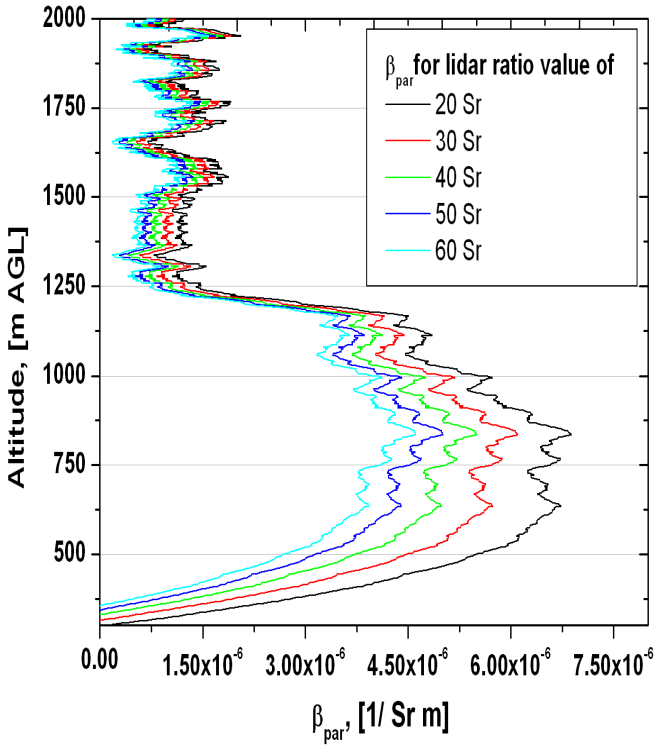

Figure C2: $\beta_{\lambda,par}(R)$ profiles for different height independent lidar ratios for determining the impact of lidar ratio in the inversion method.

For the sensitivity test concerning the assumption of calibration range, the backward integration scheme is applied only. This test inherently concerns the assumption of aerosol free atmosphere and the quality of the lidar signal at the calibration range. Figure C3 shows the results obtained from the inversion method while considering different calibration heights for the data obtained as shown in Figure C2. This figure shows that the retrieved $\beta_{\lambda,par}(R)$ value at different heights (e.g., 1.0 km, 1.1 km, 1.2.km etc.) after the calibrating the lidar signal at different heights (1.5-2.0 km, 2.0- 2.5 km, 2.5-3.0 km). The figure yields that for all heights the obtained $\beta_{\lambda,par}(R)$ value is underestimated while calibrating the lidar signal beyond 4.0-5.0 km. Additionally, the behavior of the deviation is also the same. This clarifies the fact that if one starts the calibration in the height between 4.0 and 4.5 km, then

the retrieved $\beta_{\lambda,par}(R)$ shows neither any underestimation nor any overestimation. At the same time, one should remember that as the number of steps involved in the backward integration scheme increases, faster (better) the correct $\beta_{\lambda,par}(R)$ value is obtained. Therefore, while averaging in range/height, a gliding boxcar average is applied to the case here so that the number of height steps (bins) is not decreased during the averaging procedure. Inversion technique also requires $\beta_{\lambda,par}(R)$ value at the calibration range (in the region of less aerosol loading). The value of $\beta_{\lambda,par}(R)$ at the calibration range is in general an unknown quantity. The solution is also sensitive to the assumed value of $\beta_{\lambda,par}(R)$. An iterative approach is followed here to estimate the relatively correct $\beta_{\lambda,par}(R)$ value at the calibration range. The term 'relatively correct' is used here to emphasize that the $\beta_{\lambda,par}(R)$ value at the other ranges anyway approaches to the correct value while

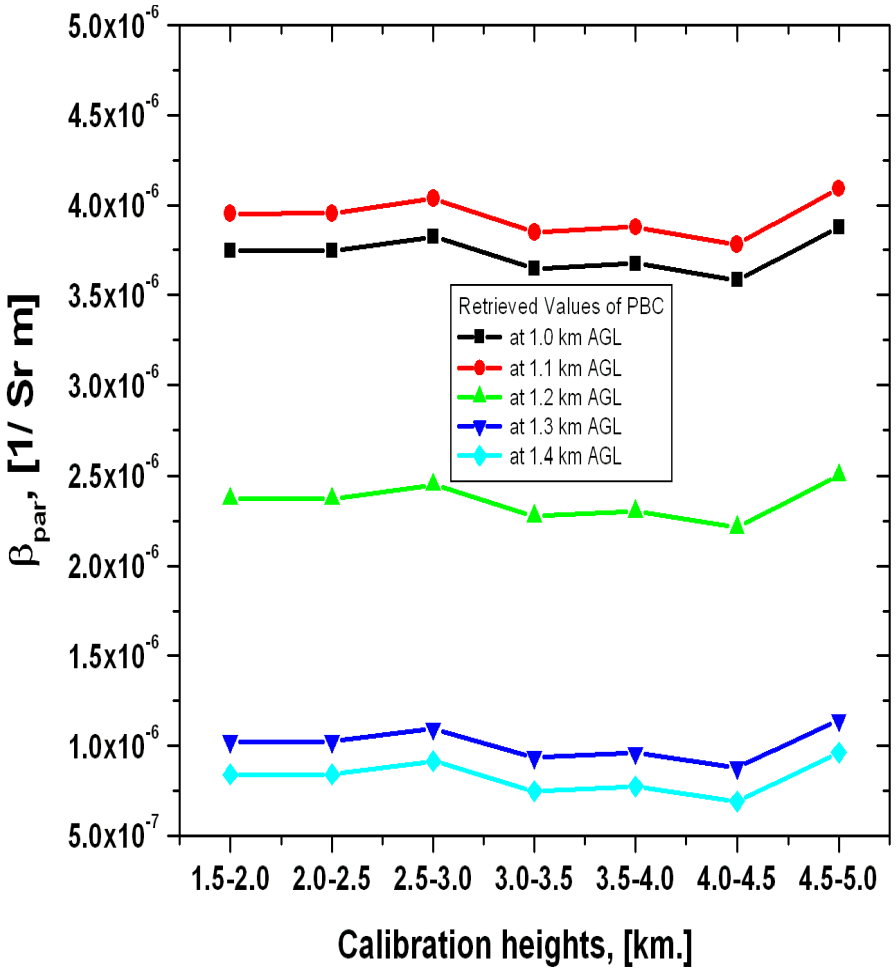

Figure C3: Sensitivity tests of the calibration height for the inversion algorithm applied

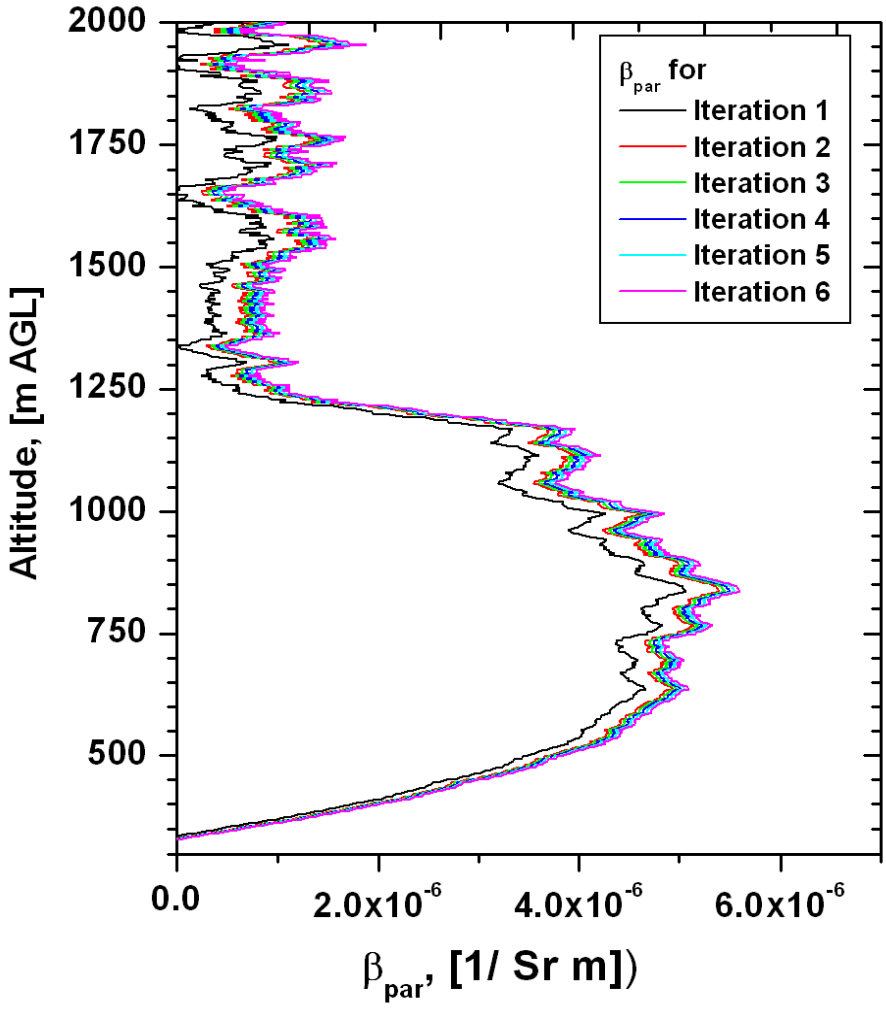

Figure C4: Determination of particle backscatter coefficient at the calibration range with the iteration method applied during the inversion technique.

while backward integration is applied. Figure C4 shows the vertical distribution of the $\beta_{\lambda,par}(R)$ value obtained with this iterative approach. This is clear from the figure that the there is no significant difference among the results obtained from iteration 2 to 6. These curves are obtained in the following way. Particle backscatter coefficient value of the calibration range is kept very low (1.0×10^{-7}, m^{-1} sr^{-1} or less. Then a profile of $\beta_{\lambda,par}(R)$ is resulted. For the next iteration the value of $\beta_{\lambda,par}(R)$ at the calibration range is obtained from the previously obtained $\beta_{\lambda,par}(R)$ profile. This is called iteration 2 and so on obtained the results from higher iteration steps. This is clear from the figure that the solution converges rapidly and no differences were found in the results obtained from the iteration 2, 3, 4 etc. Therefore, there is no need to recalculate the $\beta_{\lambda,par}(R)$ after iteration 2. Above all, the value of $\beta_{\lambda,par}(R)$ at the calibration range is having significantly poor effect on the solution.

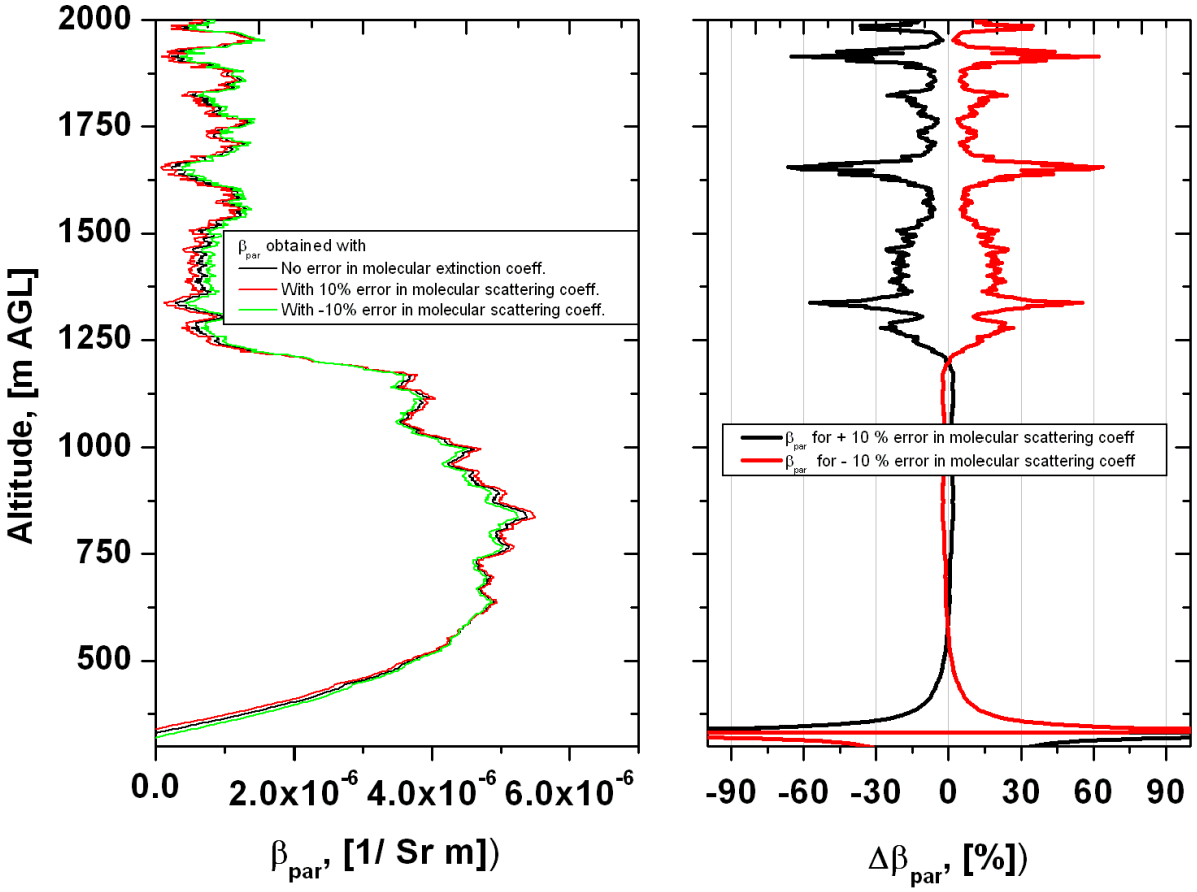

Figure C5: Impact of the error in the Rayleigh scattering cross-section on the particle backscatter coefficient profile.

Impact of the error in the calculated molecular backscatter scattering coefficient on the calculated $\beta_{\lambda,par}(R)$ is now aimed here.

Figure C5 shows the profiles of (left panel) $\beta_{\lambda,par}(R)$ obtained with no error performed during the $\beta_{\lambda,par}(R)$ calculation and with an error of ± 10 % in molecular scattering coefficient. Clearly seen are the different values of $\beta_{\lambda,par}(R)$ with height with three different molecular scattering estimates. Right panel shows the calculated deviation in percentage of the error in $\beta_{\lambda,par}(R)$ profile. This figure shows that an error of 10 % in the molecular scattering coefficient can lead to an error of up to 60 % in $\beta_{\lambda,par}(R)$ profile. Therefore, it can be concluded that more accurate the molecular scattering coefficient profile, more accurate is $\beta_{\lambda,par}(R)$ profile. In this regard a special care is taken during the calculation of Rayleigh scattering following Bucholtz (1995) as mentioned in chapter 3.

Through the above sensitivity tests one major conclusion can be easily drawn: Fernald's inversion technique takes the advantage that there is no requirement to quantify the value of system constant. The calibration value at the far range is necessary to assume. The influence of the wrong value of particle backscatter coefficient at the calibration range is mainly limited by the far end of the

measurement path. The $\beta_{\lambda,par}(R)$ value retrieved at the near range (first 2/3 of the lidar and calibration range) can be considered as very good estimates even if $\beta_{\lambda,par}(R)$ at calibration is totally wrong as far as $\beta_{\lambda,par}(R)$ is at far end is greater than 0 and lidar signal quality is good enough to apply inversion technique.

D4. Wavelet transforms analysis

The steps involved in using wavelet-based spectral analysis (see, Torrence and Compo, 1998 for a detailed discussion) are outlined here.

(i) Find the Fourier transform of the time series

(ii) Choose a wavelet function and a set of scales to analyze

(iii) Once a wavelet function is chosen, it is necessary to choose a set of scales 's' to use in the wavelet transform. It is convenient to write the scales as fractional power of two

$$S_j = S_0 2^{j\,\mathrm{d}j} \qquad \text{[D1.1]}$$

where, S_0 is the smallest resolvable scale and j = 0,1,2,……..J. J determines the largest scale. The S_0 should be chosen so that the equivalent Fourier period is approximately 2d*t*. The choice of sufficiently small dj depends on the width in the spectral space of the Wavelet function.

(iv) For each scale, construct the normalized wavelet function using

$$\psi(s\omega_k) = \left(2\pi s / \mathrm{d}t\right)^{1/2} \psi_0(s\omega_k) \qquad \text{[D1.2]}$$

(v) Wavelet transform is calculated at that scale using

$$W_n(s) = \sum_{k=0}^{N-1} X_k\, \psi^*(s\omega_k) e^{i\omega_k n\, dt} \qquad \text{[D1.3]}$$

(vi) Determine the cone of influence and the Fourier wavelength at that scale

(vii) After repeating steps III-V for all scales, remove any padding and contour plot the wavelet power spectrum

(viii) Make the scalograms together with the time series of the variable and global power spectra.

Bibliography

Althausen, D., Müller, D., Ansmann, A., Wandinger, U., Hube, H., Clauder, E., and Zörner, S.: 2000, 'Scanning 6-wavelength 11-channel aerosol lidar', *J. Atmos. Ocean. Tech*., **17**, 1469-1482.

Aneja, V. P., Blunden, J., Roelle, P. A., Schlesinger, W. H., Knighton, R., Niyogi, D., Gilliam, W., Jennings, G., and Duke, C. S.: 2008, 'Workshop on agricultural air quality: state of the science', *Atmos. Environ.,* **42**, 3195-3208.

Angevine, W. M., Grimsdell. A. W., Warnock, J. M., Clark, W. L., and Delany, A. C.: 1998, 'The flatland boundary layer experiments', *Bull. Amer. Meteorol. Soc.,* **79** (3), 419-431.

Angevine, W. M., White, A. B., and Avery, S. K.: 1994, 'Boundary layer depth and entrainment zone characterization with a boundary layer wind profiler', *Boundary-Layer. Meteorol*., **68**, 375-385.

Ansmann, A., Riebesell, M., Wandinger, U., Weitkamp, C., Voss, E., Lahmann, W., and Michaelis, W.: 1992, 'Combined Raman elastic-backscatter lidar for vertical profiling of moisture, aerosol extinction, backscatter, and lidar ratio', *Appl. Phys*., **B55**, 18-28.

Ansmann, A., Wagner, F., Althausen, D., Müller, D, Herber, A., and Wandinger, U.: 2001, 'European pollution outbreaks during ACE 2: Lofted aerosol plumes observed with Raman lidar at the Portuguese coast', *J. Geophys. Res*., **106**, 20725-20733.

Ansmann A., Wandinger, U., Wiedensohler, A., Leiterer, U.: 1998, 'Lindenberg Aerosol Characterization Experiment 1998 (LACE 98): Overview', *J.Geophys. Res*., **107**, 8129, doi:10.1029/2000JD000233, 2002.

Aron, R.: 1983, 'Mixing height – an inconsistent indicator of potential air pollution concentrations', *Atmos. Environ*., **17**, 2193–2197.

Banta, R. M., Pichugina, Y. L., and Newsom, R. K.: 2003, 'Relationship between low-level jet properties and turbulence kinetic energy in the nocturnal stable boundary layer', *J. Atmos. Sci.*, **60**, 2549-2555.

Baars, H., Ansmann, A., Englemann, R., and Althausen, D.: 2008, 'Continuous monitoring of the boundary-layer top with lidar', *Atmos. Chem. Phys. Discuss*., **8**, 10749 – 10790.

Barthlott, C., Corsmeier, U., Meißner, C., Braun, F., Kottmeier, C.: 2006, 'The influence of mesoscale circulation systems on triggering convective cells over complex terrain', *Atmos. Res*., **81**, 150-175.

Behrendt, A., Wagner, G., Petrova, A., Shiler, M., Pal, S., Schaberl, T., and Wulfmeyer, V.: 2005, 'Modular lidar systems for high-resolution 4-dimensional measurements of water vapor, temperature, and aerosols', in U. N. Singh and Kohei Mizutani (eds.)*, Lidar Remote Sensing for Industry and Environment Monitoring V, Proceedings of SPIE,* 5653, 8-12 November 2004, Honolulu, Hawaii, USA, pp. 220-227.

Behrendt, A., and Reichardt, J.: 2000, 'Atmospheric temperature profiling in the presence of clouds with a pure rotational Raman lidar by use of an interference-filter-based polychromator', *Appl. Opt*., **39** (9), 1372-1378.

Behrendt, A., Nakamura, T., Onishi, M., Baumgart, R., Tsuda, T.: 2002, 'Combined Raman lidar for the measurement of atmospheric temperature, water vapor, particle extinction coefficient, and particle backscatter coefficient', *Appl. Opt*., **36**, 7657-7666.

Behrendt, A., Wulfmeyer, V., Pal, S., Wieser, A., Radlach, M., Riede, A., Schiller, M., Träummer, K., Wagner, G., and Fix, A.: 2008, 'Synergetic measurements with three collocated scanning lidars: water vapor DIAL, rotational Raman lidar, and Doppler lidar', *Reviewed and Revised Papers of the 24th International Laser Radar Conference (ILRC),* 24 - 28 June 2008, Boulder, Colorado, ISBN 978-0-615-21489-4.

Beyrich, F. and Gryning, S.: 1998, 'Estimation of the entrainment zone depth in a shallow convective boundary layer from sodar data', *J. Appl. Meteorol.,* **37**, 255-268.

Bissonnette, L. R., and Hutt, D. L.: 1990, 'Multiple scattering lidar'*, Appl. Opt*., **29**, 5045–5046.

Bissonnette, L. R.: 1986, 'Sensitivity analysis of lidar inversion algorithms', *Appl. Opt*., **25**, 2122-2125.

Bjerg, B., Kai, P., Morsing, S., and Takai, H.: 2004, 'CFD analysis to predict close range spreading of ventilation air from livestock buildings', Agricultural Engineering International: the CGIR Journal of Scientific Research and Development. Manuscript BC 03014. Vol. VI. August, 2004.

Boers, R., Melfi, S. H., Palm, S. P.: 1995, 'Fractal nature of the planetary boundary layer depth in the trade-wind cumulus regime', *Geophys. Res. Lett*., **22** (13), 1705-1708.

Boers, R., Eloranta, E. W., and Coulter, R. L.: 1984, 'Lidar observations of mixed layer dynamics: Tests of parameterized entrainment models of mixed layer growth rate', *J. Appl. Meteorol.*, **23**, 247-266.

Boheren, C. and Huffmann, D.: 1983, 'Absorption and scattering of light by small particles', Wiley, New York, pp 530.

Brewer, Wm. A., Tucker, S. C., and Hardesty, R. M.: 2008, 'Evaluation of a motion stabilization system using random errors in wind profiles measured by a ship based scanning Doppler lidar', *Reviewed and Revised Papers of the 24th International Laser Radar Conference (ILRC),* 24 - 28 June 2008, Boulder, Colorado, ISBN 978-0-615-21489-4.

Brooks, I. M.: 2003, 'Finding boundary layer top: Application of a wavelet covariance transform to lidar backscatter profiles', *J. Atmos. Oceanic. Tech.,* **20**, 1092-1105.

Bucholtz, A.: 1995, 'Rayleigh-scattering calculations for the terrestrial atmosphere', *Appl. Opt.*, **34** (15), 2765-2773.

Charlson, R. J., Schwartz, S. E., Hales, J. M., Cess, R. D., Coakley Jr, J. A., Hansen, J. E., and Hofmann, D. J.: 1992, 'Climate forcing by anthropogenic aerosols', *Science*, **255** (5043), 423-430.

Chazette, P., Couvert, P., Randriamiarisoa, H., Sanak, J., Bonsang, B., Moral, P., Berthier, S., Salanave, S., and Toussaint, F. : 2005, 'Three-dimensional survey of pollution during winter in French Alps valley', *Atmos. Environ*., **39** (6), 1035-1047.

Chlond, A. and Wolkau, A.: 2000, 'Large-eddy simulation of a nocturnal stratocumulus-topped marine atmospheric boundary layer: An uncertainty analysis', *Boundary-layer. Meteorol*., **95**, 31-55.

Cohn, S. A., Mayor, S. D., Grund, C. J., Weckwerth, T. M., and Senff, C. J.: 1998, 'The lidars in flat terrain (LIFT) experiment' , *Bull. Amer. Meteorol. Soc.,* **79** (7), 1329–1343.

Cohn, S. A. and Angevine, W. M.: 2000, 'Boundary layer height and entrainment zone thickness measured by lidars and wind-profiling radars', *J. Appl. Meteorol.,* **39**, 1233-1247.

Collis, R. T. H.: 1966, 'LIDAR: A new atmospheric probe', *Q. J. R. Meteorol. Soc*., **92**, 220–230.

COPS Field Report, Editors: V. Wulfmeyer and A. Behrendt and the COPS Investigators 2007, https://www.uni-hohenheim.de/cops/further_reading/further_reading.htm

Cooley, J. W. and Tukey, J. W.: 1965, 'An Algorithm for Machine Calculation of Complex Fourier Series', *Math. Comput.* **19**, 297–301.

Couvreux, F., Guichard, F., Redelsperger, J. L., Kiemle, C., Masson, V., Lafore, J. P., and Flamant, C.: 2005, 'Water vapor variability within a convective boundary-layer assessed by large-eddy simulations and IHOP_2002 observations', *Quart. J. Roy. Meteorol. Soc.*, **131**, 2665-2693.

Daubechies, I., Mallat, S., and Willsky, A.: 1992, 'Introduction to the special issue on wavelet transforms and multiresolution signal analysis', *IEEE Trans. Inf. Theory.,* **38** (2), 528–531.

Davis, A., Marshak, A., Wiscombe, W., and Cahalan, R.: 1994, 'Multifractal characterizations of nonstationarity and intermittency in geophysical fields: Observed, retrieved, or simulated', *J. Geophys. Res*., **99**, 8055-8072.

Davis, K. J., Lenschow, D. H., Oncley, S. P., Kiemle, C., Ehret, G., and Giez, A.: 1997, 'Role of entrainment in surface–atmosphere interactions over a boreal Forest', *J. Geophys. Res.,* **102** (29), 29218– 29230.

Davis, K. J., Gamage, N., Hagelberg, C. R., Kiemle, C., Lenschow, D. H., and Sullivan, P. P.: 2000, 'An objective method for deriving atmospheric structure from airborne lidar observations', *J. Atmos. Oceanic. Tech.,* **17**, 1455–1468.

Dayan, U., Shenhav, R., and Graber, M.: 1988, 'The spatial and temporal behavior of the mixed layer in Israel', *J. Appl. Meteor.,* **27,** 1382– 1394.

Deardorff, J. W., Willis, G. E., and Lilly, D. K.: 1969, 'Laboratory investigation of nonsteady penetrative convection', *J. Fluid Mech.*, **35**, 7-31.

Deardorff, J. W., Willis, G. E., and Stockton, B. H.: 1980, 'Laboratory studies of the entrainment zone of a convectively mixed layer', *J. Fluid Mech.,***100**, 41-64.

Demoz, B. B., Starr, D. O'C., Chan, K. R., and Bowen, S. W.: 1997, 'Wavelet analysis of dynamical processes in Cirrus', *J. Geophys. Res*., **25** (9), 1347-1350.

Denby, B., Schaap, M., Segers, A., Builtjes, P., and Horálek, J.: 2008, 'Comparison of two data assimilation methods for assessing PM10 excedances on the European scale', *Atmos. Env*., doi:10.1016/j.atmosenv.2008.05.058

Devara, P. C. S., and Pal, S.: 2004, 'Wavelet analysis of 14 years' aerosol lidar observations over Pune, India' *Reviewed and Revised Papers of the 22nd Internatinal Laser Radar Conference (ILRC)*, Mateara, Italy, July, 2004.

De Wekker, S. F. J., Kossmann, M., and Fiedler, F.: 1997, 'Observations of daytime mixed layer heights over mountainous terrain during the TRACT field campaign', in Proceedings of the 12th AMS Symposium on Boundary Layers and Turbulence, Vancouver, BC, Canada, American Meteorological Society, 45 Beacon Street, Boston, MA, pp. 498–499.

Dong, H., Zhu, Z., Shang, B., Kang, G., Zhu, H., and Xin, H.: 2007, 'Greenhouse gas emissions from swine barns of various production stages in suburban Beijing, China', *Atmos. Env*., **41**, 2391-2399.

Dupont, E., Menut, L. B., Pelon, C. J.: 1999, 'Comparison between the atmospheric boundary layer in Paris and its rural suburbs during the ECLAP experiment', *Atmos. Environ.,* **33**, 979-994.

Eloranta, E. W., and Forrest, D. K.: 1992, 'Volume-imaging lidar observations of the convective structure surrounding the flight path of a flux-measurement aircraft', *J. Geophys. Res.*, **97**, 18383-18393.

Engelmann, R., Wandinger, U., Ansmann, A., Müller, D., Žeromskis, E., Althausen, D., and Wehner, B.: 2008, 'Lidar observations of the aerosol vertical flux in the planetary boundary layer', *J. Atmos. Ocean. Tech*., accepted.

Esler, J. G., and Polvani, L. M.: 2003, 'Kelvin-Helmholtz instability of potential vorticity layers: a route to mixing', *J. Atmos. Sci*., **61**, 1392-1405.

Farge, M.: 1992, 'Wavelet transform and their applications to turbulence', *Annu. Rev. Fluid Mech.,* **24**, 395–457.

Fernald, G. F.: 1984, 'Determination of Aerosol Height Distribution by Lidar', *Appl. Opt.*, **23** (5), 652-653.

Fernando, H. J. S.: 1991, 'Turbulent mixing in stratified fluids', *Ann. Rev. Fluid. Mech*., **23**, 455-493.

Flamant, C., Pelon, J., Flamant, P. H., Durand, P.: 1997, 'Lidar determination of the entrainment zone thickness at the top of the unstable marine boundary layer', *Boundary-Layer Meteorol*., **83**, 247-284.

Forster, P., and co-authors.: 2007, 'Changes in atmospheric constituents and radiative forcing', Ch. 2 in IPCC fourth assessment report 2007.

Freie Universität Berlin (2005). Europaeische wetterkarte. www.wetterkarte.de

Fraigneau, Y., Gonzalez, M., and Coppalle, A.: 1996, 'The influence of turbulence upon the chemical reaction of nitric oxide released from a ground source into ambient ozone', *Atmos. Env*., **30** (9), 1467-1480.

Frey, H. U., Mende, S. B., Arens, J. F., McCullough, P. R., Swenson, G. R.: 2000, 'Atmospheric gravity wave signatures in the infrared hydroxyl OH airglow', *J. Geophys. Res*., **27** (1), 41-44

Fritts, D. C., Nappo, C., Riggin, D. M., Balsley, B. B., Eichinger, W. E., and Newsom, R. K.: 2003, 'Analysis of ducted motions in the stale nocturnal boundary layer during CASES-99', *J. Atmos. Sci*., **60**, 2450-2472.

Gall, R. L., Williams, R. T., and Clark, T. L.: 1988, 'Gravity Waves Generated during Frontogenesis', *J. Atmos. Sci.,* **45**, 2204–2219.

Gamage, N. and Hagelberg, C.: 1993, 'Detection and analysis of micro fronts and associated coherent events using localized transforms', *J. Atmos. Sci.,* **50**, 750–756.

Ghan, S. J., and Schwartz, S. E.: 2007, 'Aerosol properties and processes', *Bull. Am. Metorol. Soc*., **88**, 1059-1083.

Gobbi, G. P., Barnaba, F., Giorgi, R., Santacasa, A.: 2000, 'Altitude-resolved properties of a Saharan dust event over the Mediterranean', *Atmos. Env.*, **34**, 5119 - 5127.

Godowitch, J. M.: 1986, 'Characteristics of vertical turbulent velocities in the urban convective boundary layer', *Boundary-Layer Meteorol*., **35**, 387-407.

Gong, W., Bouchet, V. S., Makar, P. A., Moran, M. D., Gong, S., and Leaitch, W. R.: 2007, in Air pollution and its application XVII, Springer US, pp 553-561, 10.1007/978-0-387-68854-1_59.

Grzeschik, M., Bauer, H.-S., Wulfmeyer, V., Engelbart, D., Wandinger, U., Mattis, I., Althausen, D., Engelmann, R., Tesche, M., and Riede, A.: 2008, 'Four-dimensional analysis of water vapor Raman lidar data and their impact on mesoscale forecasts', *J. Atmos. Oceanic Technol*., in press.

Groenemeijer, P., Barthlott, C., Behrendt, A., Corsmeier, U., Handwerker, J., Kohler, M., Kottmeier, Ch., Mahlke, H., Pal, S., Radlach, M., Trentmann, J., Wieser, A., Wulfmeyer, V.: 2008, 'Observations of kinematics and thermodynamic structure surrounding a convective storm cluster over a low mountain range', *Mon. Wea. Rev*., (in press).

Grund, C. J., and Sandberg, S. P.: 1996, 'Depolarization and backscatter lidar for unattended operation', Paper presented at the *18th International Laser Radar Conference*, OSA, Berlin, Germany, July 22-26, 1996.

Hägeli, P., Steyn, D. G., and Strawbridge, K. B.: 2000, 'Spatial and temporal variability of mixed layer depth and entrainment zone thickness', *Boundary-Layer Meteorol*., **97**, 47- 71.

Hartung, J., Seedorf, J., Trickl, T., and Gronauer, H.: 1998, 'Emission and distribution of particulates from a piggery with a central air exhaust', *Dtsch. Tierärzt. Wschr*., **105**, 244-245.

Seedorf, J., Hartung, J., Schröder, M., Linkert, K. H., Pedersen, S., Takai, H., Johnsen, J. O., Metz, J. H. M., Groot Koerkamp, P. W. G., Uenk, G. H., Phillips, V. R., Holden, M. R., Sneath, R. W., Short, J. L., White, R. P., Wathes, C. M.: 1998, 'Concentrations and emissions of airborne endotoxins and microorganisms in livestock buildings in Northern Europe*, J. Agric. Eng. Res.,* **70**, (1), 97-109.

Heederik, D., Brouwer, R., Biersteker, K., and Boleij, S. M.: 1991, 'Relationship of airborne endotoxin and bacteria levels in pig farms with the lung function and respiratory symptoms of farmers', *Int. Arch. Occup. Environ. Health.*, **62**, 595-601.

Heneghan, C., and McDarby, G.: 2000, 'Establishing the relation between detrended fluctuation analysis and power spectral density analysis for stochastic processes', *Phys. Rev. E.,* **62**, 6103-6110.

He, Q. S., Mao, J. T., Chen, J. Y., Hu, Y. Y.: 2006, 'Observational and modeling studies of urban atmospheric boundary-layer height and its evolution mechanisms', *Atmos. Environ.,* **40**, 1064-1077.

Hiscox, A. L., Nappo, C. J., Miller, D. R.: 2006, 'On the use of lidar images of smoke plumes to measure dispersion parameters in the stable boundary layer', *J. Atmos. Ocean. Tech.*, **23**, 1150-1154.

Holmén, B. A., Eichinger, W. E., and Flocchini, R. G.: 1998, 'Application of elastic lidar to PM_{10} emissions from agricultural nonpoint sources', *Environ. Sci. Technol*., **32**, 3068-3076.

Holmén, B. A., James, T. A., Lowell, L. A., and Flocchini, R. G.: 2001a, 'Lidar-assisted measurement of PM10 emissions from agricultural tiling in California's San Joaquin Valley- Part I: lidar', *Atmos. Env.*, **35**, 3251-3264.

Holmén, B. A., James, T. A., Lowell, L. A., and Flocchini, R. G.: 2001b, 'Lidar-assisted measurement of PM_{10} emissions from agricultural tiling in California's San Joaquin Valley- Part II: emission factors', *Atmos. Env.*, **35**, 3265-3277.

Holton, J. R.: 1992, An introdction to dynamic meteorology, 3rd edition, Atmospheric science, WA 98195.

Hu, K., Ivanov, P. Ch., Chen, Z., Carpena, P., and Stanley, H. E.: 2001, 'Effect of trends on detrended fluctuation analysis', *Phys. Rev.* E., **64**, 011114.

Hudgins, L., Friehe, C. A., Mayer, M. E.: 1993, 'Wavelet transforms and atmospheric turbulence', *Phys. Rev. Lett*., **71**, 3279-3282.

Hurst, H. E., Black, B. P., and Simaika, Y. M.: 1965, 'Long-term-storage: an experimental study', Constable.

IIASA 2001: International Institute for Applied Systems Analyses: Rains PM Modul, IIASA, Laxenburg, Österreich, Internet: http://www.iiasa.ac.at/~rains/PM/pm-home.html (letzter Zugriff 4.9.07).

ILRC 2008: *Reviewed and Revised Papers of the 24th International Laser Radar Conference (ILRC),* 24 - 28 June 2008, Boulder, Colorado, , ISBN 978-0-615-21489-4.

Intergovernmental Panel on Climate Change, 2001: IPCC Third Assessment Report –Climate Change 2001: The scientific basis. Eds. J. T. Houghton et al. Cambridge University Press, Cambridge, ISBN 0521807670, (http://www.ipcc.ch/pub/).

IPCC 2007: Climate change 2007: The Physical Science Basis, Summary for Policymakers, February, 5th, 2007.

IPCC, *Climate Change, 1995 : The Science of Climate Change* , Cambridge University Press, 1996, ed., J. T. Houghton, L. G. Meira Filho, B. A. Callander, N. Harris, A. Kattenberg, and K. Maskell.

Ivanova, K., Shirer, H. N., Clothiaux, E. E., Kitova, N., Mikhalev, M. A., Ackerman, T. P., Ausloos, M.: 2002, 'A case study of stratus cloud base height multifractal fluctuations', *Physica A*, **308**, 518-532.

Jongbloed, A. W. and Lenis, N. P.: 1998, 'Environmental concerns about animal manure', *J. Anim. Sci.,* **76**, 2641-2648.

Khain, A., Rosenfeld, D., and Pokrovsky, A.: 2005, 'Aerosol impact on the dynamics and microphysics of deep convective clouds', *Q. J. R. Meteorol*., **131**, 2639-2663.

Khanna, S., and Brasseur, J.: 1997, 'Analysis of Monin-Obukhov similarity from large-eddy simulation', *J. Fluid. Mech.*, **345**, 251-286.

Kiemle, C., Ehret, G., Giez, A., Davis, K. J., Lenschow, D. H., and Oncley, S. P.: 1997, 'Estimation of boundary layer humidity fluxes and statistics from airborne differential absorption lidar (DIAL)', *J. Geophys Res.,* **102** , 29189-29203.

Klett, J. D.: 1981, 'Stable analytical inversion solution for processing lidar returns', *Appl. Opt.*, **20** (2), 211-220.

Kolmogorov, A. N.: 1941, 'The local structure of turbulence in incompressible viscous fluid for very large Reynolds numbers', Dokalady, **ANSSSR 30**, 301-304.

Kossmann, M., Vögtlin, R., Corsmeier, U., Vogel, B., Fiedler, F., Binder, H.-J., Kalthoff, N., and Beyrich, F.: 1998, 'Aspects of the Convective Boundary Layer Structure over Complex Terrain', *Atmos. Environ*., **32**, 1323–1348.

Kovalev, V.A.: 1995, 'Sensitivity of the lidar solution to errors of the aerosol backscatter-to-extinction ratio: influence of a monotonic change in the aerosol extinction coefficient', *Appl. Opt.*, **34**, 3457- 3462.

Kovalev, V., and Eichinger, W. E.: 2002, 'Elastic lidar: Theory, Practice, and Analysis method', Wiley.

Kunz, G. J., de Leeuw, G., Becker, E., O'Dowd, C. D.: 2002, 'Lidar observations of atmospheric boundary layer structure and sea spray aerosol plumes generation and transport at Mace Head, Ireland, PARFORCE experiment', *J. Geophys. Res*., **107**(D19), 8106-8116.

Kunz, G. J.: 1996, 'Transmission as an input boundary value for an analytical solution of a single-scatter lidar equation', *Appl. Opt*., **35**, 3255-3260.

Lalas, D. P. and Einaudi, F.: 1976, 'On characteristics of gravity waves generated by atmospheric shear layers', *J. Atmos. Sci*., **33**, 1248–1259.

Lammel G., Schneider F., Brüggemann E., Gnauk T., Röhrl A., Wieser, P.: 2004, 'Aerosols emitted from a livestock farm in southern Germany', *Water Air Soil Poll*., **154**, 313-330.

Lammel., G., Engelhardt, T., Leip, A., Neusüß, C., Röhrl A., Wehner, B., Wiedensohler, A., Wieser, P.: 2005, 'Transformation of aerosol chemical properties due to transport over a city', *J. Atmos. Chem.*, **51**, 95-117.

Lammel, G., Wulfmeyer, V., Pal, S., Valdebenito, A. M., Behrendt, A., Müller, F, Radlach, M.: 2006, 'Aerosole aus der Nutztierhaltung (Aerosols in Livestock Farming), Förderkennzeichen' ZO3K23005 and ZO3K23007, Interim Report, 2007.

Lammel, G., Wulfmeyer, V., Pal, S., Valdebenito, A. M., Behrendt, A., Müller, F, Radlach, M.: 2007, 'Aerosole aus der Nutztierhaltung (Aerosols in Livestock Farming), Förderkennzeichen: ZO3K23005 and ZO3K23007, Jan, 2007. http://bwplus.fzk.de/berichte/SBer/ZO3K23005+ZO3K23007SBer.pdf

Lange, K. de., Nyachoti, M., and Birkett, S. : 1999, 'Manipulation of diets to minimize the contribution to environemntal pollution', *Advances in Pork Production,* 10, 173-186.

Larsen, M., Swartz, W., and Woodman, R.: 1982, 'Gravity-wave generation by thunderstorms observed with a vertically pointing 430MHz radar', *Geophys. Res. Lett.* **9**, 571–574.

Larson, V. E., Wood, R., Field, P. R., Golaz, J. C., Vonder Haar, T. H. and Cotton, W. R.: 2001, 'Small-scale and mesoscale variability of scalars in cloudy boundary layers: one-dimensional probability density functions', *J. Atmos. Sci.,* **58**, 1978-1994.

Lee, J. and Zhang, Y.: 2006, 'Determination of ammonia and odor emissions from animal buildings dusts', 2006 ASAE Annual Meeting.

Lenschow, D. H., Wulfmeyer, V., and Senff, C. J.: 2000, 'Measuring second-through fourth-order moments in noisy data', *J. Atmos. Oceanic. Tech.*, **17**, 1330-1347.

Lenschow, D. H., Stankov, B. B., and Mahrt, L.: 1979, 'The rapid morning boundary-layer transition', *J. Atmos. Sci*., **36**, 2108-2124.

Lilley, M., Lovejoy, S., Strawbridge, K. B., Schertzer, D. and Radkevich, A.: 2008, 'Scaling turbulent atmospheric stratification. II: Spatial stratification and intermittency from lidar data', *Q. J. R. Meteorol*., **134**, 301-315.

Lovejoy, S., Schertzer, D. Lilley, M., Strawbridge, K. B., and Radkevich, A.: 2008, 'Scaling turbulent atmospheric stratification. I: Turbulence and waves', *Q. J. R. Meteorol*., **134**, 277-300.

Mackiewicz, B.: 1998, 'Study on exposure of pig farm workers to bioaerosols, immunologic reactivity and health effects', *Ann. Agric. Environ. Med.,* **5**, 169-175.

McFarlane, N. A.: 1987, 'The effect of orographically excited gravity-wave drag on the circulation of the lower stratosphere and troposphere', *J. Atmos. Sci*., **44**, 1175–1800.

Mahrt, L.: 1991, 'Boundary layer moisture regimes', *Quart. J. Roy. Meteorol. Soc.,* **117**, 151-176.

Matthias, I., et al., 2004: Multiyear aerosol observations with dual wavelength Raman lidar in the framework of EARLINET. *J. Geophys. Res*., **109**, D13203, doi:10.1029/2004JD004600.

Mayor, S. D.: 2001, 'Volume imaging lidar observations and large-eddy simulations of convective internal boundary layers', PhD thesis, University of Wisconsin- Madison.

Mayor, S. D., Spalart, P. R., Tripoli, G. J.: 2003, 'Application of a perturbation recycling method in the large-eddy simulation of a mesoscale convective internal boundary layer', *J. Atmos. Sci*., **59**, 2385-2395.

Mayor, S. D., and Spuler, S. M.: 2004, 'Raman-shifted eye-safe aerosol lidar', *Appl. Opt.*, **43**, 3915-3924.

McKendry, I. G., Steyn, D. G., Lundgren, J., Hoff, R. M., Strapp, W., Anlauf, K., Froude, F., Martin, J. B., Banta, R. M., and Oliver, L. D.: 1997, 'Elevated ozone layers and vertical down-mixing over the lower Frazer valley , BC', *Atmos. Environ*., **31**, 2135-2146.

Meißner , C., Kalthoff, N., Kunz, M., and Adrian, G.: 2007, 'Initiation of shallow convection in the Black Forest mountains', *Atmos. Res*., **86**, 42-60.

Melfi, S. H., Spinhirne, J. D., Chou, S. H., and Palm, S. P.: 1985, 'Lidar observations of vertically organized convection in the planetary boundary layer over the ocean', *J. Climate Appl. Meteorol.,* **24**, 806-821.

Melfi, S. H., Whiteman, D., and Ferrare, R.: 1989, 'Observation of atmospheric fronts using Raman lidar moisture measurements', *J. Appl. Meteorol*., **28**, 789-806.

Menut, L., Flamant, C., Pelon, J., and Flamant, P. H.: 1999, 'Urban boundary-layer height determination from lidar measurements over the Paris area', *Appl. Opt.,* **38**, 945-954.

Menzies, R. T., and Tratt, D. M.: 1995, 'Evidence of seasonally dependent stratosphere-troposphere exchange and purging of lower stratospheric aerosol from multiyear lidar data set', *J. Geophys. Res*., **100** (D2), 3139-3148.

Meyers, S. D., Kelly, B. G., O'Brien, J. J.: 1993, 'An introduction to wavelet analysis in oceanography and meteorology: With application to the dispersion of Yanai waves', *Mon. Wea. Rev.,* **11**, 2858-2866.

Moeng, C. H., and Wyngaard, J. C.: 1984, 'Statistics of conservative scalars in the convective boundary layer', *J. Atmos. Sci.,* **41**, 3161-3169.

Moeng, C. H., and Wyngaard, J. C.: 1989, 'Evaluation of turbulent transport and dissipation closures in second-order modeling', *J. Atmos. Sci*., **46**, 2311-2330.

Mueller, D., U. Wandinger, D. Althausen, I. Mattis, and A. Ansmann, A.: 1998, 'Retrieval of physical particle properties from lidar observations of extinction and backscatter at multiple wavelengths', *Appl. Opt*., **37**, 2260–2263.

Mueller, G., and Chlond, A.: 1996, 'Three-dimensional numerical study of cell boarding during cold-air-outbreaks', *Boundary Layer. Meteorol*., **81**, 289-323.

Murayama et al.: 2001, 'Ground-based network observation of Asian dust events of April 1998 in East Asia', *J. Geophys. Res*., **106**, 18345–18360.

Newsom, R. B. and Banta, R. M.: 2003, 'Shear-flow instability in the stable boundary layer as observed by Doppler lidar during CASES-99', *J. Atmos. Sci.,* **60**, 16-33.

Otte, M. J., and Wyngaard, J. C.: 2001, 'Stably stratified interfacial layer turbulence from large-eddy simulation', *J. Atmos. Sci.*, **58**, 3424 –3442.

Pahlow, M., Kleissl, J., Parlange, M. B., Ondov, J. M., Harrison, D.: 2005, 'Atmospheric boundary-layer structure observed during a haze event due to Forest-fire smoke', *Boundary-Layer Meteorol*., **114**, 53-70.

Pal, S., Behrendt, A., Bauer, H., Radlach, M., Riede, A., Schiller, M., Wagner, G. and Wulfmeyer, V.: 2008, '3-dimensional observations of atmospheric variables during field campaign COPS'*, IOP Conference series: Earth and environmental sciences,* **1**, 012031, (http://www.iop.org/EJ/journal/ees).

Pal, S., Behrendt, A., Radlach, M., Schaberl, T., Wulfmeyer, V.: 2006, 'Eye safe scanning aerosol lidar at 355 nm', *Reviewed and Revised Papers of the 23rd International Laser Radar Conference (ILRC 2006).*

Pal, S.: 2004, 'LIRAD (LIdar and RADiometer) Sounding of the Atmospheric Aerosols and Pre-cursor Gases over Pune, India' , Master thesis, Department of Physics, University of Pune, Pune, India.

Patadia, F., Gupta, P., and Christopher, S. A.: 2008, 'First observational estimates of global clear sky shortwave aerosol direct radiative effect over land', *Geophys. Res. Lett*., **35**, doi:10.1029/2007GL032314

Pappalardo G., Amodo, A., Mona, L., and Pandolfi, M.: 2005, 'Systematic measurements of the aerosol extinction-to-backscatter ratio', *Lidar Remote Sensing for Industry and Environmental Monitoring* V, edited by Upendra N. Singh, Kohei Mizutani, Proceedings of SPIE, Vol. 5653, 77-87, doi: 10.1117/12.578809

Plamen, S., Skakalova, T. S., Kolev, I. N., and Ludwig, F. L.: 2002, 'Lidar investigations of the temporal and spatial distribution of atmospheric aerosols', *J. Appl. Meteorol.,* **41** (5), 528-541.

Platt, C. M.: 1978, 'Lidar backscatter from horizontal ice crystal plates', *J. Appl. Meteorol.,* **17**, 482-2488.

Petrova, A.: 2008, 'Development of an eye-safe solid-state tunable laser transmitter around 1.45 μm based on Cr4+:YAG crystal for lidar applications', PhD Thesis, University of Hohenheim, Stuttgart, Germany.

Peng, C.-K., Buldyrev, S. V., Havlin, S., Simmons, M., Stanley, H. E., and Goldberger, A. L.: 1994, 'Mosaic organization of DNA nucleotides', *Phys. Rev. E.,* **49**, 1685-1689.

Pelletier, J. D.: 1997, 'Kardar-Parisi-Zhang scaling of the height of the convective boundary layer and multifarctal structure of cumulus cloud fields', *Phys. Rev. Lett.*, **78** (13), 2672-2675.

Perrier, V., Philopovitch, T., and Basdevant, C.: 1995, 'Wavelet Spectra compared to Fourier Spectra', *Journal Math. Phys .,* **36**, 1506-1519.
in mountain valleys', *J. Appl. Meteol.*, **41**, 528-541.

Piironen, P., and Eloranta, E. W.: 1994, 'High spectral resolution lidar', *Opt. Lett.,* **19**, 234-244.

Powell, D. M., Reagan, J. A., Rubio, M. A., Erxleben, W. H., and Spinhirne, J. D.: 2000, 'ACE-2 multiple angle micro-pulse lidar observations from Las Galletas, Tenerife, Canary Islands', *Tellus B.*, **52** (2), 652-661.

Powell, D. C., and Elderkin, C. E.: 1974, 'An investigation of the application of Taylor's hypothesis to atmospheric boundary layer turbulence', *J. Atmos. Sci*., **31**, 990-1002.

Praml, G. J., Zeitler-Feicht, M. H., Hartmann, A. L., and Riedel, H.: 1990, 'Dust exposure of man and animal in swine confinement buildings: Benefits of full shift continuous registration', *J. Aerosol. Sci.*, **21**, S751-S754.

Prueger, J. H., Eichinger, W. E., Hipps, L. E., Hatfield, J. L., Cooper, D. I.: 2008, 'Air flow distortion and turbulence statistics near an animal facitliy', *Atmos. Env*., doi:10.1016/j.atmosenv.2007.08.048

Radkevich, A., Lovejoy, S., Strawbridge, K. B., Schertzer, D. and Lilley, M.: 2008, 'Scaling turbulent atmospheric stratification. III: Space-time stratification of passive scalars from lidar data', *Q. J. R. Meteorol*., **134**, 317-335.

Radlach, M., Behrendt, A., Pal, S., Schaberl, T., and Wulfmeyer, V.: 2006, 'Scanning rotational Raman lidar at 355 nm for the measurement of tropospheric temperature fields' *Reviewed and Revised Papers of the 23rd International Laser Radar Conference (ILRC),* 22 - 27 July 2006, Nara, Japan.

Radlach, M., Behrendt, A., Wulfmeyer, V.: 2008a, 'Scanning rotational Raman lidar at 355 nm for the measurement of tropospheric temperature fields', *Atmos. Chem. Phys*., **8**, 159-169, http://www.atmos-chem-phys.net/8/159/2008/acp-8-159-2008.pdf.

Radlach, M., Behrendt, A., Pal, S., Riede, A., and Wulfmeyer, V.: 2008b, 'State-of-the-art daytime scanning temperature measurements by rotational Raman lidar' *Reviewed and Revised Papers of the 24th International Laser Radar Conference (ILRC),* 24 - 28 June 2008, Boulder, Colorado, ISBN 978-0-615-21489-4

Radlach, M.: 2008c, 'A scanning eye-safe rotational Raman lidar in the ultraviolet for measurements of tropospheric temperature fields', PhD thesis submitted to University of Hohenheim, Germany.

Rotach, M., Andretta, M., Calanca, P., Weigel, A. P., and Weiss, A.: 2008, 'Boundary layer characteristics and turbulent exchange mechanisms in highly complex terrain', *Act. Geophys*., **56**, 194-219.

Rotach, M.W., and Zardi, D.: 2007, **'**On the boundary layer structure over highly complex terrain:key findings from map', *Q. J. R. Meteorol.,* **133**, 937-948.

Russell, P. B., Uthe, E. E., Ludwig, F. L., and Shaw, N. A.: 1974, 'A comparison of atmospheric structure as observed with monostatic acoustic sounder and lidar techniques', *J. Geophys. Res*., **79**, 5555-5566.

Ryalander, R., Donham, K. J., Peterson, Y. (eds).: 1986, 'Health effects of organic dust in the farm environment', *In: Proceedings of an International Workshop,* Skokloster, Sweden, April 23-25, 1985. *Am. J. Ind. Med*., **10**, 193-340.

Salmond, J. A.: 2005, 'Wavelet analysis of intermittent turbulence in a very stable nocturnal boundary layer: implications for the vertical mixing of ozone', *Bound. Layer. Meterol*., **114**, 463-488.

Sasano, Y, Browell, E. V, Ismail, S.: 1985, 'Error caused by using a constant extinction/backscattering ratio in the lidar solution', *Appl Opt,* **24**, 3929-3932.

Sasano, Y.: 1996, 'Tropospheric aerosol extinction coefficient profiles derived from scanning lidar measurements over Tsukuba, Japan, from 1990 to 1993', *Appl. Opt*., **35**, 4941-4952.

Schiller, M., Wagner, G., and Wulfmeyer, V.: 2007, 'A high-power, single-frequency Ti-Sapphire laser for water vapor DIAL', *In: Conference on Lasers and Electro-Optics (CLEO-2007)*, 6-11 May, 2007, Baltimore, Maryland, USA.

Schiller, M.: 2009, 'High-power laser transmitter for ground-based and airborne water-vapor measurements in troposphere', PhD thesis, University of Hohenheim.

Schwemmer, G. K., Miller, D. O., Wilkerson, T. D., and Lee, S.: 2004, 'Lidar data products and applications enabled by conical scanning', in G. Pappalardo, and A. Amodo (eds.), *Reviewed and revised papers presented at 22nd International Laser Radar Conference, 12-16 July 2004*, Matera, Italy, European Space Agency (SP-561), pp. 17-20.

Schotland, R. M.: 1966, Proc. Fourth symp. On remote sensing of the environment, Ann Arbor, MI, Environmental research instiute of Michigan, University of Michigan, 273-283.

Scorer, R. S.: 1997, Dynamics of meteorology and climate, Wiley, Chichester, UK, 686 pp.

Seibert, P., Beyrich, F., Gryning, S. -E., Joffre, S., Rasmussen, A., and Tercier, P.: 2000, 'Review and intercomparison of operational methods for the determination of mixing height', *Atmos. Environ*., **34**, 1001-1027.

Seifert, P., Engelmann, R., Ansmann, R., Wandinger, U., Mattis, I., Althausen, D., and Fruntke, J.: 2008, 'Characterization of specular reflections in mixed--phase and ice clouds based on scanning, polarization, and Raman lidar', *Reviewed and Revised Papers of the 24th International Laser Radar Conference (ILRC),* 24 - 28 June 2008, Boulder, Colorado, ISBN 978-0-615-21489-4.

Seifert, P., Ansmann, R., Müller, D., Wandinger, U., Althausen, D., Heymsfield, A. J., Massie, S. T., and Schmitt, C.: 2007, 'Cirrus optical properties observed with lidar, radiosonde, and satellite over the tropical Indian Ocean during the aerosol-polluted northeast and clean maritime southwest monsoon', J. Geophys. Res., 112, D17205, doi:10.1029/2006JD008352.

Senff, C. J., Bösenberg, J., and Peters, G.: 1994, 'Measurement of water vapor flux profiles in the convective boundary layer with lidar and Radar-RASS', *J. Atmos. Oceanic. Technol*., **11**, 85-93.

Senff, C. J., Bösenberg, J., Peters, G., and Schaberl, T.: 1996, 'Remote sensing of turbulent ozone fluxes and the ozone budget in the convective boundary layer with DIAL and radar-RASS: A case study', *Contribu. Atmos. Phys.,* **69**, 161-176.

Senff, C. J., Banta, R. M., Darby, L. S., Alvarez, R. J., Sandberg, S. P., Hardesty, R. M., Angevine, W. M.: 2002, 'Ozone distribution and transport in the Houston area: Insights gained by airborne lidar', *Proceedings of AGU Fall Meeting*, *6-10 December 2002*, San Francisco, California, USA, pp. 173.

Sicard, M., Perez, C., Rocadenbosch, F., Baldasano, J. M., and Garcia-Vizcaino, D.: 2006, 'Mixed-layer depth determination in the Barcelona coastal area from regular lidar measurements: Methods, results and limitations', *Boundary Layer Meteorol.*, **119**, 135-157.

Smith, S. A. and Jonas, P. R.: 1997, 'Wavelet analysis of turbulence in cirrus clouds', *Ann. Geophysicae.*, **15**, 1447-1456.

Sorbjan, Z.: 1990, 'Similarity scales and universal profiles of statistical moments in the convective boundary layer', *J. Appl Meteorol.,* **29**, 762-775.

Sorbjan, Z.: 1995, 'Toward evaluation of heat fluxes in the convective boundary layer', *J. Appl. Meteorol*., **34**, 1092-1098.

Sorbjan, Z.: 1996, 'Effects caused by varying the strength of the capping inversion based on a large eddy simulation model of the shear-free convective boundary layer', *J. Atmos. Sci.,* **53**, 101–112.

Soriano, C., Baldasano, J. M., Buttler, W. T., and Moore, K.: 2001, 'Circulatory patterns of air pollutants within the Barcelona air basin in a summertime situation: lidar and numerical approaches', *Boundary-Layer Meteorol*., **98**, 33-55.

Spinhirne, J. D.: 1993, 'Micropulse lidar', *IEEE Trans. Geosci. Remote Sens*., **31**, 48-55.

Spinhirne, J. D., Rall, J. A. R., and Scott, V. S.: 1995a,'Compact eye-safe lidar systems', *Rev. Laser. Eng*., **23**, 112-118.

Spinhirne, J. D., Rall, J. A. R., and Scott, V. S.: 1995b,'Compact eye-safe lidar systems', *Rev. Laser. Eng*., **23**, 26-32.

Spuler, M. S., and Mayor, S.D.: 2005, 'Scanning Eye-Safe Elastic Backscatter Lidar at 1.54 μm', *J. Atmos. Ocean. Tech.*, **22**, 696-703.

Spuler, M. S., and Mayor, S. D.: 2007, 'Raman shifter optimised for lidar at 1.5-micron wavelength', *Appl. Opt*., **46**, 2990-2995.

Strawbridge, K. B., and Snyder, B. J.: 2004, 'Planetary boundary layer height determination during Pacific 2001 using the advantage of a scanning lidar instrument', *Atmos. Environ.,* **38**, 5861-5871.

Stevens, B., and Lenschow, D. H.: 2001, **'**Observations, Experiments and Large-Eddy Simulation', *Bull. Amer. Meteorol. Soc*., **82**, 283–294.

Steyn, D. G., Baldi, M., and Hoff, R. M.: 1999, 'The detection of mixed layer depth and entrainment zone thickness from lidar backscatter profiles', *J. Atmos. Oceanic. Tech.*, **16**, 953– 959.

Stokes, G. M., and Schwartz, S. E.: 1994, 'The Atmospheric Radiation Measurement (ARM) program: Programmatic background and design of the cloud and radiation testbed', *Bull. Amer. Meteor. Soc*., **75**, 1201-1221.

Stull, R. B.: 1988, *An Introduction to Boundary Layer Meteorology*, Kluwer Acad. Publ., Dordrecht, 666 pp.

Stull, R. B. and Eloranta, E. W.: 1984, 'Boundary layer experiment', *Bull. Amer. Meteorol. Soc.,* **65**, 450-456.

Takai, H., Pedersen, S., Johnsen, J. O., Metz, J. H. M., Groot Koerkamp, P. W. G., Uenk, G. H.: 1998, 'Concentrations and emissions of airborne dust in livestock buildings in northern Europe' *J. Agric. Eng. Res.,* **70**, 59–77.

Takano, Y., and Liou, K. L.: 1989, 'Solar radiative transfer in cirrus clouds. Part: Single-scattering and optical properties of Hexagonal ice crystals', *J. Atmos. Sci*., **46**, 3-19.

Talkner, P., and Weber, R. O.: 2000, 'Power spectrum and detrended fluctuation analysis: Application to daily temperatures', *Phys. Rev*., **E62**, 150-160.

Taylor, G. I.: 1921, **'**Diffusion by Continuous Movements', *Proc. London Math. Soc.,* **20,** 196.

Terradellas, E., Soler, M. R., Ferreres, E., Bravo, M.: 2005, 'Analysis of oscillations in the stable atmospheric boundary layer using wavelet methods', *Boun. Lay. Meteor*., **114**, 489-518.

Torrence, C. and Compo, G. P.: 1998, 'A practical guide to wavelet analysis', *Bull. Amer. Meteorol. Soc.,* **79** (1), 61-77.

Trentmann, J., Keil, C., Salzmann, M., Barthlott, C., Bauer, H. -S., Schwitalla, T., Lawrence, M. G., Leuenberger, D., Wulfmeyer, V., Corsmeier, U., Kottmeier, C., and Wernli, H.: 2008, 'Multi-model simulations of a convective situation in low-mountain terrain in central Europe', *Metorol. Atmos. Phys*., DOI 10.1007/s00703-008-0323-6, 1-9.

Turner, B. J., and Leclerc, M. Y.: 1994, 'Conditional sampling of coherent structures in atmospheric turbulence using wavelet transform', *J. Atmos. Ocean. Tech*., **11**, 205-209.

Turner, J. S.: 1973, 'Wave propagation in a turbulent medium', translated from Russian by R. A. Silverman, Dover, New York, 285 pp.

Uccellini, L. W. and Koch, S. E.: 1987, 'The Synoptic Setting and Possible Energy Sources for Mesoscale Wave Disturbances', *Mon. Wea. Rev*. **115**, 721–729.

Vaughan, M., Young, S., Winker, D., Powell, K., Omar, A., Liu, Z., Hu, Y., Hosteler, C.: 2004, 'Fully automated analysis of space-based lidar data: an overview of the CALIPSO retrieval algorithms and data products', in U. N. Singh (ed.)*, Laser Radar Techniques for Atmospheric Sensing, Proceedings of SPIE* 5575, Bellingham, WA, USA, pp. 16-30.

Valdebenito, A. M.: 2008, 'Development and application of a high-resolving atmosphere-microphysics-chemistry model for prediction of aerosol characterisation in the vicinity of sources', PhD thesis submitted to University of Hamburg, Germany.

Venkatram, A.: 1988, 'Vertical dispersion of ground-level releases in the surface layer', *Lectures on Air Pollution Modeling,* A. Venkatram and J. C. Wyngaard, Eds., Amer. Meteor. Soc., 229–265.

Wandinger, U.: 1994, 'Theoretische und experimentelle studien zur messung stratospärischen aerosols sowie zum einfluss der mehrfachstreuung auf wolkenmessungen mit einem polarisations-Raman-lidar. PhD Thesis, University of Hamburg. 125 S.

Wandinger, U., Ansmann, A., Reichardt, J., and Deshler, T.: 1995, 'Determination of stratospheric aerosol microphysical properties from independent extinction and backscattering measurements with a Raman lidar', *Appl. Opt.,* **34** (36), 8315-8329.

Weckwerth, T.M., Wilson, J. W., and Wakimoto, R. M.: 1996, 'Thermodynamic variability within the convective boundary layer due to horizontal convective rolls', *Mon. Weath. Rev*., **124**, 769-784.

Weigel, A. H. P.: 2005, 'On the atmospheric boundary layer over highly complex topography', Diss. ETH No. 15972.

Weinman, J. A.: 1976, 'Effects of multiple scattering on light pulses reflected by turbid atmospheres', *J. Atmos. Sci.*, **33**, 1763-1771.

Weitkamp, C.: 2005, 'Lidar: Range-resolved optical remote sensing of the atmosphere' in Springer Series in Optical Sciences, Springer Netherlands.

Welton, E. J., Campbell, J. R., Spinhirne, J. D., and Scott, V. S.: 2001, 'Global monitoring of clouds and aerosols using a network of micro-pulse lidar systems. In: *Lidar Remote Sensing for Industry and Environmental Monitoring* [Singh, U.N., T. Itabe, and N. Sugimoto (eds.)]. SPIE, Bellingham, WA, pp. 151–158.

Welton, J. E., and Campbell, J. R.: 2002, 'Micropulse lidar signals: Uncertainity analysis', *J. Atmos. Oceanic. Tech*., **19**, 2089-2094.

Westwater, E. R.: 1997, 'Remote sensing of tropospheric temperature and water vapor by integrated observing systems', *Bull. Amer. Meteor. Soc.*, **78**, 1991-2006.

Wulfmeyer, V.: 1999a, 'Investigation of turbulent processes in the lower troposphere with water vapor DIAL and radar-RASS', *J. Atmos. Sci.,* **56**, 1055-1076.

Wulfmeyer, V.: 1999b, 'Investigations of humidity skewness and variance profiles in the convective boundary layer and comparison of the latter with large eddy simulation results', *J. Atmos. Sci.,* **56**, 1077-1087.

Wulfmeyer, V. and Feingold, G.: 2000, 'On the relationship between relative humidity and particle backscattering coefficient in the marine boundary layer determined with differential absorption lidar', *J. Geophys Res.,* **105** (D4), 4729-4741.

Wulfmeyer, V. and Janjic′, T.: 2005, '24-h observations of the marine boundary layer using ship-borne NOAA high-resolution doppler lidar', *J. Appl Meteor.,* **44**, 1723-1744.

Wulfmeyer, V., Behrendt, A., Bauer, H. S., Kottmeier, C., Corsmeier, U., Blyth, A., Craig, G., Schumann, U., Hagen, M., Crewell, S., Di Girolamo, P., Flamant, C., Miller, M., Montani, A., Mobbs, S., Richard, E., Rotach, M. W., Arpagaus, M., Russchenberg, H., Schlüssel, P., König,, M., Gärtner, V., Steinacker, R., Dorninger, M., Turner, D. D., Weckwerth, T., Hense, A., and Simmer, C.: 2008a, 'The convective and orographically-induced precipitation study: a research and development project of the world weather reasearch program for improving quantitative precipitation forecasting in low-mountain regions, *Bull. Amer. Meteor. Soc.* (doi: 10.1175/2008BAMS2367.1).

Wulfmeyer, V., Behrendt, A., Bauer, H.-S., Corsmeier, U., Kottmeier, Craig, G., Ehret, G., Hagen, M., Schumann, U., Volkert, H., Blyth, A., Crewell, S., Di Girolamo, P., Flamant, C., Miller, M., Montani, A., Mobbs, S., Richard., E., Rotach, M. W., Arpagaus, M., Russchenberg, H., Schlüssel, P., König, M., Gärtner, V., Steinacker, R., Dorninger, M., Turner, D. D., Weckwerth, T. : 2008b, 'The convective and orographically-induced precipitation study: A research and development project of the world weather research program', *Reviewed and Revised Papers of the 24th International Laser Radar Conference (ILRC),* 24 - 28 June 2008, Boulder, Colorado, , ISBN 978-0-615-21489-4.

Wulfmeyer, V., Bauer, H.-S., Grzeschik, M., Behrendt, A., Vandenberghe, F., Browell, E. V., Ismail, S., and Ferrare, R.: 2006, '4-dimensional variational assimilation of water vapor differential absorption lidar data. The first case study within IHOP 2002', *Mon. Weath. Rev*., **134**, 1, 209-230.

Wulfmeyer V and Behrendt A (Eds.) and the COPS Investigators.: 2007 COPS Field Report, https://www.uni-hohenheim.de/cops/further_reading/further_reading.htm.

Wieser, P., and Wurster, R.: 1986, 'Application of the laser microprobe mass analysis to particle collections', In: Physical and chemical characterization of individual airborne particles, p. 251-270. Ed. K. R. Spurny, Ellis Horwood Publisher, Chichester, England.

Wyngaard, J. C. and Brost, R. A.: 1984, 'Top-down and bottom-up diffusion of a scalar in the convective boundary layer', *J. Atmos. Sci.,* **41**, 102-112.